Numerical and Theoretical Study of Homogeneous Rotating Turbulence

Lydia Bourouiba
Department of Atmospheric and Oceanic Sciences
McGill University, Montréal
2008

A thesis submitted to McGill University in partial fulfillment of the requirements of the degree of Doctor of Philosophy

Your file Votre référence
ISBN: 978-0-494-66627-2
Our file Notre référence
ISBN: 978-0-494-66627-2

Si la nature n' était pas belle, elle ne vaudrait pas la peine d'être connue, la vie ne vaudrait pas la peine d'être vécue...Poincaré (1908)

Abstract

The Coriolis force has a subtle, but significant impact on the dynamics of geophysical and astrophysical flows. The Rossby number, Ro, is the nondimensional parameter measuring the relative strength of the Coriolis term to the nonlinear advection terms in the equations of motion. When the rotation is strong, Ro goes to zero and three-dimensional flows are observed to two-dimensionalize. The broad aim of this work is to examine the effect of the strength of rotation on the nonlinear dynamics of turbulent homogeneous flows. Our approach is to decompose the rotating turbulent flow modes into two classes: the zero-frequency 2-dimensional (2D) modes; and the high-frequency inertial waves (3D).

First, using numerical simulations of decaying turbulence over a large range of Ro we identified three regimes. The *large Ro regime* is similar to non-rotating, isotropic turbulence. The *intermediate Ro regime* shows strong 3D-to-2D energy transfers and asymmetry between cyclones (corotating) and anticyclones (couter-rotating), whereas at *small Ro regime* these features are much reduced.

We then studied discreteness effects and constructed a kinematic model to quantify the threshold of nonlinear broadening below which the 2D-3D interactions critical to the intermediate Ro regime are not captured. These results allow for the improvement of numerical studies of rotating turbulence and refine the comparison between results obtained in finite domains and theoretical results derived in unbounded domains.

Using equilibrium statistical mechanics, we examined the hypothesis of decoupling predicted in the small Ro regime. We identified a threshold time, $t_\star = 2/\mathrm{Ro}^2$, after

which the asymptotic decoupling regime is no longer valid. Beyond $t_{\star}$, we show that the quasi-invariants of the decoupled model continue to constrain the system on the short timescales.

We found that the intermediate Ro regime is also present in forced turbulence and that interactions responsible for it are nonlocal. We explain a steep slope obtained in the 2D energy spectrum by a downscale enstrophy transfer. The energy of the 2D modes is observed to accumulate in the largest scales of the domain in the long-time limit. This is reminiscent of the "condensation" observed in classical forced 2D flows and magnetohydrodynamics.

Résumé

La force de Coriolis a un effet subtil mais important sur la dynamique des écoulements géophysiques et astrophysiques. Le nombre de Rossby, que l'on note Ro, est le nombre adimensionnel qui caractérise l'importance relative de l'advection nonlinéaire et du terme de Coriolis dans l'équation de conservation de la quantité de mouvement. Un fluide fortement tournant est caractérisé par un Ro qui tend vers 0. Dans cette limite, un fluide initialement tridimensionnel se bi-dimensionalise. L'objectif des présents travaux est d'étudier l'influence de la rotation sur la dynamique nonlinéaire d'un écoulement turbulent homogène. L'approche utilisée consiste en la décomposition des modes de l'écoulement en deux catégories majeures : les modes dont la fréquence linéaire est nulle et qui sont également bidimensionnels (notés 2D) ; et les modes ondes dont la fréquence est non-nulle (notés 3D).

Tout d'abord, nous avons mené une étude basée sur des simulations numériques de fluides en turbulence décroissante et dont le Ro a été varié de façon à couvrir une large gamme de valeurs. Nous avons ainsi identifié trois régimes d'écoulement tournant. Le premier est le *régime à large Ro* qui est similaire aux écoulements turbulents nontournants. Le second est le *régime à Ro intermédiaire* qui est caractérisé par un fort transfert d'énergie 3D-vers-2D et une nette dissymétrie entre tourbillons cycloniques et anticycloniques. Alors que le troisième *régime à petit Ro* est caractérisé par une extinction des transferts 3D-vers-2D, ainsi qu'une réduction de l'asymétrie entre cyclones et anticyclones.

Nous avons ensuite étudié les effets de la discrétisation et construit un modèle

cinématique afin de déterminer le niveau de nonlinéarité et nombre de Ro en dessous duquel les interactions intrinsèques au régime à Ro intermédiaire ne sont pas capturées par un domaine fini donné. D'une part, cette étude permet d'améliorer la planification des simulations de turbulence en rotation. D'autre part, une comparaison entre les résultats obtenus en domaines finis et les théories calculées en domaines infinies sont désormais facilitées.

Nous nous sommes ensuite tournés vers l'outil de mécanique statistique afin d'étudier le troisième régime à petit Ro. Nous avons combiné cet outil théorique à une validation numérique. Nous avons ainsi prouvé que le découplage entre les modes 2D et 3D est observable numériquement et qu'il est valide jusqu'à un temps critique $t_\star = 2/\mathrm{Ro}^2$. Au delà de $t_\star$, le régime de découplage prévu par les théories asymptotiques n'est plus valide. Par contre, un ensemble de quantités qui deviennent quasi-invariantes continuent de jouer un rôle contraignant sur la dynamique rapide.

Enfin, nous avons prouvé que le régime à Ro intermédiaire existe aussi dans les écoulements tournants forcés. Nous avons isolé les interactions clés qui causent ce régime. Il s'agit d'interactions nonlocales (en échelle spatiale) entre modes 3D et 2D. Cette identification nous a ensuite permis d'expliquer la pente du spectre d'énergie des modes 2D de l'écoulement tournant. Nous avons trouvé que cette pente correspond à une zone spectrale de transfert direct d'enstrophie 2D vers les petites échelles. De plus, nous avons montré que l'évolution sur le long terme de la projection bidimensionnelle de l'écoulement tournant a une dynamique similaire à celle d'un écoulement 2D turbulent forcé classique. Cette dernière est connue pour générer une accumulation d'énergie au sein de grandes échelles de structures cohérentes. Ce phénomène parfois appelé "condensation" a également été observé pour certains écoulements magnétohydrodynamiques forcés.

Contributions of Authors

The results of the research I have performed for my Ph.D. are presented in the form four manuscripts. Chapters 3-5 consist of papers published and under review in peer-reviewed journals. Chapter 6 is a manuscript of ongoing work to be submitted shortly. The published paper presented in Chapter 3 is co-authored with Dr. P. Bartello who provided the initial numerical code that I subsequently modified for the project and who performed some editing of the manuscript text. Chapters 4-5 are single-authored.

Statement of originality

The contributions of this thesis to original knowledge are:

- We calculated the transfers between various types of flow modes, namely the vertically averaged 2D and w modes (invariant along the direction of the axis of rotation) and the 3D modes.

- In rotating homogeneous decaying turbulence, we showed the existence of a regime separation between three rotating regimes: the *weakly rotating regime* (previously known to be close to nonrotating turbulence), the intermediate Ro regime, and the small Ro regime (also referred to as asymptotic regime).

  - The intermediate Ro regime is characterized by a peak of 3D to 2D energy transfer, coinciding with a peak of vorticity skewness, both at Rossby numbers Ro≈ 0.2.

  - In the intermediate Ro regime both the large-scale-based Rossby number (calculated using velocity) and the small-scale-based (calculated using vorticity) are shown to be equivalent.

  - The small Ro range (Ro ≤ 0.2) is characterized by a reduction of the energy transfers between the 3D and the 2D modes. The 2D energy evolves as if the 2D modes were decoupled from the 3D modes.

- We studied the effect of discreteness on the quantification of the number of resonant and near-resonant inertial wave interactions between 3D and 2D modes:

we quantified the number of the key interactions as a function of Ro and the truncation wavenumber.

  - The effects of both the size of the domain and the spectral resolution on the number of inertial interactions is clarified
  - The threshold of nonlinear broadening under which the possibility of a freezing of the energy transfers between 3D and 2D modes in a finite domain is determined.

- We derived the statistical mechanical equilibrium of the asymptotic ($Ro \to 0$) truncated rotating equations. We showed that the inviscid horizontal dynamics (perpendicular to the direction of the axis of rotation) of the small Ro range, matches the theoretical equilibrium derived for nondimensional times $t < 2/\mathrm{Ro}^2$.

  - The decoupling between 2D and 3D modes predicted by the asymptotic theories is thus valid and observable until a time $t = 2/\mathrm{Ro}^2$.
  - During the decoupling phase, the 2D energy shows an inverse energy cascade, whereas the w variance and 3D energy cascade horizontally efficiently downscale.
  - The downscale cascade of 3D energy in the vertical direction (parallel to the axis of rotation) is not as efficient as in the horizontal direction.

- The intermediate Ro regime is shown to also exist in forced rotating turbulence and to be robust to changes of forcing schemes and scales. The peak of $3D$ to $2D$ energy transfer is also found to be at $Ro \approx 0.2$.

  - The locality in scale of the nonlinear interactions responsible for the intermediate Ro range and increase of 2D energy are examined. The intermediate Ro range is found to be characterized by dominant nonlocal interactions. These extract energy from small horizontal and large vertical 3D modes and transfer it directly into the large scale 2D modes. The nonlocality of these interactions is shown to be robust to the change of scale of 3D forcing and resolution.

- This nonlocal injection of energy directly into the large horizontal scale 2D modes exlains the steep 2D energy spectra slope observed in the forced simulations of rotating turbulence.
- It is shown that the asymptotic state of the flows in the intermediate Ro range is a state similar to that identified in classical two-dimensional turbulence, where condensation of energy into dominant coherent structures is reached. The hypothetical saturation of 2D energy at long times was not observed.

Acknowledgements

I am grateful to the Natural Sciences and Engineering Research Council (NSERC) for supporting me as a doctoral graduate student and supporting this research. I am grateful to the Consortium Laval-UQUAM-McGill et l'Est du Québec (CLUMEQ) for making available the major computer resources used for this work. I thank both Peter Bartello and David Straub for making available other computer resources. I thank Peter Bartello for providing the initial version of the Boussinesq equations numerical code and I thank him for introducing me to homogeneous turbulence through courses and discussions. I also thank Sherwin Maslowe who through his course introduced me to the tools of perturbation methods. Finally, I am grateful to Marc Vincent, my first fluid dynamics teacher, whose enthusiasm about math and physics, his dedication to his students, and his confidence inspired me, long ago, to dive into the swirling world of fluids.

I am particularly grateful to my thesis supervisor, David Straub, for his light spirited but meticulous approach to research, his open mind, and his enthusiasm and availability in providing constructive feedback and edits while allowing great independence with the project and writing. It has been a great experience to work with him.

I offer many thanks to John Gyakum for his support and encouragement during some of the turbulent parts of this research adventure. I am grateful to Michael Mackey for being an inspiration and role model for young researchers, it has been a privilege to receive his encouragements and mentorship.

I thank Vaughn Thomassin for his particular dedication and kindness when helping me navigate through the administrative labyrinths and for his answers and advices along the way. I also thank Karin Braidwood, Michael Havas and Marc Lanctot for their assistance with the administrative and the unexpected technical *fluctuations* of academic life. I also had useful discussions and good times spent with many other members of the department, including Kyle Spyksma, Michael Waite, Eyad Atallah, Julie Theriault, Barbara Winter, Shawn Milrad, Blaise Gauvin St-Denis, Ruben Santos, to name a few.

Of course, the joy at work would have not been possible without the joys of the life outside work. My Ph.D. years have been remarkable thanks to the love and support of friends, the humour, the sometimes passionate and serious and other times light conversations about the state of the world, the place and role of science and scientists in it, our human condition, social justice, and more. I also shared life changing experiences and thrilling moments with some of those passionate about space exploration which raises many scientific and metaphysical questions. I benefited from the energizing and beautiful Québec nature with fellow hikers and snowshoers. The immediate high (literally) that one can achieve in climbing provided great balance to the long-term goals proper to scientific research. I particularly thank Alexandra Jahn for the many great moments of discussions and climbing over the years.

Cette aventure n'aurait certainement pas été complétée sans les encouragements et soutien de Blake Rollinson, lui qui est caractérisé par une sagesse, grandeur d'âme et de coeur, et humour qui sont rares. Je remercie mes parents qui ont été des exemples rares d'endurance, de détermination, et de dur labeur et Amine et Cynthia Bourouiba pour tous les bons moments partagés depuis leurs naissances.

Contents

List of figures

List of tables

Chapter 1

Introduction

I am an old man now, and when I die and go to Heaven there are two matters on which I hope for enlightenment. One is quantum electrodynamics and the other is the turbulent motion of fluids. And about the former I am really rather optimistic
Horace Lamb (1932)

Frisch (1995) observed that: "the Navier-Stokes equations probably contain all of turbulence. Yet it would be foolish to try to guess what its consequences are without looking at experimental facts. The phenomena are almost as varied as in the realm of life." The Navier-Stokes equations are the equations governing Newtonian fluid motion. It is the nonlinearity of this equation that gives rise to turbulence. It was in 1757 that Leonhard Euler (1707-1783) introduced the equations governing inviscid incompressible flows in his famous *Principes généraux du mouvement des fluides* (1767) [1] [2]. These were based on the Newton's second law. Newton's second law was written for the first time in vectorial form, in rectangular coordinates by Euler (1752). He introduced the notion that the m in $\mathbf{F} = m\mathbf{a}$, could be finite or

[1]This piece of work was the second in a list of four major contributions by Euler to the field of hydrodynamics. The first contribution, *Principes généraux de l'état d'équilibre des fluids*, dealt with steady flows. The third and fourth major contributions, *Continuation des recherches sur la théorie du mouvement des fluides* in 1757 and *Recherches sur le mouvement des rivières* in 1767 extended both his work and earlier work done by Bernoulli. He also treated compressible flows for the first time (Mikhailov and Stepanov, 2007).

[2]Euler who is considered to be "one of the brightest stars in the mathematical firmament" (Dunham, 2007) introduced the concept of mass-point, and used for the first time vectors for velocity and acceleration.

infinitesimal. Today, the equations of inviscid fluid motion are called *Euler equations.* They became the cornerstone of modern fluid dynamics. Like most major scientific contributions, Euler's work was embedded in a series of incremental advances made by his contemporaries and predecessors. To do history justice, we enumerate here two of these colleagues whose work was critical in that regard. Daniel Bernoulli's (1700-1782) major contribution (among numerous others) is the theorem linking pressure, velocity and elevation (or height) of the fluid. This was presented in his famous book *Hydrodynamica* completed in 1734 and published in 1738 and served as a seed from which Euler's derivations could then grow. Jean Le Rond D'Alembert's (1717-1783) work covered steady flows in the *Traité de l'équilibre et des mouvements des fluides pour servir de suite au traité de dynamique* (1744) in which the continuity equations were written for the first time as differential equations. The important notion of a local velocity component within the flow was also introduced by d'Alembert. It is worth noting here that d'Alembert also considered air as an incompressible elastic fluid composed of small particles in *Éssay d'une nouvelle théorie de la résistance des fluides* (1752), which led to d'Alembert's paradox of zero drag for inviscid flows (Anderson, 1997).

In the nineteenth century, the friction term was finally introduced to Euler's equations by two independent researchers: Claude Louis M. H. Navier (1785-1836) and George Gabriel Stokes (1819-1903). Note that this missing term was conceptually not very well understood at Euler's time. Several attempts to model friction were tried until d'Alembert gave up trying in his famous statement:

> "I do not see then, I admit, how one can explain the resistance of fluids by the theory in a satisfactory manner. It seems to me on the contrary that this theory, dealt with and studied with profound attention, gives at least in more cases resistance absolute zero: a singular paradox which I leave to a geometrician to explain" (*D'Alembert 1768*)

He was later among the first who observed that the drag was proportional to the square of the velocity (Anderson, 1997). In 1822, L. M. Navier finally derived the viscous term by means qualified by some as ironic: "The irony is that although Navier had no conception of shear stress and did not set out to obtain equations that would describe motion involving friction, he nevertheless arrived at the proper form for such equations" (Anderson, 1997). A few hundred miles away, George Gabriel Stokes (1819-1903), unaware of the results obtained by Navier, arrived at the same term using the notion of internal shear stress leading to a derivation like the one that is presented most commonly today. His work was published in 1845. The Euler equations, now completed with the viscous term, were about to become the *Navier-Stokes equations* for incompressible viscous fluids.

Since the contributions of L. Euler, H. Navier and G. Stokes, more than 150 years have passed. Although the same Navier-Stokes equations are still used to model most flows, turbulence remains one of the greatest challenges of applied mathematics and classical physics. There is not even a unified definition of turbulence. Some define it as being a phenomena that is nonlinear, diffusive, random, and dissipative (Kundu, 1990). Others focus on the vorticity (curl of velocity) in a turbulent flow. Turbulent flows are commonly represented as a sea of eddies (intuitive picture of a blob of vorticity), which are stretched and twisted by the velocity field. Corrsin (1961) described turbulence as: "a spatially complex distribution of vorticity which advects itself in a chaotic manner." He also added that "the vorticity field is random in both space and time, and exhibit a wide and continuous distribution of length and time scales." (Davidson, 2004).

When focusing on the observation of turbulent flows, one notes that although the detailed characteristics of the flow seem unpredictable, random and highly disorganized, some of its properties are reproducible. This observation led to the use of a probabilistic description of turbulence. From a theoretical standpoint, the existence and smoothness of the solutions to the 3-dimensional Navier-Stokes equations remain unproven [3]. However, it is widely conjectured that for a given initial condition there is a unique solution at all times, i.e. that the Navier-Stokes are deterministic. The

[3]Listed as one of the Clay Mathematics Institute's million dollar unsolved problems.

problem of turbulence thus belongs to the class of dynamical systems treating deterministic chaos. The unpredictable behaviour of turbulent flows is thus conjectured to not be due to a singularity or noise (Frisch, 1995). From this deterministic-versus-probabilistic duality and a century of work we are left with no unified definition, not to mention theory of turbulence. Instead, we are left with a myriad of observations (experimental and numerical), theories and results. Some are valid for boundary layer flows, some for stratified flows, others for magnetohydrodynamics, or rotating flows, etc. Nevertheless, we inherit two main approaches based on two fundamentally different conceptualizations of turbulent flows: one statistical and the other deterministic. The most popular and developed approach is statistical. It assumes that on the one hand, turbulent flows are unpredictable in detail and thus can be studied with the tools of stochastic or random variables. On the other hand, it is assumed that the statistical (or averaged) quantities are predictable. Most of the theories of homogeneous turbulence use this approach, including the famous Kolmogorov "-5/3" energy spectrum (revisited shortly). The other approach is deterministic. This approach focuses on the details of the flow, assuming that they are deterministic. The starting point is an assumption on the shape of the typical eddies of the flow. Using classical deterministic mechanics, one examines the detailed dynamics of the eddy, from birth to death. The statistical properties of the flow can then be reconstructed from the behaviour and distribution of its eddies (Davidson, 2004).

As noted in Corrsin's description of turbulence, the notion of scale is important in turbulence. However, the meaning of "scale" is hard to define with precision. Typically, it is thought that a part, or eddy, of the flow field has a scale of the order L if its Fourier transform has a peak around $k = 1/L$. Chorin (1994) pointed out the difficulty with this definition - it is very difficult to isolate an "eddy" (which is not clearly defined); but the idea of scale is intuitively clear. For example, a weather map shows highs and lows of pressure on the scale of continents. On the other hand, someone walking down the street would feel the winds on a "human" scale. In a turbulent flow, such as the flows one can observe in the atmosphere, all these scales interact and exchange energy through nonlinearity. Statistical theories of turbulence aim to extract the common features of the flow. There are two assumptions that are commonly made. First, the small scales are assumed to be independent from the large scales. This underlines the idea of locality (in scale) of the nonlinear interactions. Second, the characteristic time of the eddies (the nonlinear timescale $\sim L/U$, with L a typical length, and U a typical velocity of flow) is small compared to the time characterizing the energy decay. The main implication of these assumptions is that the particular features of the problem studied (e.g. geometry, etc) have little effect on the nature of the turbulence at small scales. This is not necessarily true for the larger scales of the flow, which are much slower to adjust and more sensitive to the details of the particular problem considered.

The Kolmogorov theory for three-dimensional isotropic and homogeneous turbulent flows relies on dimensional analysis and the observations of turbulent flows showing an energy transfer from the larger to smaller structures of the flow. Observations showed that the energy that is injected in the larger scales of the turbulent flow is dissipated at the smaller scales. The question is how the energy gets from the large to the small scales. The father of the modern concept of the "energy cascade" is Richardson (1922). His observations led him to propose a multistage process of energy cascade in which the large structures pass their energy onto slightly smaller structures, which in turn pass their energy to even smaller structures, and so on. He also suggested that for scales larger than the smallest scales of the flow, the viscosity would not play any role in the multistage process if the Reynolds number $Re = UL/\nu$ was large enough. The smallest scales, at which the viscosity becomes important, are characterized by a Re of order one. Chorin (1994) compared this process to a waterfall, with energy fed in one end of the range and then coming out on the other end, where the viscosity can mop it up, with a turnover time associated with the scale l of $t_l \sim l/v_l$. It is the typical time for which the distortion of the structures of size l is significant and v_l is the velocity of the eddies of scale l. The hypothesis behind the cascade of energy is quasi-stationarity in the inertial range. The rate at which energy is injected must equal the rate at which energy is transferred downscale, which in turn must equal the rate of dissipation taking place at the bottom of the hierarchy of scales. The underlying assumption of the cascade is the locality (in scale not in position) of the interactions in the inertial range.

Having Richardson's (1922) notion of the energy cascade, Kolmogorov (1941) considered a flow with a large range of scales k, and an energy spectrum $E(k)$. Using a dimensional analysis, he derived the famous $E(k) \sim \epsilon^{2/3}k^{-5/3}$ energy spectrum, in which ϵ is the rate of energy dissipation. This derivation will be revisited in the next chapter. The important point is that Kolmogorov's result is valid for the inertial range over which energy is cascaded. In 3D turbulence, this cascade is from larger to smaller scales. Thus, 3-dimensional turbulence can be seen as a way to increase dissipation, which occurs at small scales.

Kolmogorv's result, although well established, does not describe the full myriad of turbulent flows encountered in practice, and the search for a more complete or unified theoretical approach describing all turbulent flows remains elusive. With or without a unified theory, some pressing practical problems involving turbulence need to be tackled. For example, lack of predictability is a critical shortcoming of weather prediction—and nonlinearity is at the origin of this limitation. Therefore, an understanding of homogeneous isotropic turbulence, and the effects introduced by stratification and rotation on it, is critical for better weather predictions. The numerous planets of our solar system are also natural laboratories in which the intricate effect of turbulence combined with rotation and stratification can generate atmospheric structures like Jupiter's famous Great Red Spot (GRS; see figure 1.1). It is a storm about 25,000 km across (which could swallow the earth twice over), and impressively long-lived (first seen in the 1600s). The existence of these long-lived eddies (e.g., the GRS and the three white ovals formed in the 1930s on the Jovian planet) are atmospheric features originating from the basic processes of the fluid motion. Whether we consider the terrestrial atmosphere, ocean, mantle, or other objects of our solar system, rotation is combined with a complex range of other effects such as stratification, topography, magnetic field, etc. Understanding their dynamics is surely not just about recreating replicates of these flows, but studying and thus understanding a hierarchy of different but related systems (see Hide, 1983). Only then will we be able to truly understand the relevant mechanisms governing such flows, and thus possibly predict them. In that spirit, this thesis isolates and focuses on the effect of rotation on a homogeneous turbulent flow.

It is Gaspard Gustave Coriolis (1792-1843) who studied the relative motion associated with rotating systems, particularly the centrifugal force (Coriolis, 1835). His work was part of a movement of reform that developed with the ultimate goal of raising the education of workers, craftsman and engineers in mechanics. At that time, mechanics was dominated by statics, which is well suited for construction work, but ill-suited for machines. Coriolis called the forces isolated in a rotating system "composed centrifugal forces". He was not interested in the isolated effect of what we refer to today as the "Coriolis force". It is not before the mid-nineteenth century that any reference to Coriolis force was made in the meteorological literature. That is when the earth's rotation was debated by the contemporaries of J. B. L. Foucault's popular pendulum experiment (see Persson, 1998, for review). For practicality, the study of geophysical flows involves expressing the Navier-Stokes equations in the planet's rotating frame. The centrifugal force is larger than the Coriolis force. However, the centrifugal force can be combined with the gravity force in the equations. The net effect of this combination is to alter the geometry of the earth (i.e., it is responsible for the ellipsoidal shape of the earth). As a result, the Coriolis force, though smaller, has a more profound effect on the dynamics. It turns out to be at the heart of very intriguing phenomena.

Starting from the equations of Navier-Stokes in a rotating frame, Proudman (1916) showed that a steady, inviscid, rapidly rotating flow would have no velocity variation along the direction of the axis of rotation. In other words, if the rotation axis is chosen to be vertical, the velocity field becomes independent of the vertical direction (the direction parallel to the axis of rotation), $\hat{\mathbf{z}}$, thus becoming two-dimensional and forming "Taylor columns". Taylor (1923) verified this strange effect of Coriolis experimentally in a rotating tank. We refer to this result on the two-dimensionalization in rotating fluid as the Taylor-Proudman theorem. Despite Taylor's experiment the effect of rotation on turbulent fluids remains poorly understood. In fact, the Taylor-Proudman theorem only applies in very restrictive conditions. Numerous studies investigating the effect of rotation on turbulence followed since 1923. The striking finding is that rotating turbulence has fundamentally different dynamics compared to the non-rotating classical homogeneous turbulence described by Kolmogorov's theory. Strong rotation was observed to generate large-scale structures within the flow, reminiscent of Taylor columns, even if the conditions of validity of the Taylor-Proudman theorem were violated. Richardson's (1922) cascade of energy from the large scales to the small scales was reduced or suppressed. In addition, rotation is observed to allow incompressible liquids to support the propagation of waves, called *inertial waves* (Greenspan, 1968). We will discuss the properties of these waves in more detail in the next chapter.

The Taylor-Proudman theorem does not explain these observations, neither does it explain how the two-dimensionalization of the flow would occur in rapidly rotating turbulent flows. One thing is certain, introducing rotation to 3-dimensional turbulence leads to phenomena that are reminiscent in some aspects of 2-dimensional turbulence. A major difference between 2-dimensional and 3-dimensional turbulent flows is that 2-dimensional Navier-Stokes conserve an additional quantity, the enstrophy. This is what leads to the inhibition of the energy cascade toward the small scales (Fjortoft, 1953). In 2-dimensional turbulence the cascade is opposite to that of 3-dimensional turbulence: energy is transferred from the small to the large scales of the flow.

In the following chapters, we will discuss in more detail how incompressible flows dominated by rotation can exhibit features reminiscent of the dynamics of two-dimensional turbulent flows. As we shall see in the next chapter, the Coriolis term is a linear part of the nonlinear rotating flow equations of motion. It is this subtle effect of a linear term influencing the nonlinear dynamics that makes the study of rotating flows difficult to understand. Our goal is to study the effect of rotation on homogeneous turbulent flows. The tools that we will use are theoretical and numerical. The theoretical approach aims to obtain general reproducible results for a simplified subsystem that more applied studies could build upon. At the end of the next chapter, the detailed objectives of this work will be outlined. Next, we recall the equations, theories and tools needed for this study of rotating turbulence.

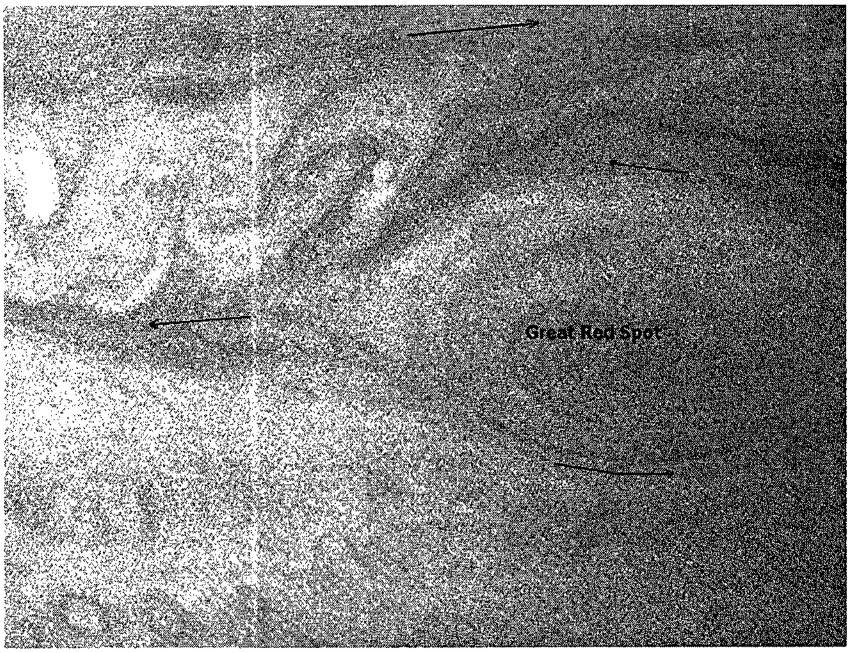

Figure 1.1: Long-lived eddy of Jupiter, named the Great Red Spot as observed by Cassini on its way to Saturn in December 2000. In 2000, to the surprise of many astronomers, a group of three thought-to-be-permanent Jovian storms merged into a single super-storm gradually developing similar colour to that of the GRS (Sparrow, 2006; Youssef and Marcus, 2003)

Chapter 2

Theoretical background and approach

In this chapter, the Navier-Stokes equations are presented for incompressible flows in a rotating frame. We discuss the Taylor-Proudman theorem and the inertial waves, which are specific to rotating flows. Given the particular tendency of rotating turbulence to two-dimensionalize a 3-dimensional flow, we revisit some of the classical theoretical results for non-rotating 3-dimensional and 2-dimensional turbulence. The most famous results are those using phenomenological approaches predicting the famous Kolmogorov energy spectrum scaling of $k^{-5/3}$ for 3-dimensional turbulence and the k^{-3} Kraichnan scaling for 2-dimensional turbulence. The use of asymptotic expansions as a tool for the study of nonlinear equations and the resulting resonant interactions are detailed. Finally, we summarize the goals of this project at the end of the chapter.

2.1 Navier-Stokes in a rotating reference frame

To isolate the effects of rotation, we ignore stratification and compressibility effects. That is, we consider flows which are unstratified, rotating and incompressible (flows with a typical velocity much smaller than the speed of sound, i.e. with a very low Mach number). The governing equations are derived from Newton's second law in a rotating frame. Consider a point within a three-dimensional region filled with fluid of constant density that has coordinate $\boldsymbol{r} = (x, y, z)$ in a frame of reference rotating with a constant angular velocity $\boldsymbol{\Omega}$. $\boldsymbol{u} = (u, v, w)$ denote the velocity field of the fluid parcel located at $\boldsymbol{r}$, at time t. For an incompressible fluid, the continuity equation is (vectors are denoted by boldface)

$$\nabla \cdot \boldsymbol{u} = 0, \tag{2.1}$$

when neglecting sound waves. Newton's second law in a rotating frame applied to a fluid element subject to external force $\mathbf{F}$ and constant density ρ leads to

$$\frac{\partial \boldsymbol{u}}{\partial t} + \underbrace{(\boldsymbol{u} \cdot \nabla)\boldsymbol{u}}_{\text{nonlinear term}} + \underbrace{2\boldsymbol{\Omega} \times \boldsymbol{u}}_{\text{Coriolis term}} = -\nabla P + \mathbf{F} + \nu \nabla^2 \boldsymbol{u}. \tag{2.2}$$

The first term on the r.h.s is a combination of the pressure, centrifugal term, and gravity potential:

$$P = \frac{1}{\rho}(p - \rho\Phi - \frac{\rho}{2}(\boldsymbol{\Omega} \times \boldsymbol{r}) \cdot (\boldsymbol{\Omega} \times \boldsymbol{r})), \tag{2.3}$$

where p, Φ, ν and $\mathbf{F}$ are the pressure, gravitational potential, kinematic viscosity coefficient and an externally applied force, respectively. In the case of inviscid flows with $\nu = 0$, the dissipation term in (2.2) vanishes. Thus, (2.2) becomes equivalent to the Euler equations in a rotating reference frame. Without loss of generality, we choose hereafter the rotation axis to be in the vertical direction $\hat{\mathbf{z}}$, and thus the angular velocity to be $\boldsymbol{\Omega} = (0, 0, \Omega)$.

2.2 Taylor-Proudman theorem and inertial waves

We choose a typical velocity U, a typical length L, and a typical timescale $T = (2\Omega)^{-1}$ for the rotation timescale, or $T = L/U$ for the nonlinear timescale, and rewrite the above equations using the new nondimensional variables

$$\boldsymbol{r}' = \frac{\boldsymbol{r}}{L}, \; \boldsymbol{u}' = \frac{\boldsymbol{u}}{U}, \; t' = \frac{t}{T}. \tag{2.4}$$

Two important dimensionless parameters can then be extracted from the dimensionless equations. The Ekman number

$$\mathrm{Ek} \equiv \frac{\nu \nabla^2 \boldsymbol{u}}{2\boldsymbol{\Omega} \times \boldsymbol{u}} \equiv \frac{\nu}{2\Omega L^2}, \tag{2.5}$$

and the Rossby number

$$\mathrm{Ro} \equiv \frac{D\boldsymbol{u}/Dt}{2\boldsymbol{\Omega} \times \boldsymbol{u}} \equiv \frac{U}{2\Omega L}, \tag{2.6}$$

where $D/Dt = \partial/\partial t + \boldsymbol{u} \cdot \nabla$. The former is an estimate of the relative strength of the viscous and Coriolis forces. The Rossby number is a ratio of the acceleration to the Coriolis force, which is also an estimate of the importance of the nonlinear term. Note that Ro/Ek= Re, the well-known Reynolds number.

When using the timescale associated with the rotation, $T \sim (2\Omega)^{-1}$, U and L to nondimensionalize (2.2), we obtain (after dropping the primes)

$$\frac{\partial \boldsymbol{u}}{\partial t} + \hat{\mathbf{z}} \times \boldsymbol{u} + \nabla P + \mathrm{Ek}\nabla^2 \boldsymbol{u} = -\mathrm{Ro}(\boldsymbol{u} \cdot \nabla)\boldsymbol{u}. \tag{2.7}$$

Flows dominated by rotation have small Ro and small Ek. Thus, they are governed by equations that are weakly nonlinear (the term on the r.h.s of (2.7) goes to zero as $\mathrm{Ro} \to 0$). If the flow is also slowly varying in time (i.e., quasi-steady, $\partial \boldsymbol{u}/\partial t = 0$), the goestrophic balance applies:

$$\hat{\mathbf{z}} \times \boldsymbol{u} = -\nabla P. \tag{2.8}$$

Streamlines of geostrophic flows are perpendicular to the gradient of pressure, thus lying on surfaces of constant pressure values, P. Examples of such motion can be found in the atmosphere, where the motion of the flow is counter-clockwise around a low pressure weather pattern in the northern hemisphere.

Pursuing further the linear analysis, we take the curl of (2.8) and use the incompressibility condition, (2.1), to recover the Taylor-Proudman theorem

$$\frac{\partial}{\partial z}\boldsymbol{u} = 0. \tag{2.9}$$

Hence, the velocity field of slowly varying, inviscid motion under rapid rotation is two-dimensional, being independent of the coordinate measured along the rotation axis. That is,

$$\boldsymbol{u} = \boldsymbol{u}(x, y). \tag{2.10}$$

This was shown by Taylor (1917) and Proudman (1916). Thus, strong rotation leads to the formation of columns of two-dimensional flows which were observed by Taylor (1923), and later by Hide and Ibbertson (1966) and Hide and Lighthill (1968), amongst others.

Although the hypotheses of the Taylor-Proudman theorem are very restrictive and violated in most flows observed both in nature and laboratory experiments, we can carry on the linear analysis a little further and try to explain how these columns would be generated in a purely linear setting. Re-introducing the variation in time in (2.8) we get

$$\frac{\partial}{\partial t}\boldsymbol{u} + \hat{\mathbf{z}} \times \boldsymbol{u} = -\nabla P. \tag{2.11}$$

This eqaution admits plane-wave-like solutions, called inertial waves, of the form

$$\boldsymbol{u}(r,t) = \Re(\hat{\boldsymbol{u}}(\boldsymbol{k})\exp(i(\boldsymbol{k}\cdot\boldsymbol{r} - \omega t))), \tag{2.12}$$

for a given wavenumber $\boldsymbol{k}$, an amplitude $\hat{\boldsymbol{u}}$, and a dispersion relation

$$\omega_{\pm}(\boldsymbol{k}) = \pm(\boldsymbol{k}\cdot\hat{\mathbf{z}})/|\boldsymbol{k}|. \tag{2.13}$$

This dispersion relation is anisotropic. The direction of propagation depends on the orientation of the wavenumber relative to the rotation axis. The frequency of these waves is bounded since $0 < |\omega_{\pm}(\boldsymbol{k})| < 1$ (dimensional frequency is bounded between 0 and 2Ω). Using (2.13), the phase velocity is $\mathbf{c}_{\phi} = \pm(\hat{\mathbf{z}}\cdot\boldsymbol{k})\boldsymbol{k}/|\mathbf{k}|^{\mathbf{3}}$, and the group velocity $\mathbf{c_g} = \pm\boldsymbol{k}\times(\hat{\mathbf{z}}\times\boldsymbol{k})/|\boldsymbol{k}|^{\mathbf{3}}$. This implies that $\mathbf{c_g}\cdot\mathbf{c}_{\phi} = 0$, which means that the energy is propagated in a direction perpendicular to the direction of the constant phase planes. The slow modes, with near-zero-frequency $\omega_{\pm} = \epsilon \ll 1$, are those propagating the energy the fastest in the direction parallel to the rotation axis. Taylor columns and inertial waves are linear effects that have been discussed and observed in several studies in bounded domains (e.g. Greenspan, 1968; McEwan, 1969) (see Heikes and Maxworthy, 1982, for an example of a study focusing on the interaction of waves with obstacles or topography). The orthogonality of the phase velocity and the group velocity, combined with the anisotropic dispersion relation of inertial waves are invoked to illustrate how Taylor columns would form in a linear problem. Taylor columns would correspond to the waves of zero-frequency (Greenspan, 1968; Görtler, 1957). However, in most experiments in which the columnar structures are observed, the Taylor-Proudman theorem still does not explain why these columns are generated for Ro numbers that are small but non-zero (which is the case for all experiments). Finally, the linear argument is only an intuitive way to understand the creation of the anisotropy, but does not explain the formation of the vertical structures within turbulent flows.

2.3 Fourier representation of a homogeneous flow

As discussed in §1, the details of the turbulent flow are not considered deterministic and are thus treated as random variables. The statistics of a random variable are the various averages of that variable. The ensemble variable of a quantity is an average over a large number of independent realizations. The time average is an average over a time window small compared to the timescale on which the averaged properties of the quantity change considerably. A spatial average is an average of the quantity over a spatial domain. When the statistics of the variable are independent of time, the process associated with the variable is said to be stationary. For a stationary process, the time average equals the ensemble average. When the statistics of the variable are independent of space or position, the process associated with the variable is said to be homogeneous. For a homogeneous process, the spatial average equals the ensemble average. We will use $< \cdot >$ to denote ensemble averages over an infinite number of independent realizations. Depending on the context, it can also denote the time average if we are discussing stationary quantities and will also denote the spatial average when discussing homogeneous quantities.

We return now to a homogeneous turbulent flow, which proved useful in the past for the study of the inherent properties of turbulence (Lin, 1961). Consider two points in 1-dimension: A at position $r = r_A$, and A' at position $r = r_{A'}$, with velocities $u(r_A)$

and $u'(r_{A'} = r_A + d)$, respectively. d is the distance between the two points A and A'. In the homogeneous flow, the correlation of the velocities at these points, denoted $< u(r_A)u(r'_A) >=< u(r_A)u(r_A + d) >$ is only a function of d. The correlation velocity components can be generalized to multiple dimensional fields. The generalized spatial correlation tensor, denoted Φ_{nm},

$$\Phi_{nm}(\mathbf{l}, t) =< u_n(\boldsymbol{r}, t)u_m(\boldsymbol{r} + \mathbf{l}, t) >, \tag{2.14}$$

is independent of the position $\boldsymbol{r}$. It depends only on the vector $\mathbf{l}$. $u_m = \boldsymbol{u} \cdot \mathbf{e}_m$ is the m^{th} component of the vector $\boldsymbol{u}$, and $\mathbf{e}_m$ is a unit vector of the frame of reference. This result makes the use of the Fourier analysis ideal for the study of homogeneous turbulence. In fact, the Fourier formalism highlights the scales instead of the positions. In (2.14), the correlation between two points that are separated by a distance l would be due to the effect of an eddy of the scale l. As a result, the Fourier analysis would extract the scale l of the eddy that is correlating two points of the flow (see Davidson, 2004, for comparison between the analysis in spectral space and real space).

Consider a homogeneous flow in a periodic domain with period L, where $\boldsymbol{u}(x + L, y, z) = \boldsymbol{u}(x, y, z)$, $\boldsymbol{u}(x, y + L, z) = \boldsymbol{u}(x, y, z)$, etc, such that the Fourier series can be used

$$\boldsymbol{u}(\boldsymbol{r}, t) = \sum_{\boldsymbol{k}=-\infty}^{\infty} \hat{\boldsymbol{u}}_{\boldsymbol{k}} \exp(i\boldsymbol{k} \cdot \boldsymbol{r}). \tag{2.15}$$

Here, $\boldsymbol{r} \cdot \boldsymbol{k} = \sum_{i=1}^{3} r_i k_i$, with $k_1 = k_x$, $k_2 = k_y$, $k_3 = k_z$, and $k_i = 2\pi l_i/L$, where the $l_{i=1,2,3}$ are integers varying from $-\infty$ and ∞. $\hat{\boldsymbol{u}}_{\boldsymbol{k}} = \hat{\boldsymbol{u}}(\boldsymbol{k}, t)$ is the Fourier vector component of the velocity field. The vector $\boldsymbol{u}(\boldsymbol{r})$ is real, forcing a reality condition on its Fourier components: $\hat{\boldsymbol{u}}_{-\boldsymbol{k}} = \hat{\boldsymbol{u}}^*_{\boldsymbol{k}}$, where * denotes a complex conjugate. The continuity equation (2.1) in Fourier representation becomes

$$\boldsymbol{k} \cdot \hat{\boldsymbol{u}}_{\boldsymbol{k}} = 0. \tag{2.16}$$

The Fourier transform of the autocorrelation tensor (2.14) is denoted $\hat{\Phi}(\boldsymbol{k}, t) = \hat{\Phi}_{nn}(\boldsymbol{k}, t)$ and corresponds to twice the kinetic energy associated with each Fourier mode $\boldsymbol{k}$. If the flow is also isotropic, the statistical quantities are independent of direction. In this case, one typically expresses quantities such as the spectral auto-correlation tensor as functions of the magnitude, k, of the modes $\boldsymbol{k}$. For example, the energy spectrum can be written as $E(k,t) = 2\pi k^2 \Phi_{nn}(k,t)$. The total energy would be

$$E(t) = \frac{1}{2} < \boldsymbol{u}^2 >= \frac{1}{2} \int \Phi_{nn} d\boldsymbol{k} = \int_0^\infty 2\pi k^2 \Phi(nn)(k,t) dk = \int_0^\infty E(k,t) dk, \quad (2.17)$$

where the sum over wavenumber $\boldsymbol{k}$ is replaced by an integral in the limit of large domain $L \to \infty$, and thus the spacing between wavenumbers, $\delta k = 2\pi/L$, goes to zero.

We know from observations that rotation introduces anisotropy in the turbulent field. The Taylor columns discussed in the previous section are anisotropic, and the dispersion relations of the inertial waves are anisotropic, depending on the direction of the wavenumber. Because of this, we introduce another spectrum definition, differentiating the vertical direction, aligned with the rotating axis, from the horizontal direction which remains symmetric in x and y in the dispersion relation (2.13). This anisotropy favours the use of cylindrical coordinates instead of the spherical coordinate system used when the statistics are isotropic. We can thus define horizontal and vertical energy spectra

$$\begin{aligned} E(t) &= \int_0^\infty \int_0^\infty E_{hz}(k_h, k_z, t) dk_h dk_z, && (2.18) \\ &= \int_0^\infty E_z(k_z, t) dk_z, && (2.19) \\ &= \int_0^\infty E_h(k_h, t) dk_h, && (2.20) \end{aligned}$$

where $E_{hz}(k_h, k_z, t) = \pi k_h \Phi_{nn}(k_h, k_z, t)$ is the k_h-k_z energy spectrum function of (k_h, k_z), $E_z(k_z, t)$ is the vertical energy spectrum, and $E_h(k_h, t)$ is the horizontal energy spectrum. $k_h = \sqrt{k_x^2 + k_y^2}$ is the horizontal wavenumber.

2.4 Theories of isotropic turbulence

The results of the Taylor-Proudman theorem predicting a two-dimensionalization of the flow initially isotropic and three-dimensional require us to briefly revisit some of the classical results of turbulence for isotropic homogeneous, non-rotating three-dimensional and two-dimensional flows. The nonlinear theoretical results of rotating turbulence that we will discuss in §2.5 require us to revisit an additional dynamics, that of the advection of a passive scalar in a two-dimensional turbulent flow.

2.4.1 Kolmogorov scaling for three-dimensional turbulence

The Kolmogorov theory for three-dimensional isotropic and homogeneous turbulent flows relies on dimensional analysis and the observations of turbulent flows showing an energy transfer from larger to smaller structures of the flow. Armed with the notion of energy cascade introduced by Richardson (1922), Kolmogorov (1941) considered a flow with a large range of scales k, an energy spectrum $E(k)$, and a dissipation spectrum of $2\nu k^2 E(k)$, where ν is the viscosity coefficient. In the large k modes, the dissipation spectrum is expected to be dominant. The scale at which the viscous effects become important is denoted l_d. The scale at which the energy spectrum is large (for example by forcing by the mean flow) is denoted l_i, such that $l_i \gg l_d$. The range of scales $l_d \ll l \ll l_i$ is referred to as the "inertial range" where the energy cascade takes place. The notion of locality (in scale) for the cascade to take place leads to an energy spectrum $E(k)$ in the "inertial range" which depends only on the scale k, and on the rate of energy dissipation ϵ. This, in turn, equals the rate of energy injection Π_{l_i}, which itself equals the rate of cascade of energy at scale l, Π_l. The energy spectrum is assumed to be independent of the viscosity in the inertial range. From these assumptions, a simple dimensional analysis gives the famous Kolmogorov spectrum (Kolmogorov, 1941)

$$E(k) = C\epsilon^{2/3}k^{-5/3}, \tag{2.21}$$

with C a dimensionless constant. This is well established by observations (e.g. Frisch, 1995). *A priori*, one might expect this relationship derived using dimensional arguments to hold for a two-dimensional flow, but it does not. Before moving on to the particularities of two-dimensional flows, we reiterate that the crux of the argument behind the famous (2.21) is the locality of the interactions in the inertial range. However, even if (2.21) is remarkably well established, the justification of the hypothesis used for its derivation remains the subject of debate (see Chorin, 1994; Frisch, 1995, for details).

2.4.2 Two-dimensional turbulence

In two-dimensional flows, the interacting triads conserve both energy, and enstrophy. The enstrophy, Z, is the variance of the vertical vorticity component, denoted ζ, i.e. $Z =< \zeta^2/2 >$. The vorticity of a two-dimensional field $\boldsymbol{u} = u(x,y)\hat{\mathbf{x}} + v(x,y)\hat{\mathbf{y}}$ only has one vertical component. One can define a spectrum of the enstrophy, $Z(k)$, analogous to the energy spectrum. The two are related by $Z(k) = k^2E(k)$. This additional conserved quantity inhibits the energy cascade toward the small scales (Fjortoft, 1953). Thus, two simultaneous cascades are occurring, one for the energy and the other for the enstrophy. Using the same approach as Kolmogorov for three-dimensional turbulence, Kraichnan (1967) considered an injection wavenumber k_i for both energy and enstrophy. In this case, consider that the enstrophy spectrum in the region in which the enstrophy is cascading forward ($k_i \ll k$) has a cascade rate equal to the injection rate, and equal to the dissipation rate, η. Assuming that $Z(k)$ only depends on k and η leads to

$$E(k) = C'\eta^{2/3}k^{-3}, \tag{2.22}$$

where C' is a dimensionless constant. On the other hand, the energy injected at a constant rate ϵ at the scale $l_i \sim 1/k_i$ (observed to cascade toward large scales) is found to have the same spectrum (2.21) recovered for the range of wavenumbers $k \ll k_i$. Note that the assumptions required for the range of cascade of energy exclude those used for the cascade of enstrophy. As a result, at scales for which an inverse cascade with a $k^{-5/3}$ spectrum is observed the enstrophy flux $\eta = 0$. The corollary is that in the spectral range of downscale enstrophy cascade with a k^{-3} spectrum, $\epsilon = 0$.

The assumption of localized interactions is underlying this phenomenology as well. However, the enstrophy cascade in two-dimensional turbulence was found to not be local (e.g. Legras et al., 1988; Borue, 1993, 1994). Several studies showed power laws for the energy spectrum that are much steeper than k^{-3}, corresponding to strong nonlocality.

2.4.3 Passive scalar in two-dimensional flow

We briefly discuss here the dynamics of a two-dimensional flow advecting a passive scalar ϕ, referred to in subsequent chapters. The equation governing advection of a passive scalar $\phi(\boldsymbol{r}, t)$ in a two-dimensional flow of velocity field $\boldsymbol{u}_{2D}(\boldsymbol{r}, t)$ is

$$\frac{\partial}{\partial t}\phi + \boldsymbol{u}_{2D} \cdot \nabla\phi = \kappa\nabla^2\phi + S, \tag{2.23}$$

where κ is the diffusivity of the tracer, and $S(\boldsymbol{r}, t)$ is the source or sink of the tracer. It is important to note that (2.23) is very similar to the equation governing the vorticity ($\boldsymbol{\omega} = \nabla \times \boldsymbol{u}_{2D} = (0, 0, \zeta)$) in two-dimensional flows, which is of the form

$$\frac{\partial}{\partial t}\zeta + \boldsymbol{u}_{2D} \cdot \nabla\zeta = \nu\nabla^2\zeta + F, \tag{2.24}$$

with ν the kinematic viscosity and F a forcing of enstrophy. A spectrum, denoted $E_\phi(\boldsymbol{k}, t)$, can be defined for the tracer. It is analogous to the energy and enstrophy spectra discussed in previous sections. The variance of the tracer is then $<\phi^2>= \frac{1}{2}\int E_\phi(\boldsymbol{k})d\boldsymbol{k}$. Consider a scale $l_i \sim 1/k_i$ at which the energy and the enstrophy are injected, and a scale $l_\phi \sim 1/k_\phi$ at which the scalar is injected. The scale of injection of the passive tracer could either be in the range of the inverse energy cascade, with energy spectrum (2.21) or be in the range where the enstrophy downscale cascade takes place, with an energy spectrum of the form (2.22). The latter is equivalent to an enstrophy spectrum of the form

$$Z(k) = C'\eta^{2/3}k^{-1}. \tag{2.25}$$

Consider the case where the passive scalar is injected in the scales associated with the enstrophy cascade. Using a similar dimensional analysis to that used in two-dimensional and three-dimensional turbulence one obtains

$$E_\phi(k) = C''\eta^{-1/3}\chi k^{-1}, \tag{2.26}$$

with C'' a nondimensional constant (see Lesieur, 1997). The underlying assumptions are that the tracer spectrum depends only on the scale k, the local timescale $\tau(k) \sim (k^3 E(k))^{-1/2}$ associated with the enstrophy cascade, and the flux of dissipation of the tracer variance, denoted χ (equal to the rate of injection and transfer from scale to scale). The assumption of locality of the transfer in the enstrophy cascade range must hold for this reasoning to hold. Note that the slopes of (2.26) and (2.25) are the same, which is due to the similarity in the governing equations (2.23) and (2.24).

2.5 Asymptotic perturbation method applied to rotating turbulence

2.5.1 Limitation of the linear results

On Earth, one typical example of a rotating flow is a large-scale storm, with wind speed of about $U \sim 10$ ms^{-1}, a typical scale of $L \sim 10^6$ m, a mid-latitude angular velocity of $\Omega \sim 10^{-4}$ rads^{-1}, and air kinematic viscosity $\nu \sim 10^{-5}$ m^{2}s^{-1}. These numbers lead to Ro $\sim 10^{-1}$ and Ek$\sim 10^{-13}$ for which the condition of Ro $\ll 1$ is not satisfied. Thus, the Taylor-Proudman theorem hypothesis would not hold for this flow. This value of Ro ≈ 0.1, as we shall see in the next chapter, is characteristic of a very particular effect of rotation that cannot be explained by the linear Taylor-Proudman theorem. Another typical terrestrial example of a flow dominated by rotation is the Gulf Stream current with lengthscales $L \sim 10^5$ m and $U \sim 1$ ms^{-1}, leading to Ro $\sim 10^{-1}$ and Ek $\sim 10^{-11}$. The Jovian Great Red Spot can be estimated to have a Rossby number of Ro ~ 0.01 using $L \sim 25000 \times 10^3$ m, a latitude of about 22.5^o south (Marcus and Lee, 1994), $U \sim 50$ ms^{-1} (Reese and Smith, 1968) and a typical jovian day of 10 hours (Sparrow, 2006). These small but non-zero Ro imply the presence of nonlinear effects. In the linear approximation, the inertial waves (2.37) exist without interacting with each other. However, for a small but non-zero Ro, (2.7) become nonlinear. The nonlinear analysis is presented in the following section. Note that for the flows above, the Ek was much smaller than Ro. Thus, we only forcus on turbulent flows for which the Ekman number, Ek, is small.

2.5.2 Nonlinear analysis

The nonlinear (2.7) in Fourier space is

$$(\frac{\partial}{\partial t} + \text{Ek } k^2)\hat{u}_n(\boldsymbol{k}, t) + \underbrace{\epsilon_{n3m}\hat{u}_m(\boldsymbol{k})}_{\text{Coriolis term}} = -\text{Ro } \underbrace{\frac{i}{2} \sum_{\boldsymbol{k}=\boldsymbol{p}+\boldsymbol{q}} P_{nml}(\boldsymbol{k})\hat{u}_m(\boldsymbol{p}, t)\hat{u}_l(\boldsymbol{q}, t)}_{\text{Nonlinear term}}, \tag{2.27}$$

with ϵ_{ijk} the alternating tensor, and

$$P_{nml}(\boldsymbol{k}) = k_l P_{nm}(\boldsymbol{k}) + k_m P_{nl}(\boldsymbol{k}). \tag{2.28}$$

The projection tensor representing the projections onto the plane perpendicular to $\boldsymbol{k}$ in wavenumber space is

$$P_{nm}(\boldsymbol{k}) = k_n k_m / k^2 - \delta_{nm}, \tag{2.29}$$

where δ_{nm} is the Kronecker delta, and n, m and l are dummy indices taking the values, 1, 2, and 3. The projection operator is used in order to obtain an equation for a nondivergent field satisfying (2.16). The nonlinear interactions resulting from the nonlinear term underlined in (2.27) shows that the modes of a triad of Fourier modes $(\boldsymbol{k}, \boldsymbol{p}, \boldsymbol{q})$ interact only if they satisfy $\boldsymbol{k} = \boldsymbol{p} + \boldsymbol{q}$.

Using (2.27), the equation governing the change in energy per wave number reads

$$(\frac{\partial}{\partial t} + 2Ek\ k^2)E(\boldsymbol{k}, t) = \text{Ro } T(\boldsymbol{k}, t), \tag{2.30}$$

where the spectral energy transfer, $T(\boldsymbol{k}, t)$ originates from the nonlinear term. It is cubic in $\hat{\boldsymbol{u}}$ and is responsible for the energy exchange between the interacting triads of Fourier modes satisfying $\boldsymbol{k} = \boldsymbol{p} + \boldsymbol{q}$.

$$T(\boldsymbol{k}, t) = \sum_{\boldsymbol{k}=\boldsymbol{p}+\boldsymbol{q}} P_{nml}(\boldsymbol{k})\Im(< \hat{u}_m(\boldsymbol{p}, t)\hat{u}_l(\boldsymbol{q}, t)\hat{u}_n^*(\boldsymbol{k}, t) >), \tag{2.31}$$

where $\Im()$ is the notation for imaginary part.

In Fourier space the velocity field can be decomposed in terms of helical modes as

$$\hat{\boldsymbol{u}}(\boldsymbol{k},t) = a_+(\boldsymbol{k},t)\mathrm{N}^+(\boldsymbol{k}) + a_-(\boldsymbol{k},t)\mathrm{N}^-(\boldsymbol{k}), \tag{2.32}$$

with

$$\mathrm{N}^{s_k}(\boldsymbol{k}) = \left(\frac{\hat{\mathbf{z}}\times\boldsymbol{k}}{|\hat{\mathbf{z}}\times\boldsymbol{k}|}\times\frac{\boldsymbol{k}}{|\boldsymbol{k}|} + is_{\boldsymbol{k}}\frac{\hat{\mathbf{z}}\times\boldsymbol{k}}{|\hat{\mathbf{z}}\times\boldsymbol{k}|}\right) \tag{2.33}$$

being the eigenmodes of the curl operator such that

$$i\boldsymbol{k}\times\mathrm{N}^{s_k}(\boldsymbol{k}) = s_{\boldsymbol{k}}|\boldsymbol{k}|\mathrm{N}^{s_k}(\boldsymbol{k}), \tag{2.34}$$

and $s_{\boldsymbol{k}} = \pm$. The helical decomposition (2.32) can be used to decompose any turbulent flow (e.g. Lesieur, 1997), but it is particularly well suited to the case of rotating flows for which helical modes are the amplitudes of the inertial waves (Cambon and Jacquin, 1989). Consider the vorticity counter-part of (2.11)

$$\frac{\partial}{\partial t}\boldsymbol{\omega} = (\hat{\mathbf{z}}\cdot\boldsymbol{\nabla})\boldsymbol{u}, \tag{2.35}$$

where the vorticity $\boldsymbol{\omega} = \boldsymbol{\nabla}\times\boldsymbol{u}$. This equation admits inertial plane wave solutions of the form

$$\begin{aligned}\boldsymbol{u}(\boldsymbol{r}) &= \sum_{\boldsymbol{k}}\boldsymbol{u}(\boldsymbol{k})\exp(i\boldsymbol{k}\cdot\boldsymbol{r}), \qquad (2.36)\\ &= \sum_{\boldsymbol{k}}\left[A_+(\boldsymbol{k},t)\mathrm{N}^+(\boldsymbol{k})\exp i(\boldsymbol{k}\cdot\boldsymbol{r}) + A_-(\boldsymbol{k},t)\mathrm{N}^-(\boldsymbol{k})\exp i(\boldsymbol{k}\cdot\boldsymbol{r})\right],\end{aligned}$$

with

$$A_s(\boldsymbol{k},t) = a_s(\boldsymbol{k})\exp(-i\omega_{s_{\boldsymbol{k}}}t),$$

and the inertial wave frequency, $\omega_{s_{\boldsymbol{k}}}(\boldsymbol{k})$, defined in (2.13).

When using the inertial wave decomposition for rotating flows, the spectral equations (2.27) governing the spectral amplitudes become (Waleffe, 1993)

$$\left(\frac{\partial}{\partial t} + i\omega_{s_k}\right)A_{s_k} = \frac{1}{2}\mathrm{Ro}\sum_{\boldsymbol{k}=\boldsymbol{p}+\boldsymbol{q}} C_{\boldsymbol{kpq}}^{s_k s_p s_q} A_{s_p}A_{s_q}, \tag{2.37}$$

with A_{s_q} a contracted notation for $A_{s=\pm}(\boldsymbol{q},t)$. The interacting coefficients were shown by Waleffe (1993) to have the form

$$C_{kpq}^{s_k s_p s_q} = \frac{1}{2}(s_p p - s_q q)\mathrm{N}^{s_p} \times \mathrm{N}^{s_q} \cdot \mathrm{N}^{s_k\,*}. \tag{2.38}$$

In three-dimensional isotropic turbulence, each interacting triad $(\boldsymbol{k},\boldsymbol{p},\boldsymbol{q})$ was shown by Kraichnan (1967) to conserve energy (and helicity). The energy conservation $E = \frac{1}{2}\langle \boldsymbol{u}^2\rangle$ implies

$$C_{kpq}^{s_k s_p s_q} + C_{pqk}^{s_p s_q s_k} + C_{qkp}^{s_q s_k s_p} = 0. \tag{2.39}$$

The helicity conservation, with helicity defined as $H = \frac{1}{2}\langle \boldsymbol{u}\cdot\boldsymbol{\omega}\rangle$, implies

$$s_k k C_{kpq}^{s_k s_p s_q} + s_p p C_{pqk}^{s_p s_q s_k} + s_q q C_{qkp}^{s_q s_k s_p} = 0. \tag{2.40}$$

If Ro$\ll 1$, (2.37) are referred to as weakly nonlinear and are of the form

$$\frac{\partial}{\partial t}\boldsymbol{u} + \hat{L}(\boldsymbol{u}) = \mathrm{Ro}\hat{N}(\boldsymbol{u}), \tag{2.41}$$

with $\hat{L}$ a linear operator, and $\hat{N}$ a nonlinear operator. In (2.41), the nonlinear term allows two waves with weak amplitudes to generate possibly a third wave with a third frequency, which in turn can interact with another two waves and generate other frequencies, and so on. Several methods for tackling these types of problems are available (see Nayfeh, 1973, for a complete introduction). These methods include the straightforward expansion of the amplitudes onto a power series about the small parameter of the equation, ϵ, corresponding in (2.37) to the Rossby number, Ro:

$$A_{s_k}(\boldsymbol{k},t;\mathrm{Ro}) = A_{s_k}^0(\boldsymbol{k},t) + \mathrm{Ro}A_{s_k}^1(\boldsymbol{k},t) + \mathrm{Ro}^2 A_{s_k}^2(\boldsymbol{k},t) + \ldots \tag{2.42}$$

Substituting (2.42) into (2.37) allows one to solve for the equations at each order of Ro.

Another method particularly well suited to the problem of rotation is the method of multiple scales, for which several scales are characteristic of the dynamics. This is the case for rotating flows where two temporal characteristic scales are present: the time associated with the rotation period $\tau_0 \sim (2\Omega)^{-1}$, and the time associated with the nonlinear eddy turnover time, $\tau_1 \sim L/U$. Note that Ro $\equiv \tau_0/\tau_1$. So, when the Rossby becomes Ro$\ll 1$, the disparity between these two timescales increases, creating a two timescale problem: a fast timescale associated with the rotation, $\tau_0 = t$, and a slower timescale associated with the nonlinear eddy overturn τ_1 $\pm$Ro t. The time derivatives become

$$\frac{\partial}{\partial t} \equiv \frac{\partial}{\partial \tau_0} + \mathrm{Ro}\,\frac{\partial}{\partial \tau_1}. \tag{2.43}$$

An expansion of the amplitudes into a power series in Ro gives

$$A_{s_k} = A^0_{s_k}(\boldsymbol{k}, \tau_0, \tau_1) + \mathrm{Ro}A^1_{s_k}(\boldsymbol{k}, \tau_0, \tau_1) + ... \tag{2.44}$$

When substituting (2.44) into (2.37), the first order in Ro terms are found to satisfy

$$\left(\frac{\partial}{\partial \tau_0} + i\omega_{\boldsymbol{k}}\right) A^0_{s_k}(\boldsymbol{k}, \tau_0, \tau_1) = 0, \tag{2.45}$$

resulting in a first order solution

$$A^0_{s_k}(\boldsymbol{k}, \tau_0, \tau_1) = a_{s_k}(\boldsymbol{k}, \tau_1) \underbrace{e^{-i\omega_{s_k}\tau_0}}_{\text{inertial wave}}. \tag{2.46}$$

When carrying the expansion to the next order, secular terms in the expression of $A^1_{s_k}$ must be removed in order to keep the solution bounded in time. The removal of the secular term introduces a new constraint on the slowly varying amplitudes $a_{s_k}(\boldsymbol{k}, \tau_1)$:

$$\frac{\partial}{\partial \tau_1} a_{s_k}(\boldsymbol{k}, \tau_1) = \frac{1}{2} \sum_{(\boldsymbol{p},\boldsymbol{q},s_p,s_q)\in R_{s_k,\boldsymbol{k}}} C^{s_k s_p s_q}_{\boldsymbol{kpq}} a_{\boldsymbol{p},s_p}(\tau_1) a_{\boldsymbol{q},s_q}(\tau_1), \tag{2.47}$$

with $R_{s_k,\boldsymbol{k}}$ the set of wavenumbers satisfying the wave resonance condition:

$$R_{s_k,\boldsymbol{k}} = \left\{ (\boldsymbol{p}, \boldsymbol{q}, s_p, s_q) | \boldsymbol{k} = \boldsymbol{p} + \boldsymbol{q} \text{ and } \omega_{s_k} = \omega_{s_p} + \omega_{s_q} \right\}. \tag{2.48}$$

Equation (2.47) shows that the nonlinear interactions are restricted to the triads of modes satisfying the *resonance condition* (2.48). When rotation is strong, i.e. Ro$\ll 1$, the nonlinear transfers would be expected to occur only by means of resonant interactions. The properties of these interactions were explored by Waleffe (1993) using the properties of the interaction coefficients (2.38) of the resonant modes. Using the conditions (2.48) and the projection of $\boldsymbol{k} = \boldsymbol{p} + \boldsymbol{q}$ on the vertical axis, one can easily show

$$\frac{cos(\theta_{\boldsymbol{k}})}{s_{\boldsymbol{p}}q - s_{\boldsymbol{q}}p} = \frac{cos(\theta_{\boldsymbol{p}})}{s_{\boldsymbol{q}}k - s_{\boldsymbol{k}}q} = \frac{cos(\theta_{\boldsymbol{q}})}{s_{\boldsymbol{k}}p - s_{\boldsymbol{p}}k}, \tag{2.49}$$

with $\omega_{\boldsymbol{k}} = s_{\boldsymbol{k}}k_z/|k| = s_{\boldsymbol{k}}cos(\theta_{\boldsymbol{k}})$. Using this expression and the instability principle introduced in Waleffe (1992), Waleffe (1993) argued that the resonant interactions between three wave modes (with non-zero frequency ω_{s_k}) transfer energy preferentially toward the wave mode with the smallest frequency. Recall that the small frequency modes for which $|\omega_{s_k}|$ is small correspond to modes $\boldsymbol{k}$ with small $|k_z|$. Thus, the Fourier amplitude $\hat{u}(\boldsymbol{k}$, with $|k_z|$ small) corresponds to velocity fields which vary little in the $\hat{\mathbf{z}}$ direction. These modes would correspond to columnar structures similar to the Taylor columns. Thus, the triple-wave resonance has a tendency to two-dimensionalize the flow through weakly nonlinear interactions between wave modes. This nonlinear two-dimensionalization tendency was observed working with a statistical model and using a quasi-normal gaussian closure scheme by Cambon and Jacquin (1989).

The properties of the resonant interactions can have a major impact on the direction and rate of the transfer of energy. Our approach throughout the thesis will rely on the mode decomposition that we have introduced here. The goal of this modal decomposition is to isolate the 2D modes from the 3D modes in order to focus on the effect of two-dimensionalization introduced by the rotation. We decompose the modes into: 1) waves, or 3D modes, 2) horizontal components of the vertically-averaged modes, and 3) the vertical component of the zero-frequency modes. An analogous decomposition is used in Babin et al. (1996). Babin et al. (1996) suggested that for $\Omega \rightarrow \infty$ and for certain conditions on the boundaries, the vertically-averaged part of the flow would transfer energy to the larger scales, while the rest of the wave modes would transfer energy to the small scales (see the time-dependent Taylor-Proudman Theorem in Babin et al., 1996). This suggests that the vertically-averaged modes behave like two-dimensional turbulence, while the wave modes behave like conventional three-dimensional turbulence.

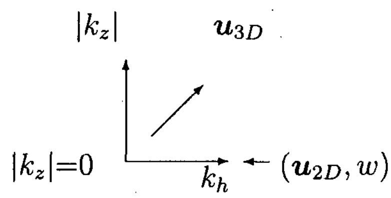

Figure 2.1: Decomposition of the Fourier modes onto $V_{\boldsymbol{k}}$ and $W_{\boldsymbol{k}}$ modes defined by (2.50).

We use the following decomposition (see figure 2.1) of the Fourier components (dropping the hats):

$$\begin{aligned} \text{If } \boldsymbol{k} \in V_{\boldsymbol{k}} &= \{\boldsymbol{k} | k \neq 0 \text{ and } k_z = 0\} \text{ then } \boldsymbol{u}(\boldsymbol{k}) = \boldsymbol{u}_{2D}(\boldsymbol{k}_h) + w(\boldsymbol{k}_h)\hat{\mathbf{z}}, \quad (2.50)\\ \text{If } \boldsymbol{k} \in W_{\boldsymbol{k}} &= \{\boldsymbol{k} | k \neq 0 \text{ and } k_z \neq 0\} \text{ then } \boldsymbol{u}(\boldsymbol{k}) = \boldsymbol{u}_{3D}(\boldsymbol{k}). \end{aligned}$$

In the above decomposition, the vertically averaged modes are those zero-frequency modes corresponding to stationary waves, which belong to the 2D Fourier-space plane defined by $k_z = 0$. They describe the real-space velocity field which is only a function of x, y and t.

The total energy (in discrete wavenumber space) $\mathrm{E} = \frac{1}{2}\sum_{\boldsymbol{k}} |\mathbf{u}(\boldsymbol{k})|^2$ becomes

$$\mathrm{E} = \mathrm{E}_{2D} + \mathrm{E}_w + \mathrm{E}_{3D}, \tag{2.51}$$

with

$$\mathrm{E}_{2D} = \frac{1}{2}\sum_{\boldsymbol{k}\in V_{\boldsymbol{k}}} |\mathbf{u}_{2D}(\boldsymbol{k})|^2, \tag{2.52}$$

$$\mathrm{E}_w = \frac{1}{2}\sum_{\boldsymbol{k}\in V_{\boldsymbol{k}}} |w(\boldsymbol{k})|^2, \tag{2.53}$$

$$\mathrm{E}_{3D} = \frac{1}{2}\sum_{\boldsymbol{k}\in W_{\boldsymbol{k}}} |\mathbf{u}(\boldsymbol{k})|^2. \tag{2.54}$$

The corresponding spectral equations are governed by (omitting forcing and dissipation):

$$\frac{\partial \mathrm{E_{3D}}}{\partial t}(\boldsymbol{k} \in W_{\boldsymbol{k}}, t) = (T_{33\to3} + T_{32\to3} + T_{3w\to3})(\boldsymbol{k} \in W_{\boldsymbol{k}}, t), \tag{2.55}$$

$$\frac{\partial \mathrm{E_{2D}}}{\partial t}(\boldsymbol{k} \in V_{\boldsymbol{k}}, t) = (T_{22\to2} + T_{33\to2})(\boldsymbol{k} \in V_{\boldsymbol{k}}, t), \tag{2.56}$$

$$\frac{\partial \mathrm{E_{w}}}{\partial t}(\boldsymbol{k} \in V_{\boldsymbol{k}}, t) = (T_{2w\to w} + T_{33\to w})(\boldsymbol{k} \in V_{\boldsymbol{k}}, t), \tag{2.57}$$

with T being the Fourier-space energy transfer. The transfers are distinguished by the types of interactions, eg. $33 \rightarrow 2$ stands for the interactions between two 3D wave modes that contribute to the 2D equation. Note that the $T_{jk \rightarrow i}$ terms are symmetric in j and k (see 2.31).

Armed with the modal decomposition (2.50) introduced here, we can adapt one additional result derived by Waleffe (1993) to the resonant interactions between two wave (3D) modes and a zero-frequency (2D) mode. Using (2.38), (2.48) and $\boldsymbol{k} = \boldsymbol{p}+\boldsymbol{q}$, one can show that resonant triads of two 3D modes and a zero-frequency mode (2D or w) exchange energy between the wave modes, but leave the energy of the zero-frequency mode (2D or w) unchanged. These interactions are referred to as *catalytic.* That is the $33 \rightarrow 2$ and $33 \rightarrow w$ interactions, when resonant, are referred to as "catalytic". We summarize the properties of the nonlinear interactions appearing in (2.55)-(2.57). The $22 \rightarrow 2$ are trivially resonant since the frequencies of the 2D modes are all identically zero. A subset of the $33 \rightarrow 3$ and $32 \rightarrow 3$ can be resonant; however, the result of Waleffe on catalytic interactions implies that the set of resonant interactions $33 \rightarrow 2$ is empty (see table (2.1)).

In §2.2, we discussed the link between Taylor columns and anisotropic properties of linear inertial waves. This discussion although illustrative, does not explain the formation the Taylor columns. The nonlinear effects play an important role in the formation of Taylor columns. Here we turn to the discussion of weakly nonlinear interactions between inertial waves and 2D modes. In fact, the results from the asymptotic expansion (2.44) combined with the particular properties of resonant interactions (table 2.1) allow for a nonlinear explanation of Taylor columns.

Combining the properties of the interactions displayed in table 2.1 with the spectral energy equations (2.55)-(2.57) leads to the following set of equations governing

Type of triad	Resonant (R) and/or Nonresonant (N) for:	
	0 <Ro≪ 1	Ro= 0
$22 \to 2$	R	R
$2w \to w$	R	R
$33 \to 2$	N	vanishes
$33 \to w$	N	vanishes
$23 \to 3$	R + N	R catalytic: no energy transfer to the 2D mode
$w3 \to 3$	R + N	R catalytic: no energy transfer to the w mode
$33 \to 3$	R + N	R : energy transfer to the 3D mode with smaller ω_{s_k}

Table 2.1: Properties of the interactions contributing to the energy transfers in (2.55-2.57)

the resonant interactions in the limit of Ro $\rightarrow$ 0:

$$\frac{\partial \mathrm{E}_{3\mathrm{D}}}{\partial t}(\boldsymbol{k} \in W_{\boldsymbol{k}}, t) = (T_{33\rightarrow 3_{res.}} + T_{32\rightarrow 3_{res.}} + T_{3w\rightarrow 3_{res.}})(\boldsymbol{k} \in W_{\boldsymbol{k}}, t), \quad (2.58)$$

$$\frac{\partial \mathrm{E}_{2\mathrm{D}}}{\partial t}(\boldsymbol{k} \in V_{\boldsymbol{k}}, t) = (T_{22\rightarrow 2_{res.}})(\boldsymbol{k} \in V_{\boldsymbol{k}}, t), \quad (2.59)$$

$$\frac{\partial \mathrm{E}_{\mathrm{w}}}{\partial t}(\boldsymbol{k} \in V_{\boldsymbol{k}}, t) = (T_{2w\rightarrow w_{res.}})(\boldsymbol{k} \in V_{\boldsymbol{k}}, t), \quad (2.60)$$

where $res.$ is the notation for resonant interactions.

To summarize, in the small Ro limit where resonant interactions are dominant, the 2D and w equations decouple from the wave mode equation. The 2D modes are governed by an equation similar to that of classical two-dimensional turbulence. Similarly to the Taylor columns, the 2D modes are independent of the vertical direction z—they are the vertically averaged modes. The w variance is governed by an equation similar to that of a passive scalar advected by the 2D flow (see §2.4).

The decoupling between the zero-frequency and 3D modes are in line with the decoupled two-dimensional subset predicted by the averaged equations derived by Babin et al. (1996) and Babin et al. (1998). However, the properties of the 3D energy cascade are not clear. On the one hand, Waleffe (1993) showed that the 33 $\rightarrow$ 3 resonant interactions transfer energy toward small wave frequencies (i.e $k_z/k_h << 1$). On the other hand, Babin et al. (1996, 1998) suggested that for Ro $\rightarrow$ 0, the 32 $\rightarrow$ 3 interactions dominate the 33 $\rightarrow$ 3 interactions in (2.58). This property would then lead to a freezing of the vertical 3D energy transfers and correspond, in spectral space, to a decoupling of the modes with different vertical wavenumber, k_z. Taylor columns would result from the horizontal (in k_h) cascade of 3D energy.

Finally, Cambon et al. (2004b) using a wave-turbulence theory approach, suggested that all modes stay coupled at small Ro, implying that the two-dimensionalization and decoupling discussed in the present section cannot rigorously occur even for infinite rotation rates.

2.6 Observations: laboratory experiments and numerical simulations

In this section we provide a review of the main experimental and numerical results of rotating turbulence. This review is kept brief in order to minimize overlap with the subsequent chapters, in which more details are provided. It is also limited to the studies which motivated this project. Results that appeared during the completion of this work are not discussed in this section. Their discussion is postponed to the sections presenting and comparing the results of this thesis.

2.6.1 Laboratory experiments

Several experiments studying small scale turbulence in rotating flows followed Taylor (1923). Among them, Traugott (1958) rotated a wind-tunnel. The measurements of this experiment were confined to a region in which the initial turbulence generation processes were still influential. The measurements indicated that the rotation was causing a slower decay of the energy (Tritton, 1978).

Ibbetson and Tritton (1975) compared turbulence with and without rotation. They were interested in determining whether or not the energy decay would be accelerated or slowed down by the effect of rotation. They observed an increase of the decay rate with rotation, but no mechanism was proposed, other than inertial wave propagation, which could transport energy from place to place in a way that is not possible in familiar turbulent flows. Phillips (1963) provided a theory of inertial wave propagation and dissipative reflection that Ibbetson and Tritton (1975) applied to their results.

McEwan (1973, 1976) argued that a rotating turbulent flow would tend to develop cyclonic vortices, i.e. vortices corotating with the background rotation. Cyclonic vortices were observed to dominate the flow. The rotating tank experiment carried out by Görtler (1957) and discussed in Greenspan (1968) showed that rotation induces an incompressible flow to support the propagation of waves. Hopfinger et al. (1982)

confirmed the presence of inertial waves. Hopfinger et al. (1982) and Dickinson and Long (1983) reported that an initially nearly isotropic turbulent flow organized into large-scale cyclonic and anticyclonic vortices. Hopfinger et al. (1982) observed a tendency to obtain more cyclones than anticyclones.

To summarize, most of the studies above agree on the generation of anisotropy due to rotation and observed a reduction of the downscale energy transfers expected in 3-dimensional turbulence. As exception was the overly-dissipative study of Ibbetson and Tritton (1975). These studies mainly focused on the short timescale τ_0 that is characteristic of the rotation rate. They showed a tendency toward two-dimensionality consistent with the linear theories discussed in §2.2. This, however, explains neither the predominance of the cyclones over the anticyclones nor the reduction of the energy transfer. Finally, although a two-dimensionalization was observed, no evidence of an inverse cascade was detected.

2.6.2 Numerical simulations

More recently, numerical simulations of turbulent flows became an important tool, complementing laboratory and theoretical studies of turbulence. Direct numerical simulations (DNS), in particular, compute each eddy of the flow at all scales without any parameterization. It is in a sense equivalent to a lab experiment, but with the advantageous possibility of controlling the initial conditions, which is important when dealing with a chaotic problem like turbulence. In addition, the range of possible data and statistics of the flow that one can measure is much wider compared to the options available in the laboratory. The only limitation of this tool is the restriction on the Reynolds numbers that are achievable. Numerical simulations of turbulence started in the 1970s, with resolutions of 32^3 and a Reynolds number of 35 for the earliest simulations carried out by Orszag and Patterson (1972), but this dramatically improved with the increase of computer power leading to Reynolds numbers that can now exceed those in most laboratory experiments (see Moin and Mahesh, 1998, for a more complete discussion). More importantly, when using DNS as a research tool for the study of turbulence, the goal is not to reproduce the real-life flows, but to perform controlled numerical experiments that could give a better insight and thus help to improve current turbulent models. To quote Moin and Mahesh (1998) "our response to the question *How high Re is high enough* would be *For what?* DNS need not obtain real-life Reynolds numbers to be useful in the study of real-life applications."

Several numerical studies have focused on rotating turbulence. Bardina et al. (1985), Bartello et al. (1994), and Cambon et al. (1997) all observed a clear tendency toward two-dimensionalization of decaying rotating turbulence. They focused on the nonlinear effects. The simulations of decaying rotating turbulence by Bardina et al. (1985) showed a tendency of the length scales along the axis of rotation to grow with rotation. They found that large-scale motions take the form of inertial waves and that the energy cascade to smaller scales is reduced by the effect of rotation. Bartello et al. (1994) reported the emergence of two-dimensional coherent structures from a rotating three-dimensional turbulent flow. They observed that for Ro of the order of unity, the counter-rotating columnar structures were unstable.

In forced simulations, Hossain (1994) showed that the three-dimensional turbulent flow became two-dimensional in a low resolution simulation (32^3). This tendency toward two-dimensionality could be characterized by a net energy transfer toward the zero-frequency modes $k_z = 0$, but some argued that the observed trend did not exactly lead to a classical two-dimensional field with two components (Cambon and Jacquin, 1989; Cambon et al., 1997). Godeferd and Lollini (1999) worked on reproducing the experimental results of Hopfinger et al. (1982) using numerical simulations in which they did not observe the inverse cascade expected in two-dimensional turbulence (discussed in §2.4.2). They conjectured that they did not observe the inverse cascade that Hossain (1994) observed due to the predominant effect of the three-dimensional field of waves in their forced simulations. A DNS by Morinishi et al. (2001) showed a directional anisotropy in the distribution of energy between the wave modes of high frequency and those of low frequency (2.13). Smith and Waleffe (1999) focused on forced rotating turbulence with a small scale forcing. They observed the generation of a k^{-3} energy spectrum with a concentration of the energy in the large scales (reminiscent of two-dimensional turbulence phenomenology). They argued that a spectrum of the form $E(k) \sim \Omega^2 k^{-3}$ would be recovered if one considered only Ω and k as relevant parameters in the inertial range. This k^{-3} would be distinct from the k^{-3} of the phenomenology of two-dimensional turbulence. On the other hand, Zhou (1995) derived a spectrum of k^{-2} for rapidly rotating turbulence, using a cascade argument similar to those presented in §2.4. The local energy transfer condition was assumed and the relevant timescales were considered. This k^{-2} scaling was retrieved in the simulations of Canuto and Dubovikov (1997) and Yeung and Zhou (1998) forcing in the large scales of the flow.

Most of the results reported above were obtained with simulations ran for relatively small integration times and were carried out for only few values of Ro. In addition, the definitions used to calculate the Rossby numbers differ widely from one study to another, making it difficult to articulate a general understanding of the effect of rotation on the turbulence and many issues need further investigation. The issues of the two-dimensionalization and the decoupling of the 2D modes from the 3D modes of the flow for small, but finite Ro remains open. The question of the overall energy transfer and the associated direction of the energy cascade must be clarified. The influence of the forcing scales used in previous studies that observed the inverse cascade vs. those that did not is still unknown. The roles of linear, nonlinear and resonant interactions in the generation of the coherent two-dimensional structures need to be studied. The question of how the idea of two-dimensionalization can be reconciled with the asymmetry between cyclones and anticyclones observed in the experiments also remains unanswered. This asymmetry is not a property of two-dimensional flows. In the following section, we summarize the questions that we intend to address in the next chapters.

2.7 Objectives

The overall aim of this thesis is to study how the nonlinear dynamics in turbulent flows is modified by rotation for a range of Rossby numbers less than one. We intend to isolate the nonlinear interactions, and to study how the rate of rotation affects their behaviour. Our approach is to solve the equations with direct numerical simulations complemented with theory. The objectives of this work are listed below:

- **To isolate the effect of rotation on the evolution of the nonlinear transfers of energy between the wave modes and vertically-averaged modes in decaying turbulence**: We aim to follow the transition of the rotating turbulent flow as Ro$\rightarrow 0$. Numerical simulations of decaying turbulence are subjected to 33 different rates of rotation. The size of the domain could influence the number of resonant and near-resonant interactions acting at certain Rossby numbers. We investigate this effect of a change of the domain size on the results obtained. (Chapter 3)

- **To investigate the kinematics of the problem, focusing on the resonant and near-resonant interactions**: In particular, we focus on the $33 \rightarrow 2$ interactions, that are relevant for the decoupling theories discussed in conjunction with (2.58)-(2.60). The relative number of resonant and near-resonant $33 \rightarrow 3$ and $32 \rightarrow 3$ interactions is also investigated. This is particularly important when examining the influence of the Ro on the wave energy transfers discussed in §2.5. We will examine how the number of resonant and near-resonant interactions vary with the Rossby number. A kinematic quantification of the number of interactions of each type will be discussed for various domain sizes and a wide range of Rossby numbers. (Chapter 4)

- **To test the predictions of the asymptotic theories of decoupling at the first order of the expansion**: We aim to determine how small Ro must be for the theories to hold, if they hold at all. We use both the tools of equilibrium statistical mechanics and inviscid numerical simulations. We use the inviscid analysis to investigate further, depending on Ro, how accurately and on which timescale the decoupled equations (2.58)-(2.60) would model the energy transfers of the full inviscid equations. (Chapter 5)

- **To investigate the effect of various forcing schemes on some of the results obtained in the previous items**: We investigate the reasons behind the k^{-3} energy spectrum scaling observed in previous forced simulations. We also examine the inverse cascade mechanism, including its similarities and discrepancies with the classical dynamics of two-dimensional turbulence. The role of forcing scales and the hypothesis of locality in scale for the nonlinear interactions are also examined. We use a set of numerical simulations of forced rotating turbulence. Some are forced at large horizontal scales and the others are forced at small horizontal scales. A dozen Rossby numbers are explored for each forcing scheme. We investigate the effect of the resolution on the results obtained. (Chapter 6)

Chapters 3-6 are written to be published separately. They are meant to be self-contained, which creates an unavoidable overlap between chapters.

Chapter 3

Freely decaying turbulence

In this chapter we present the results that we obtained using a large set of direct numerical simulations, covering a wide range of rotating ranges. This allowed us to observe a nonmonotonic tendency when *Ro* is varied from large to moderate-to-small *Ro* number limit. This behaviour is robust to changes of domain size. Three rotating regimes are identified: the *weakly rotating*, the *intermediate*, and the *asymptotic Ro* regimes. We argue that previous results in rotating turbulence can be reconciled in the light of this regime separation. The *intermediate Ro* regime is characterized by a positive transfer of energy from wave (3D) to the vortices modes (2D).

The three regimes separation has been tested in multiple ways. A robustness test is given in this chapter. This test, shows that a change in the size of the domain of the computation does not have an effect on the identified regime boundaries.

In addition to this test, another argument concerning the capture of the long term effect of the near-resonant interactions was examined. This latter study is described in more details in Chapter 4.

This chapter is based on the following manuscript published in the *Journal of Fluid Mechanics*:

- Bourouiba, L., and Bartello, P. (2007) The intermediate Rossby number range and 2D-3D transfers in rotating decaying homogeneous turbulence *J. Fluid Mech.*, **587**, 139-161. © 2007 Cambridge University Press. Reprinted with permission.

The intermediate Rossby number range and 2D-3D transfers in rotating decaying homogeneous turbulence

Abstract

Rotating homogeneous turbulence in a finite domain is studied using numerical simulations, with a particular emphasis on the interactions between the wave and zero-frequency modes. Numerical simulations of decaying homogeneous turbulence subject to a wide range of background rotation rates are presented. The effect of rotation is examined in two finite periodic domains in order to test the effect of the size of the computational domain on the results obtained, thereby testing the accurate sampling of near-resonant interactions. We observe a non-monotonic tendency when *Ro* is varied from large values to the small-*Ro* number limit, which is robust to the change of domain size. Three rotating regimes are identified and discussed: the *large*, the *intermediate*, and the *small Ro* regimes. The *intermediate Ro* regime is characterized by a positive transfer of energy from wave modes to vortices. The 3D to 2D transfer reaches an initial maximum for $Ro \approx 0.2$ and it is associated with a maximum skewness of vertical vorticity in favour of positive vortices. This maximum is also reached at $Ro \approx 0.2$. In the intermediate range an overall reduction of vertical energy transfer is observed. Additional characteristic horizontal and vertical scales of this particular rotation regime are presented and discussed.

3.1 Introduction

Rotating frame effects have a crucial influence on large scale atmospheric and oceanic flows as well as some astrophysical and engineering flows in bounded domains (turbine rotor, rotating spacecraft reservoirs or Jupiter's atmosphere, for example). The Coriolis force appears only in the linear part of the momentum equations, but if strong enough, it can radically change the nonlinear dynamics. The strength of the applied rotation is only appreciable if it is comparable to the nonlinear term. The Rossby number, $Ro = U/2\Omega L$, is a dimensionless measure of the relative size of these terms. Here, Ω is the background rotation rate and U and L are characteristic length and velocity scales, respectively.

When the Coriolis force is applied, inertial waves are solutions of the linear momentum equations. Their frequencies vary from zero to 2Ω (Greenspan 1968). The zero linear frequency modes correspond to two-dimensional structures (e.g. shear layers, vortices, etc.), independent of the direction parallel to the rotation axis.

Unlike the rotating-stratified case, the zero-frequency modes in the rotating problem are not related to a third normal mode of the linear operator. However, it is common to still refer to these modes as vortical modes as discussed below in §3.2. In the full nonlinear problem, the large range of frequencies of the inertial waves is at the origin of a complex nonlinear interplay of interactions involving the two-dimensional structures and the wave modes (e.g. resonant triad interactions, quartets, etc.). The dynamics of the two-dimensional structures are, however, slow compared to the timescale of the three-dimensional flow, if Ro is low. This motivated previous work by Benney and Saffman (1966) and Newell (1969) among others. They employed multiple timescale asymptotic techniques in the strong rotation limit. Newell (1969) showed that the exact and near-resonant interactions play an important role on a timescale of $O(1/Ro)$, given that the linear timescale is of $O(Ro)$. In this limit, only the resonant and the near-resonant triads are thought to make a significant contribution on the slow timescale, thereby governing the nature of 2D-3D interactions in that limit.

In this limit, several modal decompositions can be used. One decomposition is the helical mode decomposition employed by Greenspan (1968), Cambon and Jacquin (1989), Waleffe (1993), Smith and Waleffe (1999) and Morinishi et al. (2001). Starting from this or similar decompositions, resonant wave theories have been developed. Leading to the derivation of an averaged equation. For example, Babin et al. (1998) showed that the Navier-Stokes equations can be decomposed into equations governing a three-dimensional (wave modes) subset, a decoupled two-dimensional subset (the averaged equation), and a component that behaves as a passive scalar. Using the resonant wave theory approach, Waleffe (1993) also argued that nonlinear transfers in rotating turbulence are preferentially towards larger, but non-vortical (i.e. not zero-frequency or 2D), vertical scales in the strong rotation limit.

Several experiments in rotating turbulence have been performed, such as those by McEwan (1969, 1976), Hopfinger et al. (1982), Jacquin et al. (1990), Baroud et al. (2002) and Morize, Moisy and Rabaud (2005). The experiments showed an increase of the correlation lengths along the axis of rotation. In other words, rapid rotation leads to a tendency for two-dimensionalisation of an initially-isotropic flow. A predominance of cyclonic over anticyclonic activity and a reduction of energy decay have also been observed for certain rotation rates ($Ro \sim O(1)$).

Various numerical simulations have been performed to examine the problem of rotating turbulence, such as the decaying turbulence simulations of Bardina, Ferziger and Rogallo (1985) and Bartello, Métais and Lesieur (1994). The latter was the first to demonstrate numerically the breaking of the vorticity symmetry for Rossby numbers of order one in decaying homogeneous turbulence. Note that this preferential destabilization of anticyclones in rotating flows for a Rossby number of order one had previously been observed in confined and free shear flows (mixing layers and plane wakes). Examples are found in Johnson (1963), Rothe and Johnsto (1979), Witt and Joubert (1985), Tritton (1992) and Bidokhti and Tritto (1992). The results above support the idea of the emergence of a strong anisotropy by the alignment of the vorticity vector to the rotation axis and the stability of this configuration. They are *a priori* consistent with the tendency of the flow to two-dimensionalise, except for the symmetry breaking, which is not a property of two-dimensional turbulence.

Many studies of forced rotating homogeneous turbulent flow simulations have been performed, including Yeung and Zhou (1998), Smith and Waleffe (1999) and Chen etal (2005). They observed a strong upscale transfer of energy toward larger vertical scales for low *Ro* numbers. Unlike the 2D inverse cascade, a k_h^{-3} spectrum was observed in forced simulations by Smith & Waleffe (1999), where k_h is the horizontal wavenumber smaller than that of the forcing. A similar behaviour is present at only the higher of the two Rossby numbers examined in Chen etal (2005). The lower *Ro* simulation displayed behaviour is consistent with a reduction of the interactions between two-dimensional modes and the rest of the flow. The breaking of the vorticity symmetry, identified in the decay simulations of Bartello et al. (1994), also appeared in the forced simulation of Smith & Waleffe (1999). This non-two-dimensional property is not taken into account in current theories involving resonant triads. Smith & Lee (2005) found that near-resonant triads have an important role in the vorticity asymmetry.

The scope of this paper is restricted to flows in bounded domains, with discrete wavenumbers. The numerical studies in finite and infinite domains are both idealizations of the rotating flows found in nature and industry. Both approaches have advantages and major limitations to direct practical applications. In any case, if, as has been observed, the integral scale along the rotation axis grows, then presumably it will eventually fill a large part of the flow domain. When this occurs further progress in understanding the flow will depend on the precise details of its geometry. It is therefore worth mentioning the numerous studies of the problem in unbounded domains (continuous wavenumbers), even if the real flows of interest targeted by this paper are those found in finite natural or manufactured domains. Such studies include such as axisymmetric EDQNM developments on the basis of helical modes two-point closure found in Cambon and Jacquin (1989) and Cambon et al. (1997). The two-point closure model used in the former showed a positive 'angular energy transfer' toward the zero-frequency spectral plane (i.e. 2D modes), which is consistent with the weak turbulence analysis, performed in Waleffe (1992) and Waleffe (1993). In Cambon et al. (1997) numerical simulations of the first order decoupling at finite *Ro* are said to be inconclusive. The unrealistic geometry is said to lead to a lack of angular resolution of the discrete set of wave vectors. Following the standard weak turbulence approach (Benney & Newell 1969), several analytical studies have been performed in which nonlinear interactions govern the long-time behaviour in various flows (e.g. Caillol & Zeitlin 2000 for the internal gravity waves, Galtier etal 2000 for incompressible magnetohydrodynamics, Galtier 2003 and Bellet etal 2006 for the specific case of inertial waves). Cambon, Rubinstein & Godeferd's (2004) extended wave turbulence theory suggested that two-dimensionalisation cannot rigorously be reached even for infinite rotation rates in continuous and unbounded domains. They demonstrated the presence of new volume and principal value integrals that maintain the coupling between slow and rapid modes.

Bellet etal (2006) aimed to capture the dynamics for asymptotically high rotation rates, for which resonant interactions are predicted by wave-turbulence theories to have a dominant contribution to the dynamics. An Asymptotic Quasi-Normal Markovian (AQNM) model was developed by the authors, investigating the dynamics of only the resonant inertial wave interactions between 3D modes. In fact, the AQNM model can not capture the resonant triads involving zero-frequency (2D) modes. An angular energy spectrum is obtained numerically and it is found that the energy density is large near the perpendicular wave vector plane. The singularity is found to be integrable like in other wave-turbulence results such as Galtier (2003). AQNM is discussed further below in §3.2.

The remainder of the paper in presented as follows. In section 3.2 the governing equations, the normal mode decomposition and wave theory are reviewed and the modal decomposition is introduced. The numerical methodologies are presented in more detail in section 3.3. In section 3.4, three rotating regimes are identified, showing a non-monotonic tendency of the dynamics and vorticity asymmetry as *Ro* decreases.

A general dynamical picture of decaying turbulent flows for moderate to small *Ro* in bounded domains is discussed and summarized. Conclusions are given in section 3.5.

3.2 Equations and rotating turbulence theories

In a rotating frame of reference, the incompressible momentum equations are:

$$\frac{\partial \boldsymbol{u}}{\partial t} + (\boldsymbol{u} \cdot \nabla)\boldsymbol{u} + 2\Omega\hat{\mathbf{z}} \times \boldsymbol{u} = -\nabla\tilde{\mathbf{p}} + \mathbf{d}_{\mathbf{p}}(\boldsymbol{u}), \qquad \nabla \cdot \boldsymbol{u} = 0, \tag{3.1}$$

where $\boldsymbol{\Omega} = \Omega\hat{\mathbf{z}}$ is the rotation vector, the velocity is $\boldsymbol{u} = (u, v, w)$ and $\tilde{p}$ includes the pressure term of the inertial frame, the centrifugal term and other contributions from conservative forces. The usual viscous term corresponds to $p = 1$ in the hyperviscosity $\mathbf{d}_p(\boldsymbol{u}) = (-1)^{p+1}\nu_p(-\nabla^2)^p\ \boldsymbol{u}$. Without loss of generality, the rotation axis has been chosen to be the vertical. For the nondimensionalisation we use $(2\Omega)^{-1}$, L and U as characteristic time, length and velocity, respectively. The nondimensional equations become

$$\frac{\partial \boldsymbol{u}}{\partial t} + Ro\ (\boldsymbol{u} \cdot \nabla)\boldsymbol{u} + \hat{\mathbf{z}} \times \boldsymbol{u} = -\nabla\mathbf{p} + \mathbf{D}_{\mathbf{p}}(\boldsymbol{u}), \qquad \nabla \cdot \boldsymbol{u} = 0, \tag{3.2}$$

where *Ro* is the Rossby number. As $Ro \longrightarrow 0$, (3.2) evolves on both a slow vortical timescale $\tau_1 = Ro\ t$ and a fast wave timescale $\tau_0 = t$, where t is the nondimensional time. A two-timescale asymptotic expansion can be performed. The leading-order contribution has inertial wave solutions of nondimensional frequencies $\omega_{s_k}(\boldsymbol{k}) = s_{\boldsymbol{k}}\hat{\mathbf{z}} \cdot \boldsymbol{k}/|\boldsymbol{k}| = \mathrm{s}_{\boldsymbol{k}}\mathrm{k}_{\mathbf{z}}/\mathrm{k} = \mathrm{s}_{\boldsymbol{k}}\cos(\theta_{\boldsymbol{k}})$, where $s_{\boldsymbol{k}} = \pm 1$ and $\theta_{\boldsymbol{k}}$ is the angle between the axis of rotation (here $\hat{\mathbf{z}}$) and the Fourier-space wavevector $\boldsymbol{k}$. In the following $\omega_{s_k}(\boldsymbol{k})$ is also referred to as ω_{s_k}. The associated normal modes, also called *helical modes* (Waleffe 1993), are

$$\mathrm{N}^{s_k} = \left(\frac{\hat{\mathbf{z}} \times \boldsymbol{k}}{|\hat{\mathbf{z}} \times \boldsymbol{k}|} \times \frac{\boldsymbol{k}}{|\boldsymbol{k}|} + i s_{\boldsymbol{k}} \frac{\hat{\mathbf{z}} \times \boldsymbol{k}}{|\hat{\mathbf{z}} \times \boldsymbol{k}|}\right), \tag{3.3}$$

where $i^2 = -1$ and $\mathrm{N}^{s_k}(\boldsymbol{k})$ are the eigenmodes of the curl operator obtained by solving

$$i\boldsymbol{k} \times \boldsymbol{n}(\boldsymbol{k}) = \lambda \boldsymbol{n}(\boldsymbol{k}). \tag{3.4}$$

The solutions for λ are $+|\boldsymbol{k}|$ and $-|\boldsymbol{k}|$, which give the eigenvectors $\mathbf{N}^+$ and $\mathbf{N}^-$ for $\boldsymbol{n}$. Using these solutions in (3.2) gives us the expression for the eigenmodes associated with the linear rotation operator. They are called inertial waves (Greenspan 1968) and are given by

$$\mathbf{N}^{s_k}(\boldsymbol{k}) \exp(i\omega_{s_k}(\boldsymbol{k})t), \tag{3.5}$$

where $\mathbf{N}^+(\boldsymbol{k})$ is the complex conjugate of $\mathbf{N}^-(\boldsymbol{k})$ (e.g. Cambon & Jacquin 1989, Waleffe 1992, 1993). The velocity field in Fourier-space can therefore be written

$$\boldsymbol{u}(\boldsymbol{k}, \tau_0, \tau_1) = \sum_{s_k=\pm} A_{s_k}(\mathbf{k}, \tau_1)\ \mathbf{N}^{s_k}(\boldsymbol{k}) e^{i\omega_{s_k}\tau_0}. \tag{3.6}$$

Note that even if a timescale separation analysis is used here ($\partial_t \to \partial_{\tau_0} + Ro\ \partial_{\tau_1}$), low frequency waves are still present in the system. The analysis gives an equation for the slow evolution of the amplitudes A_{s_k}

$$\partial_{\tau_1} A_{s_k}(\boldsymbol{k}, \tau_1) = -\frac{1}{4} \sum_{\substack{\boldsymbol{k}=\boldsymbol{p}+\boldsymbol{q} \\ s_p, s_q}}^{\omega_{s_k}+\omega_{s_p}+\omega_{s_q}=0} C^{s_k s_p s_q}_{\boldsymbol{kpq}} A_{s_p}(\boldsymbol{p}, \tau_1)\ A_{s_q}(\boldsymbol{q}, \tau_1). \tag{3.7}$$

$C^{s_k s_p s_q}_{\boldsymbol{kpq}}$ are the interaction coefficients shown by Waleffe (1992) to have the form

$$C^{s_k s_p s_q}_{\boldsymbol{kpq}} = (s_p p - s_q q)\ (\mathbf{N}^{s_p} \times \mathbf{N}^{s_q}) \cdot \mathbf{N}^{*\ s_k}, \tag{3.8}$$

where the star stands for the complex conjugate. The only interacting triads that have a significant contribution on the slow timescale τ_1 in (3.7) are those that satisfy the *resonance condition*

$$\omega_{s_k}(\boldsymbol{k}) = \omega_{s_p}(\boldsymbol{p}) + \omega_{s_q}(\boldsymbol{q}). \tag{3.9}$$

In other words, those satisfying

$$\boldsymbol{k} = \boldsymbol{p} + \boldsymbol{q} \quad \text{and} \quad s_k \frac{\boldsymbol{k}_z}{|\boldsymbol{k}|} = s_p \frac{\boldsymbol{p}_z}{|\boldsymbol{p}|} + s_q \frac{\boldsymbol{q}_z}{|\boldsymbol{q}|}. \tag{3.10}$$

The frequencies of the inertial waves vary from 0 to 2Ω. The zero-frequency modes belong to the 2D Fourier-space plane defined by $k_z = 0$, corresponding to the vertically-averaged real-space velocity field. In the rotating-stratified case, the linear operator has two inertia-gravity wave eigenmodes and a third distinct vortical quasi-geostrophic normal mode with zero frequency. Unlike that case, the zero-frequency mode of the present problem with rotation only is not a third normal mode of the linear operator. It is only derived from the wave modes for the particular value of $k_z = 0$. In that sense, it is analogous to the stratified shear modes, found on the 1-D k_z axis in Fourier-space. In the problem with rotation alone, however, the zero-frequency modes describe a 2D Fourier-space plane (defined by $k_z = 0$). As these modes form the slowly-varying components of the flow, we refer to them as vortical. We introduce the following notation [1]

$$\text{If } \boldsymbol{k} \in V_{\boldsymbol{k}} = \{\boldsymbol{k}|k \neq 0 \text{ and } k_z = 0\} \text{ then } \boldsymbol{u}(\boldsymbol{k}) = \boldsymbol{u}_{2D}(\boldsymbol{k}_h) + w(\boldsymbol{k}_h)\ \hat{\mathbf{z}}. \tag{3.11}$$

$$\text{If } \boldsymbol{k} \in W_{\boldsymbol{k}} = \{\boldsymbol{k}|k \neq 0 \text{ and } k_z \neq 0\} \text{ then } \boldsymbol{u}(\boldsymbol{k}) = \boldsymbol{u}_{3D}(\boldsymbol{k}).$$

We can also decompose the total energy $\mathrm{E} = \frac{1}{2}\sum\limits_{\boldsymbol{k}} |\mathbf{u}(\boldsymbol{k})|^2$ into three contributions [2]

$$\mathrm{E} = \mathrm{E}_{2D} + \mathrm{E}_w + \mathrm{E}_{3D}, \tag{3.12}$$

with

$$\mathrm{E}_{2D} = \frac{1}{2}\sum_{\boldsymbol{k}\in V_{\boldsymbol{k}}} |\mathbf{u}_{2D}(\boldsymbol{k})|^2, \quad \mathrm{E}_w = \frac{1}{2}\sum_{\boldsymbol{k}\in V_{\boldsymbol{k}}} |w(\boldsymbol{k})|^2 \quad \text{and} \tag{3.13}$$

$$\mathrm{E}_{3D} = \frac{1}{2}\sum_{\boldsymbol{k}\in W_{\boldsymbol{k}}} |\mathbf{u}(\boldsymbol{k})|^2,$$

along with their corresponding spectra. The latter are governed by

$$\frac{\partial \mathrm{E_{3D}}}{\partial t}(\boldsymbol{k} \in W_{\boldsymbol{k}}, t) = (T_{3-33} + T_{3-32} + T_{3-3w})(\boldsymbol{k} \in W_{\boldsymbol{k}}, t) - \tilde{D}_{p,3D}(\boldsymbol{k} \in W_{\boldsymbol{k}}, t), \tag{3.14}$$

$$\frac{\partial \mathrm{E_{2D}}}{\partial t}(\boldsymbol{k} \in V_{\boldsymbol{k}}, t) = (T_{2-22} + T_{2-33})(\boldsymbol{k} \in V_{\boldsymbol{k}}, t) - \tilde{D}_{p,2D}(\boldsymbol{k} \in V_{\boldsymbol{k}}, t),$$

$$\frac{\partial \mathrm{E_{w}}}{\partial t}(\boldsymbol{k} \in V_{\boldsymbol{k}}, t) = (T_{w-2w} + T_{w-33})(\boldsymbol{k} \in V_{\boldsymbol{k}}, t) - \tilde{D}_{p,w}(\boldsymbol{k} \in V_{\boldsymbol{k}}, t),$$

with T being the Fourier-space energy transfer and $\tilde{D}_{p,2D \text{ or } 3D \text{ or } w}$ the 2D, 3D and vertically-averaged w spectral dissipation terms, respectively. Transfers are distinguished by the types of interactions, eg. 2-33 stands for the interactions between two

[1] An analogous semi-axisymmetric decomposition was introduced by Cambon and Jacquin (1989) in terms of energy, polarization and helicity, noted $e(k, \cos\theta)$, $Z(k, \cos\theta)$ and $h(k, \cos\theta)$, respectively.

[2] E_{3D}, E_{2D} and E_w correspond to $e(k, \cos\theta \neq 0)$, $(e - Z)|_{\cos\theta=0}$ and $(e + Z)|_{\cos\theta=0}$, respectively.

3D wave modes that contribute to the 2D equation. Note that the T_{i-jk} terms are symmetric in j and k. Only a subset of 3D wavenumbers can satisfy the resonance condition in the 3-33, 3-32 and 3-3w interactions, but from (3.8) it follows that 3-32 and 3-3w resonant triads do not transfer energy to the 2D and w modes, respectively (Waleffe 1993). They are therefore said to be "catalytic" for interactions between the two wave modes of the same frequency. This last property is a key point in asymptotic decoupling theories. In the $Ro \to 0$ limit, it is thought that only resonant interactions make a significant contribution to the slow dynamics. Therefore, the asymptotic energy equations in this limit are

$$\frac{\partial \mathrm{E}_{3\mathrm{D}}}{\partial t}(\boldsymbol{k} \in W_{\boldsymbol{k}}, t) = T_{3-33,res} + T_{3-32,res} + T_{3-3w,res} - \tilde{D}_{p,3D}, \tag{3.15}$$

$$\frac{\partial \mathrm{E}_{2\mathrm{D}}}{\partial t}(\boldsymbol{k} \in V_{\boldsymbol{k}}, t) = T_{2-22} - \tilde{D}_{p,2D},$$

$$\frac{\partial \mathrm{E}_{\mathrm{w}}}{\partial t}(\boldsymbol{k} \in V_{\boldsymbol{k}}, t) = T_{w-2w} - \tilde{D}_{p,w},$$

where the subscript $\{i - jk, res\}$ stands for resonant $i - jk$ interactions (3.10). The time and wavenumber dependence in (3.15) has been omitted. 2-22 and w-2w interactions are trivially resonant, since all modes involved have zero frequency. It appears from (3.15) that the equation for E_{2D} is decoupled from the E_{3D} equation and is also identical to that governing two-dimensional turbulence. The equation for E_w is also decoupled from that of E_{3D} and takes the form of that of a passive tracer advected by the 2D velocity field $\boldsymbol{u}_{2D}$. On the other hand, the E_{3D} equation is not decoupled since the 3D energy interactions remain affected by the $k_z = 0$ dynamics through the set of catalytic resonant triads 3-32 and 3-3w.

Waleffe (1993) and Cambon etal (1997) found that the 3-33 resonant subset plays an important role in the quasi-two-dimensionalisation of the flow. According to their argument, these interactions transfer the E_{3D} energy preferentially in an angular sense to close to, but not exactly, zero-frequency waves. Based on the greater complexity of the resonant subset of 3-33 interactions compared to that of 3-23, it has been argued by Babin etal (1996, 1998) that flow in the $Ro \to 0$ limit would display not only the E_{2D} decoupled dynamics, but an infinity of approximate adiabatic invariants corresponding to a decoupling of each constant k_z Fourier-space surface. Such a result implies a freezing of vertical transfer in the strong rotation limit.

In Bellet et al. (2006), the AQNM model is intended to specifically capture only the resonant interactions and thus only the asymptotic regime. The equations used in AQNM are those of an unbounded domain in real space, corresponding to a continuous distribution of wave vectors in Fourier space. A cautious correspondence with the equations presented here is nevertheless possible. In fact, in Bellet et al. (2006) the resonance condition is not applicable in the vicinity of the $k_z = 0$ Fourier plane. 2D and w modes introduced in (3.11) are therefore excluded from the AQNM model. Thus, AQNM is equivalent to a modified (3.15), in which only the 3D modes are retained, i.e equivalent to [3]

$$\frac{\partial \mathrm{E}_{3\mathrm{D}}}{\partial t}(\boldsymbol{k} \in W_{\boldsymbol{k}}, t) = T_{3-33,res}(\boldsymbol{k} \in W_{\boldsymbol{k}}, t), \tag{3.16}$$

where both $T_{3-32,res}$ and $T_{3-3w,res}$ terms are removed. Given that the aim of this paper is to focus on 2D-3D interactions at finite Rossby number and that there are no strictly resonant interactions capable of such transfer, we necessarily restrict ourselves to a regime where non-resonant interactions are still present. In addition, given that the redistribution of wave energy via the catalytic 2D-3D resonant-interaction term in the E_{3D} equation is also of interest, we are forced to conclude that there is limited scope in comparing our results with AQNM-type studies.

3.3 Numerical method and Rossby number

Equations (3.2) are solved numerically using a direct (de-aliased) pseudo-spectral method. The integration domain is triply periodic of length 2π. We use the leapfrog time differencing and the Asselin-Robert filter in order to control the computational mode (eg. R. Asselin 1972). The filter factor was set to be 10^{-3}. Due to the anisotropy of the problem we used cylindrical truncation for all our simulations, i.e.

[3]The viscosity term is omitted for brevity.

k_h, $|k_z| < k_t = N/3$, where N^3 is the number of spatial collocation points (referred to as resolution) and $k_h = \sqrt{k_x^2 + k_y^2}$ is the horizontal wavenumber. The "two-thirds rule" was chosen in order to filter the aliasing of the misrepresented wavenumbers introduced by the computation of the nonlinear terms (Boyd 1989). We used a hypervisosity $\mathbf{D}_p(\boldsymbol{u})$ in (3.2), with $p = 4$ in order to obtain higher effective Reynolds numbers (e.g. Bartello etal 1994).

Our strategy has been to decompose the fields into waves ($k_z \neq 0$), 2D and w components as in (3.11) and (3.14). The Rossby number is the dimensionless measure of the relative size of the rotation to the advection terms. It can be defined as $Ro = U/2\Omega L$, where U and L are characteristic length and velocity scales, respectively. Jacquin et al. (1990) showed experimental evidence of two relevant Rossby numbers, a *macro*-Rossby number, Ro_{macro}, based on a large length scale (e.g. an integral Length scale L) and a *micro*-Rossby, R_{micro}, based on a smaller length scale (a Taylor micro-scale λ). They observed two distinct and successive transitions at $Ro_{macro} \approx 1$ and $Ro_{micro} \approx 1$. In the reminder of this paper, the following definition of Ro is used:

$$Ro_m = \sqrt{[\omega_z^2]}/(2\Omega), \tag{3.17}$$

with [.] the spatial average and ω_z the vertical vorticity component. Due to the use of the vorticity in 3.17, this definition would correspond to the *micro*-Rossby number in Jacquin et al. (1990) and Cambon et al. (1997) for close to isotropy 3D flows. For this latter flow configuration another definition, $Ro_M = U/2\Omega L$, with L based on the energy containing large scales would also be relevant. Ro_M would correspond to the Ro_{macro} in Jacquin et al. (1990). For comparison, we computed both Ro_M and Ro_m. Both values are displayed in table 3.1, thereby testing the sensitivity of the results to the use of either definition. Unless noted otherwise (3.17) is used to compute the Rossby number and it is denoted Ro in the remainder of the paper.

3.4 Decaying rotating turbulence simulations

3.4.1 Non-monotonic tendency as $Ro \to 0$ and its robustness to the change of the size of the domain

A set of simulations were initialized with fully-developed isotropic decaying turbulent fields generated in domains of different sizes. Different rotation rates were then imposed on the resulting fields (table 3.1).

We choose to present results of the simulations obtained from grids of resolutions 100^3 and 200^3. For the small domain simulation (S) (resolution 100^3) the preliminary non-rotating simulation is initialized with an isotropic Gaussian spectrum centered around $k_{i,S} = 6.4$, with width $\sigma_S = 1.6$ and total energy $E_S = 0.41$. The truncation wavenumber is $k_{t,S} = 32$. The set-up for the large domain (resolution 200^3) (L) (twice as as large as S) leads to $k_{t,L} = 66$ and a rescaled spectra using a stretching coefficient of $\gamma = k_{t,L}/k_{t,S}$ giving $k_{i,L} = 13.2$, $\sigma_L = 3.3$ and $E_L = 3.59$. Initial non-rotating spectra of total energy E are displayed for both simulations in figure 3.1 (left).

We chose this two domains and rescaling described above in order to study the sensitivity of the results to a change in the size of the computational domain, rather than a change of resolution[4]. This also indirectly allows us to check both the influence of the angular resolution of the discrete domain, and the adequacy of sampling of near-resonant interactions that are linked to the size of the domain.

These preliminary non-rotating simulations were run until the enstrophy maximum was reached (after about 10 large-scale turnover times). The non-rotating fully-developed turbulent energy spectra obtained at the end of the preliminary runs are compared in figure 3.1 (right). The collapse outside of the dissipation range is still good. A horizontal (x,y) slice of the vertical vorticity field ω_z in the large computational domain is displayed in figure 3.2.

At this point, different rotation rates are applied to the isotropic fully developed

[4]This is implemented by both a change of resolution and a rescaling argument of the initial fields.

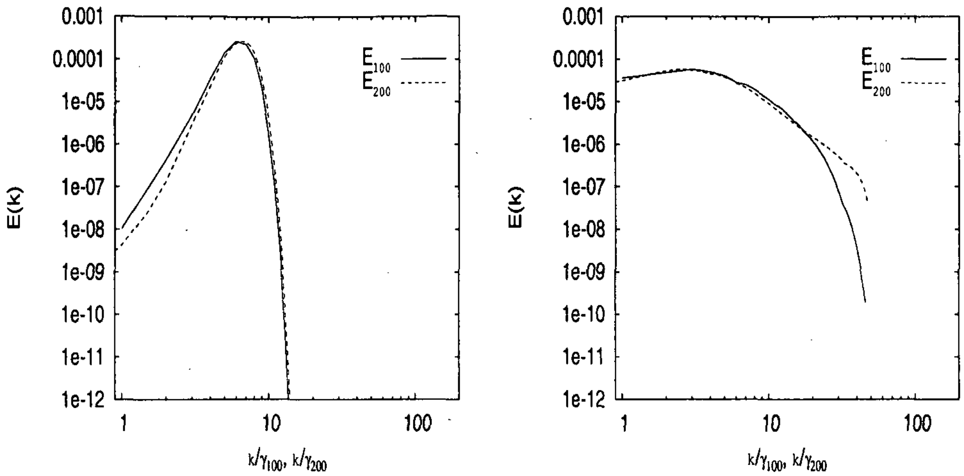

Figure 3.1: Total energy spectra for preliminary non-rotating simulations. Spectra of E_S and E_L used to initiate the preliminary run (left) and corresponding final spectra of the flow used to initiate the rotating simulations (right). We present results of the large and small size boxes, with $\gamma_S = 1$ and $\gamma_L = 2.062$.

turbulence. Parameters such as initial energies, hyperviscosity coefficients and eddy turnover timescales at the end of the preliminary non-rotating simulation are given in table 3.1. High rotation rates require very long calculations due to timestep limitations imposed by the explicit treatment of the Coriolis term. The initial *Ro* and associated timesteps are also given in table 3.1. The equivalent large-scale based Ro_M for each of the simulations in domains L and S is given in table 3.1.

Figure 3.3 displays the normalized energy time series of 2D and wave modes as a function of nondimensional time for the large box runs. The curves for the small box are similar and are therefore not shown here. Time has been nondimensionalised using the initial eddy turnover timescales (table 3.1). The preliminary non-rotating run shows little vortical energy with respect to wave energy, as expected for an isotropic system where the decomposition has no meaning. At the end of this preliminary run, different rotation rates were applied (table 3.1). We observe three types of behaviour.

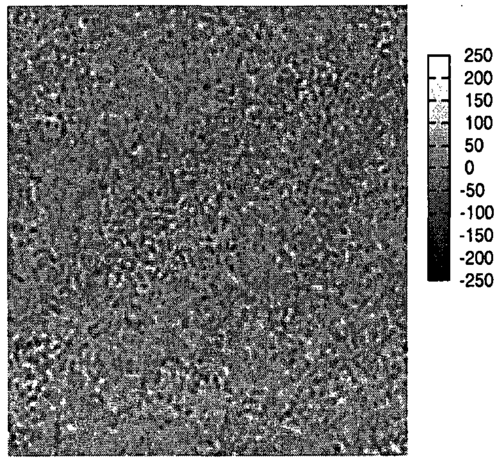

Figure 3.2: Horizontal slice (x,y) of the vorticity field ω_z at the end of the isotropic simulation. The field is used to initialize the subsequent rotating simulations of the large computational domain

First, *large Ro* simulations display a time evolution similar to that of isotropic simulations, where both 2D and 3D energies have the same decay rate (e.g. $Ro = 100$). As rotation increases, we observe a transition to a second regime of slow total energy decay. We call this regime the *intermediate Ro* range or regime. It is characterized by a growth of E_{2D} with time, while the wave energy decay is reduced. The E_{2D} growth rate reaches a maximum for $Ro \approx 0.2$. We therefore chose to display this particular Ro as an example. Throughout this paper, our discussion of the $Ro \approx 0.2$ simulation applies qualitatively to all *intermediate Ro* range simulations. Around $t/\tau \approx 300$ vortical and wave energy curves cross in figure 3.3 (bottom-left). After that time, most of the energy is two-dimensional. This increase of two-dimensional energy implies a transfer from three-dimensional modes. This is an important characteristic of the *intermediate-Ro* range. Finally, more rapidly-rotating simulations do not display this wave-vortex energy transfer. In fact, the time series show an expected slower decay rate of wave energy, E_{3D}, at $Ro = 0.01$, but only a slight dissipation of E_{2D}, consistent with a negligible transfer between V_k and W_p modes. Recall that energy does not decay in 2D turbulence in the limit $Re \to \infty$. We refer to this third Ro

range as the *small* regime. Its characteristic is the apparent decoupling of wave and vortex modes that seems to be in agreement with the first order resonant theories introduced in §3.2.

We observe an overall reduction of both total energy and enstrophy decay with rotation. This is consistent with the expected reduction of the energy cascade in rotating turbulence due to phase scrambling. Thus, high values of enstrophy and energy are observed for a longer period of time as Ro decreases. We have already observed that a range of rotation rates, referred to as the *intermediate* range, is characterized by an increase of vortical energy and therefore a strong interaction between wave and vortical modes. Both enstrophy and energy are decomposed following (3.11). We display the resulting time series in figures 3.4 and 3.5. Figure 3.4 displays the large box time series of E_{3D}, E_{2D} and E_w. Figure 3.5 displays the large domain size time series of 3D enstrophy given by

$$V_{3D} = \frac{1}{2} \sum_{\boldsymbol{k} \in W_{\boldsymbol{k}}} |\boldsymbol{\omega}(\boldsymbol{k})|^2 , \tag{3.18}$$

w enstrophy V_w given by

$$V_w = \frac{1}{2} \sum_{\boldsymbol{k} \in V_{\boldsymbol{k}}} |\boldsymbol{\omega}_h(\boldsymbol{k})|^2 , \tag{3.19}$$

and the 2D enstrophy V_{2D} given by

$$V_{2D} = \frac{1}{2} \sum_{\boldsymbol{k} \in V_{\boldsymbol{k}}} |\boldsymbol{\omega}_z(\boldsymbol{k})|^2. \tag{3.20}$$

In these equations $\boldsymbol{\omega}$ is the total vorticity field, $\boldsymbol{\omega}_h = \omega_x \mathbf{x} + \omega_y \mathbf{y}$ is its horizontal component and $\boldsymbol{\omega}_z$ its vertical component.

Outside of the *intermediate Ro* range the total energy is dominated by wave energy, E_{3D}. The *intermediate Ro* simulations show an increase of E_{2D} with time. The maximum growth rate is reached for $Ro \approx 0.2$ (figure 3.4). Meanwhile, the enstrophy V_{2D} shows a maximum growth for that same Ro (figure 3.5). For all Ro numbers E_w decreases with time, i.e the transfer of energy from modes in $W_{\boldsymbol{k}}$ to modes in $V_{\boldsymbol{k}}$ does

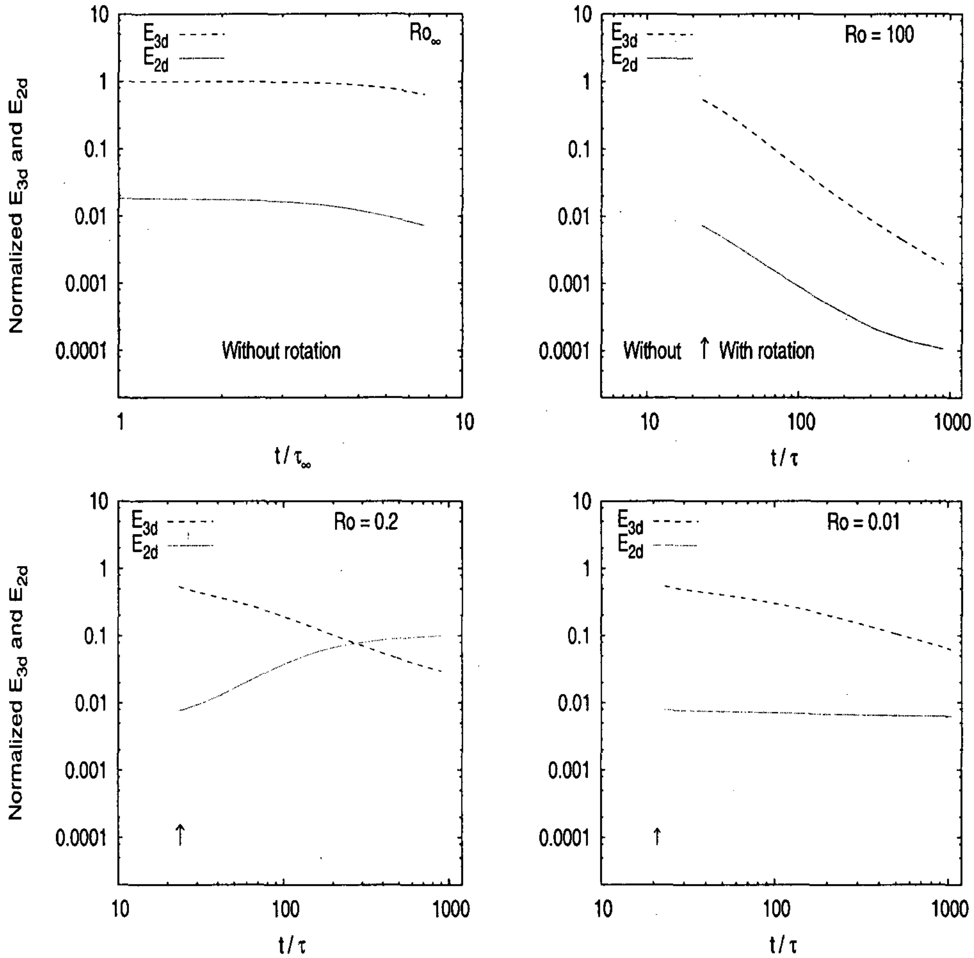

Figure 3.3: Time series of normalized E_{2D} and E_{3D} as a function of the nondimensional time t/τ, where the eddy turnover timescale for the initial non-rotating run is $\tau_\infty = 0.032$ and the initial eddy turnover timescale for the rotating runs is $\tau = 0.012$. The initial non-rotating run is presented on the top left, $Ro = 100$ on the top right, $Ro = 0.2$ on the bottom left and $Ro = 0.01$ on the bottom right. All these results were obtained with the large computational box size.

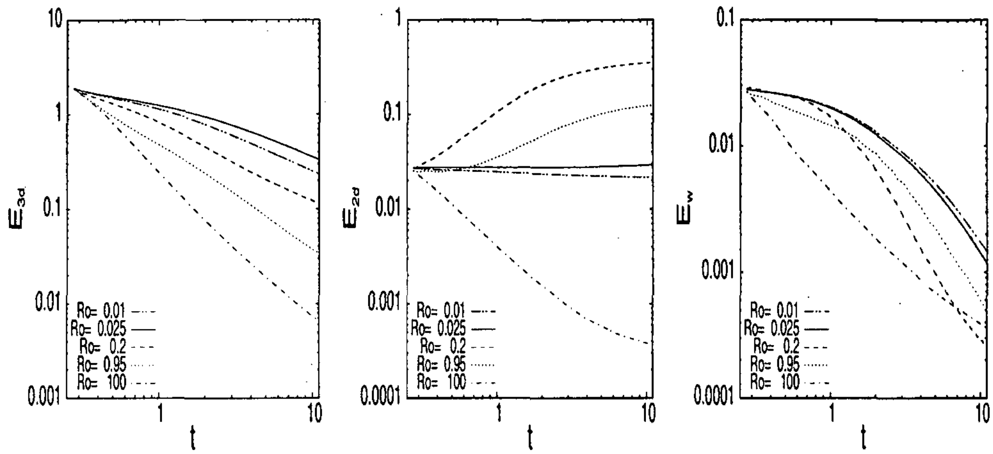

Figure 3.4: Time series for the large box simulations of the wave energy (left), the vortical energy (middle) and the volume mean square of w, E_w (right)(3.14) for *Ro* = 100, 0.95, 0.2, 0.025 and 0.01. Qualitatively similar results were obtained for the small box.

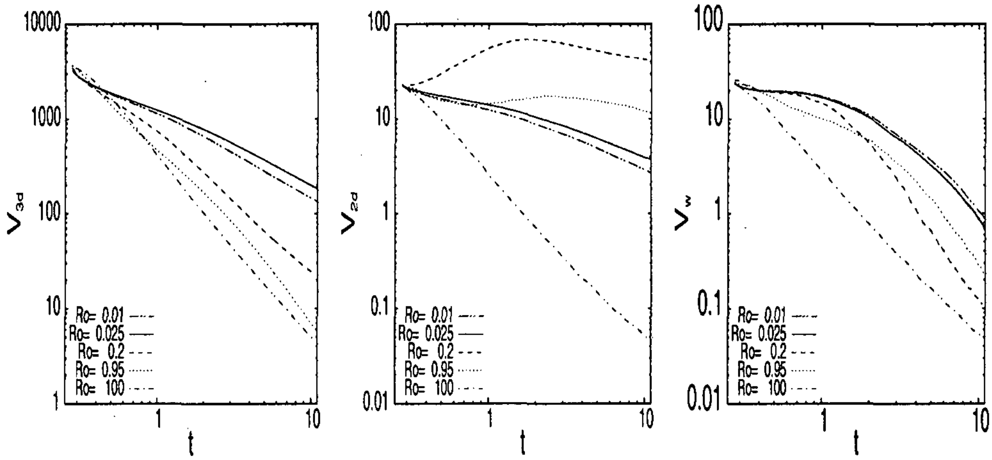

Figure 3.5: Time series for the large box simulations of the total 3D enstrophy V (left), the 2D enstrophy V_{2D} (middle) and V_w (right), for *Ro* = 100, 0.95, 0.2, 0.025 and 0.01. Similar results were obtained for the small box.

Ro	Ro_{MS}	Ro_{ML}	Δt_{100}	Δt_{200}	Ro	Ro_{MS}	Ro_{ML}	Δt_{100}	Δt_{200}
0.01	0.008	0.008	5.6×10^{-4}	8.55×10^{-5}	0.172	0.14	0.14	a_1	a_2
0.015	0.012	0.012	8.4×10^{-4}	1.28×10^{-4}	0.189	0.16	0.15	a_1	a_2
0.022	0.018	0.018	1.26×10^{-3}	1.92×10^{-4}	0.20	0.17	0.16	a_1	a_2
0.034	0.028	0.0275	1.9×10^{-3}	2.91×10^{-4}	0.23	0.19	0.191	a_1	a_2
0.05	0.042	0.04	2.8×10^{-3}	4.28×10^{-4}	0.28	0.24	0.23	a_1	a_2
0.060	0.05	0.049	3.39×10^{-3}	5.18×10^{-4}	0.3	0.25	0.25	a_1	a_2
0.066	0.056	0.054	3.7×10^{-3}	5.65×10^{-4}	0.47	0.41	0.4	a_1	a_2
0.073	0.061	0.059	4.1×10^{-3}	6.25×10^{-4}	0.6	0.52	0.5	a_1	a_2
0.08	0.067	0.065	4.5×10^{-3}	6.84×10^{-4}	0.75	0.65	0.63	a_1	a_2
0.088	0.074	0.072	4.94×10^{-3}	7.53×10^{-4}	0.95	0.82	0.8	a_1	a_2
0.097	0.082	0.079	5.44×10^{-3}	8.29×10^{-4}	1.2	1	1.01	a_1	a_2
0.107	0.091	0.088	a_1	9.15×10^{-4}	1.5	1.29	1.26	a_1	a_2
0.117	0.1	0.096	a_1	9.85×10^{-4}	3	2.59	2.5	a_1	a_2
0.13	0.11	0.11	a_1	a_2	10	8.7	8.4	a_1	a_2
0.142	0.12	0.12	a_1	a_2	100	86.3	84.2	a_1	a_2
0.156	0.13	0.13	a_1	a_2	∞	∞	∞	a_1	a_2

Table 3.1: Timesteps for the simulations in domains L and S, for each initial *Ro* number, with $a_1 = 5.84 \times 10^{-3}$ and $a_2 = 9.87 \times 10^{-4}$. The micro Rossby is referred to as *Ro*. The *macro*-Rossby numbers are denoted Ro_{MS} and Ro_{ML} for the S and L domains, respectively. We introduce rotation on fully developed turbulence with total energies $E_S = 0.234$ and $E_L = 2.254$. Hyperviscosity coefficients were $\nu_{4,S} = 2.602 \times 10^{-11}$ and $\nu_{4,L} = 2.927 \times 10^{-13}$. The initial eddy turnover timescales were $\tau_S = 0.1038$ and $\tau_L = 0.01189$

not extend to the w mode in the *intermediate* range. We note from the $Ro = 0.2$ curves in figures 3.4 and 3.5 that the rate of decay of E_w and V_w increases when E_{2D} and V_{2D} are large. In fact, if we exclude $Ro = 100$ from this analysis, the $Ro = 0.2$ decay rate of E_w and V_w is the highest in the *intermediate* and *small Ro* ranges. This is in agreement with the asymptotic equation (3.15) governing E_w, i.e. a decaying passive scalar advected by the 2D flow. On the other hand, the *intermediate Ro* range is obviously not described by the decoupled equations (3.15), and so further comparisons can not be made. Concerning the *small Ro* range, $E_{2d} \approx const$ and $V_{2D} \sim t^{-0.625}$. With all necessary caution, it is interesting to note that this decay rate is consistent with recent observed decaying 2D turbulence results.

In order to solidify the observed separation of regimes with Ro and the non-monotonic tendency to reach the $Ro \to 0$ limit, we consider the integrated energy transfer between one mode in $V_{\boldsymbol{k}}$ and two modes in $W_{\boldsymbol{k}}$. The integration of (3.14) over wave vectors gives

$$\frac{\partial \mathrm{E_{3D}}}{\partial t} = -(\mathcal{T}_{23} + \mathcal{T}_{w3}) - \tilde{D}_{p,3D}, \tag{3.21}$$

$$\frac{\partial \mathrm{E_{2D}}}{\partial t} = \mathcal{T}_{23} - \tilde{D}_{p,2D},$$

$$\frac{\partial \mathrm{E}_w}{\partial t} = \mathcal{T}_{w3} - \tilde{D}_{p,w},$$

where,

$$\mathcal{T}_{23}(t; Ro) = \int T_{2-33}(\boldsymbol{k} \in V_{\boldsymbol{k}}, t; Ro)\; d^3\boldsymbol{k} \;= -\int T_{3-23}(\boldsymbol{k} \in W_{\boldsymbol{k}}, t; Ro)\; d^3\boldsymbol{k} \tag{3.22}$$

and

$$\mathcal{T}_{w3}(t; Ro) = \int T_{w-33}(\boldsymbol{k} \in V_{\boldsymbol{k}}, t; Ro)\; d^3\boldsymbol{k} = -\int T_{3-3w}(\boldsymbol{k} \in W_{\boldsymbol{k}}, t; Ro)\; d^3\boldsymbol{k}.$$

Due to high frequency waves in rapidly rotating simulations, rapidly fluctuating time series of the integrated energy transfer (3.22) are obtained. We therefore averaged the instantaneous transfer over small intervals of time (table 3.2). The difficulty in choosing the right way to average such quantities temporally is first due to our

Ro	$T_{i,S}$	$T_{f,S}$	$T_{i,L}$	$T_{f,L}$	Intervals
0.01	3	6.33	0.47	1.01	$I_{\binom{S}{L}}1$
0.2	3	7.05	0.48	1.10	$I_{\binom{S}{L}}1$
100	2.88	8.1	0.47	1.27	$I_{\binom{S}{L}}1$
0.01	4.73	8.55	0.75	1.35	$I_{\binom{S}{L}}2$
0.2	5	10.14	0.75	1.35	$I_{\binom{S}{L}}2$
100	5.13	14.25	0.8	2.16	$I_{\binom{S}{L}}2$
0.01	7.1	11.41	1.12	1.8	$I_{\binom{S}{L}}3$
0.2	8	14.6	1.25	2.23	$I_{\binom{S}{L}}3$
100	9.9	27.2	1.52	4.01	$I_{\binom{S}{L}}3$
0.01	10.5	15.5	1.65	2.43	$I_{\binom{S}{L}}4$
0.2	13.2	21.64	2.01	3.3	$I_{\binom{S}{L}}4$
100	22.22	58.4	3.3	8.5	$I_{\binom{S}{L}}4$

Table 3.2: Calculated time intervals for each resolution and Ro such that: $I_{\binom{S}{L}}1$, $I_{\binom{S}{L}}2$, $I_{\binom{S}{L}}3$ and $I_{\binom{S}{L}}4$ start at the 10^{th}, 20^{th}, 35^{th} and 50^{th} eddy-turnover time for both the large and the small box. S and L stand for small box and large box, respectively. All intervals are about $N_{t_i,t_f} \approx 20$ eddy turnover time in length.

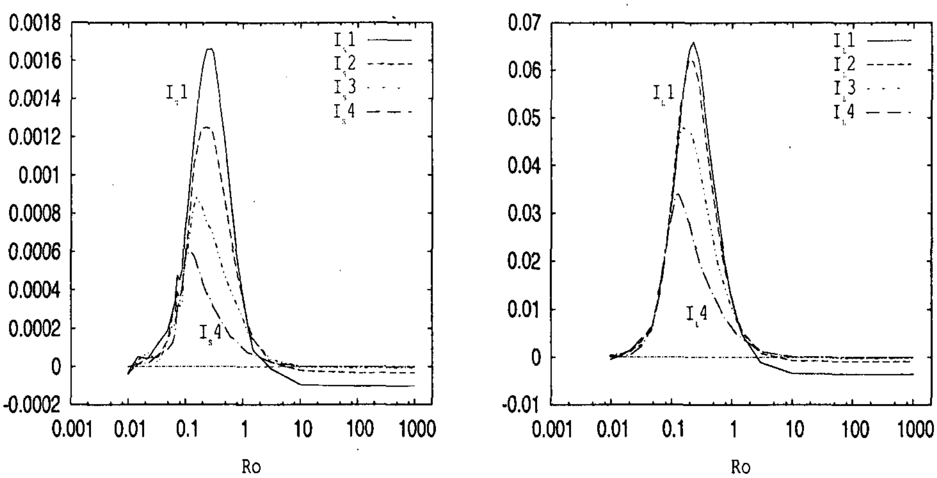

Figure 3.6: Integrated transfer spectra T_{23} using 4 time intervals of about 20 eddy turnover times (3.23). We start the time intervals $I_{\binom{S}{L}}1, I_{\binom{S}{L}}2, I_{\binom{S}{L}}3$ and $I_{\binom{S}{L}}4$ at about 10, 21, 34 and 50 eddy turnover timescales, respectively. The small (S) domain is presented on the left and the large domain (L) on the right.

choice not to force the dynamics. Second, a wide range of rotation rates were investigated, implying a large diversity in the dynamical timescales of the turbulence. Finally, we aim to study the influence of the domain size on the turbulence. All these factors lead to the need for careful consideration of the best choice of time intervals on which to average in order to assure a comparison of results that are dynamically consistent. In order to estimate the dynamical timescale for each rotation rate and resolution, we used a different definition of the eddy turnover time that has proven useful in decaying simulations. Following Bartello and Warn (1996)

$$N_{t_i,t_f} = \int_{t_i}^{t_f} V(t')^{1/2} dt', \tag{3.23}$$

where N_{t_i,t_f} is the number of eddy turnover times, $V = \frac{1}{2}\int\int\int |\boldsymbol{\omega}|^2 dv$ is the enstrophy and t_i, t_f are initial and final times of integration, respectively. The selected time averaging protocol uses N as our measure of the dynamical time for each Ro and for each of the grids. Starting from that point we constructed several time intervals of approximately 20 eddy turnover times (calculated using N_{t_i,t_f} and given in table 3.2

for three Ro as examples). We integrated $\mathcal{T}_{23}(t; Ro)$ on each of these intervals. The transfers

$$T_{23}(Ro) = \int_{I_{\binom{S}{L}}{}^i} \mathcal{T}_{23}(t; Ro)\, dt \; = \int_{I_{\binom{S}{L}}{}^i} \int T_{2-33}(\boldsymbol{k} \in V_{\boldsymbol{k}}, t; Ro)\, d^3\boldsymbol{k}\, dt \qquad (3.24)$$

are shown in figure 3.6 for time intervals $i = 1, 2, 3$ and 4 as a function of Ro. $Ro \longrightarrow \infty$ was replaced by $Ro = 10^3$ to fit in figure 3.6. Linear and logarithmically spaced time intervals gave similar results. Nevertheless, the intervals described above and used in figure 3.6 allow for a better comparison between the small and large domains.

The result is a systematic peak of T_{23} centred around the same Rossby numbers for both computational domains. In addition, the Rossby number of maximum 2D-3D transfer shows the same systematic translation to lower Ro with time for both domain sizes. This translation is due to the decrease of Ro with time in all of our decaying simulations. We conclude that the shape of the curves is robust.

In figure 3.6, we display the integrated transfer T_{23} as a function of the Ro defined in (3.17). Table 3.1 gives the equivalent *macro-Ro* for each domain size. From table 3.1 we can check that doubling the size of the computational domain did not change the values of the *macro-Ro*. We conclude that the use of either (3.17) or the *macro-Ro* definition does not affect the shape of the curves given in figure 3.6. In other words, both the small and the large box $T_{23}(Ro)$ curves peak around the same value of Ro and evolve similarly regardless of which of our two definitions of Ro is used. The peaks are at $Ro \approx 0.2$, $Ro_{MS} \approx 0.17$ and $Ro_{ML} \approx 0.16$, where Ro_{MS} and Ro_{ML} are the *macro- Ro* numbers of the small and large domains, respectively.

For rotations weaker than $Ro \approx 1$, energy transfers are similar to the non-rotating 2D-3D transfer, where such a decomposition is irrelevant. In fact, it is due to a balance of energy transfer from 2D to 3D with that from 3D to 2D modes. Both grids show this *large Ro* behaviour, at all times. One might expect these turbulent statistics to be monotonic with rotation but figure 3.6 shows that this is clearly not the case. In fact, the peak of energy transfer is reached around $Ro \approx 0.2$ at early times and is robust to the change of domain size. The sign of this transfer is positive, implying an

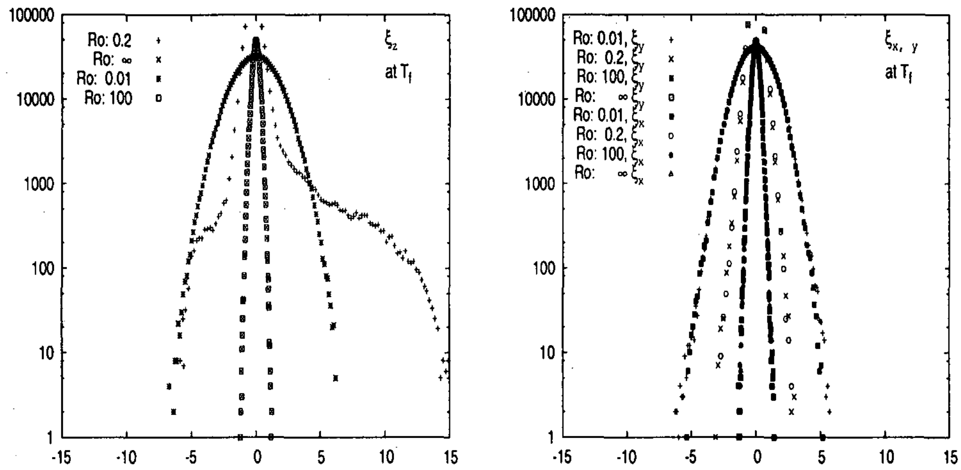

Figure 3.7: Histogram of the three components of the vorticity vector for different Ro at the final time of the simulation T_f. The vertical vorticity component is on the left and (x,y) components are on the right. The histograms are shown for the small box. The strongest skewness of the intermediate zone is observed for $Ro = 0.2$.

energy flow from wave to vortical energy. This *intermediate* range is observable for Ro between $Ro \approx 0.03$ and $Ro \approx 1$. We refer to the third region, for which Ro is less than approximately 0.03, as *the small Ro range.* In this last regime, the integrated transfer T_{23} between waves and vortices is considerably reduced. The increase of the numerical box size reduces the variability on the low Ro side. The amplitude of the T_{23} peak for the small box decreases faster than that of the large box. This is likely due to the differing dissipation ranges. The low Ro wing of the peak seems to be time invariant, unlike the high Ro wing. Again, this property is independent of domain size. Due to similar behaviour in both domain sizes, we conclude that the peak's centre is not shifted by a change of the numerical sampling of near-resonant interactions nor by the change in sampling of discrete Fourier modes and the subsequent angular resolution in **k**.

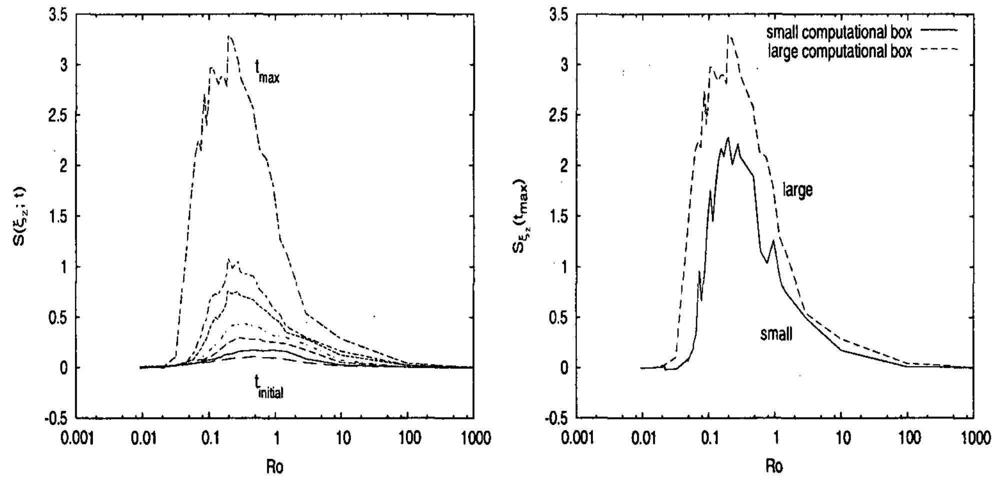

Figure 3.8: Skewness of the vorticity component $S(\omega_z)$ as a function of Ro in the large-box simulation, at 7 times (left). The largest skewness is observed at the last output time, $t_{max,large} = 8.5$. On the right, the value of $S(\omega_z)$ at the end of the simulations are displayed with Ro, for both the small and large boxes, respectively (i.e. at times $t_{max,small} = 27$ and $t_{max,large} = 8.5$).

(a)
(b)
(c)
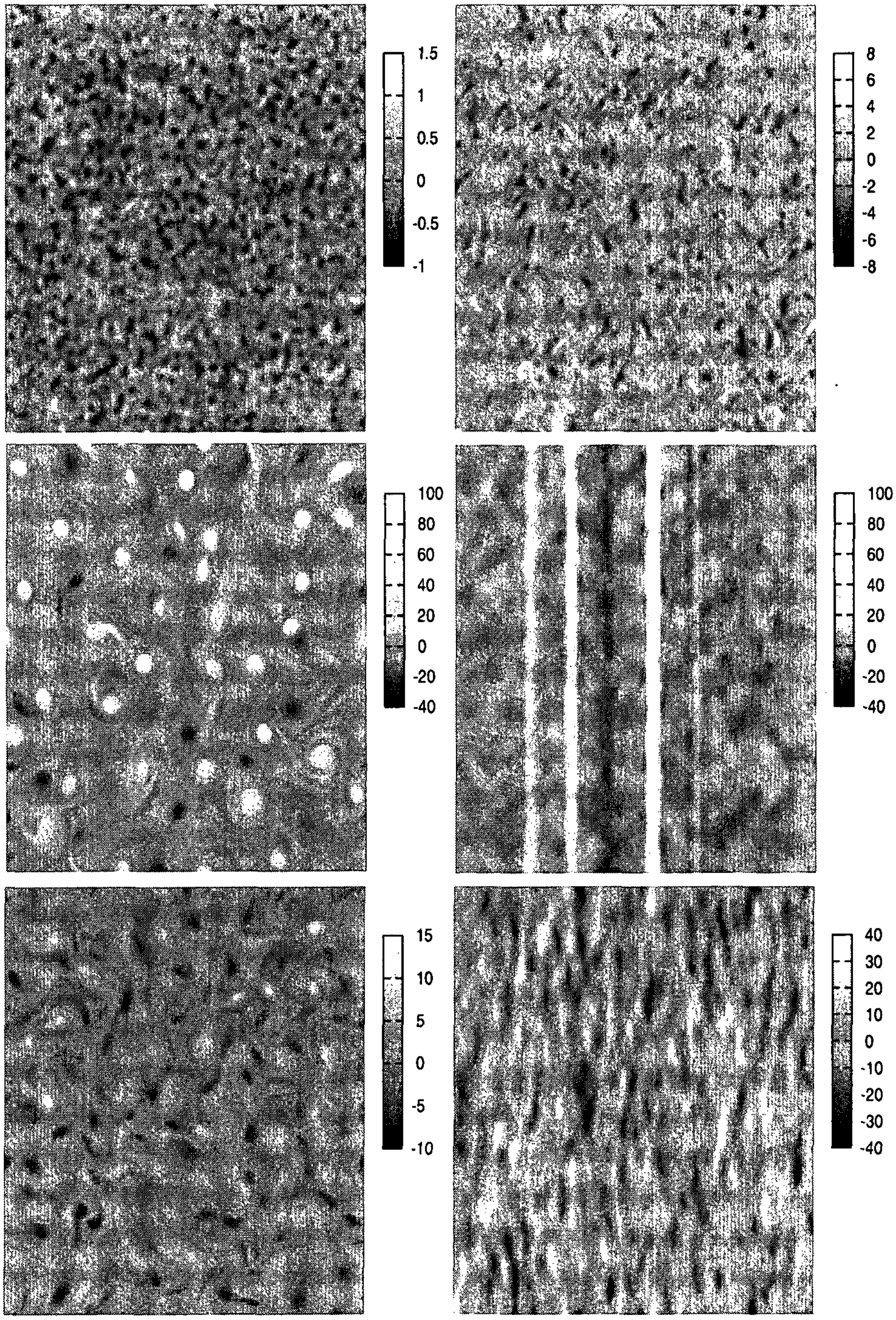

Figure 3.9: Horizontal slices (x,y) of the 2D vertical vorticity field $\omega_{z,2D}$ (left column) for (a) $Ro = 100$, (b) $Ro = 0.2$ and (c) $Ro = 0.01$. Vertical slices (y,z) (right column) of the total vertical vorticity field ω_z for (a) $Ro = 100$, (b) $Ro = 0.2$ and (c) $Ro = 0.01$. The snapshots are taken at t=8.5 and from the large domain simulations.

3.4.2 Skewness

The skewness of the vertical component of the vorticity $S(\omega_z)$ shows a maximum growth in the *intermediate Ro* range for both domain sizes (the histogram for the small box run is shown in figure 3.7 (left)). Horizontal components of vorticity never show this asymmetry, independently of Ro and the size of the computational box (figure 3.7 right). The growth of the skewness with time in figure 3.8 (left) is particularly strong for the *intermediate Ro* zone. We observe that its maximum is reached toward the end of the simulations. The maximum skewness value occurs for $Ro \approx 0.2$. These last two results are observable in figure 3.8 (left) for the large box. We then compare the $S(\omega_z) = f(Ro)$ curves for both domain sizes. We chose to display $S_{small}(\omega_z)(t_{max}; Ro)$ and $S_{large}(\omega_z)(t_{max}; Ro)$ in figure 3.8 (right), where t_{max} is the time at which $S(\omega_z)$ is a maximum, which occurs at the end of the simulation. Both curves displayed in figure 3.8 (right) show a maximum skewness for $Ro \approx 0.2$. This strong asymmetry in favour of cyclonic vortices coincides with a strong energy transfer from waves to 2D modes. Finally, the left wing of the histogram in figure 3.7 seems Gaussian, which might suggest a reduction of energy transfer for anticyclonic vorticity, as noted by Bartello etal (1994).

Real space horizontal slices (x,y) of the 2D vertical vorticity field $\omega_{z,2D}$ and vertical slices (y,z) of the total vertical vorticity field ω_z are shown in figure 3.9 for $Ro = 100, 0.2$ and 0.01. A strongest skewness is observed in the horizontal slices of the 2D vertical vorticity field for $Ro = 0.2$, in which the highest value of vorticity is 100, while the lowest value is -40. This suggests that a transfer of energy from 3D is either preferentially toward cyclonic vortices or that a destabilization of the anticyclones occurs as they are formed (or fed energy). This instability may be similar to that observed in channel or free shear rotating flows mentioned in §3.1. The $Ro = 0.2$ vertical slice of $\boldsymbol{\omega}_z$ is dominated by $\boldsymbol{\omega}_{z,2D}$. On the other hand, $Ro = 100$ and 0.01 vertical slices are dominated by the the $3D$ wave vorticity. At $Ro = 0.01$ a slight asymmetry in the cyclone/anticyclone distribution persists, but the intensity of the vortices, from -10 to 15 is weaker than that observed in the 2D horizontal field at $Ro = 0.2$. Finally, the simulations of the weak rotation regime with $Ro = 100$ are similar to those observed for isotropic non-rotating flows: no significant asymmetry is noticed, the intensity of the vortices is reduced with time and no anisotropy is noted.

In the present section we identified three distinct rotation ranges. Among these, the *intermediate Ro* range is characterized by a strong 3D to 2D transfer. We illustrated that our main result was robust to the doubling of the domain size, thus confirming the adequate sampling of near-resonances. Moreover, we showed that the maximum 3D to 2D transfer is associated with the maximum vertical vorticity skewness, both reached in the *intermediate Ro* range for $Ro \approx 0.2$. This is also robust to the change of computational domain size. We further examine the three rotating regimes in the following section §3.4.3.

3.4.3 Large, intermediate and small Ro regimes

In figure 3.10 we display horizontal energy spectra of E_{2D}, E_w and E_{3D} and vertical spectra of 3D energy, E_{3D}, for three characteristic Ro numbers. The vertical spectra $E_{3D}(k_z)$ displayed for all Ro were offset for clarity. Spectra are averaged over two time intervals $t \in [1,\ 2]$ and $t \in [7,\ 10]$ of the large-box simulations. As in figure 3.3, the three values of Ro chosen are 100, 0.2 and 0.01. Figure 3.11 shows the energy transfer spectra for the simulation in the *intermediate range* only. The displayed quantities were introduced in (3.14). For consistency, we used the same time averaging intervals as those used in figure 3.10. The transfers shown in the left column are averaged at an early stage of the simulation, namely $t \in [1,\ 2]$. The right column shows transfers that were averaged later in the simulation on $t \in [7,\ 10]$. The upper panel displays both $T_{2-22}(k_h)$ and $T_{2-33}(k_h)$ spectra as they appear in the $E_{2D}(k_h, t)$ equation (3.14). The middle panel shows horizontal transfer spectra that appear in the $E_{3D}(k_h, t)$ equation (3.14). The $T_{2-33}(k_h, t)$ curves have been added to these middle graphs for comparison purposes. Finally, the bottom panel shows the vertical energy transfer

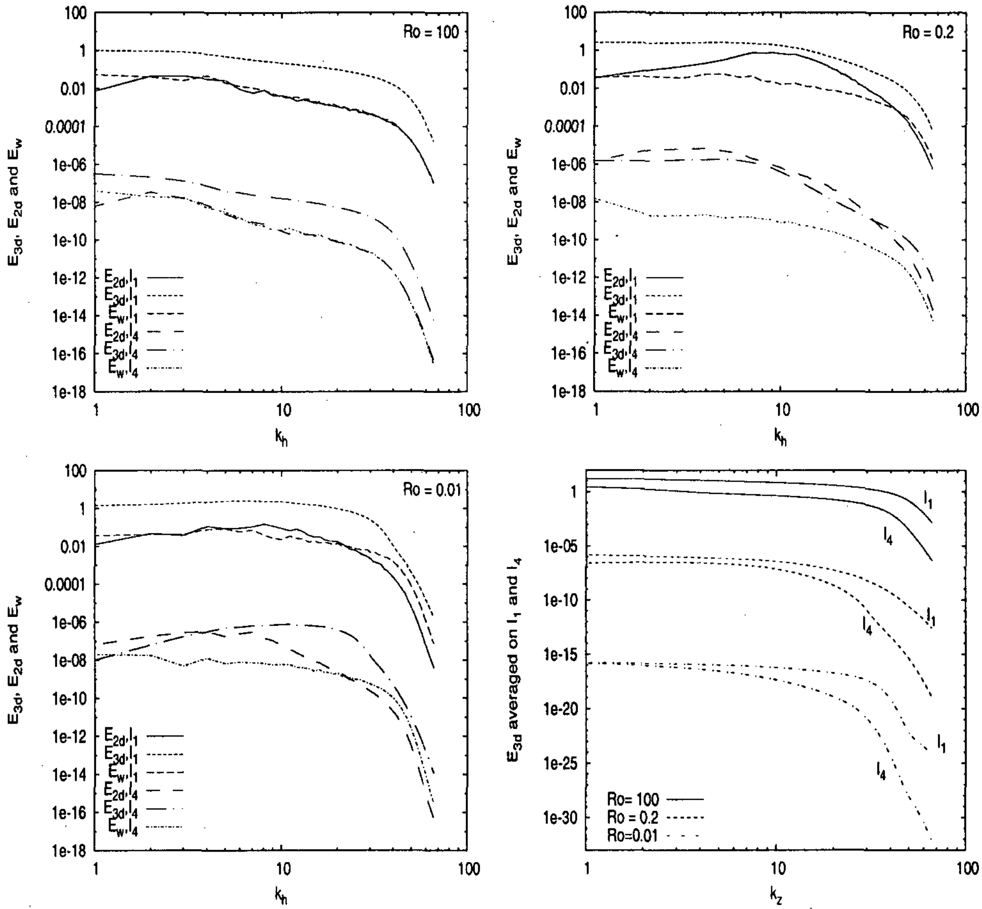

Figure 3.10: The large box simulations' horizontal spectra of E_{2D}, E_{3D} and E_w averaged on $I_1 = [1,\ 2]$ and $I_4 = [7,\ 10]$ time intervals. The spectra averaged on I_1 have been translated upward for clarity. The vertical spectra of E_{3D} averaged on I_1 and I_4 are also shown (bottom right). Vertical spectra are displayed for each of *Ro*= 0.01, 0.2, 100 simulations and have been rescaled for clarity. The small box spectra are similar and are therefore not shown.

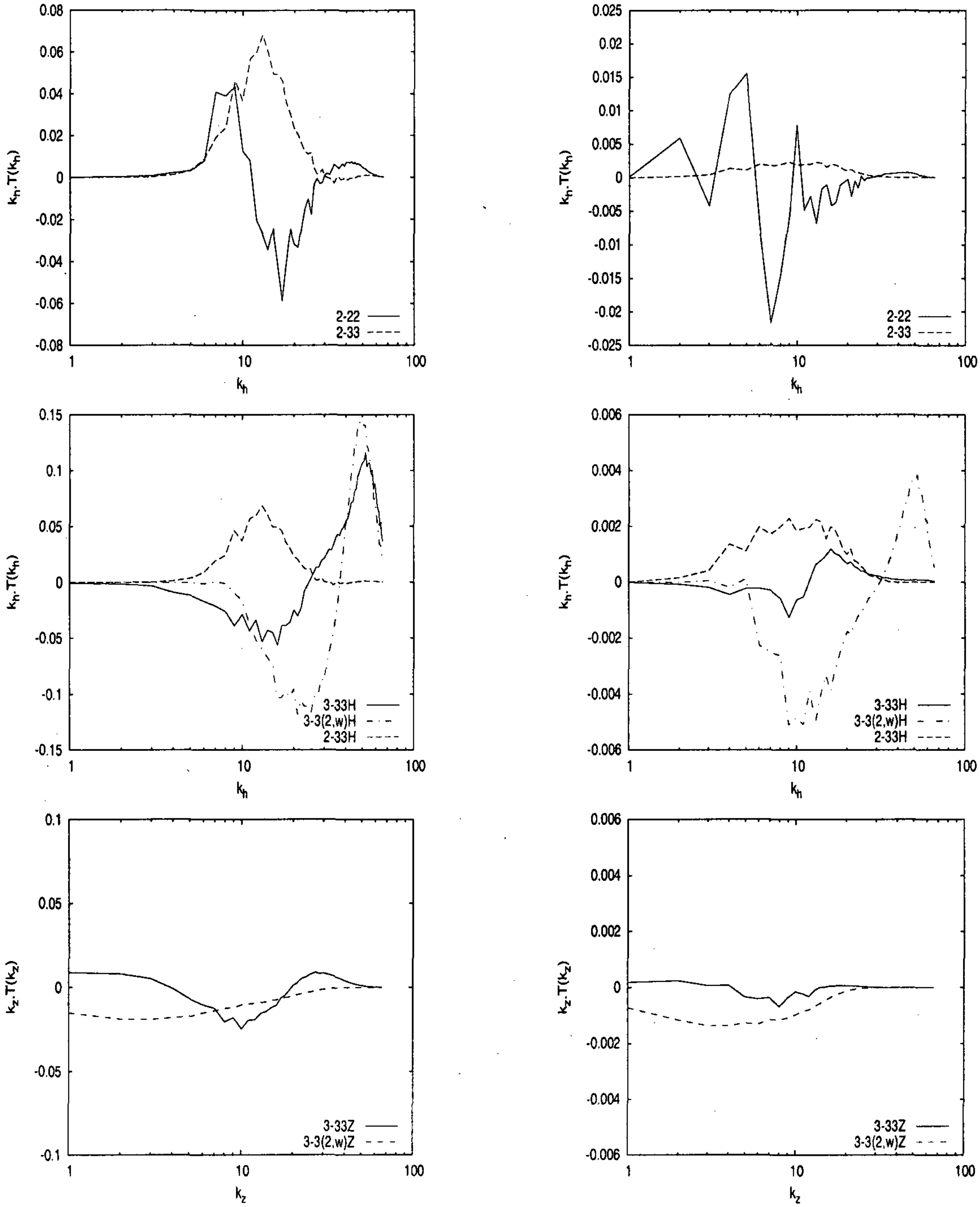

Figure 3.11: Transfer spectra for $Ro = 0.2$ for time intervals $I_1 = [1,\ 2]$ (left column) and $I_4 = [7,\ 10]$ (right column).

spectra of equation (3.14) for $E_{3D}(k_z, t)$.

From the vertical spectra $E_{3D}(k_z)$ of figure 3.10, we can see that the vertical transfers are weaker overall than the horizontal for the three *Ro* and for all times.

The horizontal spectra in 3.10 and 3.11 of the *intermediate Ro* regime show an increase of the 2D energy spectra around $k_h = 10$ early in the simulations. This maximum is due to a preferential transfer from wave modes $k_h \approx 20$ to vortical modes $k_h \approx 10$. Later, these interactions involve a wider range of horizontal wavenumbers. However, the vortical modes that are involved in the injection of 2D energy by the 3D modes remain relatively localized around $k_h = 10$. Later in the simulation, the maximum of the E_{2D} energy spectrum averaged on $t \in [7,\ 10]$ shows a migration of its maximum toward larger horizontal scales and a slope $E_{2D}(k_h)/E \sim k_h^{-2.1}$. This is due to the triple-vortex interactions (see $T_{2-22}(k_h)$) transferring the 2D energy from the injection wavenumber $k_h \approx 10$ to larger horizontal scales (figure 3.11 top). Later we still observe this upscale transfer of vortical energy in the $T_{2-22}(k_h)$ spectrum (3.11 top-right).

Over the $Ro = 0.2$ simulation, the E_{3D} is transferred to small horizontal scales via 3-33 and 3-2(w)3 interactions. The associated spectrum gives $E_{3D}(k_h)/E \approx k_h^{-4}$. The decrease of 3D energy with time in favour of the increase of 2D energy leads to a dominant contribution of the $T_{3-2(w)3}$ with time. These 3-2(w)3 interactions appear to transfer E_{3D} downscale horizontally, but vertically upscale and toward the 2D modes. Unlike the horizontal scale, there is no preferential vertical scale from which energy is extracted to be injected in the $k_z = 0$ modes. The overall amplitudes of the 3-33 vertical transfers ($T_{3-33}(k_z)$) become smaller compared to those of the 3-2(w)3 ($T_{3-2(w)3}(k_z)$) with time. This explains the overall flatness of the vertical spectra $E_{3D}(k_z)$. From both energy and transfer spectra in the *intermediate* range we conclude that the 3-2(w)3 interactions are the main actors in the transfer of 3D energy to dissipation. This transfer is stronger in the horizontal. They also extract 3D energy from all vertical wave scales but from a range of preferred horizontal scales. This extracted energy is preferentially injected in horizontal 2D scales $k_h \approx 10$. In figure (3.11), the $Ro = 0.2$ energy transfer spectra of $E_w(k_h)$ display a downscale cascade to dissipation scales (not shown). Thus, E_w is systematically dissipated, as observed in figures 3.4 and 3.5.

For $Ro = 0.01$, we do not observe a maximum for $E_{2D}(k_h)$ early in the simulation but a maximum of the 2D energy spectrum is noticeable for the second time interval $t \in [7,\ 10]$ at low wavenumbers. This suggests a migration of 2D energy to larger horizontal scales, but the behaviour is distinct from that observed at $Ro = 0.2$. In fact, the $E_{3D}(k_h)$ spectrum shows a decrease of energy in time for low k_h and a very steep slope between $k_h \approx 20$ and the dissipation range. A comparison of the final values of the $E_{2D}(k_h)$ spectra show that more 2D energy is contained in large horizontal scales for $Ro \approx 0.2$ than for $Ro \approx 0.01$, thus underlining again the distinction between the *small* and the *intermediate Ro* regimes. The latter shows a stronger 2D upscale energy transfer.

For reference purposes, we provide the *large Ro* regime spectra for $Ro = 100$. In fact, no increase of 2D energy is observed with time for any particular wavenumber, nor is there a sign of 2D energy cascade toward small k_h.

Finally note that low-rotation-rate simulations have been examined in previous studies and their characteristics are similar to those of isotropic turbulence. We therefore chose not to include them in the spectra discussion. Our examination of transfer spectra of the *small Ro range*, such as those at $Ro = 0.01$, is very difficult due to the significant phase scrambling associated with such high frequency waves. Ensemble-averaged spectra are necessary to determine how 2D-3D catalytic resonant interactions compare to those of triple-wave resonant interactions. We do not cover this additional work in the present paper since we chose to focus on what we identified as the *intermediate Ro* range.

3.4.4 Discussion of the *intermediate* regime

Coming back to the vertical transfers and spectra, the overall weakening of vertical transfers observed in §3.4.3 are reminiscent of the vertical freezing of energy transfer described by Babin etal (1996) in the limit $Ro \to 0$ (discussed in §3.2). Their result is based on the assumption of decoupling in the form of vanishing wave-vortex interactions. However, the $Ro \approx 0.2$ and the *intermediate Ro* range in general is characterized by a maximum transfer of energy from wave to 2D modes. Therefore, these two dynamics are different. Moreover, the freezing of vertical energy transfer in Babin etal (1996) is based on their prediction of the dominance of catalytic resonant wave-vortex interactions over resonant triple-wave interactions in (3.15). It is nevertheless interesting to notice that the *intermediate Ro* range shows a dominance of wave-vortex (3-2(w)3) energy transfer over the energy transfer due to triple-wave (3-33) interactions, both horizontally and vertically. So, from this observation one could apply a similar reasoning to that applied to resonant interactions by Babin etal (1996). This could explain the overall reduction of vertical energy transfers compared to those in the horizontal in the *intermediate Ro range.* This assumes that 3-2(w)3 transfers dominate 3-33 transfers.

The upscale energy transfer observed in the forced simulations of Smith & Waleffe (1999) and the higher *Ro* examined by Chen etal (2005) are consistent with the energy transfer in the *intermediate* simulations range (e.g. $Ro \approx 0.2$) of our decay simulations. The growth of the mean energy-containing scale that is observed in §3.4.3 is weaker than that of the forced simulations of Smith and Waleffe (1999) and Chen etal (2005). This is possibly due to the lack of forcing. Moreover, we initialized our rotating simulations with an isotropic spectrum not strongly peaked at a particular wavenumber.

Based on our results in §3.4.1, the *intermediate Ro* regime is also associated with a strong vorticity asymmetry in favour of cyclones. This last characteristic is also in agreement with Smith and Lee (2005) and shows that the results discussed in Smith and Waleffe (1999), Chen etal (2005) (the highest of the two *Ro* simulations) and Smith and Lee (2005) all belong to the *intermediate Ro* range that we identified above. This, combined with §3.4.3 suggests that the lower of the two *Ro* simulations discussed in Chen etal (2005) belongs to the *small Ro* range. The regime separation that we observe should also be evident in forced simulations. Clearly, an investigation in that configuration is needed.

3.5 Conclusions

We examined the general picture of rotating turbulence for a large range of Ro (32 values were used). We observe a non-monotonic tendency as $Ro \to 0$. Moreover, we identify three distinct rotating ranges. The *large Ro* regime ($Ro > 1$), the *intermediate* ($0.03 < Ro < 1$) and the *small Ro* ($Ro < 0.03$) ranges. This identification is robust to a doubling of the computational domain size and is therefore not due to poor sampling of the key wave-vortex near-resonant interactions. It is also robust to whether a velocity- or a vorticity-based Rossby number is employed. We show that the *intermediate Ro* range is characterized by a maximum leakage of energy from 3D to 2D modes that is initially reached at $Ro \approx 0.2$ for both domain sizes. This transfer is associated with a maximum of vertical vorticity skewness, also reached at $Ro \approx 0.2$. This is also robust to the change of domain size. These results lead us to present a general picture of rotating turbulence.

It is interesting to note the analogy between the zero-frequency two-dimensional modes in rotating turbulence and the zero-frequency vertically sheared horizontal flow modes in stratified turbulence. Such an analogy has been mentioned by Smith & Waleffe (2002) concerning the accumulation of zero-frequency energy in either rotating or stratified cases. Moreover, Smith & Waleffe (2002) observed a pile-up of energy in shear modes in their forced numerical simulations. In their forced simulations, Waite & Bartello (2004) observed a similar significant increase of shear-mode energy as the horizontal Froude number decreased down to a threshold value, followed by a significant drop as stratification increased. This last non-monotonic tendency is reminiscent of the non-monotonic behaviour of the *intermediate Ro* range in our rotating decaying simulations. A more systematic study of the stratified case would be necessary to push this analogy further.

The wave-vortex interactions responsible for the *intermediate Ro* range preferentially inject wave energy to intermediate-to-small horizontal zero-frequency mode scales ($k_h \approx 10$). They extract 3D energy from all vertical wave scales but preferentially from rather localized intermediate-to-small horizontal scales. Most of the resulting 2D energy is contained in cyclonic vortices of medium horizontal scale. The contribution of triple-wave interactions to the 3D energy transfer is weaker in this regime. Triple-wave interactions have weaker contribution in vertical energy transfers that are mostly done by wave-vortex interactions.

Finally, the *intermediate Ro* range shows a stronger 2D upscale energy transfer than that observed in the *small Ro* range. In fact, we could schematically say that the 2D turbulence of the *intermediate Ro* range is forced by an injection of energy from wave modes, thus a stronger growth of the 2D energy-containing scale is observed. On the other hand, the integrated transfer, energy spectra and energy time series of the *small Ro* range show a vanishing conversion of wave to vortex energy. This is consistent with the vortical dynamics being quasi-independent from the background wave turbulence, but a further computationally-demanding study of this last range is necessary for a more complete investigation of the theories discussed in §3.1.

Chapter 4

The key nonlinear interactions

The Navier-Stokes equations in a rotating frame lead to solutions that can be modeled as interactions between inertial waves of frequencies between 0 and 2Ω, where Ω is the rotation rate. In asymptotic and weak-turbulence theories, resonant and near-resonant interactions are expected to be dominant. The asymptotic theories are derived assuming an unbounded domain. When considering an unbounded domain, the modes satisfying the resonance equations are real-valued wavenumbers. In most numerical simulations of turbulence and in experimental settings, the domains are periodic and bounded, respectively. In periodic or finite domains, the modes satisfying the resonance equations are integers. Studies of wave-turbulence problems other than rotating turbulence showed the existence of a discreteness effect. The effect can be considered as twofold. First, there is an effect intrinsic to the finite property of bounded domains, i.e. due to the integer-wavenumbers versus the real-wavenumbers. Second, there is an effect due to the truncation of the wavenumbers or resolutions used in a particular bounded domain considered. The effect of the discretization has been shown, under certain conditions, to lead to a disparity between the observed energy transfers in bounded domains and results predicted by the theories of wave-turbulence derived for unbounded domains. A similar type of discreteness effect has been speculated to exist for inertial waves, but has not previously been investigated.

In the small and intermediate regimes identified in the previous chapter, the resonant and near-resonant interactions are likely playing an important role. It is thus critical to ensure that these key interactions are well captured by the domains used for our future studies. In this chapter we investigate discreteness effects on the exactly-resonant and near-resonant interactions in a periodic domain. This is done by quantifying the finite-size effect on the number of exact and near-resonant interactions resolved by a given computational domain as a function of the truncation wavenumber and the Rossby number. We investigate whether the production of an energy cascade via these key interactions is affected by the discreteness effect. If so, then how do the Rossby number and the resolution of the domain affect the cascade?

The preliminary results of this study were presented at the 11^{th} EUROMECH European Turbulence Conference. The published paper resulting from this conference is:

- Bourouiba, L. (2007) Quantification of the discretization effects in the representation of key inertial-wave interactions in rotating turbulence. *Advances in turbulence XI Proceedings of the 11th EUROMECH European Turbulence Conference*, 679-682.

This chapter is based on the paper:

- Bourouiba, L. (2008) Discreteness effects in rapidly rotating turbulence, *Phys. Rev. E*, under review.

Discreteness and resolution effects in rapidly rotating turbulence

Abstract

Rotating turbulence is characterized by the nondimensional Rossby number, Ro, which is a measure of the strength of the Coriolis term relative to that of the nonlinear term. For rapid rotation (Ro $\rightarrow$ 0), nonlinear interactions between inertial waves are weak, and the theoretical approaches used for other weak (wave) turbulence problems can be applied. The important interactions are those between modes satisfying the resonant and near-resonant conditions. Often, discussions comparing theoretical results and numerical simulations are questioned because of a speculated problem regarding the discreteness of the modes in finite numerical domains versus continuous modes in unbounded continuous theoretical domains. This argument finds its origin in a previous study of capillary waves, for which resonant interactions have a very particular property that is not shared by inertial waves. This possible restriction on numerical simulations of rotating turbulence to moderate Ro has never been quantified. As a first step, we quantify the number of resonant and near-resonant interactions as a function of the nonlinear broadening and the resolution in a finite domain. We focus on Rossby numbers ranging from 0 to 1 and on periodic domains due to their relevance to direct numerical simulations of turbulence. We use a kinematic model of the cascade of energy via selected types of resonant and near-resonant interactions to determine the threshold of Ro below which discreteness effects become important enough to render an energy cascade impossible.

4.1 Introduction

Rotation affects the nonlinear dynamics of turbulent flows. The Rossby number is $\mathrm{Ro} = U/2\Omega L$, with U a typical flow velocity, Ω the rotation rate, and L the characteristic lengthscale of the flow. It is the dimensionless ratio of the magnitude of the nonlinear term in the Navier-Stokes equation ($(\boldsymbol{u} \cdot \nabla)\boldsymbol{u}$, where $\boldsymbol{u}$ is the velocity vector) to the Coriolis term ($2\boldsymbol{\Omega} \times \boldsymbol{u}$, where $\boldsymbol{\Omega}$ is the rotation vector). When $\mathrm{Ro} = 0$, the Navier-Stokes equations in a rotating frame are linear and admit inertial wave solutions with anisotropic dispersion relation $\omega_{s_k} = s_{\boldsymbol{k}} 2\boldsymbol{\Omega} \cdot \boldsymbol{k}/|\boldsymbol{k}|$, where $s_{\boldsymbol{k}} = \pm$, and $\boldsymbol{k}$ is the wavenumber (Greenspan, 1968). The modes with zero frequency ω_{s_k} are modes that correspond to vertically-averaged real-space velocity fields (for example columnar vertically-averaged modes aligned with the rotation axis). When $\mathrm{Ro} \to 0$ three-dimensional isotropic rapidly rotating turbulent flows have been observed to generate two-dimensional columnar structures experimentally (e.g. Taylor, 1923; McEwan, 1976; Baroud et al., 2002), and numerically in decay turbulence (e.g. Bardina et al., 1985; Bartello et al., 1994; Bourouiba and Bartello, 2007) and in forced turbulence (e.g. Hossain, 1994; Yeung and Zhou, 1998; Smith and Waleffe, 1999; Chen et al., 2005).

When $\mathrm{Ro} \to 0$, matched asymptotic expansion methods can be used for this weakly nonlinear problem. At first order in the expansion, energy transfers are restricted to interactions between triads of inertial waves that satisfy a condition of resonance (Newell, 1969). However, similarly to other wave-turbulence systems, near-resonant (resonant condition only approximately satisfied) interactions and higher order processes can play an important role in the cascade of energy dynamics. For example, the forced numerical simulations of Smith and Lee (2005) confirmed that near-resonant intertial waves can play a critical role in the generation of the anisotropy observed in rotating flows for a certain range of Ro.

When comparing simulations and experiments to theory, one should keep in mind that simulations and experiments are necessarily carried out in finite domains, whereas wave turbulence theories often assume an infinite domain. More specifically, numerical simulations usually assume periodic boundaries, and experiments are obviously carried out in bounded domains. In unbounded domains, the components of the wavectors satisfying resonant and near-resonant conditions are real numbers, whereas they are restricted to the set of integers in bounded and periodic domains. This seemingly benign difference turns out to have major implications. In fact, Kartashova (1994) investigated the peculiar characteristics of several resonances (planetary waves, gravity waves, capillary waves and drift waves in plasmas) satisfied only by integer wavenumber solutions in periodic domains. Kartashova (1998) considered the existence of solutions for various wave systems including gravity, Rossby and capillary waves and showed that capillary waves in a finite domain (integer-valued wavevector) cannot be resonant. Their resonance condition only has real-valued wavevector solutions. This *kinematic* result turns out to have major implications on the applicability of wave-turbulence results which are derived in infinite domains. In fact, several numerical studies of this effect showed that a sufficient level of nonlinearity is needed for the amplitudes of the capillary waves described by integer-valued wavectors to overcome the discreteness and satisfy an approximate resonance, i.e. a near-resonance (Pushkarev, 1999; Connaughton et al., 2001). Nazarenko (2006, 2007) explicitly addressed the issue of applicability of wave-turbulence in discrete wave-number domains for the case of MHD and water-wave turbulence, respectively. In a discrete domain, a sufficient threshold nonlinear broadening of the resonance condition is needed for the near-resonant conditions to generate nonlinear energy transfers. Below this threshold, the near-resonant interactions are not easily formed. Thus, given that no resonant interactions are possible, the energy cascade is stopped altogether. This regime is referred to as "frozen turbulence" (Pushkarev, 1999). Similar discreteness effects were also investigated for water-waves by Tanaka and Yokoyama (2004), Zakharov et al. (2005), and Lvov et al. (2006) (revisited in the subsequent sections).

The main distinction between inertial-waves and capillary waves is that for the former, a subset of integer-valued wavenumber resonance solutions do exist. The resonant inertial wave interactions are thus always present in bounded and periodic domains. In contrast to capillary waves, there is no *a priori* need for a sufficient level of nonlinearity in order to trigger nonlinear energy transfers. However, the dispersion relation of inertial waves can lead to complicated resonant surfaces (see Bellet et al., 2006, for an example of the $33 \rightarrow 3$ resonant surfaces defined below). Therefore, a similar effect to that of frozen capillary wave turbulence effect could exist for inertial waves. If that were the case, the discreteness effect would be expected to reduce the possibility of energy transfers both via the resonant interactions alone or combined with near-resonant interactions. In fact, an effect of this nature has been speculated (although not verified). For example, Cambon et al. (1997) speculated that the use of numerical simulations for the study of small Ro flow could miss the slow mode dynamics.

Using decay simulations, Bourouiba and Bartello (2007) showed the existence of three rotating turbulent regimes: 1) A *weakly* rotating Rossby regime, for which the turbulent flow is not affected by rotation; 2) A *intermediate* Rossby range characterized by a strong transfer of energy from the wave to the zero-frequency modes, with a peak at $Ro \sim 0.2$[1]; 3) A *small*, or asymptotic Rossby range, for which the zero-frequency modes receive less and less energy from the wave modes—tending to confirm decoupling theories in this regime. When forcing their simulations at intermediate scales, Smith and Lee (2005) speculated that their own simulations using $\mathrm{Ro} = 0.1$ guaranteed a sufficient nonlinear amplitude to allow for the capture of the near-resonant interactions while other simulations of Chen et al. (2005) (also forced at intermediate scales) investigating a lower Ro, were not able to accurately capture the necessary near-resonant interactions. Thus, it was implied that the dynamics observed by Chen et al. (2005) for their smaller Ro was a numerical artefact. Although Smith and Lee (2005) studied the effect of near-resonant interactions for $\mathrm{Ro} \sim O(0.1)$, they did not quantify the effect of discreteness. However, they did call for the need

[1]The intermediate regime in decay simulations share most of the properties observed in the simulations using only near-resonant interactions in the forced simulations of Smith and Lee (2005). This regime is almost certainly due to a property of the near-resonant interactions for this range of Ro.

of doing this work "Although the latter statement [capturing the near-resonances in finite domains] begs to be quantified, such a study is beyond the scope of the present paper".

The finite domain effect on rapidly rotating flows is inherent to both numerical and experimental studies. However, studying such an effect using experiments can be delicate. One could envision comparing statistics obtained in a series of different sized rotating tanks. Note however that Ro at which the asymptotic theories apply (e.g., Ro = 0.01, Bourouiba (2008)) are considerably smaller that those typical or rotating tank experiments (e.g. Ro = 2 was the lowest Rossby number obtained in experiments of Morize and Moisy (2006). A difficulty is that boundary layer effects quickly become important when rotation rates are high, e.g., Ibbetson and Tritton (1975). Moreover, in a more recent study, the confinement effect was argued to inevitably generate inhomogeneous turbulence (see Bewley et al. (2007)). A possible alternative to rotating tanks is the setup used by Jacquin et al. (1990), in which a flow of air was passing through a large rotating cylinder and a dense honeycomb. This produces elongated structures which could be less affected by boundary layers and inhomogeneity effects.

We now focus on the discreteness effects in numerical domains. In particular, goal is to clarify this issue and to investigate how the reduction of Ro affects the distribution and number of resonant and near-resonant interactions as $Ro \to 0$ in periodic domains. When carrying out and interpreting the results of simulations of rotating turbulence, there are two aspects to the discreteness effect. One is the difference between bounded and unbounded domains in general. Unbounded domains with $L \to \infty$ lead to $\Delta_{\boldsymbol{k}} \to 0$ and real-valued wavenumbers in spectral space. Bounded and periodic domains with L finite lead to a finite $\Delta_{\boldsymbol{k}}$ and integer-valued wavenumbers. The second is related to the spatial resolution of a given bounded domain of interest. When a bounded domain of interest is selected, the spatial resolution determines the truncation wavenumber. We inquire whether a discreteness effect leading to a phenomenon similar to the "frozen turbulence" observed with capillary waves is also present here. How does the resolution affect the different types of interactions relevant for rotating inertial wave turbulence theories (see table 4.1)?

This study aims at allowing a better interpretation and comparison of the results obtained in bounded domains with the results derived in unbounded domains. More particularly, it also aims at improving the setup of future numerical simulations of rapidly rotating turbulence. We find that discreteness effects are present for the system of inertial waves. We quantify the minimum nonlinear broadening Rossby number, Ro_{min}, below which the domain does not contain interactions coupling the zero-frequency 2D modes to the 3D inertial wave modes. Thus a regime of decoupling would be observed for simulations with $\mathrm{Ro} < \mathrm{Ro}_{min}$. We also find the critical nonlinear broadening, Ro_c below which the theories predicting the freezing of vertical transfers in inertial-wave turbulence would be observed in bounded domains. Finally, given a domain of interest for numerical simulations, we investigate whether a freezing of the energy cascade is present for inertial waves and find this to be the case. We quantify the threshold nonlinear broadening, Ro_f, below which such a freezing occurs. This is done for various resolutions. This freezing of the energy cascade is found to be an inherent property of bounded systems vs. unbounded systems.

First, the notation used to classify the various types of interactions are presented in 4.2. The properties of the interactions and their interaction coefficients are recalled. In section 4.3, the number of near-resonant interactions and resonant interactions are quantified as a function of the nonlinear broadening and the truncation wavenumbers. In section 4.4, we investigate the effect of the nonlinear broadening on the capacity of the resonant and near-resonant interactions to generate a propagation of energy transfers to all the modes of the model. Threshold values of nonlinear broadening are obtained for various resolutions. In section 4.5 we discuss the results obtained in the light of recent dynamical numerical simulations of rotating turbulent flows.

4.2 Modal decomposition and types of interactions

We focus on a triply periodic domain as it is the domain most relevant for direct numerical simulations of homogeneous turbulence. In a triply-periodic domain of size $L \times L \times L$ the velocity field of an incompressible fluid can be represented by a Fourier series

$$\boldsymbol{u}(\boldsymbol{r},t) = \sum_{\boldsymbol{k}} \boldsymbol{u}(\boldsymbol{k},t) e^{i\boldsymbol{k}\cdot\boldsymbol{r}}, \tag{4.1}$$

where $\boldsymbol{r} = (x,y,z)$ is the position vector in real-space with three components, $i = \sqrt{-1}$, $\boldsymbol{k} = \Delta_k(k_x, k_y, k_z)$, with $\Delta_k = 2\pi/L$, and with $k_{x,y,z}$ integer wavenumbers taking the values $0, \pm1, \pm2...$ The continuity equation in Fourier space is $\boldsymbol{u}(\boldsymbol{k})\cdot\boldsymbol{k} = 0$.

Solutions of the linear rotating flow equations (with $\mathrm{Ro} = 0$) can be expressed as a superposition of inertial waves with nondimensional inertial frequencies

$$\omega_{s_{\boldsymbol{k}}} = s_{\boldsymbol{k}} \hat{\mathbf{z}} \cdot \boldsymbol{k}/|\boldsymbol{k}|, \tag{4.2}$$

where $s_{\boldsymbol{k}} = \pm$, and $\hat{\mathbf{z}}$ is the unit vector for the direction corresponding to the rotation axis (see Greenspan, 1968, for details). The inertial waves turn out to have the same structure as the helical modes (eigenmodes of the curl operator), which are defined as (Greenspan, 1968; Waleffe, 1992)

$$\mathrm{N}^{s_k} = \left(\frac{\hat{\mathbf{z}} \times \boldsymbol{k}}{|\hat{\mathbf{z}} \times \boldsymbol{k}|} \times \frac{\boldsymbol{k}}{|\boldsymbol{k}|} + i s_{\boldsymbol{k}} \frac{\hat{\mathbf{z}} \times \boldsymbol{k}}{|\hat{\mathbf{z}} \times \boldsymbol{k}|} \right). \tag{4.3}$$

When Ro is small but non-zero, a two-timescale asymptotic expansion can be performed with a fast time scale $\tau_0 = t$ associated with the rotation timescale, and a slow timescale $\tau_1 = \mathrm{Ro}t$ associated with the nonlinearity. The velocity field becomes

$$\boldsymbol{u}(\boldsymbol{k},\tau_0,\tau_1) = \sum_{s_{\boldsymbol{k}}=\pm} A_{s_{\boldsymbol{k}}}(\mathbf{k},\tau_1)\, \mathrm{N}^{s_k}(\boldsymbol{k}) e^{i\omega_{s_k}\tau_0}, \tag{4.4}$$

When carrying the expansion to the second order (e.g. Greenspan, 1968; Waleffe, 1993) the equation governing the evolution of the amplitudes $A_{s_{\boldsymbol{k}_1}}$ is obtained. The nonlinear interactions are restricted to interactions between modes $(\boldsymbol{k}_1, \boldsymbol{k}_2, \boldsymbol{k}_3)$ satisfying the *resonant* condition

$$\omega_{s_{\boldsymbol{k}_1}} + \omega_{s_{\boldsymbol{k}_2}} + \omega_{s_{\boldsymbol{k}_3}} = 0, \qquad \boldsymbol{k}_1 + \boldsymbol{k}_2 + \boldsymbol{k}_3 = 0. \tag{4.5}$$

The nonlinear interactions that are resonant are thus the interactions contributing on the long-time scale τ_1 to the long-term evolution of the wave amplitudes; omitting viscosity:

$$\partial_{\tau_1} A_{s_{k_1}}(\boldsymbol{k}_1, \tau_1) = -\frac{1}{4}\mathrm{Ro} \sum_{\substack{\boldsymbol{k}_1+\boldsymbol{k}_2+\boldsymbol{k}_3=0 \\ s_{k_1}, s_{k_2}}}^{\omega_{s_{k_1}}+\omega_{s_{k_2}}+\omega_{s_{k_3}}=0} C^{s_{k_2} s_{k_3} s_{k_1}}_{\boldsymbol{k}_2 \boldsymbol{k}_3 \to \boldsymbol{k}_1} A^*_{s_{k_2}}(\boldsymbol{k}_2, \tau_1)\, A^*_{s_{k_3}}(\boldsymbol{k}_3, \tau_1). \quad (4.6)$$

where $C^{s_{k_2} s_{k_3} s_{k_1}}_{\boldsymbol{k}_2 \boldsymbol{k}_3 \to \boldsymbol{k}_1}$ is the interaction coefficient of the triad $(\boldsymbol{k}_1, \boldsymbol{k}_2, \boldsymbol{k}_3)$ that contributes to the equation governing the amplitude of the mode $\boldsymbol{k}_1$. Waleffe (1992) showed that

$$C^{s_{k_2} s_{k_3} s_{k_1}}_{\boldsymbol{k}_2 \boldsymbol{k}_3 \to \boldsymbol{k}_1} = (s_{k_2} k_2 - s_{k_3} k_3)\left(\mathbf{N}^{*s_{k_2}} \times \mathbf{N}^{*s_{k_3}}\right) \cdot \mathbf{N}^{*s_{k_1}}. \quad (4.7)$$

Each interacting triad satisfying $\boldsymbol{k}_1+\boldsymbol{k}_2+\boldsymbol{k}_3 = 0$ conserves energy and helicity implying that:

$$C^{s_{k_3} s_{k_2} s_{k_1}}_{\boldsymbol{k}_3 \boldsymbol{k}_2 \to \boldsymbol{k}_1} + C^{s_{k_1} s_{k_3} s_{k_2}}_{\boldsymbol{k}_1 \boldsymbol{k}_3 \to \boldsymbol{k}_2} + C^{s_{k_1} s_{k_2} s_{k_3}}_{\boldsymbol{k}_1 \boldsymbol{k}_2 \to \boldsymbol{k}_3} = 0, \quad (4.8a)$$

and

$$s_{k_1} k_1 C^{s_{k_3} s_{k_2} s_{k_1}}_{\boldsymbol{k}_3 \boldsymbol{k}_2 \to \boldsymbol{k}_1} + s_{k_2} k_2 C^{s_{k_1} s_{k_3} s_{k_2}}_{\boldsymbol{k}_1 \boldsymbol{k}_3 \to \boldsymbol{k}_2} + s_{k_3} k_3 C^{s_{k_1} s_{k_2} s_{k_3}}_{\boldsymbol{k}_1 \boldsymbol{k}_2 \to \boldsymbol{k}_3} = 0. \quad (4.8b)$$

We decomposed the modes into two categories: the modes corresponding to the non-zero inertial waves (with $k_z \neq 0$), denoted 3 or 3D,

$$\text{If } \boldsymbol{k} \in W_{\boldsymbol{k}} = \{\boldsymbol{k} | k \neq 0 \text{ and } k_z \neq 0\} \text{ then } \boldsymbol{u}(\boldsymbol{k}) = \boldsymbol{u}_{3D}(\boldsymbol{k}); \quad (4.9)$$

and the modes with a null inertial wave frequency (with $k_z = 0$), denoted 2 or 2D, which correspond to a real-space velocity field that is averaged vertically

$$\text{If } \boldsymbol{k} \in V_{\boldsymbol{k}} = \{\boldsymbol{k} | k \neq 0 \text{ and } k_z = 0\} \text{ then } \boldsymbol{u}(\boldsymbol{k}) = \boldsymbol{u}_{2D}(\boldsymbol{k}_h), \quad (4.10)$$

where $k_h = \sqrt{k_x^2 + k_y^2}$ is the horizontal wavenumber. The total energy $E = \frac{1}{2}\sum_{\boldsymbol{k}} |\mathbf{u}(\boldsymbol{k})|^2$ becomes $\mathrm{E} = \mathrm{E}_{2D} + \mathrm{E}_{3D}$, with

$$\mathrm{E}_{2D} = \frac{1}{2}\sum_{\boldsymbol{k} \in V_{\boldsymbol{k}}} |\mathbf{u}_{2D}(\boldsymbol{k})|^2, \quad \mathrm{E}_{3D} = \frac{1}{2}\sum_{\boldsymbol{k} \in W_{\boldsymbol{k}}} |\mathbf{u}_{3D}(\boldsymbol{k})|^2. \quad (4.11)$$

Using (4.9-4.10), the nonlinear interactions between triads in (4.6) can be classified as $(33 \to 2)$, $(23 \to 3)$, $(33 \to 3)$, and $(22 \to 2)$. Note that the notation $(jk \to i)$ stands for interaction between modes j, k and i contributing to the equation of evolution for the mode i, with an interaction coefficient $C_{jk\to i}^{s_j,s_k,s_i} \neq 0$. It is symmetric in j and k.

In the Ro $\to 0$ limit, where the two-timescale expansion is valid, only the resonant interactions satisfying (4.5) make a significant contribution to the nonlinear energy transfers. The interactions $22 \to 2$ are all trivially resonant. The resonant interactions $33 \to 2$ were shown by Waleffe (1993) to have no contribution to the energetic of the 2D modes. That is, if $(\boldsymbol{k}_1, \boldsymbol{k}_2, \boldsymbol{k}_3)$ is a resonant triad, with $(\boldsymbol{k}_2, \boldsymbol{k}_3) \in W_{\boldsymbol{k}}$ and $\boldsymbol{k}_1 \in V_{\boldsymbol{k}}$, then the interaction coefficient $C_{\boldsymbol{k}_3\boldsymbol{k}_2\to\boldsymbol{k}_1}^{s_{k_3}s_{k_2}s_{k_1}} = 0$, and the two other interacting coefficients satisfy $C_{\boldsymbol{k}_1\boldsymbol{k}_2\to\boldsymbol{k}_3}^{s_{k_1}s_{k_2}s_{k_3}} = -C_{\boldsymbol{k}_3\boldsymbol{k}_1\to\boldsymbol{k}_2}^{s_{k_3}s_{k_1}s_{k_2}}$ (from 4.8a). The resonant interactions $32 \to 3$ are referred to as catalytic. If this property is combined with our definition of interaction $ij \to k$ as an interaction with $C_{ij\to k}^{ijk} \neq 0$, then the resonant interactions $33 \to 2$ do not exist. The equations only with resonant interactions can then be written as

$$
\begin{aligned}
\frac{\partial \mathrm{E_{3D}}}{\partial t}(\boldsymbol{k} \in W_{\boldsymbol{k}}, t) &= (T_{33\to 3res.} + T_{32\to 3res.})(\boldsymbol{k} \in W_{\boldsymbol{k}}, t), && (4.12)\\
\frac{\partial \mathrm{E_{2D}}}{\partial t}(\boldsymbol{k} \in V_{\boldsymbol{k}}, t) &= T_{22\to 2res.}(\boldsymbol{k} \in V_{\boldsymbol{k}}, t), && (4.13)
\end{aligned}
$$

where T represents the Fourier-space energy transfer terms and $T_{33\to 2.res} = 0$. In contrast to the resonant $33 \to 2$, the near-resonant interactions $33 \to 2$ are active. They exchange energy with the 2D modes, i.e. $C_{33\to 2}^{s_3s_3s_2} \neq 0$. Note also that the near-resonant interactions denoted $33 \to 2$ and $32 \to 3$ are essentially denoting the same active triads, except when considering only the resonant interactions (4.5) the $23 \to 3$ are the only type that remains active in the spectral energy transfer equations.

The resonant $33 \to 2$ property is at the origin of the decoupling theories, which predict a decoupling between the inertial waves and the two-dimensional coherent structures in a rapidly rotating flow. This is coherent with the work of Babin et al. (1996, 1998), who averaged the equations and separated the fast waves and the slow modes. They obtained an equation governing the vertically-averaged 2D structures of the flow decoupled from the wave dynamics in the limit of small Ro. However, Cambon et al. (2004a) later argued that for an unbounded domain, coupling terms between the 2D and the wave modes remain active even at Ro = 0. That is, no decoupling is achievable in unbounded domains.

Concerning the 3D dynamics (4.12), Waleffe (1993) showed that the resonant $33 \rightarrow 3$ interactions transfer energy to the $W_{\boldsymbol{k}}$ mode of the triad with the lowest frequency, ω_{s_k}. Cambon et al. (1997) observed an inhibition of the overall energy transfers (including both 2D and 3D modes), but no inverse cascade. They argued that an inverse cascade could only be achieved by resonant interactions. However, using a closure model, they confirmed the tendency of the nonlinear interactions to transfer energy toward the slow frequency modes. Another dynamics was proposed for the resonant 3D modes. Babin et al. (1998) suggested that more $32 \rightarrow 3$ resonant interactions are possible compared to the number $33 \rightarrow 3$. As a result, energy transfers in (4.12) would be dominated by $32 \rightarrow 3$ interactions and this would lead to a reduced vertical 3D energy transfers as Ro $\rightarrow 0$.

Using a kinematic approach, Kartashova (2007) showed that near-resonant interactions in discrete domains are much more numerous than exact-resonances in three-wave interactions systems—Inertial waves fall into three-wave interaction system. This is not necessarily the case for four-(and more)-wave interaction systems, where the number of exact-resonances in a discrete domain can be very large even in small spectral domains. The results of the forced numerical simulations of rotating turbulence in periodic domain by Smith and Lee (2005) showed that the near-resonant interactions satisfying an approximate resonance modeled by

$$|\omega_{s_{k_1}} + \omega_{s_{k_2}} + \omega_{s_{k_3}}| \leq Ro, \qquad \boldsymbol{k}_1 + \boldsymbol{k}_2 + \boldsymbol{k}_3 = 0 \tag{4.14}$$

played an important role in the energy transfers at moderately small values of Ro. Note that here, the frequencies are nondimensional as defined in Eq. (4.2). The small parameter Ro in (4.14) is the nonlinear broadening of the resonant interaction. It depends on the spectrum of the flow and the level of nonlinearity of the turbulence for the scales associated with the interacting triads. Due to the dispersion relation of capillary waves, Kartashova (1998) showed that *only* near-resonant interactions are possible in a discrete domain. Note that in an unbounded domain, both resonances and near-resonances would contribute to nonlinear transfers. In contrast to capillary waves, inertial wave modes can be both exact resonances (4.5) and near resonances (4.14) in both a discrete and continuous spectral domain.

4.3 Number of exact and near-resonances

As a first step in evaluating the influence of the 1) discreteness, and the 2) resolution affect, we consider a range of spectral domains corresponding to a fixed size $L \times L \times L$ but with various spatial resolutions $N \approx 64, 100, 133, 150, 166$. These correspond to spectral truncation wavenumbers of $k_t \approx 21, 33, 50, 55$ ($k_t \approx N/3$ for dealiasing, Boyd (1989)). Note that due to the anisotropy of the inertial dispersion relation (4.2), we consider a spectral domain with a cylindrical truncation such that $\max(|k_z|) = k_{max}$, and $\max(k_h) = k_{max}$. We ignore the range of modes corresponding to the dissipation range $k_d < k < k_t$. Assuming that $k_d \approx 0.9\ k_t$, we only consider the modes of the spectral domain with $|k_z| \leq k_{max}$ and $k_h \leq k_{max}$, with $k_{max} = 20, 30, 40, 45, 50$.

To give some perspective we recall that the numerical studies of rotating turbulence performed by Hossain (1994) were obtained in a 32^3 numerical domain which would correspond to $k_t = 10$. Simulations of Smith and Lee (2005) used a resolution of 64^3, which correspond to $k_t = 21$. Simulations of Smith and Waleffe (1999) and Chen et al. (2005) used resolutions of 128^3, which correspond to $k_t = 42$. Bourouiba and Bartello (2007) used resolutions of 100^3 and 200^3, which correspond to $k_t = 33$ and 66. The recent large-scale forcing simulations of Müller and Thiele (2007) used a resolution of 512^3, which correspond to $k_t = 170$.

We counted the number of interactions satisfying (4.14) for a fixed domain size

Type of triad	Resonant (R) and/or Near-resonant (N):	
	$0 < \mathrm{Ro} \ll 1$	$\mathrm{Ro} = 0$
$22 \to 2$	R	R
$33 \to 2$	N with $C_{33\to 2} \neq 0$	vanishes with $C_{33\to 2} = 0$
$23 \to 3$	R & N	R catalytic: no energy transfer to the 2D mode
$33 \to 3$	R & N	R : energy transfer to the 3D mode with smallest ω_{s_k}

Table 4.1: Properties of the interactions of interest contributing to the energy transfers.

with varying truncation numbers corresponding $k_{max} = 20, 30, 40, 45, 50$. For each triad, we consider the eight possible types of interactions defined by $(s_{k_1}, s_{k_2}, s_{k_3})$. We summarize in table 4.1 the type of interactions on which we focus. When calculating the number of $(3_a 3_b \to 3_c)$ and $(2_a 2_b \to 2_c)$ interactions, we only consider the interactions with all three non-null interacting coefficients ($C^{s3_a s3_b s3_c}_{3_a 3_b \to 3_c}$,$C^{s3_b s3_c s3_a}_{3_b 3_c \to 3_a}$, $C^{s3_a s3_c s3_b}_{3_a 3_c \to 3_b}$) and ($C^{s2_a s2_b s2_c}_{2_a 2_b \to 2_c}$, $C^{s2_b s2_c s2_a}_{2_b 2_c \to 2_a}$, $C^{s2_a s2_c s2_b}_{2_a 2_c \to 2_b}$), respectively. The $32 \to 3$ interactions are those with at most one zero interaction coefficient. The $3_a 3_b \to 2$ are restricted to the interactions with $C^{s3_a s3_b s2}_{3_a 3_b \to 2} \neq 0$. In other words, the number of $32 \to 3$ contains both resonances and near-resonances, whereas the $33 \to 2$ are only near-resonances.

Figure 4.1 shows the resulting numbers of $33 \to 3$, $33 \to 2$ and $32 \to 3$ satisfying (4.14) for a range of nonlinear broadening Ro between 0 and 1. The number of $33 \to 2$ and the $33 \to 3$ interactions (top and lower panels) both show a decrease with Ro and reach a plateau for small Ro, whereas, $33 \to 2$ (middle panel) near-resonances clearly decrease with Ro and vanish for sufficiently small Ro.

As the nonlinear broadening is decreased, the number of $33 \to 3$ interactions reaches a non-zero plateau that varies with the truncation wavenumber considered.

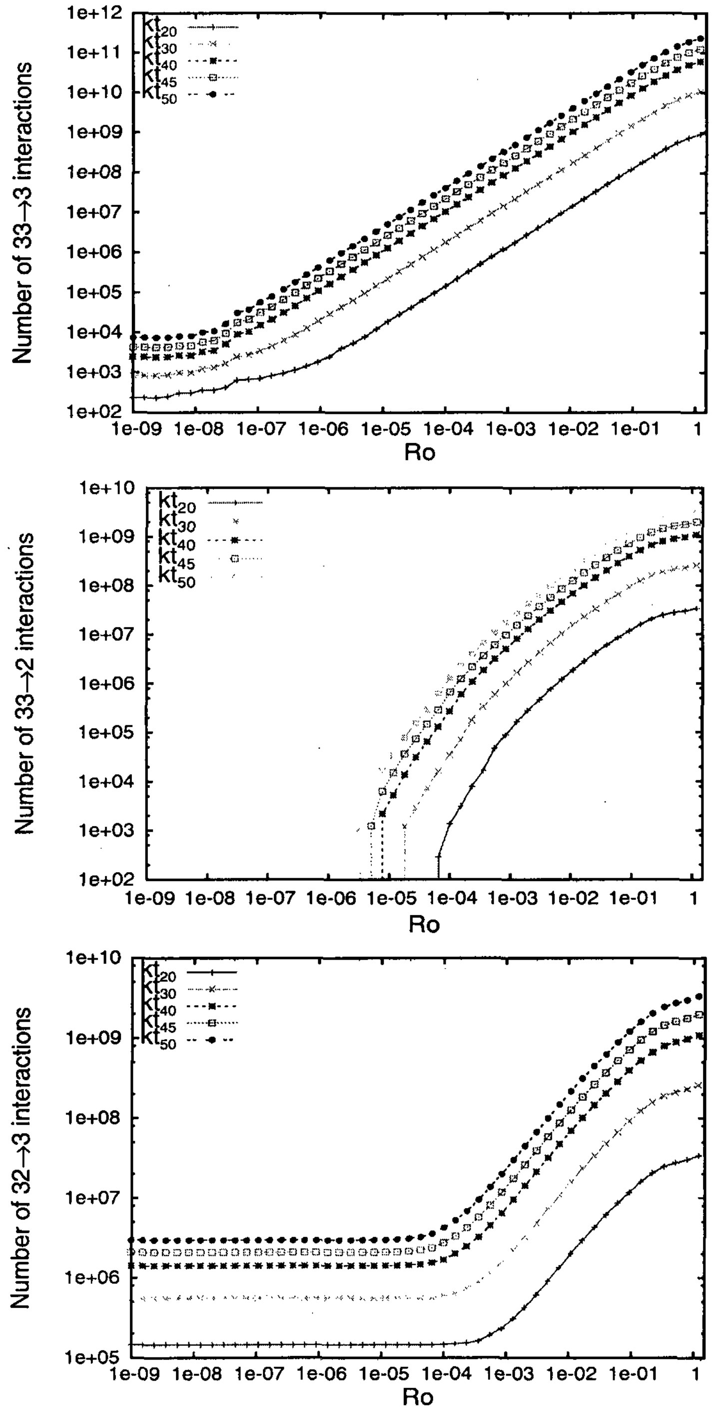

Figure 4.1: Total number of active resonant and near-resonant $33 \to 3$, $23 \to 3$ and $33 \to 2$ (see table 4.1 and Eq. (4.14)) as a function of nonlinear broadening Ro and the spatial resolutions used.

This plateau corresponds to the number of exactly resonant interactions satisfying (4.5). The number of $33 \rightarrow 3$ resonances varies from $R_{33\rightarrow 3} = 232$ for $k_{max} = 20$ to $R_{33\rightarrow 3} = 7408$ for $k_{max} = 50$. Note that this remains quite small compared to the number of near-resonances, $N_{33\rightarrow 3}$, obtained for higher values of nonlinear broadening. This latter increases rapidly with Ro and this is true for all truncations. For example, for a truncation of $k_{max} = 20$, the number of near-resonances $N_{33\rightarrow 3}$ increases dramatically from 704 (for $\mathrm{Ro} = 1 \times 10^{-7}$) to 7.43×10^{8} (for $\mathrm{Ro} = 0.8$). The plateau corresponding to the number of exact-resonances followed by a rapid increase of the number of near-resonances as Ro increases is reminiscent of the results obtained for near-resonant surface gravity waves (Tanaka and Yokoyama, 2004). They found that the number of near-resonances reaches a non-zero plateau as their nonlinear broadening decreased. However, the number of resonant interactions on the plateau was found to be sufficiently large to preclude a regime similar to capillary wave "frozen" turbulence .

The decoupling between the 3D and 2D modes was predicted by decoupling theories derived in continuous domains for Ro infinitesimally small. These theories rely on the vanishing coupling coefficient between the 2D and the 3D modes in the $33 \rightarrow 2$ interactions. In other words, we know the fact that in unbounded domains $C_{33\rightarrow 2} \rightarrow 0$ as $Ro \rightarrow 0$ implies a decoupled dynamics. In bounded domains, the Ro for which these theories would apply is finite.

We counted the number of $33 \rightarrow 2$ near-resonances in a given bounded domain. Recall that our definition of the $33 \rightarrow 2$ interactions imposes a non-zero interacting coefficient on the 2D mode. Figure 4.1 shows clearly that there is minimum finite nonlinear broadening, below which the $33 \rightarrow 2$ interactions vanish. We will refer to this minimum as Ro_{min}. It varies with the resolution used. From the figure, Ro_{min} changes from $\mathrm{Ro}_{min} = 6.6 \times 10^{-5}$ at spectral truncation $k_{max} = 20$ to $\mathrm{Ro}_{min} = 3.3 \times 10^{-6}$ for a truncation of $k_{max} = 50$. For $\mathrm{Ro} < \mathrm{Ro}_{min}$ the only interactions between the $V_{\boldsymbol{k}}$ and the $W_{\boldsymbol{k}}$ modes are those labelled $32 \rightarrow 3$. In other words, for $\mathrm{Ro} < \mathrm{Ro}_{min}$ only resonant interactions between the modes $V_{\boldsymbol{k}}$ and $W_{\boldsymbol{k}}$ are active. Since these are catalytic, a decoupling between the 2D and the 3D dynamics is expected. Note that for Ro $<$ Ro_{min}, the catalytic interactions do not exchange energy between scales. However, they do redistribute the 3D energy horizontally (between various (k_x, k_y) modes of fixed k_h). Finally, note that the values of Ro_{min} (from figure 4.1) are far lower than Rossby numbers found in the literature on numerical simulations of rotating turbulence. For example, with a resolution of 128^3—with a maximum wavenumber close to 40—numerical simulations performed with a nonlinear broadening of Ro $<$ $\mathrm{Ro}_{min} = 7.8 \times 10^{-6}$ would automatically produce a decoupling between 3D and 2D modes. For Ro $>$ Ro_{min}, near-resonances transferring energy between 2D and 3D modes are still present. If a decoupling is observed numerically at these Rossby numbers, it is an intrinsic property of the flow and not an artefact of the numerics.

In the context of resonant interaction theories, Babin et al. (1998) suggested that reduced vertical energy transfers would be observed. The reason for this lies with the assumption that number of exact resonances $R_{32\to3}$ would be greater than $R_{33\to3}$. A similar stalling of the vertical transfers was predicted and observed for weak Alfvén turbulence (Galtier et al., 2000). These predictions contrasts with the results suggesting the creation of anisotropy by the predominant resonances $33 \to 3$.

In order, to examine whether a Babin et al. (1998) regime is observable in bounded domains we examined its underlying hypothesis by comparing the number of all the $33 \to 3$ and $32 \to 3$ interactions. Figure 4.2 shows that both regimes exist. In one regime, the $33 \to 3$ are dominant and in other, the $32 \to 3$ are dominant. A critical nonlinear broadening, Ro_c, delimits the two regimes. For $Ro < \mathrm{Ro}_c$, the number of $33 \to 3$ near-resonances, $N_{33\to3}$, is smaller than the number of $32 \to 3$ near-resonances, $N_{32\to3}$. For Ro $>$ Ro_c, $N_{33\to3} > N_{32\to3}$. Ro_c is a function of the truncation wavenumber. The higher the k_t, the smaller the Ro_c. For $Ro < \mathrm{Ro}_c$, the regime of Babin et al. (1998) could be observable in bounded domains, whereas for $Ro > \mathrm{Ro}_c$, the dominant $33 \to 3$ would be at the origin of energy transfers toward the smaller frequencies.

Note that $\mathrm{Ro}_c < \mathrm{Ro}_{min}$ for all the k_{max} used here. This implies that for a nonlinear

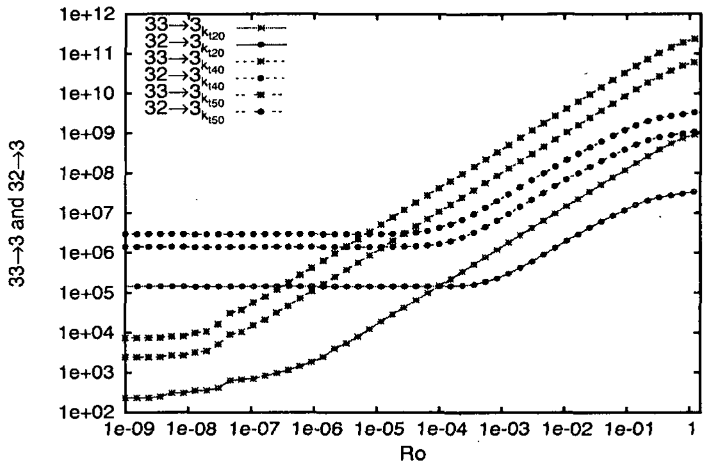

Figure 4.2: Comparison of the number of resonant and near-resonant interactions $33 \rightarrow 3$ and $32 \rightarrow 3$ as a function of the nonlinear broadening and the truncation of the spectral domain used.

broadening of Ro $<$ Ro$_c$ $<$ Ro$_{min}$, the inter-scale energy transfers in a given simulation would be due to $33 \rightarrow 3$ interactions. For sufficiently large Ro, there are fewer resonances than near-resonances (for all types of interactions). For example, varying the nonlinear broadening from $\sim 10^{-5}$ to $\sim 10^{-3}$, the number of near-resonances increases by a factor 100, with the $N_{33\rightarrow 2}$ increasing from 288 to 10^5 ($k_{max} = 20$). As a result, if one is interested in the small Ro limit, the question becomes whether resonances, even in these small numbers, are sufficient to guarantee that energy transfers occur in such bounded domains.

In a continuous spectral space truncated at k_t, the number of $33 \rightarrow 3$ interactions are expected to increase with $\sim k_t^6$ with the truncation wavenumber. Similarly, the number of $32 \rightarrow 3$ and $33 \rightarrow 2$ is expected to increase as $\sim k_t^5$. Using these scalings, and for different truncation wavenumbers, we normalized the results of figure 4.1. Figure 4.3 shows the number of $33 \rightarrow 3$ interactions normalized with k_t^6 and the number of $32 \rightarrow 3$ and $33 \rightarrow 2$ normalized with k_t^5. For sufficiently large Ro, the normalized curves are indistinguishable. In other words, for large Ro, there are no differences expected to arise between results in bounded domains and those in

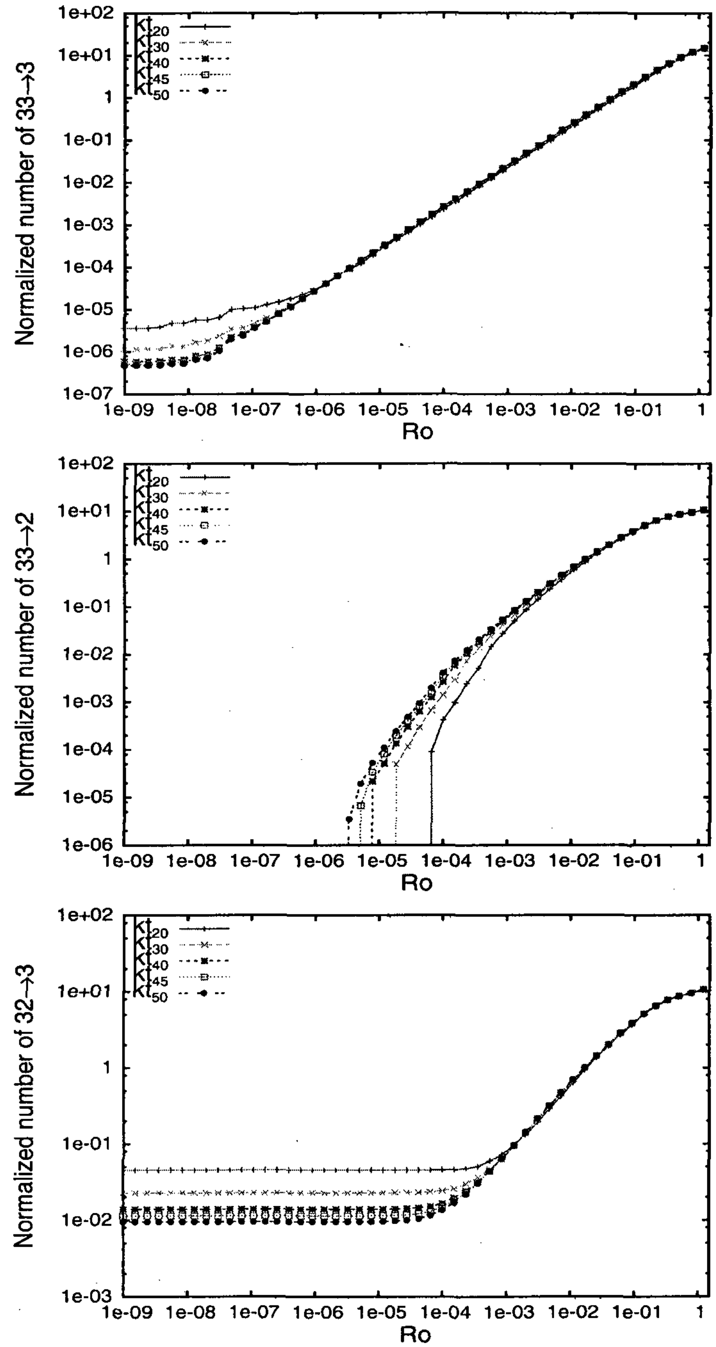

Figure 4.3: Effect of the discreteness on the variation of the number of resonant and near-resonant $33 \longrightarrow 3$, $23 \longrightarrow 3$ and $33 \longrightarrow 2$ as a function of nonlinear broadening Ro. The number of $33 \longrightarrow 3$ interactions are normalized with k_t^6 and the number of $32 \longrightarrow 3$ and $33 \longrightarrow 2$ normalized with k_t^5.

unbounded domains. However, below a certain value of the nonlinear broadening, this scaling is weaker: the scaled curves differ from one another for small Ro. The discrepancy in the collapse of the scaled curves is particularly striking for the near-resonances $N_{33\to 2}$. For example, $k_t = 20$ curve starts diverging from the larger k_t curve occurs at Ro $\approx O(10^{-3})$. Note that this is larger than Ro_{min} which was identified as threshold for decoupling. Hence, in the domains considered here, discreteness effects are increasingly important for a nonlinear broadening larger than Ro_{min}. As a result, it becomes important to have a better evaluation of the consequences of discreteness effects.

To summarize, in the present section, we discussed the results of wave-turbulence, which was derived for unbounded domains. We examined whether these theoretical results (e.g. decoupling and freezing of the vertical energy transfers) would be observable in bounded domains. For domains typically used in numerical simulations we found and quantified a threshold, Ro_{min}, below which the assumptions behind the 2D-3D decoupling theories is valid in finite domains. We found and quantified a nonlinear broadening threshold, Ro_c, below which the vertical freezing prediction of Babin et al. (1998) would be observable in bounded domains. A nonlinear broadening above Ro_c corresponds to a dynamics dominated by triple-wave interactions.

We investigated the discrepancies between the number of interactions resolved in unbounded and bounded domains (for a given truncation wavenumber). We found that for all dynamical regimes discussed (decoupling, vertical freezing, etc), discreteness effects related both to intrinsic bounded domain effects and to resolution effects lead to differences between number of near-resonances obtained in bounded domains for relatively small Ro.

For the domains considered here, we found that discreteness effects become important for nonlinear broadenings larger than Ro_{min}. However, based on these results alone, we cannot determine this transition with more precision. We denote this transition nonlinear broadening Ro_f, and now turn to a kinematic model of cascade in order to obtain a more precise assessment of Ro_f. Below Ro_f the dynamics could become significantly affected by discreteness effects. This is investigated using a kinematic model of cascade initiated with given sets of modes.

4.4 Kinematic model

In his study of near-resonant capillary waves Pushkarev (1999) built two-dimensional maps (k_x, k_y) of modes satisfying the capillary three-wave near-resonance. Using this, he showed that the density of active modes changed significantly with the nonlinear broadening. Connaughton et al. (2001) proposed a kinematic model to study the discreteness effect on the transfer of energy via near-resonant capillary waves. They started from an initial map of excited or activated modes, then given a level of non-linear broadening, obtained subsequent maps of activated modes interacting with the initial set. The series of subsequent sets of active modes satisfied the near-resonant condition. This approach allowed them to determine the nonlinear broadening threshold below which no energy cascade could occur in a discrete spectral space.

Following a similar approach, we construct an iterative kinematic model of energy cascade through near-resonant inertial wave interactions (4.14). The dispersion relation of inertial waves is anisotropic and we therefore distinguish between the vertical and the horizontal wavenumbers. The map of modes is constructed for three-dimensional wavenumbers (k_x, k_y, k_z). We consider a discrete spectral domain of truncation k_t and start by assuming that only the modes in the initial set S_0 are active. For a given value of nonlinear broadening, Ro, we construct the set of modes $\boldsymbol{k}$ of generation 1, S_1, such that $\boldsymbol{k} \in S_1$ if $\boldsymbol{k} \in S_0$ or

$$\left.\boldsymbol{k} + \boldsymbol{k}_1 + \boldsymbol{k}_2 = 0 \;\&\; |\omega_{s_k} + \omega_{s_{k_1}} + \omega_{s_{k_2}}| \leq \mathrm{Ro} \text{ with } (\boldsymbol{k}_1, \boldsymbol{k}_2) \in S_0 \times S_0. \right\} \tag{4.15}$$

That is, S_1 includes all modes $\boldsymbol{k}$ interacting with two modes of S_0 through near-resonances and with at most one zero interacting coefficient and $S_0 \subset S_1$. The procedure can then be repeated using S_1 as the initial set of active modes. We obtain successive generations of active modes $S_0, ...S_n, ...S_N$. The last set S_N includes all the modes that were activated by the cascade. All the sets with $n > N$ are identical to S_N, i.e. they do not contain any new activated modes. When S_N is reached, there are two possibilities. The first is that S_N contains all available modes of the domain. In other words, the propagation of the initial excitation reaches all modes. The second possibility is that not all the modes of the domain are contained in S_N, thus a subset of modes does not participate in the dynamics. Hence, discreteness effects clearly are present and can compromise numerical representation of the dynamics in the domain considered. In this last case, we say that the cascade is halted or that a freezing of the kinematic model cascade is taking place.

In addition to the general propagation of active modes throughout the spectral domain, we are also interested in investigating the role played by the various types of near-resonant interactions described in table 4.1. When going through the interactive steps described in (4.15) we also test for the type of modes involved ($V_{\boldsymbol{k}}$ or $W_{\boldsymbol{k}}$). For the $22 \to 2$ and $33 \to 3$ interactions we further require all three interaction coefficients to be nonzero. The $32 \to 3$ interactions have at least one nonzero interaction coefficient. Finally, the 2D interaction coefficient of the $33 \to 2$ interaction is nonzero.

We investigated two sets of initial modes: S_{0a} and S_{0b}. S_{0a} was chosen such that $|\boldsymbol{k}| \leq 5$ and contains a small number (424) of modes (figure 4.4 top panels). As such, this series, S_{na}, $n = 0, 1, 2, \ldots$ mimics a forward cascade in a spectral domain. S_{0b} contains 2856 modes and is defined by $S_{0b} = \{\boldsymbol{k} : 11 < |\boldsymbol{k}| \leq 12\}$ in order to mimic a cascade initiated with a forcing at intermediate to small spectral scales.

Figure 4.5 shows the maximum number of generations in the kinematic model when initialized with S_{0a} and for $k_t = 20$. For small values of the nonlinear broadening, the sequence is frozen after three generations. At $\mathrm{Ro} = \mathrm{Ro}_f \approx 5.95 \times 10^{-4}$, there is an abrupt transition. For Ro larger than this "freezing" threshold, S_{aN} includes all modes. Note, however, that for Ro only marginally larger than Ro_f, a larger number of generations are needed before this occurs. Nevertheless, for all $\mathrm{Ro} > \mathrm{Ro}_f$ all modes are eventually activated and we conclude that discreteness effects are not precluding

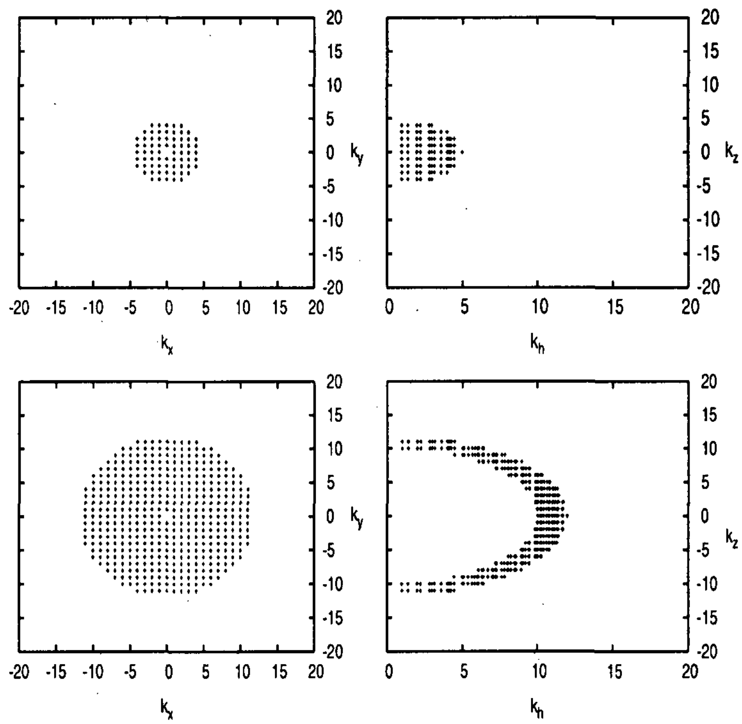

Figure 4.4: Initial maps of active modes S_{0a} (top panel) and S_{0b} (bottom panel). Here the domain is truncated at $k_t = 20$. The map of the horizontal components of the active modes are shown on $k_x - k_y$ plane (left panel) and the vertical components of the active modes on a $k_h - k_z$ plane (right panel).

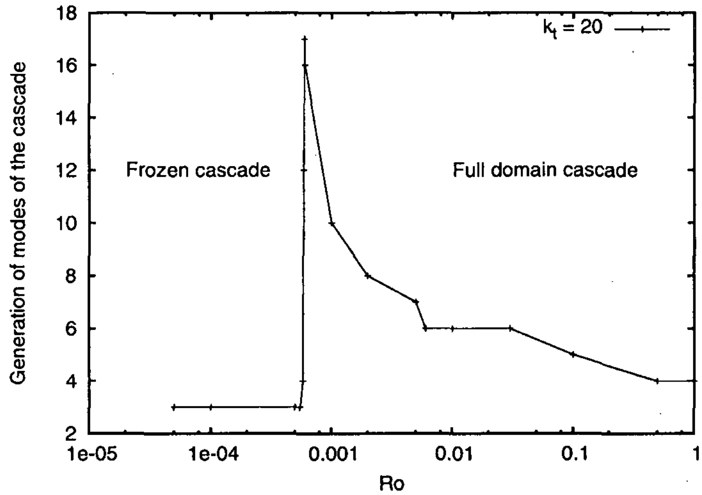

Figure 4.5: Maximum number of iterations, N, of generation in the sequence S_{0n} initiated with S_{a0} and for $k_t = 20$. For a nonlinear broadening less than about 6×10^{-4} the series was frozen after few interactions. For larger Ro, S_{aN} included all modes.

an energy cascade. It is also noteworthy that Ro_f appears to be only weakly dependent on resolution. For example, a doubling of k_t resulted in only a small decrease in Ro_f, i.e. from $\mathrm{Ro}_f = 5.95 \times 10^{-4}$ for $k_t = 20$ to $\mathrm{Ro}_f = 5.87 \times 10^{-4}$ for $k_t = 40$. It thus appears that, at least in this instance, discreteness effects become problematic at Ro considerably larger than Ro_{min}. Note however, that Rossby numbers typically used in simulations (e.g. 10^{-2}) are comfortably larger than Ro_f.

As was the model of Connaughton et al. (2001), our model is kinematic only. It does not give information about the direction of exchange of energy between modes involved. However, from previous numerical studies of rapidly rotating turbulence, we know that modes with low linear frequencies are preferentially excited. These correspond to modes with $k_h \gg k_z$. Also, in the decaying numerical simulations of Bourouiba and Bartello (2007), horizontal 3D energy transfers were more efficient than 3D energy vertical transfers. The kinematic model shows a similar anisotropy. That is, fewer generations are needed before all horizontal wavenumbers are excited,

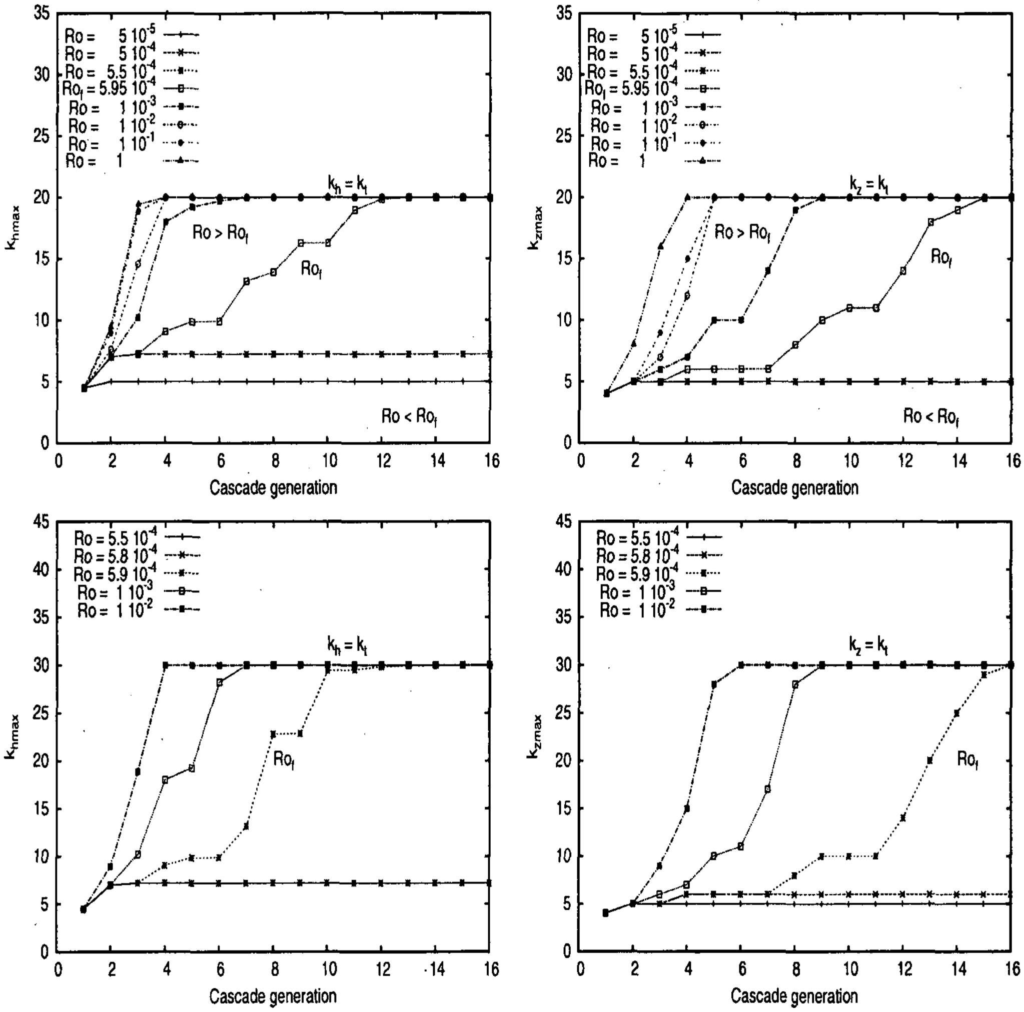

Figure 4.6: Maximum horizontal (left panel) and vertical (right panel) wavenumbers at each step of the cascade generation initiated with the set of excited modes S_{a0}, and for a domain of $k_t = 20$ (top panel) and $k_t = 30$ (lower panel). The critical freezing nonlinear broadening is the smallest Ro value to allow the cascade to extend to the smallest horizontal and vertical scales of the domains.

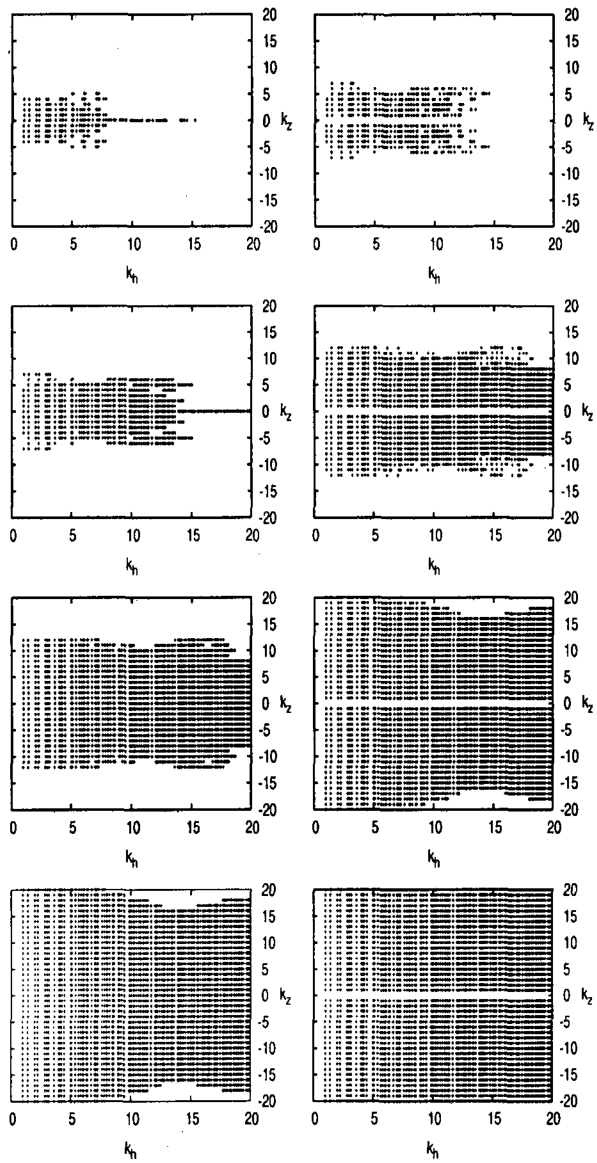

Figure 4.7: $k_h - k_z$ maps of modes activated at generations S_2 (top panel) to S_5 (bottom panel) by the $32 \to 3$ interactions (left panel) and the $33 \to 3$ interactions (right panel) with Ro $= 0.01$, $k_t = 20$ and initial active modes S_{a0} (see figure 4.4). The final state of the cascade corresponds to the activation of all the modes of the domain.

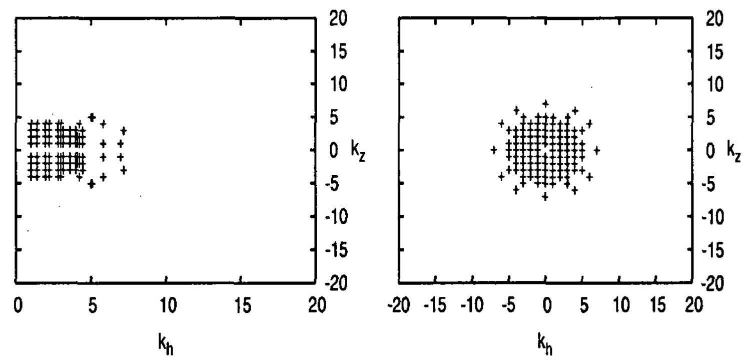

Figure 4.8: Maps of the modes of generation S_{aN}, with $N = 3$ at which the cascade is halted when $\mathrm{Ro} = 5.5 \times 10^{-4}$ and $k_t = 20$.

whereas more are needed to excite all available vertical wavenumbers. This is shown in figure 4.6, which plots the maximum horizontal and vertical wavenumbers reached at each generation for various values of Ro and for both S_{an} and S_{bn}. For comparison we also show this for both resolutions 64^3 and 100^3.

The point is further illustrated in figure 4.7, which shows the horizontal and vertical modes activated for the first few generations of the kinematic model initialized with S_{a0} and for $k_t = 20$. From the figure, it is clear that large horizontal wavenumbers are activated prior to the activation of large vertical wavenumbers. This anisotropy is visible in both the $33 \rightarrow 3$ and the $32 \rightarrow 3$ interactions. Note, however that the $33 \rightarrow 3$ interactions lead to a faster excitation (i.e. an excitation in fewer iterations of the kinematic model) than is the case for the $32 \rightarrow 3$ interactions. Finally, figure 4.8 shows the paucity of S_{aN} for a case where $\mathrm{Ro} < \mathrm{Ro}_f$ and for which the propagation was halted at $N = 3$.

Note that $22 \rightarrow 2$ interactions do not show any freezing of the propagation of the excitation among 2D modes. In fact, the propagation of the active modes among the set of 2D modes always takes only 3 generations.

4.5 Discussion

The discreteness of wavenumbers in a periodic domain has proven to be at the origin of the freezing of the nonlinear transfers between modes dominated by resonant capillary wave interactions. A similar effect was also suspected in rotating turbulence. In contrast to capillary waves, however, inertial waves can satisfy the resonant condition for integer-value wavenumbers, suggesting that a freezing might not occur in that system.

We studied the discreteness effects in order to clarify this issue. The discreteness effects are twofold. One aspect is the integer-valued wavenumbers, i.e. the finiteness intrinsic property of bounded domains versus unbounded domains. The other aspect is the resolution used in a particular bounded domain of interest. We examined how the reduction of the nonlinear broadening Ro affects the distribution and number of resonant and near-resonant interactions on a range of Ro in periodic domains relevant for numerical studies. We constructed a kinematic model of resonant and near-resonant interactions and used it to show that discreteness effects are detected for small nonlinear broadenings. We also showed that, as with capillary waves, a freezing of the energy transfers is also possible in discrete inertial waves, provided Ro was sufficiently small. This latter effect was not sensitive to a change of resolution.

Concerning the decoupling between the dynamics of the 2D and 3D modes predicted for the limit of Ro $\rightarrow 0$, we showed the existence of a minimum nonlinear broadening Ro_{min} below which 3D-2D interactions do not exchange energy. In a continuous domain, only the Ro $= 0$ limit strictly prevents the resonant 3D-2D interactions from exchanging energy. However, in a discrete domain, this value is nonzero. We quantified Ro_{min} for different resolutions. For example, Ro_{min} varies from $\mathrm{Ro}_{min} = 6.6\times10^{-5}$ for a resolution 64^3 to $\mathrm{Ro}_{min} = 3.3 \times 10^{-6}$ for a resolution 166^3. Thus, a resolution of 128^3 with a minimum nonlinear broadening of $\mathrm{Ro} < \mathrm{Ro}_{min} = 7.8 \times 10^{-6}$ would automatically show a decoupling between the 3D and the 2D. These values are comfortably below the Ro used in most numerical simulations in the literature of rotating turbulence.

In addition, another threshold of nonlinear broadening is found and denoted Ro_c. For $\mathrm{Ro} < \mathrm{Ro}_c$, the number of $32 \rightarrow 3$ interactions is larger than the triple wave interactions. In this regime, the freezing of the vertical energy transfers predicted by Babin et al. (1998) would be hypothetically possible. Above Ro_c no such regime would be possible in the domains considered in the present study. The kinematic model also showed that both $32 \rightarrow 3$ and triple wave interactions favour the propagation of the cascade to small horizontal scales and large vertical scales. We find that it takes a smaller number of generations for these interactions to excite the maximum horizontal wavenumbers of the domain compared to the number of generations needed to reach the maximum vertical wavenumbers. This is consistent with the anisotropy predicted by wave turbulence with a concentration of energy into small inertial frequency modes.

We found the regime of freezing of energy transfers observed for capillary waves to be also present in the system of inertial waves. We quantified the threshold nonlinear broadening Ro_f below which no energy cascade develops throughout the entire domain. Ro_f depends on the initial set of excited modes (scale of the forcing). Surprisingly, it only varies slightly with changes of domain resolution. For example, the kinematic model showed that a simulation in a domain with a resolution of about 64^3 would not be subject to an energy transfer freezing except for nonlinear broadening values Ro_f as small as 5.95×10^{-4}. This threshold decreases only slightly to $\mathrm{Ro}_f = 5.87 \times 10^{-4}$ for resolution of 133^3. These values of Ro_f are much smaller than Rossby numbers used in most numerical simulations of rotating turbulence.

The existence of the Ro_f threshold and existence of exact resonances in discrete domains is reminiscent of water-wave systems, where an interesting discreteness phenomenon is seen in a weakly forced setting Lvov et al. (2006). In that system energy was observed to accumulate around the forcing scale until such time as the nonlinear broadening of resonant interactions attained a critical value sufficient to overcome the discreteness of the modes. This was a followed by a sudden discharge or "avalanche" of energy in the form of a cascade. The system then oscillates between stages where the energy builds up and stages where it is discharged (Nazarenko, 2006). One might speculate, that weak forcing of inertial-wave turbulence could lead to a similar oscillation, with energy building up until Ro reaches Ro_f, above which energy transfers can occur.

In the domains examined here, we found that $\mathrm{Ro}_f > \mathrm{Ro}_{min} > \mathrm{Ro}_c$. From a practical standpoint, this implies that dynamical theories related to the properties of the resonances alone—that is the decoupling theories and the vertical energy freezing—would not be applicable in simulations with $\mathrm{Ro} > \mathrm{Ro}_f$, for which the number of interactions scale as in an infinite domain. In other words, in these domains, if a decoupling or a reduced energy transfer is observed, it is an intrinsic dynamical property of the flow in the bounded domain considered, and not a numerical artefact of resolution effects.

When comparing to Ro_f, it is important to use the relevant definition of Ro. Several definitions of Rossby numbers are used in the literature. Some calculate Ro based on the forcing scale, which guarantees a constant value. Some use a Rossby number based on the statistics of the flow. These include, for example the mean velocity or vorticity (see macro and micro-Rossby number definitions in Jacquin et al., 1990). As an illustration, consider the example of Smith and Lee (2005), who estimated their Ro based on the forcing of the flow. They obtained a $\mathrm{Ro} = 8.6 \times 10^{-2}$. However, they found that a reduced model of near-resonances calculated using $\mathrm{Ro} \approx 2.58 \times 10^{-2}$ (in 4.14) better reproduced the increase of 2D energy of the full flow (with all interactions). Using their spectra, we estimate that their macro-Ro is $\mathrm{Ro} = U/2\Omega L \approx 0.0255$. This value matches the nonlinear broadening 0.0258 of the near-resonances found to reproduce better the dynamics of the full equations. This suggests that when comparing Ro of simulations with values such as Ro_f or Ro_{min} one should consider that the relevant Ro is that obtained from averaged quantities of the flow such as the macro-Ro or micro-Ro calculated based on the averaged velocity or vorticity of the evolving flow, respectively. Note that Bourouiba and Bartello (2007) found that the macro and micro Ro were equivalent in the intermediate Ro regime simulations.

In sum, given the relatively small value of Ro_f and its weak dependence on resolution, we submit that most numerical simulations on rotating turbulence carried out so far would have been free of discreteness effects. However, it is important to note that when comparing the Rossby number of a simulation to the freezing Ro estimated in this study, the relevant definition of Rossby number is that related to the evolving average quantities of the flow.

Chapter 5

Inviscid Analysis

In the previous chapters, we identified three rotating regimes and focused on the properties of the intermediate Ro regime in decay simulations. The role of the near-resonant interactions in a bounded domain was discussed and discreteness effects identified. In this chapter, we focus on the small Ro regime. Asymptotic theories for this limit are reviewed and tested. Because large rotation rates impose severe restrictions on the numerical tool (e.g. small timestep and long integration times), study of the small Ro regime using DNS is difficult. We use the theoretical tool of equilibrium statistical mechanics and complement this study with the use of simulations of a rotating flow model in the limit of infinite Reynolds number.

If 2D-3D decoupling theories hold in the small Ro range, equilibrium statistical mechanics allows us to identify a set of new quantities which are invariant and which determines equilibrium spectra to which the inviscid system is expected to relax. We find that decoupling and its associated theoretical spectra are recovered by the inviscid numerical simulations until a nondimensional time of the order of $tf \approx 2/\mathrm{Ro}^2$. Beyond this threshold time, the set of invariants become slowly-varying, but continue to play a constraining role on the short-time dynamics of the rotating flow. The intermediate and large Ro regimes are also briefly examined numerically. This chapter is based on the following manuscript:

- Bourouiba L. (2008) Model of truncated fast rotating flow at infinite Reynolds number. The final version was published in *Physics of Fluids*, **20**, 075112-1–14.

Model of truncated fast rotating flow at infinite Reynolds number

Abstract

The purpose of this study is to examine the strongly rotating limit of a turbulent flow theoretically and numerically. The goal is to test the predictions of asymptotic theories. Given the limitations of experimental and dissipative numerical approaches to this problem, we use classical equilibrium statistical mechanics. We apply the statistical mechanics approach to the inviscid truncated model of strongly rotating turbulence (in the *small Rossby* number range) and derive the theoretical spectra of the decoupled model. We use numerical simulations to complement these derivations and examine the relaxation to equilibrium of the inviscid unforced truncated rotating turbulent system for different sets of initial conditions. We separate our discussion into two time-domains: an early time for which 2D modes are decoupled from 3D modes, for which a new set of invariants, S, are identified, and a later time for which the 2D and 3D dynamics are coupled and the quantities, S, are no longer invariants. We obtain a numerical evaluation of the threshold time, $t_{\star}$, between the decoupled and coupled phases. The values of $t_{\star}$ that we find are consistent with theoretical asymptotic expansions. We also examine whether the slowly varying quantities S play a constraining role on the coupled dynamics beyond $t = t_{\star}$. We find that the theoretical statistical predictions in the decoupled phase capture the horizontal dynamics of the flow. In the coupled phase, the invariants S are found to still play a constraining rôle on the short-timescale horizontal dynamics of the flow. These results are discussed in the larger context of previous rotating turbulence studies.

5.1 Introduction

Rotation plays an important role on the dynamics of large scale geophysical and astrophysical flows. The Coriolis force appears only in the linear part of the momentum equations, but if strong enough, can radically change the dynamics. The strength of the applied rotation, Ω, only has an appreciable influence when it is comparable or larger than the nonlinear term. The nondimensional Rossby number, Ro, is a measure of the strength of the rotation. When $\Omega \to \infty$, Ro $\to 0$. When the Coriolis force is applied, inertial waves are solutions of the linear momentum equations. Their frequencies vary from zero to 2Ω (Greenspan, 1968). The zero linear frequency modes correspond to two-dimensional (2D) structures, aligned with the rotation axis. In the fully nonlinear problem, the large range of frequencies of the inertial waves is at the origin of a complex nonlinear interplay of interactions involving the two-dimensional (2D) structures and the wave [three-dimensional (3D)] modes.

Rotating turbulence has been studied using various approaches: experimental studies (McEwan, 1969, 1976; Hopfinger et al., 1982; Jacquin et al., 1990; Baroud et al., 2002; Morize et al., 2005) and numerical simulations of forced (Yeung and Zhou, 1998; Smith and Waleffe, 1999; Chen et al., 2005) and decaying (Bardina et al., 1985; Bartello et al., 1994) rotating turbulence have been performed. Three distinct rotation regimes were identified for decaying rotating turbulent flows (Bourouiba and Bartello, 2007): the *weakly rotating* range, the *intermediate Ro* range, and the *small Ro* range. The *intermediate* range is characterized by a mechanism of maximum leakage of energy from 3D (wave) modes toward 2D zero-frequency modes and an asymmetry of the vorticity distribution. The *small Ro* range was characterized by a minimal energy transfer between zero-frequency modes and wave (3D) modes, an upscale transfer of energy for the zero-frequency modes, and no significant vorticity distribution asymmetry. *A posteriori*, most results of experimental and numerical studies cited above, which observe an increasing asymmetry in the vorticity distribution and show growth of 2D energy fall into the intermediate Ro range. The mechanisms causing the growth of the 2D modes in this regime are still unclear. Both nonlinear effects, such as near-resonant interactions (Smith and Lee, 2005) in forced numerical simulations, and linear effects (Davidson et al., 2006) in decay inhomogeneous flow experiments are argued to be at the origin of the generation of columnar structures repeatedly observed in this regime (Hopfinger et al., 1982). More investigation is needed of the asymmetry mechanisms typical of this intermediate Ro regime and the timescales of the mechanisms involved.

All of the above approaches (experimental, forced and decay numerical simulations in homogeneous and inhomogeneous rotating turbulence), can be used to pursue the understanding of the intermediate Ro regime. This is not the case for the small Ro regime. The tools available to study the small Ro regime are less obvious. An attempt using a statistical approach and quasinormal Markovian approximations was used (Bellet et al., 2006) and focused on the dynamics of the resonant interactions. However, this study only captures the dynamics of the 3D wave modes and the effects of the pure resonant interactions, which are not the only interactions present for asymptotically small but nonzero Ro numbers. Using an experimental approach to study this extreme regime is difficult due to the strength of rotation rates needed. In addition, there is difficulty in interpreting the experimental results when other effects are involved (e.g., Ekman layer dynamics or inhomogeneity of the flow). Direct numerical simulations of both forced and decaying rotating turbulence in the strong rotation limit have the advantage with regards to these constraints. However, they also have limitations. When performing forced and decay simulations of the small Ro regime, like for all other rotating regimes, a sufficient resolution of the inertial range is needed in order to limit the effect of the dissipation range on the scales of interest. In the small Ro regime, this need for a sufficiently large inertial range, combined with (1) a typically slow nonlinear timescale that imposes a long numerical integration time in order to analyze the long-timescale dynamics and (2) a large amplitude for the Coriolis force which imposes a small timestep needed for the numerical integration, lead to major numerical limitations.

Due to the limitations of both forced and decaying simulations, we choose to focus this study of the small Ro regime on the statistical equilibrium and inviscid dynamics of its truncated governing equations. The inviscid approach takes root in equilibrium statistical mechanics, which is our primary theoretical tool. In addition, we use complementary numerical simulations of the inviscid spectrally truncated equations of the rotating flow. This approach has the advantage of allowing a lower resolution and thus a much longer integration time. A sufficiently long integration time is critical for the better understanding of the small Ro regime. The study of inviscid flows with the method of equilibrium statistical mechanics is a theoretical approach to an idealized problem. However, this theoretical approach has proven helpful in understanding numerous fundamental turbulence problems. In fact, the use of equilibrium statistical mechanics theory for the study of inviscid flows captured the inverse energy cascade of 2D turbulence and the forward energy cascade of isotropic turbulence (Kraichnan, 1967, 1973, 1975). The inviscid flow is expected to relax to absolute equilibrium. For a review of the statistical theories and equilibrium spectra see Holloway (1986) and for a complete exposé of the latest statistical theories for geophysical flows see Majda and Wang (2006).

In addition, the numerical study of truncated inviscid flow models has been used to investigate the relaxation to equilibrium for 2D turbulence (Fox and Orszag, 1972), and provided a general agreement with equilibrium statistical theory. Statistical equilibria of other sets of truncated equations were also investigated: quasigeostrophic flows (Salmon et al., 1976; Abramov and Majda, 2003; Majda and Wang, 2006), weak turbulence flows for shallow water equations (Warn, 1986), the nonhydrostatic rotating Boussinesq equations (Bartello, 1995), 2D turbulence shear flow (Kaneda et al., 1989), and stratified flows (Waite and Bartello, 2004). The relaxation to equilibrium of a spectrally truncated 3D isotropic flow was also recently studied numerically

(Cichowlas et al., 2005; Bos and Bertoglio, 2006). Finally, spectrally truncated 3D rotating turbulence was studied numerically by Yamazaki *et al.* (2002). They examined moderate rotation rates and observed a relaxation to isotropic equipartition. They also observed that rotation introduced a delay and scale dependency on the relaxation-to-equilibrium timescale. The fundamental difference among the inviscid truncated systems listed above is the number and properties of their physical invariants. These invariants, or conserved quantities, play a key role in both the formalism of the inviscid statistical equilibrium and the understanding of the dissipative dynamical counterpart.

In this study, we apply the equilibrium statistical mechanics approach to truncated inviscid flows subject to a strong rotation. The model equations predicted by the asymptotic expansions in this regime conserves a new set of invariants. Using this, we first derive the equilibrium spectra associated with the new invariant quantities. We then turn to numerical simulations to compare the theoretical spectra obtained to the numerical inviscid truncated solutions. We thus intend to examine four primary questions: (1) Does the theoretical model of decoupled equations derived based on the assumptions of the asymptotic expansions capture the dynamics of the spectrally truncated solutions? (2) If that is not the case, are some features of the small Ro regime nevertheless captured? (3) If this is the case, on what timescale does this hold, and is that time consistent with the timescale predicted by the asymptotic theories? (4) How do the dynamics change beyond this threshold time and are the invariants still playing a constraining role?

In §5.2, the problem and equations of rotating turbulence are introduced and the timescales of the problems are discussed. In §5.3, we apply the method of equilibrium statistical mechanics to the rotating turbulence problem, and discuss its new invariants. We also derive their associated statistical equilibrium spectra. The theoretical spectra are then compared with the numerical solutions of the truncated inviscid equations in §5.4. We further discuss our approach and the results in §5.5.

5.2 Equations and rotating turbulence theories

5.2.1 Full equations

In a rotating frame of reference, the incompressible inviscid nondimensional momentum equation is

$$\frac{\partial \boldsymbol{u}}{\partial t} + \mathrm{R}o\ (\boldsymbol{u}\cdot\nabla)\boldsymbol{u} + \hat{\mathbf{z}}\times\boldsymbol{u} = -\nabla \mathrm{p}, \qquad \nabla\cdot\boldsymbol{u} = 0. \tag{5.1}$$

where Ro $= U/2\Omega L$ is the Rossby number, a dimensionless measure of the relative size of the advection and rotation terms, $\boldsymbol{\Omega} = \Omega\hat{\mathbf{z}}$ is the rotation vector, $f = 2\Omega$, $\boldsymbol{u} = (u, v, w)$ is the velocity vector, and p is the reduced pressure that includes the centrifugal term. Without loss of generality, the rotation axis has been chosen to be in the vertical direction $\hat{\mathbf{z}}$. Nondimensionalization was done using $(2\Omega)^{-1}$, L and U as characteristic time, length and velocity, respectively. When linearized about a rest state, the normal modes $\boldsymbol{n}_{\lambda_s}$, with the eigenvalues $\lambda_s = sfk_z/k$ with $s = \pm$ can be derived (see APPENDIX for details). This new basis can be used to re-express the implicitly nondivergent velocity field as

$$\boldsymbol{u}(\boldsymbol{r}) = \sum_{\boldsymbol{k}} \boldsymbol{u}(\boldsymbol{k})\exp(i\boldsymbol{k}\cdot\boldsymbol{r}) = \sum_{\boldsymbol{k}} (A_+(\boldsymbol{k},t)\boldsymbol{n}_+(\boldsymbol{k}) + A_-(\boldsymbol{k},t)\boldsymbol{n}_-(\boldsymbol{k}))\exp(i\boldsymbol{k}\cdot\boldsymbol{r}), \tag{5.2}$$

with $A_s(\boldsymbol{k},t) = a_s(\boldsymbol{k})\exp(i\lambda_s t)$. The reality condition ($\boldsymbol{u}(\boldsymbol{r})$ must be real) implies that $\boldsymbol{u}^*(\boldsymbol{k}) = \boldsymbol{u}(-\boldsymbol{k})$. Thus, the Fourier components $a_s(\boldsymbol{k})$ satisfy $a_s^*(\boldsymbol{k}) = a_s(-\boldsymbol{k})$.

5.2.2 Two-timescale problem, resonance condition

The Ro number can also be considered as the ratio between two timescales: Ro $= T_1/T_2$, where $T_1 = (2\Omega)^{-1}$ is a rapid timescale associated with the rotation and $T_2 = L/U$ is a slow timescale associated with the nonlinear interactions.

When rotation is strong, Ro $\to 0$ and the timescale separation between T_1 and T_2 become larger. Thus, Eq. (5.1) evolves on both a slow vortical timescale that could be re-expressed as τ_1 = Ro t and a fast wave timescale $\tau_0 = t$, where t is the nondimensional time $t = f\tilde{t}$, with $\tilde{t}$ the physical dimensional time. A multiple timescale asymptotic expansion can thus be performed. The leading-order part of this two-timescale problem is equivalent to the linear counterpart of (5.1) and has inertial wave solutions (as seen in APPENDIX). The nondimensional counterpart of the dimensional frequencies λ_s are $\omega_{s_k}(\boldsymbol{k}) = s_{\boldsymbol{k}}\hat{\mathbf{z}} \cdot \boldsymbol{k}/|\boldsymbol{k}| = \mathrm{s}_{\boldsymbol{k}}\mathbf{k_z}/\mathbf{k} = \mathrm{s}_{\boldsymbol{k}}\cos(\theta_{\boldsymbol{k}})$, with $s_{\boldsymbol{k}} = \pm 1$ and $\theta_{\boldsymbol{k}}$ being the angle between $\boldsymbol{k}$ and the axis of rotation. In the following, $\omega_{s_k(\boldsymbol{k})}$ is also denoted by ω_{s_k}.

At first order in the expansion, the only interacting triads that have a significant contribution on the slow timescale τ_1 are those that satisfy the *resonance condition* (Greenspan, 1968; Waleffe, 1993)

$$\omega_{s_k}(\boldsymbol{k}) + \omega_{s_p}(\boldsymbol{p}) + \omega_{s_q}(\boldsymbol{q}) = 0. \tag{5.3}$$

In other words, the modal solutions are given by the two equations

$$\boldsymbol{k} + \boldsymbol{p} + \boldsymbol{q} = 0 \quad \text{and} \quad s_{\boldsymbol{k}}\frac{\boldsymbol{k}_z}{|\boldsymbol{k}|} + s_{\boldsymbol{p}}\frac{\boldsymbol{p}_z}{|\boldsymbol{p}|} + s_{\boldsymbol{q}}\frac{\boldsymbol{q}_z}{|\boldsymbol{q}|} = 0. \tag{5.4}$$

The zero-frequency modes belong to the Fourier-space plane defined by $k_z = 0$, corresponding to the vertically-averaged real-space velocity field.

5.2.3 Modal decomposition

Our approach is to classify the modes into two groups: wave modes with nonzero frequencies, corresponding to $k_z \neq 0$ in Fourier space (also referred to as 3D modes), and zero-frequency modes. The following notation is used:

$$\text{If } \boldsymbol{k} \in V_{\boldsymbol{k}} = \{\boldsymbol{k} | k \neq 0 \text{ and } k_z = 0\} \text{ then } \boldsymbol{u}(\boldsymbol{k}) = \boldsymbol{u}_{2D}(\boldsymbol{k}_h) + w(\boldsymbol{k}_h)\,\hat{\mathbf{z}}, \tag{5.5}$$

$$\text{If } \boldsymbol{k} \in W_{\boldsymbol{k}} = \{\boldsymbol{k} | k \neq 0 \text{ and } k_z \neq 0\} \text{ then } \boldsymbol{u}(\boldsymbol{k}) = \boldsymbol{u}_{3D}(\boldsymbol{k}).$$

The total energy

$$E = \frac{1}{2}\sum_{\boldsymbol{k}} |\mathbf{u}(\boldsymbol{k})|^2 \tag{5.6}$$

becomes

$$\mathrm{E} = \mathrm{E}_{2D} + \mathrm{E}_w + \mathrm{E}_{3D}, \tag{5.7}$$

with

$$\mathrm{E}_{2D} = \frac{1}{2}\sum_{\boldsymbol{k}\in V_{\boldsymbol{k}}} |\mathbf{u}_{2D}(\boldsymbol{k})|^2, \quad \mathrm{E}_w = \frac{1}{2}\sum_{\boldsymbol{k}\in V_{\boldsymbol{k}}} |w(\boldsymbol{k})|^2 \quad \text{and} \tag{5.8}$$

$$\mathrm{E}_{3D} = \frac{1}{2}\sum_{\boldsymbol{k}\in W_{\boldsymbol{k}}} |\mathbf{u}(\boldsymbol{k})|^2,$$

which have corresponding spectra. The latter are governed by

$$\frac{\partial \mathrm{E}_{3\mathrm{D}}}{\partial t}(\boldsymbol{k} \in W_{\boldsymbol{k}}, t) = (T_{33\to 3} + T_{32\to 3} + T_{3w\to 3})(\boldsymbol{k} \in W_{\boldsymbol{k}}, t), \tag{5.9}$$

$$\frac{\partial \mathrm{E}_{2\mathrm{D}}}{\partial t}(\boldsymbol{k} \in V_{\boldsymbol{k}}, t) = (T_{22\to 2} + T_{33\to 2})(\boldsymbol{k} \in V_{\boldsymbol{k}}, t),$$

$$\frac{\partial \mathrm{E}_{\mathrm{w}}}{\partial t}(\boldsymbol{k} \in V_{\boldsymbol{k}}, t) = (T_{2w\to w} + T_{33\to w})(\boldsymbol{k} \in V_{\boldsymbol{k}}, t),$$

where T is the Fourier-space energy transfer. Transfers are distinguished by the types of interactions, eg. $33 \to 2$ stands for the interactions between two 3D wave modes that contribute to the 2D equation.

In the Ro$\to$ 0 limit, it is thought that only resonant interactions make a significant contribution to the slow dynamics until a certain time, at which a higher order expansion can be continued (Newell, 1969). Only a subset of 3D wavenumbers can satisfy the resonance condition in the $33 \to 3$, $32 \to 3$ and $3w \to 3$ interactions, but the $32 \to 3$ and $3w \to 3$ resonant triads do not transfer energy to the 2D and w modes, respectively. In fact, the interaction coefficient of the 2D mode in these resonant interactions was shown to be zero (Waleffe, 1993). The transfers are thus said to be "catalytic". For example, in the $32 \to 3$ interaction, the 2D mode plays the role of a catalyzer, facilitating the nonlinear interaction and energy exchange between the two 3D modes, but without receiving or losing energy itself (the 2D mode). This last property is a key point in asymptotic theories, predicting a decoupling between the inertial waves and the 2Dcoherent structures in a rapidly rotating flow. Averaging the interactions between fast waves led Babin *et al.* (1996) (Babin et al., 1996) to obtain an equation governing the vertically averaged 2D structures of the flow decoupled from the wave dynamics in the limit of small Ro. However, Cambon *et al.* (2004)

Cambon et al. (2004a) argued later that for an unbounded domain, coupling terms between the 2D and wave modes remain active even at Ro = 0. That is, no decoupling was achievable.

When only resonant interactions contribute to the energy transfers, the asymptotic energy equations are

$$\frac{\partial \mathrm{E}_{3\mathrm{D}}}{\partial t}(\boldsymbol{k} \in W_{\boldsymbol{k}}, t) = T_{33\to 3,res} + T_{32\to 3,res} + T_{3w\to 3,res}, \tag{5.10}$$
$$\frac{\partial \mathrm{E}_{2\mathrm{D}}}{\partial t}(\boldsymbol{k} \in V_{\boldsymbol{k}}, t) = T_{22\to 2},$$
$$\frac{\partial \mathrm{E}_{\mathrm{w}}}{\partial t}(\boldsymbol{k} \in V_{\boldsymbol{k}}, t) = T_{2w\to w},$$

where the subscript $\{jk \to i, res\}$ denotes resonant $jk \to i$ interactions (5.4). The time and wavenumber dependence in Eq. (5.10) has been omitted. $22 \to 2$ and $2w \to w$ interactions are trivially resonant, since all modes involved have zero frequency. It appears from Eq. (5.10) that the equation for E_{2D} is decoupled from the E_{3D} equation and is also similar to that governing 2D turbulence. The equation for E_w is also decoupled from that of E_{3D} and takes the form of a passive tracer advected by the 2D velocity field $\boldsymbol{u}_{2D}$. On the other hand, the E_{3D} equation remains affected by the $k_z = 0$ dynamics through the set of catalytic resonant triads $32 \to 3$ and $3w \to 3$. We will refer to Eq. (5.10) as the reduced system of decoupled equations. In addition to the total energy and helicity, this system (valid for the resonant interactions that are assumed to be present in the small Ro regime) conserves a new set of quantities.

5.3 Invariant quantities and statistical equilibrium of the small Ro regime

The systems of equations (5.9) and (5.10) conserve different sets of invariants. We use the new set of invariants of (5.10) to derive a statistical equilibrium for the strongly rotating turbulent flow limit (small Ro regime). Only quadratic quantities are considered below. Note that, spectrally truncated periodic representations of flows conserve only quadratic invariants. For example, the 2D Navier-Stokes conserve energy and enstrophy, but also an infinite number of invariants which are functions of the enstrophy. The spectrally truncated periodic counterpart of the 2D Navier-Stokes flow conserves only the first two quadratic invariants. The shallow water equations and both the rotating and nonrotating nonhydrostatic stratified Boussinesq equations conserve energy and a specific form of potential vorticity. The latter is not quadratic and is therefore not conserved by the periodic spectral truncation.

All calculations are carried out using a cylindrical spectrally truncated domain such that $k_h, |k_z| < k_T$, with k_T the truncation wavenumber. The discrete wavenumber increment is $\delta_{\boldsymbol{k}} = 2\pi/L$, where L^3 is the size of the domain occupied by the fluid.

5.3.1 Analysis of the full equations

Similarly to classical 3D Euler equations, rotating inviscid equations (5.9) conserve total energy (the helicity is also conserved, but we do not consider its effect on the analysis). Note that for nonrotating 3D turbulence, Kraichnan argued that the helicity did not change the forward cascade of energy to small scales, but could eventually delay such a cascade (Kraichnan, 1973). Using Eq. (5.2), the total energy (5.6) can be re-written as

$$E = \langle \boldsymbol{u}\, \boldsymbol{u}^* \rangle = \langle e(\boldsymbol{k}) \rangle = \sum_{\boldsymbol{k}} |a_+(\boldsymbol{k})|^2 + |a_-(\boldsymbol{k})|^2, \tag{5.11}$$

where $\langle \cdot \rangle$ is the volume average and $k = |\boldsymbol{k}| = \sqrt{k_h^2 + k_z^2}$. Consider the phase space of $4N$ elements $(\Re(a_+(k_1)),\ \Im(a_+(k_1)),\ \Re(a_-(k_1)),\ \Im(a_-(k_1)),\ldots,\ \Im(a_-(k_N)))$, where N is the number of Fourier modes. The most probable probability density function in the phase space, or *Gibbs canonical distribution*, is

$$P_\alpha = C\exp(-\alpha E) = C\exp -\alpha\left[\sum_{\boldsymbol{k}} |a_+(\boldsymbol{k})|^2 + |a_-(\boldsymbol{k})|^2\right] \tag{5.12}$$

where C is the normalization constant of P_α such that $\int_{4N} P_\alpha = 1$, giving

$$C^{-1} =$$
$$\int_{R^{4N}} \exp\left[-\alpha \sum_{\boldsymbol{k}} |a_+(\boldsymbol{k})|^2 + |a_-(\boldsymbol{k})|^2\right] d^N\Re(a_+)d^N\Im(a_+)d^N\Re(a_-)d^N\Im(a_-)$$
$$= \left[\frac{1}{2}\sqrt{\frac{\pi}{\alpha}}\right]^{4N}, \tag{5.13}$$

where α is the Lagrange multiplier determined by the ensemble averaged energy. The classical result for the mean energy spectra can be recovered

$$\langle e(\boldsymbol{k})\rangle_P = \langle |a_+(\boldsymbol{k})|^2 + |a_-(\boldsymbol{k})|^2\rangle_P = \frac{2}{\alpha}, \tag{5.14}$$

with $\alpha \neq 0$ and $\langle\cdot\rangle_P$ being the ensemble average calculated using P_α.

We consider the limit of large L to carry out the calculations using the integrals in the spectral domain. We introduce the horizontal and vertical spectra, $E_h(k_h)$ and $E_z(k_z)$:

$$E = \int_0^{k_T}\int_{-k_T}^{k_T}\int_0^{2\pi} e(\mathbf{k})d\mathbf{k}, \tag{5.15}$$
$$= \int_0^{k_T} E_h(k_h)dk_h, \tag{5.16}$$
$$= \int_{-k_T}^{k_T} E_z(k_z)dk_z \tag{5.17}$$

Equations (5.14)-(5.17) lead to the horizontal and vertical mean equipartiton energy spectra:

$$\langle E_h(k_h)\rangle_P = \frac{8\pi k_T}{\alpha}k_h, \quad \langle E_z(k_z)\rangle_P = \frac{2\pi k_T^2}{\alpha}. \tag{5.18}$$

α can then be obtained from the total initial energy that is conserved and known, E_0, ($E_0 = \langle E\rangle = \langle E\rangle_P$) using

$$\alpha = \frac{4\pi k_T^3}{E_0}. \tag{5.19}$$

In the weakly rotating limit, the flow is considered to be like classical isotropic non-rotating turbulence. It would thus be expected to relax to equipartition (5.18) (Lee, 1952). This relaxation was in fact observed to be delayed by rotation in the simulations of inviscid weakly rotating flows. In addition, the large scales of the total isotropic spectrum were observed not to reach the equilibrium for some of the initial conditions (ICs) (Y. Yamazaki and Rubeinstein, 2002).

When focusing on the strongly rotating limit, we argue that the effects of the timescale separation and the much slower nonlinear timescale τ_1 discussed in §5.2.2 must be incorporated into this analysis. In the next section, we examine the statistical equilibrium of this limit.

5.3.2 Analysis of the decoupled reduced equations

In the strong rotation limit, Eq. (5.10) has a new set of possible invariants (in addition to the total energy E). The quantities, elements of the set S=(E_{3D}, E_{2D}, V_{2D},E_w), are conserved by Eq. (5.10), where V_{2D} is the two-dimensional enstrophy, defined by

$$V_{2D} = \frac{1}{2} \sum_{\boldsymbol{k} \in V_{\boldsymbol{k}}} |\omega_z(\boldsymbol{k})|^2, \tag{5.20}$$

and ω_z is the vertical component of the vorticity in spectral space.

The quantities in S are new constraints on the system's dynamics. Taking them into account gives a new expression for the probability density function

$$P_{\alpha_1,\alpha_2,\alpha_3,\alpha_4} = C' \exp(-\alpha_1 E_{3D} - \alpha_2 E_{2D} - \alpha_3 V_{2D} - \alpha_4 E_w) \tag{5.21}$$

where C' is the normalization constant.

Considering the normal mode decomposition introduced in §5.2.1 to be valid for all modes $\boldsymbol{k}$ such that $k_h \neq 0$, we can express the set of quantities S as follows using the same phase space variables introduced in §5.3.1. The use of the normal mode decomposition for all the modes leads to the generation of nonquadratic terms. We thus restrict the use of the helical normal mode decomposition to the nonzero frequency modes $\boldsymbol{k} \in W_{\boldsymbol{k}}$ such that both conditions $k_z \neq 0$ and $k_h \neq 0$ are imposed. For the modes in $V_{\boldsymbol{k}}$ we have

$$|\tilde{a}_+(\boldsymbol{k})|^2 + |\tilde{a}_-(\boldsymbol{k})|^2 - (\tilde{a}_+\tilde{a}_-^*(\boldsymbol{k}) + \tilde{a}_+^*\tilde{a}_-(\boldsymbol{k})) = |\boldsymbol{u}_{2D}(\boldsymbol{k})|^2 \quad \text{for } \boldsymbol{k} \in V_{\boldsymbol{k}}, \tag{5.22a}$$

$$|\tilde{a}_+(\boldsymbol{k})|^2 + |\tilde{a}_-(\boldsymbol{k})|^2 + (\tilde{a}_+\tilde{a}_-^*(\boldsymbol{k}) + \tilde{a}_+^*\tilde{a}_-(\boldsymbol{k})) = |w(\boldsymbol{k})|^2 \quad \text{for } \boldsymbol{k} \in V_{\boldsymbol{k}}, \tag{5.22b}$$

implying that

$$|\tilde{a}_+(\boldsymbol{k})|^2 + |\tilde{a}_-(\boldsymbol{k})|^2 = \frac{1}{2}(|\boldsymbol{u}_{2D}(\boldsymbol{k})|^2 + |w(\boldsymbol{k})|^2) \text{ for } \boldsymbol{k} \in V_{\boldsymbol{k}}. \tag{5.23}$$

The phase space can be re-expressed as the space of $4N$ modes,

$$\Big[\Re(a_+(k_1)), \Im(a_+(k_1)) \quad, \Re(a_-(k_1)), \Im(a_-(k_1)), ..., \Im(a_-(k_M)),$$

$$\Re(u_{2D}(k_{M+1}), \Im(u_{2D}(k_{M+1})) \quad, \Re(w(k_{M+1})), \Im(w(k_{M+1})), ..., \Im(w(k_N))\Big],$$

with N number of Fourier modes and the last $N-M$ wavenumbers, $k_{i\in[M+1,N]}$, being those satisfying $\boldsymbol{k} \in V_{\boldsymbol{k}}$, where $i \in N$. Using the probability density function (5.21) and (5.23) we can rewrite the probability density function as

$$\begin{aligned} P_{\alpha_1,\alpha_2,\alpha_3,\alpha_4} &= \\ & C' \quad \exp\Big[-\alpha_1 \sum_{k_1}^{k_M}([\Re(a_+)]^2 + [\Re(a_-)]^2 + [\Im(a_+)]^2 + [\Im(a_-)]^2) \\ &- \sum_{k_{M+1}}^{k_N}(\alpha_2 + \alpha_3 k_h^2)([\Re(\boldsymbol{u}_{2D})]^2 + [\Im(\boldsymbol{u}_{2D})]^2) \\ &- \alpha_4 \sum_{k_{M+1}}^{k_N}([\Re(w)]^2 + [\Im(w)]^2)\Big]. \end{aligned} \tag{5.24}$$

We obtain the ensemble averaged equilibrium spectra using (5.24),

$$\langle E_{3D}(k_h)\rangle_{P_{\alpha_1,\alpha_2,\alpha_3,\alpha_4}} = \frac{8\pi k_T}{\alpha_1}k_h, \quad \langle E_{3D}(k_z)\rangle_{P_{\alpha_1,\alpha_2,\alpha_3,\alpha_4}} = \frac{2\pi k_T^2}{\alpha_1}, \tag{5.25}$$

$$\langle E_{2D}(k_h)\rangle_{P_{\alpha_1,\alpha_2,\alpha_3,\alpha_4}} = \frac{2\pi k_h}{\alpha_2 + \alpha_3 k_h^2}, \tag{5.26}$$

$$\langle V_{2D}(k_h)\rangle_{P_{\alpha_1,\alpha_2,\alpha_3,\alpha_4}} = \frac{2\pi k_h^2}{\alpha_2 + \alpha_3 k_h^2}, \tag{5.27}$$

$$\langle E_w(k_h)\rangle_{P_{\alpha_1,\alpha_2,\alpha_3,\alpha_4}} = \frac{2\pi}{\alpha_4}k_h. \tag{5.28}$$

We can then estimate the four Lagrange multipliers using the values of (E_{3D}, E_{2D}, V_{2D}, E_w). This leads to

$$\alpha_1 = \frac{4\pi k_T^3}{E_{3D}}, \tag{5.29a}$$

$$E_{2D} = \frac{\pi}{\alpha_3}\ln\left|1+\frac{\alpha_3}{\alpha_2}k_T^2\right|, \tag{5.29b}$$

$$V_{2D} = \pi\left[\frac{k_T^2}{\alpha_3} - \frac{\alpha_2}{\alpha_3^2}\ln\left|1+\frac{\alpha_3}{\alpha_2}k_T^2\right|\right], \tag{5.29c}$$

$$\alpha_4 = \frac{\pi k_T^2}{E_w}. \tag{5.29d}$$

The constants α_2 and α_3 are solutions of the coupled system (5.29b)-(5.29c). They are obtained numerically starting from a first analytical estimation, valid when $(\alpha_3/\alpha_2)(V_{2D}/E_{2D}) \gg 1$:

$$\alpha_3 \approx \frac{\pi k_T^2/V_{2D}}{1+\frac{E_{2D}}{V_{2D}}k_T^2/(\exp\left[k_T^2\frac{E_{2D}}{V_{2D}}\right]-1)}, \tag{5.30a}$$

$$\alpha_2 = \frac{\pi k_T^2}{E_{2D}} - \frac{\alpha_3 V_{2D}}{E_{2D}}. \tag{5.30b}$$

5.4 Comparison with numerical solutions

We now compare the results we derived in §5.3.2 with the numerical solutions that we obtained from solving (5.1).

We choose to focus on the homogeneous inviscid solutions in a finite domain. Both studies in finite and infinite domains are idealizations of rotating flows. Both approaches have advantages and limitations to direct applications. Here we use Direct Numerical Simulations in a periodic domain to solve the Euler equations. The difficulty arises when the integral scales of the W_k and V_k modes grow and fill a large part of the domain, as the solutions become more dependent on the specific geometry of the domain of study.

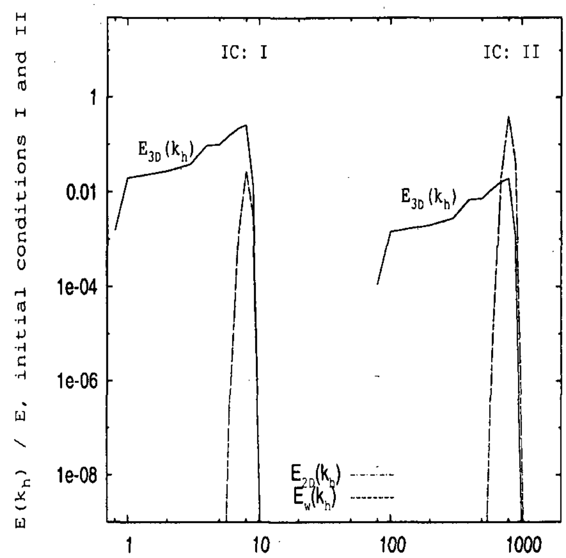

Figure 5.1: Initial horizontal spectra of ICs *IC: I*, dominated by 3D energy (left) and *IC: II*, dominated by zero-frequency energy (right).

Equation (5.1) is solved numerically using a direct (dealiased) pseudo-spectral method with a resolution 90^3. A high resolution is not needed to obtain the statistical equilibrium of this truncated system. The integration domain is triply periodic of length 2π. We use the leapfrog time differencing and the Asselin-Robert filter to control the computational mode (Asselin, 1972). This leads to a non exact conservation of the high frequency modes. In fact, the filter preferentially damps high frequency $W_{\boldsymbol{k}}$ modes in order to guarantee the stability of the computational mode of the leap-frog time-integration scheme. The "two-thirds rule" was chosen for dealiasing.

One set of simulations is initialized isotropically while the ICs of the second set are anisotropic, for which most of the energy is contained in the zero-frequency modes $V_{\boldsymbol{k}}$. With these choices we were able to investigate the tendencies of the system as it approaches its equilibrium state for various rotating rates. A range of rotation rates, and the resulting inviscid spectra are compared to the results derived above.

The initial spectra are shown in Fig. 5.1. The set I of isotropic ICs , denoted *IC:*

I, is initiated with the energy spectrum

$$E(k) = A\exp((k-8)/0.5)^2, \tag{5.31}$$

where $k = \sqrt{k_h^2 + k_z^2}$ is the isotropic wavenumber. Most of the energy is thus contained in the wave modes, $W_{\boldsymbol{k}}$. The initial energy is peaked around $k_h = 8$ and $k_z = 7$. The constant A is chosen to give a total energy of $E = 0.1$.

The set II of ICs, denoted *IC: II*, is initiated with

$$E_{3D}(\boldsymbol{k} \in W_{\boldsymbol{k}}) = 0.0005B\exp((k-8)/0.5)^2 \text{ and} \tag{5.32}$$

$$E(\boldsymbol{k} \in V_{\boldsymbol{k}}) = (E_{2D} + E_w)(\boldsymbol{k} \in V_{\boldsymbol{k}}) = 0.0995B\exp((k-8)/0.5)^2.$$

B is a normalization constant set so that $E = 0.1$. Most of the initial energy in this configuration is contained in the zero-frequency modes $V_{\boldsymbol{k}}$.

A range of rotation rates was investigated. We only selected to display three key values of Ro. These values are similar to those identified in the three Ro regimes found previous decay simulations (Bourouiba and Bartello, 2007). The Rossby numbers were computed as

$$\mathrm{Ro} = \frac{\sqrt{\langle\omega_z^2\rangle}}{f} \text{ and } \mathrm{Ro}_{2D} = \frac{\sqrt{\langle\bar{\omega}_z^2\rangle}}{f}, \tag{5.33}$$

where $\bar{\omega}_z$ is the vertically averaged vertical component of the vorticity field corresponding to 2D $V_{\boldsymbol{k}}$ Fourier modes (with $k_z = 0$). Ro_{2D} gives a Rossby number specifically for the 2D modes.

The summary of the relevant parameters is displayed in Table 5.1. The simulations with Ro $= 0.01$ initiated with both IC: I and II were particularly difficult to run numerically. Their completion time was about 20 days of CPU time on an AMD Opteron 250, 2390 Mhz.

5.4.1 Conservation and timescale

Figure 5.2 shows the time series of E_{2D} and E_{3D} for three values of Ro $= 0.01, 0.2$ and ∞ and up to dimensional time $\tilde{t} = 100$. The simulations initiated with nearly

Ro	Δt	t_e	ρ	IC: I		IC: II	
				f	Ro_{2D}	f	Ro_{2D}
0.01	2×10^{-4}	800	1×10^{-4}	206.3	0.003	251.7	1×10^{-4}
0.2	2×10^{-4}	100	8×10^{-4}	10.3	0.062	12.6	0.2
∞	1×10^{-3}	100	8×10^{-4}	0	∞	0	∞

Table 5.1: The timestep Δt, the final output time t_e, the Robert filter parameter ρ, the rotation rate $f = 2\Omega$, and the two-dimensional Rossby number Ro_{2D} for each of the selected simulations.

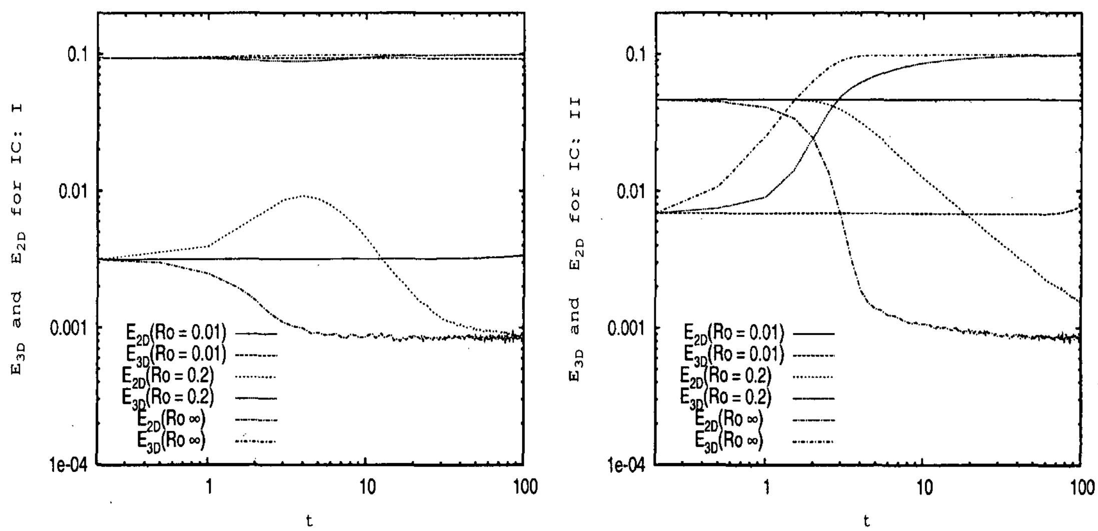

Figure 5.2: Time series of the energy contributions E_{3D} and E_{2D} for Ro $=$ ∞, 0.2, 0.01, initiated with ICs IC: I (left) and IC: II (right). The time-axis is the dimensional time $\tilde{t} = t/f$, where t is the nondimensional time.

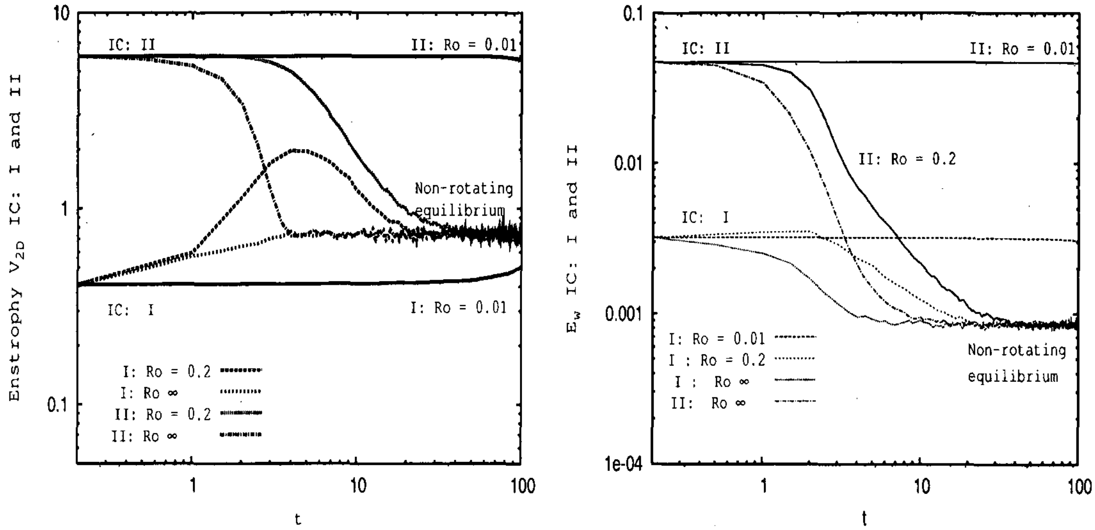

Figure 5.3: Time series of the 2D enstrophy V_{2D} (left) and the energy of the vertical component of the 2D field E_w (right) for Ro $= \infty$, 0.2, 0.01 for both ICs IC: I and II. The time-axis is the dimensional time $\tilde{t} = t/f$, where t is the nondimensional time.

isotropic conditions, IC: I, are displayed on the left. The simulations initiated with most of the energy containing modes in $V_{\boldsymbol{k}}$ are displayed on the right. Figure 5.3 shows the time series of V_{2D} and E_w for three values of Ro $= 0.01, 0.2$ and ∞. The timeseries are also displayed up to the dimensional time $\tilde{t} = 100$ and for both ICs IC: I and IC: II.

The nonrotating simulations for Ro $\rightarrow \infty$ initiated with both ICs, I and II, rapidly relax to a state of equilibrium. This equilibrium corresponds to the classical equipartition of isotropic turbulence (not shown), i.e. to the equipartitioned spectrum of conserved total energy (5.18). The breakdown of the isotropic equipartition reads: $E_{3D} = 0.098$ and $E_{2D} = 0.001$, $E_w = 0.001$ and for the enstrophy, $V_{2D} = 0.7$.

For both ICs , IC: I and II, the Ro $= 0.2$ solution approaches the values of the isotropic nonrotating equilibrium. When initiated with IC: I, E_{2D} and V_{2D} show an initial increase of which reach a maximum at $\tilde{t} = 4$. This corresponds to the nondimensional time $t = 40.2$, after which E_{2D} decreases and approaches the inviscid system's equilibrium. This increase is surprising given that the equilibrium value of E_{2D} is actually lower than the initial value of E_{2D}. A mechanism of transfer from $W_{\boldsymbol{k}}$ to 2D modes is inducing this increase. This is reminiscent of the range of rotation identified in Bourouiba & Bartello (2007), denoted the *intermediate Ro* range. The mechanism responsible for this increase could be attributed to near-resonant interactions since the timescale at which these interactions would be effective would correspond to $t \sim O(1/\mathrm{Ro}^2) = 25$ (Newell, 1969) (dimensional time $\tilde{t} = 2.42$). However, a smaller steady growth of the 2D energy is observable earlier in the simulation and occurs on a short timescale comparable to the linear timescale of the order $\tilde{t} = 1/f = 0.097$ (Ro = 0.2 curve on Fig. 5.2 left). The mechanisms involved in the growth of 2D energy in this regime are still not well understood, however, this is beyond the scope of the present study.

Note also that the increase of E_{2D} is not observable when starting with nearly $2D$ initial conditions, IC: II (Ro = 0.2 curve on Fig. 5.2 right). Another mechanism is acting in this configuration, and is likely related to the destabilization of 2D structures and isotropization of two-dimensional flows. The difference between IC: I and II for the Ro = 0.2 simulations suggest a dependence of the mechanism favouring the energy transfer from 3D to 2D modes on the initial distribution of energy between $W_{\boldsymbol{k}}$ and $V_{\boldsymbol{k}}$.

The focus of this study is the stronger rotation rate, Ro = 0.01. The Ro = 0.01 simulations reveal a new set of quasi-invariants which is coherent with the set S of quantities conserved by the decoupled model (5.10). These are E_{2D}, E_{3D} in Fig. 5.2 and V_{2D}, E_w in Fig. 5.3. They are conserved when starting from both ICs (quasi-2D, IC: II, and quasi-isotropic 3D ICs, IC: I). However, Eq. (5.10) is valid at the first order of the asymptotic development only. We aim to quantify, using the simulations, the time to which the asymptotic expansion is valid and examine the behaviour of the system at long times when the asymptotic development is no longer strictly valid. Thus, we extended the simulations of the smaller Ro started with both ICs

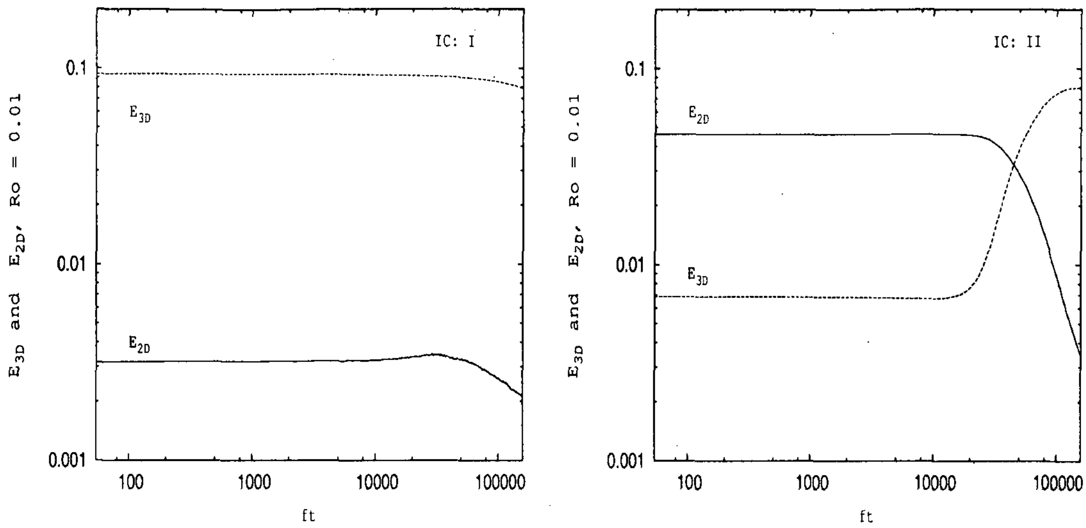

Figure 5.4: Time series of the E_{2D} and E_{3D} for the Ro $= 0.01$ simulation initialized with IC: I (left) and IC: II (right). The time-axis is the nondimensional time $t = f\tilde{t}$, where $\tilde{t}$ is the dimensional time.

(I and II) in order to investigate the timescale on which the invariants S are conserved.

Figure 5.4 shows the timeseries of the extended simulations of Ro $= 0.01$ with IC: I and II. The time has been rescaled to the nondimensional timescale $f\tilde{t}$. We can extract a relevant timescale at which the invariant regime is numerically valid. For both IC: I and II, E_{3D} and E_{2D} are quasiconstant (E_{3D} is conserved at about 85% at the end of the simulations for both IC: I and II due to the discriminating effect of the Robert filter) until a threshold time. This time is of the same order of magnitude for both sets of ICs: $t_\star \approx 20000$. This seems to confirm the asymptotic theories which predict that the decoupling is valid until $t_{\star,theory} \sim O(1/\text{Ro}^2) \approx 10^4$.

Note that the increase of E_{2D} observed for $IC : I$,Ro $= 0.01$ is weak. This is consistent with the fact that the mechanism(s) responsible for the initial increase of 2D energy for $IC : I$,Ro $= 0.2$ is specific to the *intermediate Ro range*.

In this section, we identified the time-range on which the new set of invariants

S critical for Eq. (5.21) are observable numerically. For $t < t_\star$, the quantities S are constant and the theoretical spectra derived are constant and compared to the numerical spectra. For $t > t_\star$, the quantities S are now varying, so one would expect the theoretical spectra based on the existence of the invariants S to no longer be valid. The two questions addressed in the subsequent sections are: how do the theoretical spectra (5.25)-(5.28) compare to those of the numerical solutions on the timer ange of conservation of S ($t < t_\star$), and how do the theoretical spectra compare to the simulation results beyond this time range ($t > t_\star$)?

5.4.2 Horizontal dynamics

We first focus on the horizontal dynamics. The time evolution of the spectra $E_{2D}(k_h)$, $E_w(k_h)$, and $E_{3D}(k_h)$ for both $t < t_\star$ for which the asymptotic first order decoupling is observed to hold, and $t > t_\star$ for which it doesn't. Spectra are displayed in Figs. 5.5 and 5.7. The horizontal spectra $E_{2D}(k_h)$, $\mathrm{E}_w(k_h)$ and $E_{3D}(k_h)$ for simulations initiated with IC: I and IC: II are shown for $t \in [0,\ ft_e]$. For $t < t_\star$, S are conserved and the decoupled description Sec. III B holds. This is the $V_{\boldsymbol{k}}$ decoupled phase. Hence, the theoretical spectra [Eqs. (5.25)-(5.28)] are constant, with those constants being calaculated based on the invariants E_{2D}, E_{3D}, E_w and V_{2D}. The numerical spectra agree with the theory: They quickly relax toward the predicted equilibrium spectra. In particular, for both ICs the numerical spectra display the increase in E_{2D} horizontal large scales consistent with the theoretical predicted spectra, as shown in Fig. 5.5. The horizontal wavenumber characteristic of the 2D energy spectrum is defined as

$$\kappa_{h2D}(t) = \frac{\int_{\boldsymbol{k}\in V_{\boldsymbol{k}}} k_h E_{2D}(k_h, t) dk_h}{\int_{\boldsymbol{k}\in V_{\boldsymbol{k}}} E_{2D}(k_h, t) dk_h}. \tag{5.34}$$

It is used to indicate the direction of the transfer of the energy in classical 2D turbulence, and is called the centroid. We display the time evolution of the centroid, κ_{h2D}, for both IC: I and II in Fig. 5.6.

For $t < t_\star$, the centroid of 2D energy for the simulations initiated with IC: I starts decreasing after initially staying constant. It decreases until $t \approx t_\star$. The decrease of

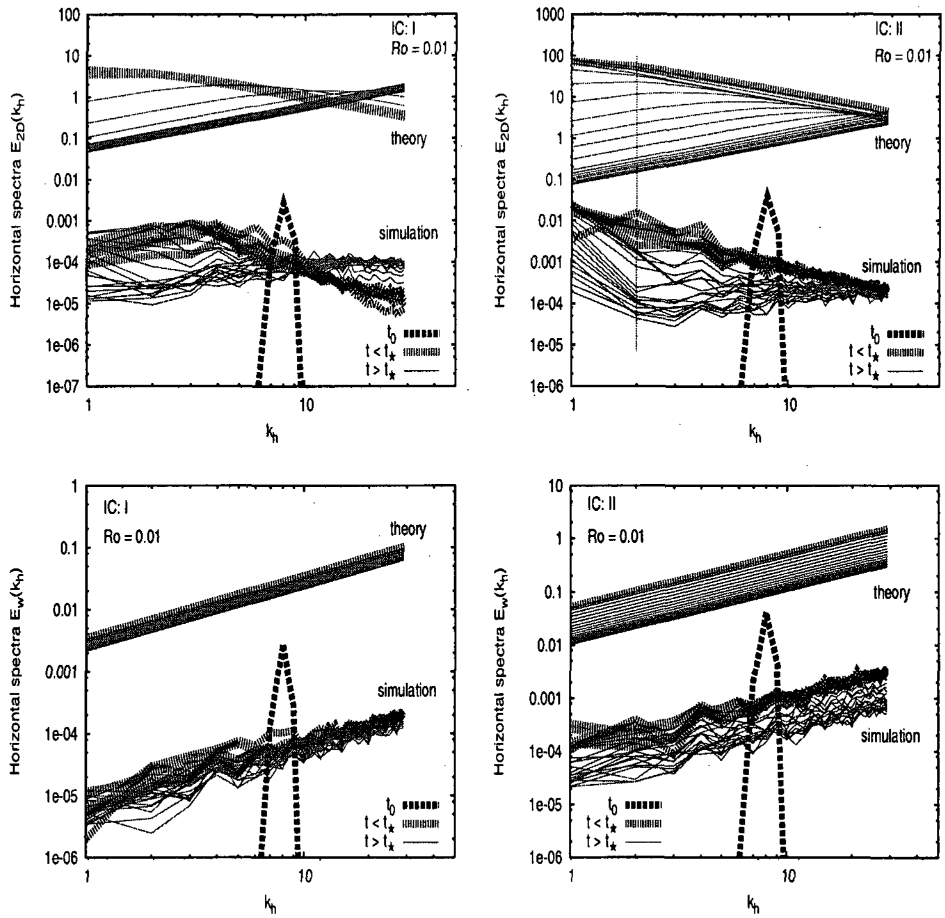

Figure 5.5: Horizontal wavenumber spectra of E_{2D} (upper panels) and E_w (bottom panels) for Ro= 0.01 and for ICs IC: I (left column) and II (right column). The theoretical spectra have been offset for clarity. The initial numerical spectra are denoted t_0, and multiple lines are for different times.

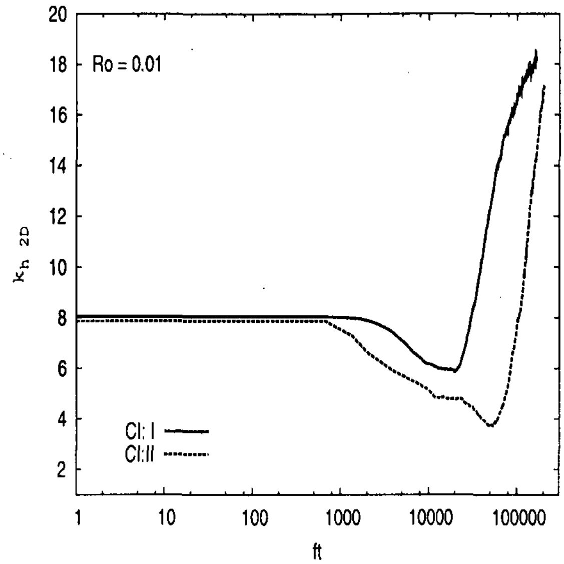

Figure 5.6: Time-series of κ_{h2D} (centroid of 2D energy spectra defined by (5.34)), with nondimensional time $\tau_0 = ft$ and for $Ro = 0.01$. Both simulations started with IC: I and II are shown.

κ_{h2D} corresponds to an upscale transfer of E_{2D} similar to that observed in classical 2D turbulence. When starting with IC: II, the centroid of energy shows a similar dynamics and reaches a plateau at $t \approx t_\star$. However, it decreases again for times $t_\star < t < 5 \times 10^4$ while the total E_{2D} is no longer invariant as in Figs. 5.4 (left). Figs. 5.5 shows that during the decoupled phase $t < t_\star$ and for both IC: I and II the $E_w(k_h)$ theoretical and numerical spectra are in good agreement. They show a horizontal forward cascade of the w energy, consistent with the passive scalar dynamics predicted by Eq. (5.10).

For $t > t_\star$, quantities S are no longer invariants. We consider the instantaneous values of the quantities S—now varying in time—to estimate the theoretical spectra (5.25-5.28). At each time, instantaneous theoretical spectra are obtained via (5.29a-5.29d). The reversal in the slope of $E_{2D}(k_h)$ showing a return to a downscale cascade is captured for both IC: I and II. However, the largest horizontal 2D scales $k_h = 1$ for the IC: II simulations retain more 2D energy compared to the theoretical prediction.

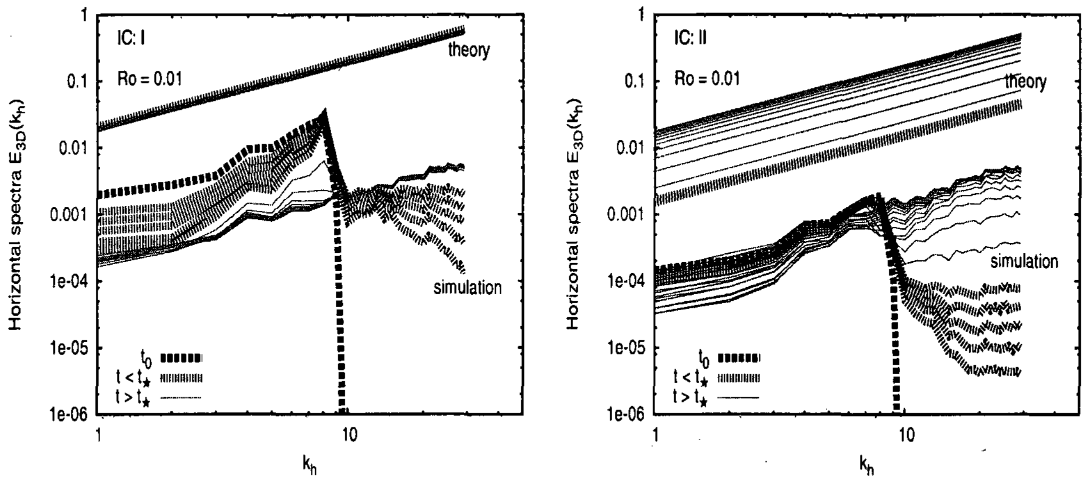

Figure 5.7: Horizontal wavenumber spectra E_{3D} for Ro= 0.01 and for ICs IC: I (left) and II (right). The theoretical spectra have been offset for clarity. The initial numerical spectra are denoted t_0 and the multiple lines are for different times.

For this time period, κ_{h2D} increases, which shows a reversal of dynamics and confirms the downscale 2D energy transfer (Fig. 5.6). For $t > t_\star$, $E_w(k_h)$ has similar dynamics to that of the decoupled phase. It correspond to a forward horizontal energy transfer and an instantaneous equilibrium of equipartition of E_w among w modes.

Finally, concerning $E_{3D}(k_h)$, Figs. 5.7 (left) shows that the theoretical equilibrium horizontal spectra initiated with IC: I vary very little in time. The simulation results for $E_{3D}(k_h)$ show that the 3D horizontal scales appear to lose energy in favour of the smaller horizontal 3D scales. When starting farther from the equipartition equilibrium, (IC: II on Fig. 5.7 right), the theoretical spectra keep the same slope, but increase in amplitude as E_{3D} increases. The numerical spectra show a tendency of $E_{3D}(k_h)$ to relax toward the theoretical equilibrium for both ICs. However, 3D modes reach the theoretical equilibria predicted slower than their V_k counterpart modes. The 3D equilibrium spectra are reached by the simulation for $t > t_\star$.

To summarize, equilibrium statistical mechanics captures the horizontal dynami-

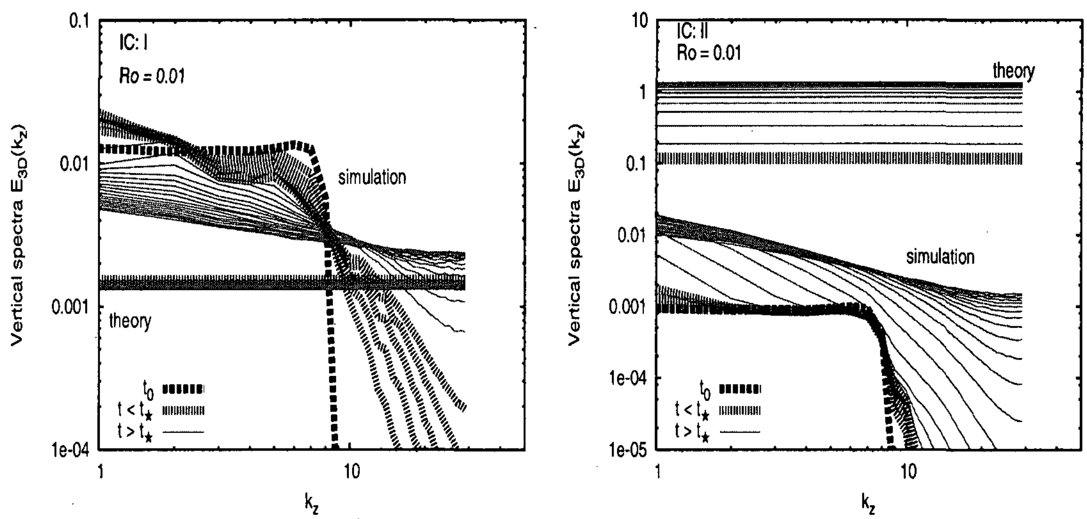

Figure 5.8: Vertical spectra of $W_{\boldsymbol{k}}$ 3D energy, $E_{3D}(k_z)$, for Ro $= 0.01$ simulations initiated with IC: I (left) and IC:II (right). The initial numerical spectra are denoted t_0 and the multiple lines are for different times. The theoretical spectra have been offset for clarity only for the simulation IC: II (left).

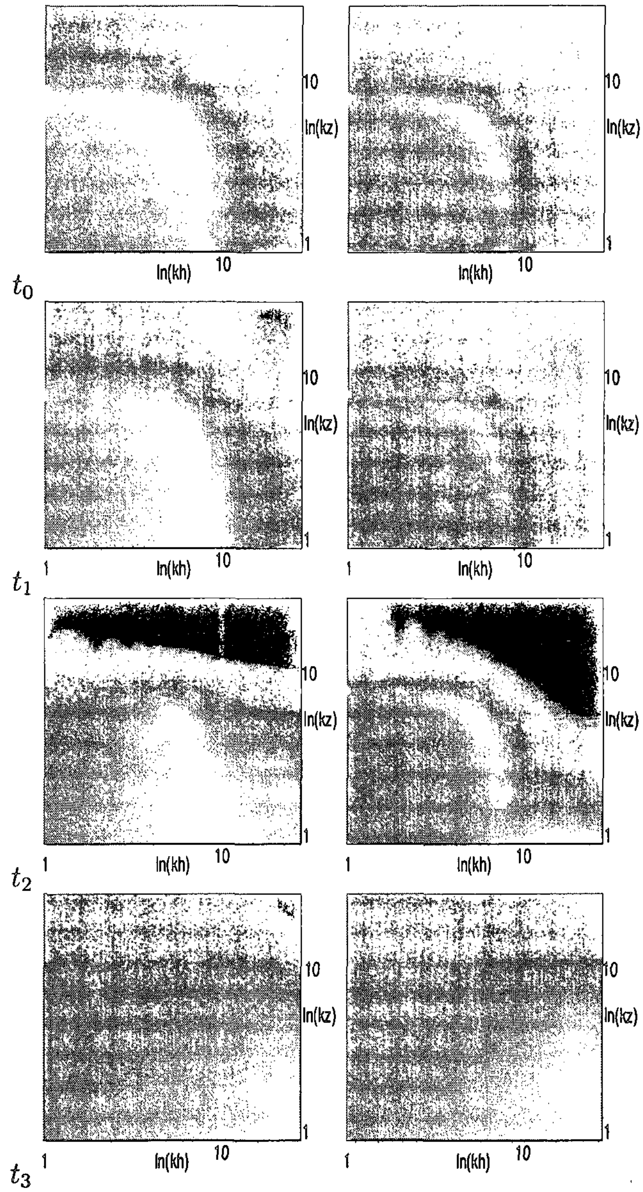

Figure 5.9: Time averaged 3D energy spectrum $e_{3D}(k_h, k_z)$ in log-log scale at: an initial time t_0 (top), an intermediate time-range below t_* such that $t_1 \in [460 \;\; 1.38 \times 10^4]$, an intermediate time $t_2 \in [2.3 \times 10^4 \;\; 4.6 \times 10^4]$, and the end of the simulations with $t_3 \in [1.6 \times 10^5 \;\; 1.8 \times 10^5]$ (bottom panels). Both the t_2 and t_3 time-ranges correspond to times larger than t_*, i.e. beyond the decoupled phase. Ro = 0.01 and the ICs are IC: I (left) and IC: II (right). The colours are normalized for each graph such that the maximum (minimum) value of the modal spectrum is represented by the brightest (darkest) color.

cal tendencies of the V_k and W_k modes accurately for both time-windows $t < t_\star$ (strict validity of the decoupled model) and $t > t_\star$ (set of quantities S vary in time). Thus, when the set of quantities S is varying in time ($t > t_\star$), their variation is slow enough to allow the sub-system of V_k modes to relax to "instantaneous equilibrium" spectra on a short timescale. The horizontal dynamics of the W_k modes for IC: II suggests that the large scale 2D modes are losing energy in favour of the small horizontal scales of W_k modes.

5.4.3 Vertical dynamics and anisotropy

In Figure 5.8, the vertical spectra of the W_k modes, $E_{3D}(k_z)$, are displayed for both ICs. The vertical equipartition of energy is not reached even at the end of the simulation for either initial condition. When starting with near-isotropy as initial condition, IC: I, the 3D energy increases initially in the smallest k_z modes. This shows a transfer of 3D energy to larger vertical scales. Beyond $t_\star$ when the quantities S are determining the instantaneous horizontal short-time spectral equilibrium, the vertical dynamics of W_k seems very different. In both IC: I and II, the vertical downscale transfers are weaker than what is expected by the equipartition Eq. (5.25) for both the $t < t_\star$ and $t > t_\star$ time windows.

Fig. 5.9 shows the 3D energy density spectrum $e_{3D}(k_h, k_z)$ defined by

$$e_{3D}(k_h, k_z) = \frac{|\boldsymbol{u}_{3D}(k_h, k_z)|^2}{Mo(k_h, k_z)}, \tag{5.35}$$

where $Mo(k_h, k_z)$ is the number of modes such that $k_h - 1/2 < k'_h < k_h + 1/2$ and $|k_z| - 1/2 < |k'_z| < |k_z| + 1/2$. This spectrum provides more information about the anisotropy noted above. Note that an equipartition of 3D energy corresponds to a flat $k_h - k_z$ spectrum. The initial isotropic distribution of energy corresponding to IC: I and II is shown by a $e_{3D}(k_h, k_z, t_0)$ spectrum in the top panels of Fig. 5.9. Note that only the intensity of energy contained in the 3D modes changes from IC: I to IC: II (see Eqs. (5.31) and (5.32)), but the distribution of the energetic W_k modes does not change.

In the initial phase of decoupling ($t < t_\star$), the 3D energy spectrum does not vary much for either initial condition. However, a slight preferential redistribution of energy occurs in favour of the energy-containing modes with smaller frequencies (small k_z/k in Fig. 5.9), especially for IC: I (see region below the $k_h = k_z$ diagonal). This is not surprising given the tendency of the resonant $33 \rightarrow 3$ interactions to transfer $3D$ energy toward $W_{\boldsymbol{k}}$ modes of smaller frequency $\omega_{\boldsymbol{k}}$ (Waleffe, 1993). Recall that the resonant interactions in Eq. (5.10) are assumed to be predominant in the decoupled regime of time $t < t_\star$. Our observation is consistent with the theoretical analysis of Galtier (2003) in which an anisotropic decomposition of wave numbers in $k_h - k_z$ confirmed theoretically the tendency of the resonant interactions to develop and maintain anisotropy.

For $t > t_\star$, however, it is expected that nonresonant interactions are active. We can see in Fig. 5.9 that the apparent transfer of 3D energy to the larger vertical 3D scales (observable in the vertical spectra, see Fig. 5.8) still acts to preferentially concentrate energy in the large vertical scale (small k_z) and small horizontal scale (large k_h) $W_{\boldsymbol{k}}$ modes (bottom right corners in Fig. 5.9). This is particularly true toward the end of both simulations IC: I and II (bottom panels of Fig. 5.9).

When looking at the set of quasi-2D ICs IC: II, we note that the preferential region of transfer of energy from the $V_{\boldsymbol{k}}$ 2D modes to the $W_{\boldsymbol{k}}$ 3D modes is in favour of the small horizontal and large vertical scales. At the end of both simulations the equipartition is not reached (here we are referring to the equipartition expected to be reached when $\mathrm{Ro} \rightarrow \infty$, i.e. flat spectrum) and if the process of redistribution toward equipartition is occurring it seems to be much reduced by the effect of rotation, even in the coupled stage (involving interactions that are not resonant).

The vertical dynamics of the $W_{\boldsymbol{k}}$ wave modes suggest that energy is preferentially transferred to the region of low frequency (large k_h and small k_z) modes, when a significant 3D energy is present initially (i.e. IC: I). When starting with a dominant

2D energy, the energy transfers from 2D to 3D modes is done locally frequencywise, leading to a transfer in favour of the low wave frequencies (large k_h and small k_z) in the figure. This anisotropy in favour of the small frequency spectral region is very long lasting and coincides with an inhibition of the 3D energy transfers toward small vertical small horizontal scales (top right corner in Fig. 5.9) during both the decoupled and coupled stages ($t < t_\star$ and $t > t_\star$).

5.5 Discussion

The main purpose of this study has been to examine the dynamics of the *small Ro* range. This is the third of three rotating ranges previously identified: weakly, intermediate and strongly rotating (Bourouiba and Bartello, 2007). In the small Ro limit several dynamics were discussed in the literature. On the one hand some theoretical results predict a decoupling of the wave from the zero-frequency modes. These results include the analysis of Babin et al. (1996, 1998), the studies of weakly resonant waves (Waleffe, 1993), and the wave-turbulence approach used by Galtier (2003). However, note that theoretical results of the wave-turbulence approach are not valid in the small k_z, and the large k_h spectral domain. On the other hand extended wave turbulence results by Cambon et al. (2004a) suggested that such decoupling cannot be reached due to coupling terms remaining active even in the Ro $\rightarrow$ 0 limit.

Our focus has been to investigate the inviscid dynamics of a strongly rotating spectrally truncated turbulent flow, starting with the analysis of the statistical equilibrium of a model of flow in which zero-frequency and wave modes are decoupled. Our tool of study was equilibrium statistical mechanics. For comparison, we also examined numerically the effect of rotation on the equilibrium of an inviscid unforced truncated rotating turbulent system for different ICs and for moderate to strong rotation rates.

We started by deriving the theoretical spectra for the decoupled wave and zero-frequency modes. This was complemented by a numerical study of the inviscid dynamics which showed two phases: a first decoupled phase for $t < t_\star$, and a coupled phase for $t > t_\star$. Thus, the prediction of decoupling of the wave and zero-frequency modes in the asymptotic limit of $\mathrm{Ro} \to 0$ is valid and observable numerically. For both coupled and decoupled time phases, we find a reduction of the vertical energy transfers to small vertical scales.

During the decoupled time phase ($t < t_\star$) the new set of invariants characteristic of the theoretical model of decoupled equations are found to be in agreement with the numerical simulation of the full truncated inviscid equations. The time until which the decoupling is observable is found to be $t_\star \sim 2/\mathrm{Ro}^2$, which is consistent with the weakly nonlinear resonant wave theory prediction. This evaluation is robust to the change of ICs from 2D to 3D initial flows. The theoretical spectra derived from statistical equilibrium assumptions captured the horizontal dynamics of the decoupled system accurately. We observed an upscale horizontal transfer of the 2D energy and a forward horizontal transfer of 3D and w energies. This dynamics is in agreement with the "global splitting" result by Babin *et al.* (1996), predicting a decoupling of the 2D and w modes from the 3D modes, an inverse cascade of 2D energy, a direct cascade of 3D energy and a passive scalar dynamics for the w modes.
The equilibrium statistical mechanics spectra predicted a vertical equipartition of the 3D energy, however we observe a preferential concentration of wave energy in the smaller frequency wave modes. This preferential concentration is not consistent with the vertical dynamics of the decoupled model of Babin et al. (1998). In fact, they predict a "freezing" of the vertical 3D energy transfers. On the other hand, weak wave theories predict that triple inertial wave resonant interactions transfer energy to smaller frequency modes (excluding the zero-frequency modes) (Waleffe, 1993). The anisotropy was also found to be consistent with the spectral predictions of wave-turbulence kinetic energy equations built on the resonant inertial wave interactions (Galtier, 2003). The numerical results obtained by Bellet *et al.* (2006) simulating inertial wave resonant interactions only between nonzero frequency modes showed a

tendency of the 3D wave modes to concentrate the energy in the lower frequency modes. However, these wave-turbulence results are valid in a restricted spectral domain not including the zero-frequency modes. Hence, the advantage of the inviscid simulations presented here is that they confirm the development of anisotropy in the decoupled system of modes containing all the modes (both the zero-frequency and the 3D modes). Finally, another conserved quantity is necessary in order to improve the prediction of the decoupled vertical dynamics. Accounting for the influence of the conservation of the wave mode's helicity or the conservation of energy by triple resonant wave mode interactions could also help improve the wave equilibrium statistical mechanics spectra derived.

In the coupled phase ($t > t_\star$), the set of invariants corresponding to the decoupled equations are no longer conserved quantities. However, the simulations show that their variation timescale is long enough to consider them quasi-invariants on the short timescale. The corresponding time-varying theoretical horizontal spectra are in agreement with the instantaneous numerical spectra, accurately capturing the instantaneous horizontal dynamics of the now-coupled wave and zero-frequency modes. Hence, the set of slowly varying "invariants" still plays a constraining role on the short-time dynamics. This is reminiscent of the example of the inviscid stratified truncated Boussinesq equations which have constraining quasi-invariants on the short-time dynamics of the slow modes (Waite and Bartello, 2004).

The large horizontal scales of the zero-frequency modes lose energy to the now coupled wave modes. After an initial upscale horizontal transfer taking place during the decoupled phase, the transfer of 2D energy starts to favour the 2D small horizontal scales. In this coupled phase, the vertical anisotropy observed in the decoupled phase persists. In fact, the wave energy remains predominantly contained in the large vertical and small horizontal scales.

Finally, in the coupled phase, an initially 3D flow led to a transient increase of E_{2D}. The 2D energy reaches its statistical equilibrium after a phase of increase and then decrease with time. The initial growth is not observed for either initial condition. When the initial condition is 2D, the growth is not observed, suggesting that the mechanism leading to the transient growth 2D energy depends on the initial ratio of energy between W_k and V_k. The rate of this 2D energy increase varies with Ro. It is stronger for a flow with Ro ≈ 0.2 compared to the flow with Ro $= 0.01$. The energy transfer from 3D to 2D causing the increase of 2D energy is reminiscent of the *intermediate Ro* range identified in the decaying simulations of Bourouiba & Bartello (2007). The mechanisms responsible for this increase could be attributed to near-resonance. In fact, the forced simulations of Smith and Lee (2005) suggested that near-resonant interactions were responsible for the 3D to 2D transfers at the moderately small Ro that they examined. If that were the case, we would expect the timescale on which near-resonant interactions act to correspond to $t \sim O(1/\mathrm{Ro}^2)$ (Newell, 1969). However, we observe that the steady growth of 2D energy occurs earlier in the Ro $= 0.2$ simulation. It starts at a time comparable to the linear timescale of rotation of the order of $1/f$. This timescale suggests that the mechanism responsible for the transient 2D energy increase could also be initiated by linear effects. In fact, linear effects were proposed as an explanation to the increase of 2D energy in an inhomogeneous rotating flow (Davidson et al., 2006). Finally, much more understanding is needed to explain the mechanisms occurring beyond the decoupled phase ($t > t_\star$). In the small Ro limit, where a clear coupling phase follows the decoupling phase, this mechanism remains weaker than that observed in the coupled phase of flows with larger Ro. What the present inviscid simulations suggest is a confirmation of the existence of the a mechanism depending nonmonotonically on Ro, inherent to the rotating flow dynamics in the coupled phase, and which is at the origin of the intermediate Ro regime observed in decaying rotating flows.

APPENDIX: Normal modes

The linearization of the rotating barotropic vorticity equations around a rest basestate give

$$\frac{\partial \boldsymbol{\omega}}{\partial t} = (f\hat{\mathbf{z}} \cdot \nabla)\boldsymbol{u}, \tag{5.36}$$

with $\boldsymbol{\omega} = (\omega_x, \omega_y, \omega_z)$ the vorticity vector, $\boldsymbol{u} = (u, v, w)$ is the velocity vector. Its transformation to Fourier-space leads to

$$\frac{\partial}{\partial t}\mathbf{W}_{\boldsymbol{k}} = M_{\boldsymbol{k}}\mathbf{W}_{\boldsymbol{k}}, \tag{5.37}$$

with

$$\mathbf{W}_{\boldsymbol{k}} = \begin{pmatrix} \hat{\omega}_x \\ \hat{\omega}_y \\ \hat{\omega}_z \end{pmatrix}, \quad M_{\boldsymbol{k}} = \begin{pmatrix} 0 & -ifk_z^2/k^2 & +ifk_zk_y/k^2 \\ +ifk_z^2/k^2 & 0 & -ik_zk_x/k^2 \\ -ifk_zk_y/k^2 & +ifk_zk_x/k^2 & 0 \end{pmatrix}, \tag{5.38}$$

where

$$\begin{pmatrix} \omega_x \\ \omega_y \\ \omega_z \end{pmatrix}(x, y, z, t) = \Sigma_{\boldsymbol{k}} \begin{pmatrix} \hat{\omega}_x \\ \hat{\omega}_y \\ \hat{\omega}_z \end{pmatrix} \exp(i\boldsymbol{k} \cdot \mathbf{r}), \tag{5.39}$$

with $\mathbf{r}$ being the position vector (x, y, z), and $i^2 = -1$. If we restrict ourselves to fluids in a periodic domain of size $L \times L \times L$, we have: $\boldsymbol{k} = (k_x, k_y, k_z) = (m_x, m_y, m_z)2\pi/L$, with $(m_x, m_y, m_z) \in Z^3$, the set of integers.

The diagonalization of this system leads to the eigenvalues

$$\lambda_s = sfk_z/k \quad \text{and} \quad \lambda_0 = 0, \tag{5.40}$$

with $s = \pm$. The associated eigenvectors are

$$\boldsymbol{n}_{\lambda_s} = \boldsymbol{n}_s = \begin{pmatrix} -k_xk_z/k_h^2 + isk_yk/k_h^2 \\ -k_yk_z/k_h^2 - isk_xk/k_h^2 \\ 1 \end{pmatrix}, \quad \boldsymbol{n}_{\lambda_0} = \boldsymbol{k} = \begin{pmatrix} k_x \\ k_y \\ k_z \end{pmatrix}. \tag{5.41}$$

The horizontal wavevector is $k_h = \sqrt{k_x^2 + k_y^2}$. The derivation of the eigenvectors requires that $k_z \neq 0$ and $k_h \neq 0$. From (5.41) we see that $\boldsymbol{n}_s$ and $\boldsymbol{n}_{-s}$ are complex conjugates and that $(\boldsymbol{k}, \boldsymbol{n}_s, \boldsymbol{n}_{-s})$ forms an orthogonal basis, $\boldsymbol{n}_s^* = \boldsymbol{n}_{-s}$ and $\boldsymbol{k} \cdot \boldsymbol{n}_s^* = \boldsymbol{k} \cdot \boldsymbol{n}_{-s}^* = \boldsymbol{n}_s \cdot \boldsymbol{n}_{-s}^* = 0$ (* is used for complex conjugate). It is easy from (5.41) to show that $\boldsymbol{n}_s(-\boldsymbol{k}) = \boldsymbol{n}_{-s}(\boldsymbol{k})$ and that $|\boldsymbol{n}_s| = 2$.

Due to the continuity equation, $\boldsymbol{\nabla} \cdot \boldsymbol{u} = 0$, the decomposition of the velocity field leads to components only on $(\boldsymbol{n}_+, \boldsymbol{n}_-)$, a zero-component on $\boldsymbol{k}$. This gives a decomposition of the implicitly nondivergent velocity field

$$\boldsymbol{u}(\boldsymbol{r}) = \sum_{\boldsymbol{k}} \boldsymbol{u}(\boldsymbol{k}) \exp(i\boldsymbol{k} \cdot \boldsymbol{r}) = \sum_{\boldsymbol{k}} (A_+(\boldsymbol{k}, t)\boldsymbol{n}_+(\boldsymbol{k}) + A_-(\boldsymbol{k}, t)\boldsymbol{n}_-(\boldsymbol{k})) \exp(i\boldsymbol{k} \cdot \boldsymbol{r}), \quad (5.42)$$

with $A_s(\boldsymbol{k}, t) = a_s(\boldsymbol{k}) \exp(i\lambda_s t)$. The reality condition ($\boldsymbol{u}(\boldsymbol{r})$ must be real) implies that $\boldsymbol{u}^*(\boldsymbol{k}) = \boldsymbol{u}(-\boldsymbol{k})$. Thus, the Fourier components $a_s(\boldsymbol{k})$ satisfy $a_s^*(\boldsymbol{k}) = a_s(-\boldsymbol{k})$.

The decomposition of the flow field into these *inertial waves* (5.42) corresponds to the *helical mode* decomposition (Greenspan, 1968; Waleffe, 1992). Equivalent decompositions include the Craya-Herring decomposition (Craya, 1958; Herring, 1974) and the Poloidal-toroidal decomposition (Bellet et al., 2006; Waleffe, 1992).

Chapter 6

Forced flow

In the previous chapters, we identified three rotating ranges, then examined more closely the role played by resonant and near-resonant interactions when considering discrete modes. We also examined the small Rossby number range and decoupling theories in this regime. We now turn the focus to the *intermediate Ro range* in forced turbulence. We first show that the three regime separation prevails in forced turbulence, and that this is true for various 3D forcing scales and configurations. The rate of energy transfer from the 3D to the 2D modes peaks around $Ro \approx 0.2$ whether the forcing is in the small or large horizontal length scales. The dynamics of the two-dimensional modes in the intermediate regime shows a slope of -3 or steeper, which is consistent with previous forced simulations of rotating turbulence despite the use of different forcing schemes. This shows the robustness of this steep slope, but does not explain its origin.

When the emergence of two-dimensional structures was observed in previous forced simulations, it was conjectured that their dynamics were not consistent with the classical two-dimensional turbulence phenomenology predicting a $k^{-5/3}$ spectrum for scales larger than that of the forcing and k^{-3} for scales smaller than the forcing scale. We examine these conjectures by focusing on the two-dimensional dynamics using various forcing configurations and resolutions. We find that the dominant transfers from the 3D to the 2D modes are nonlocal and that this is true for all forcing schemes used. This nonlocality is found to be robust to an extension of the inertial range via an increase of resolution. In fact, the dominant 3D to 2D transfers are those involving two 3D modes of medium-to-small horizontal scales and a 2D mode of large horizontal scale. We show that after the early-time dynamics, the steep ≈ -3 slope of the 2D energy spectrum corresponds to a direct downscale 2D enstrophy transfer. This finding suggests that the two-dimensional dynamics emerging from rotating forced simulations is close to that of classical purely two-dimensional turbulence and that the former could possibly be modeled by the latter.

In the intermediate *Ro* range, the rate of 3D to 2D transfer reaches a quasi-stationarity; however, the 2D energy continues to increase. The latter is no surprise given that no large-scale dissipation is used. However, this accumulation of 2D energy in the larger scales of the domain poses a question. Is this accumulation of 2D energy in the intermediate *Ro* regime of rotating turbulence ultimately leading to an asymptotic state of condensation similar to that observed in recent numerical simulations of forced two-dimensional turbulence? Condensation DNS studies of two-dimensional turbulence show a transition of the spectrum slope from $-5/3$ to -3 or greater in the larger scales as the condensate formed. Alternatively, could this accumulation of 2D energy in the larger horizontal scales ultimately be stalled when the 2D energy reaches a saturation level?

This chapter is a manuscript in preparation for submission.

Two-dimensionalization and nonlocal interactions of the intermediate Rossby number range in forced rotating turbulence

Abstract

We investigate whether a three regime separation identified in homogeneous decaying rotating turbulence by Bourouiba and Bartello (2007) is also present in forced rotating turbulence. Using several forcing schemes and resolutions exciting only the 3D wave modes we recover the three regime separation consistently as the forcing scheme and resolutions are changed. We then focus on the *intermediate Ro range* which is characterized by a maximum transfer of the injected energy from the 3D to the 2D modes. This peaks at Ro ≈ 0.2 and gives a 2D energy spectrum slope of -3 or steeper. This is consistent with previous studies of forced rotating turbulence that used forcing schemes different from our own. We investigate the detailed transfers responsible for the 3D to 2D energy transfers and whether or not they are local or nonlocal in scale. We find that the dominant interactions are nonlocal in spectral space, and that the scales of the k_h^{-3} part of the spectrum do not correspond to an inverse 2D energy cascade as one could expect when assuming locality of the spectral transfers, but rather to a range of downscale 2D enstrophy transfer to the dissipation scales. Finally, we examine whether a saturation or condensation of the 2D energy is the long-time state of the turbulence in the intermediate Ro regime and in the absence of large-scale dissipation. We find a long-time dynamics similar to that of condensation observed in classical forced two-dimensional turbulent flows.

6.1 Introduction

The Rossby number, $\mathrm{Ro} = U/L2\Omega$, is the nondimensional number characterizing rotating flows. Here U is the characteristic velocity, L the characteristic length scale, and 2Ω is the Coriolis parameter. When $\mathrm{Ro} \to 0$ the nonlinearity of the equations of motion becomes weak, and the theories of weak wave interactions apply. Rotating turbulent flows have been observed to generate large-scale two-dimensional columnar structures in initially isotropic turbulence in experiments (e.g. McEwan, 1976; Baroud et al., 2002) and numerical simulations of both forced (e.g. Yeung and Zhou, 1998; Smith and Waleffe, 1999; Chen et al., 2005) and decaying turbulence (e.g. Bardina et al., 1985; Bartello et al., 1994). In forced turbulence, Smith and Lee (2005) showed that the near-resonant interactions between inertial wave modes are the main interactions responsible for the generation of the columnar 2D structures. Decaying turbulence simulations of Bourouiba and Bartello (2007) showed that this generation was dependent on the Rossby number and showed the existence of three regimes: 1) the *weakly* rotating Ro regime, for which the turbulent flow is essentially unaffected by rotation; 2) the *intermediate* Ro range, characterized by a strong transfer of energy from the wave to the 2D modes, with a peak at $\mathrm{Ro} \sim 0.2$; and 3) the *small* or asymptotic Ro range for which the zero-frequency modes receive less and less energy from the wave modes as $\mathrm{Ro} \to 0$.

In this study we examine and compare various types of flows using direct numerical simulations in triply periodic domains. We vary the scale and type of forcing. First, we investigate whether a regime separation similar to that identified in decaying turbulence is present when observing forced turbulence. We find that the rotating regime separation identified in Bourouiba and Bartello (2007) is also present for forced turbulent flows, and that this is robust to the change of forcing schemes and resolution.

In most classical turbulence theories, a locality of the interactions between scales of the flow is assumed. For a rotating three-dimensional flow in the intermediate Ro range forced at scales of the order of l_f, most of the 2D energy increase is due to the 3D to 2D energy transfers, denoted 3D-to-2D hereafter. When assuming locality of the nonlinear interactions, the 3D-to-2D transfers are expected to inject energy in 2D horizontal scales around l_f. If one assumes that the 2D modes forced by the 3D-to-2D transfers follow a similar phenomenology to that of classical two-dimensional turbulence, then: 1) the scales smaller than the forcing scale l_f would lead to the Kraichnan -3 scaling for direct enstrophy cascade; 2) the scales larger than the forcing scale l_f would lead to the Kolmogorov $-5/3$ scaling for the inverse 2D energy cascade. However, these expected scalings have not been observed in previous forced simulations of rotating turbulence. Instead, in forced rotating turbulence studies, where both the 2D and the 3D modes were forced at the same scales (e.g. Smith and Waleffe, 1999; Chen et al., 2005), show a -3 slope for the 2D modes for scales *larger* than the forcing scale. This led to the conclusion that the -3 scaling of the 2D modes of forced rotating three-dimensional flows is distinct from the scaling of classical two-dimensional turbulence.

Scaling theories are difficult to formulate for rotating turbulence due to the lack of understanding of the elementary processes contributing to the energy transfers, particularly between the 3D and 2D modes. In order to clarify this discussion for the intermediate Ro regime, we investigate the nonlocal or local nature of the dominant interactions, with a particular focus on the interactions between the 2D and the 3D modes. We find that nonlocal energy transfers between 3D and 2D modes dominate the nonlinear interactions. We find these nonlocal interactions to directly inject 3D energy to medium-to-large horizontal 2D scales.

With these new results in mind, we revisit and discuss how the preferred scales of interaction explain the -3 slope for the 2D energy spectrum observed in forced rotating turbulence. In fact, this slope is found to coincide with a direct transfer of 2D enstrophy to the dissipative scales. We examine the effect of the resolution, and thus the scale separation in the selection of the dominant interacting scales.

Finally, given that the intermediate Ro range is characterized by an accumulation of the 2D energy in the larger scales of the domain, we examine whether saturation or condensation of the 2D energy occurs in the long-time asymptotic state of this regime. The question is whether or not a saturation of the growth of the 2D energy in the large scales would ultimately stop the growth of 2D energy. In non-rotating flows, 2D turbulence is known to be unstable to 3D perturbations, and the instability serves to damp the 2D flow (e.g. Ngan et al., 2004). In the case of rotating flows, does a similar mechanism of destabilization in which large 2D modes transfer energy to large horizontal and small vertical scales occur and stall the growth of the 2D energy? Or, is the observed pile-up of energy in the larger scales a similar phenomenon to that observed in studies of classical two-dimensional turbulence in finite size domains (e.g. Chertkov et al., 2007; Smith and Yakhot, 1993)?

In §6.2 the equations of rotating incompressible flows and the notation is introduced. In §6.3 the numerical experiments and details are provided. The existence of the intermediate Ro range in forced turbulence is discussed in §6.4. In §6.5 detailed interactions and nonlocality are discussed. The two-dimensional spectral dynamics and the long-time state of the two-dimensional energy in the larger scales of the domain are discussed in §6.6. We conclude in §6.7.

6.2 Governing equations and notation

The nondimensional incompressible equations of motion in a rotating frame are

$$\frac{\partial \boldsymbol{u}}{\partial t} + \mathrm{Ro}\,(\boldsymbol{u}\cdot\nabla)\boldsymbol{u} + \hat{\mathbf{z}}\times\boldsymbol{u} = -\nabla \mathrm{p} + \mathbf{F}(\boldsymbol{u}) + \mathbf{D}(\boldsymbol{u}), \qquad \nabla\cdot\boldsymbol{u} = \mathbf{0}, \qquad (6.1)$$

where $\boldsymbol{u} = u\hat{\mathbf{x}} + v\hat{\mathbf{y}} + w\hat{\mathbf{z}}$, p is the pressure, $\mathbf{F}$ is the forcing, and $\mathbf{D}$ is the dissipation. Recall that $\mathrm{Ro} = U/Lf$ is the Rossby number, with $f = 2\Omega$. Without loss of generality, we choose the rotating vector to be aligned with the vertical direction of unit vector $\hat{\mathbf{z}}$. When $\mathrm{Ro} = 0$ in (6.1), the equation is linear and admits inertial wave solutions. The inertial waves have the same structure as the helical modes. Helical modes are the normal modes of the curl operator (Waleffe, 1992). When using the helical mode decomposition, the Fourier-transformed equations of motion read

$$\left(\frac{\partial}{\partial t} + i\omega_{s_k}\right) A_{s_k} = \mathrm{Ro} \sum_{k+p+q=0} C_{kpq}^{s_k s_p s_q} A_{s_p}^* A_{s_q}^* + \hat{F}_k + \hat{D}_k, \tag{6.2}$$

where A_{s_k} are the normal mode amplitudes of wavector $\boldsymbol{k}$, $()^*$ stands for complex conjugate, and $C_{kpq}^{s_k s_p s_q}$ are the interaction coefficients between the triads of modes $(\boldsymbol{k}, \boldsymbol{p}, \boldsymbol{q})$. The linear inertial frequencies are $\omega_{s_k} = s_k k_z/|\boldsymbol{k}|$,with $s_k = \pm$. The zero-frequency modes are the Fourier modes with $k_z = 0$. They correspond to a vertically-averaged real-space velocity field.

We classify the modes into two groups. Wave modes, which have nonzero frequency and correspond to $k_z \neq 0$ in Fourier-space. They are denoted 3D

$$\text{If } \boldsymbol{k} \in W_k = \{\boldsymbol{k} | k \neq 0 \text{ and } k_z \neq 0\} \text{ then } \boldsymbol{u}(\boldsymbol{k}) = \boldsymbol{u}_{3D}(\boldsymbol{k}), \tag{6.2}$$

and the zero-frequency modes, denoted 2D and w

$$\text{If } \boldsymbol{k} \in V_k = \{\boldsymbol{k} | k \neq 0 \text{ and } k_z = 0\} \text{ then } \boldsymbol{u}(\boldsymbol{k}) = \boldsymbol{u}_{2D}(\boldsymbol{k}_h) + w(\boldsymbol{k}_h)\ \hat{\mathbf{z}}, \tag{6.3}$$

where $k_h = \sqrt{k_x^2 + k_y^2}$ is the horizontal wavenumber. Using this decomposition, the total energy and total energy spectrum can be decomposed into three contributions: $E = E_{2D} + E_w + E_{3D}$, with associated spectra $E_{2D} = \frac{1}{2} \sum_{k \in V_k} |\mathbf{u}_{2D}(\boldsymbol{k})|^2$, $E_w = \frac{1}{2} \sum_{k \in V_k} |w(\boldsymbol{k})|^2$, and $E_{3D} = \frac{1}{2} \sum_{k \in W_k} |\mathbf{u}(\boldsymbol{k})|^2$.

6.3 Numerical and forcing approaches

The equations are solved using a pseudo-spectral method. The integration domain is triply periodic of length 2π. For comparison, the results were obtained in domains with 64, 128 and 200 grid points in each direction and the de-aliased (Boyd, 1989) spectral domain was cylindrically truncated at k_h, $k_z = 21, 42$ and 66. In what follows, we will display only results obtained with the latter two resolutions. We used a leapfrog time differencing and the Asselin-Robert filter in order to control the computational mode (Asselin, 1972), with the highest value of the filter being

$\rho = 0.035$. We used an eighth order cylindrical hyperviscosity to increase the inertial range. The viscosity operator is of the form $D(\boldsymbol{u}) = -\nu(\nabla_h^{2p} + \frac{\partial^{2p}}{\partial z^{2p}})\boldsymbol{u}$, with $p = 8$, and the viscosity coefficient ν is given in subsequent sections for each set of simulations. All simulations are initiated with seed energy of ≈ 0.01, with a random phase and a spectrum peaked around the modes that are forced (which vary from one forcing scheme to another).

We focus on the transfers between the 2D and 3D modes. Thus, contrary to previous numerical studies of forced rotating turbulence, we force the $W_{\boldsymbol{k}}$ (6.2)modes only. That is,

$$\frac{\partial \mathrm{E}_{3\mathrm{D}}}{\partial t}(\boldsymbol{k} \in W_{\boldsymbol{k}}, t) = (T_{3D} + F - D_{3D})(\boldsymbol{k} \in W_{\boldsymbol{k}}, t), \tag{6.4}$$

where T_{3D} is the total Fourier-space transfer contributing to the 3D energy equations, and F is the 3D energy input at each timestep. The forcing function in the ith component of the velocity field equation is

$$f_i(\boldsymbol{k}, t) = \epsilon(\boldsymbol{k})/u_i^*(\boldsymbol{k}, t), \tag{6.5}$$

with $u_i^*(\boldsymbol{k}, t)$ the complex conjugate of the Fourier component i of the velocity vector. The energy input, $F = 3\sum_{\boldsymbol{k}} \epsilon(\boldsymbol{k})$, is constant for all the forcing schemes, but different sets of modes are forced. For the set of simulations carried out we performed several types of forcing of the modes $W_{\boldsymbol{k}}$.

Table 6.1 gives detailed descriptions of the four forcing types presented and denoted F1, F2, F3 and F4. They differ by the form of $\epsilon(\boldsymbol{k})$ used in (6.5). Each forcing is designed to excite a specific range of scales and frequencies of interest. Forcings F1 and F2 are used in §6.4. F1 excites small horizontal scales and all vertical scales and F2 excites large horizontal scales and small vertical scales. F3 is similar to F1, but used in a higher resolution simulation. The comparison between F1 and F3 allows us to test the influence of the scale separation between the horizontal forced scales and the larger horizontal scales of the domain. Finally, F4 is used to force the large horizontal 3D scales for a resolution of 200^3. This latter forcing scheme is discussed

Forcing type	$\epsilon(\boldsymbol{k})$	k_h	k_z	Resolution
F1	$a_1(28-k_h)(k_h-26)$	[26 28]	$\neq 0$	128^3
F2	$a_2(28-k_z)(k_z-32)/k_h^2$		[28 32]	128^3
F3	$a_3(42-k_h)(k_h-39)$	[39 42]	$\neq 0$	200^3
F4	$a_4(5-k_h)(k_h-2)/k_h^2$	[2 5]	$\neq 0$	200^3

Table 6.1: Types of forcing used. The total input in (6.4) at each time step is constant. The amplitudes a_j with j = 1,2,3,4 are varied to obtain different levels of forcing, F. The values of the a_j in each simulation are given with additional detail in subsequent sections

in more detail in §6.6 when discussing the condensation versus saturation issue for the large 2D scales.

6.4 Intermediate Ro regime in forced turbulence

In this section we present two sets of simulations forced with F1 and F2. The rotation rate is fixed at $f = 2\Omega = 22.6$. In each of the two sets, the value of the forcing, F, is varied from one simulation to the next so that a total of 14 Rossby numbers between ≈ 1.5 and $\approx 8 \times 10^{-2}$ are covered. Unless otherwise indicated, the Rossby number, Ro, is calculated based on the the vertical component of the entire vorticity field $\boldsymbol{\omega} = \nabla \times \boldsymbol{u}$,

$$\mathrm{Ro} = \sqrt{[\omega_z^2]}/(2\Omega). \tag{6.6}$$

Similarly, unless otherwise indicated, the 2D Rossby number, denoted Ro_{2D}, is obtained using the vertical component of the vorticity field restricted to the $V_{\boldsymbol{k}}$ modes only. The level of forcing injected at each time step, Ro, Ro_{2D}, and the time steps and viscosity coefficients are given in table 6.2. Most of the simulations will be discussed for times of integration between $t = 0$ and $t = 130$, corresponding to nondimensional times $\tilde{t} = tf$ from 0 to 2938. Various quantities have been averaged over the time interval $[65, 125]$. These include the Rossby numbers in table 6.2. The simulations

Forcing 1 (F1)				Forcing 2 (F2)			
Ro	Ro_{2D}	F	Δt	Ro	Ro_{2D}	F	Δt
0.1	0.036	3.3×10^{-3}	2.6×10^{-3}	0.08	0.04	4.9×10^{-3}	2.6×10^{-3}
0.12	0.046	4.5×10^{-3}	2.6×10^{-3}	0.11	0.06	9.9×10^{-3}	2.6×10^{-3}
0.19	0.07	1.2×10^{-2}	2.6×10^{-3}	0.24	0.11	4.8×10^{-2}	2.6×10^{-3}
0.31	0.093	4.2×10^{-2}	2.6×10^{-3}	0.32	0.128	9.6×10^{-2}	2.6×10^{-3}
0.36	0.106	5.8×10^{-2}	2.6×10^{-3}	0.47	0.18	2.36×10^{-1}	2.6×10^{-3}
0.43	0.113	9.6×10^{-2}	2.6×10^{-3}	0.54	0.2	3.3×10^{-1}	2.6×10^{-3}
0.48	0.112	1.27×10^{-1}	2.2×10^{-3}	0.62	0.2	4.7×10^{-1}	2.6×10^{-3}
0.6	0.123	2.18×10^{-1}	1.5×10^{-3}	0.72	0.22	6.5×10^{-1}	2.6×10^{-3}
0.67	0.119	3.11×10^{-1}	1.5×10^{-3}	0.85	0.26	9.3×10^{-1}	1.9×10^{-3}
0.77	0.120	4.33×10^{-1}	1.5×10^{-3}	0.99	0.3	1.4	1.9×10^{-3}
0.94	0.117	7.22×10^{-1}	1.5×10^{-3}	1.15	0.2	1.87	1.9×10^{-3}
0.98	0.120	8.23×10^{-1}	1.5×10^{-3}	1.36	0.19	2.8	1.6×10^{-3}
1.5	0.166	3	1.5×10^{-3}	1.52	0.21	3.7	1.6×10^{-3}
2.3	0.242	9.7	1.5×10^{-3}	1.96	0.26	7.4	1.6×10^{-3}

Table 6.2: Ro, Ro_{2D}, forcing F, and time step Δt for each simulation of the set forced with the Forcing F1 (left column), and F2 (right column). The hyperviscosity coefficient used for both sets is $\nu = 1.8 \times 10^{-24}$.

with smaller Ro values in each of the sets displayed in table 6.2 were run much longer, out to $t = 500$.

The timeseries of E_{2D}, E_w and E_{3D} contributions normalized by the total energy are shown in figures 6.1-6.2 for various Ro and for both forcings F1 and F2. The 3D energy is injected directly by the forcing, while E_{2D} and E_w result from nonlinear interactions between 3D and 2D modes and 3D and w modes, respectively. For large Ro, the 2D energy reaches stationarity rapidly and remains less than 1 % of the total energy, while the 3D energy dominates the total energy. This changes as Ro decreases and the 2D energy becomes about 90 % of the total energy for the Ro ≈ 0.2 simulation

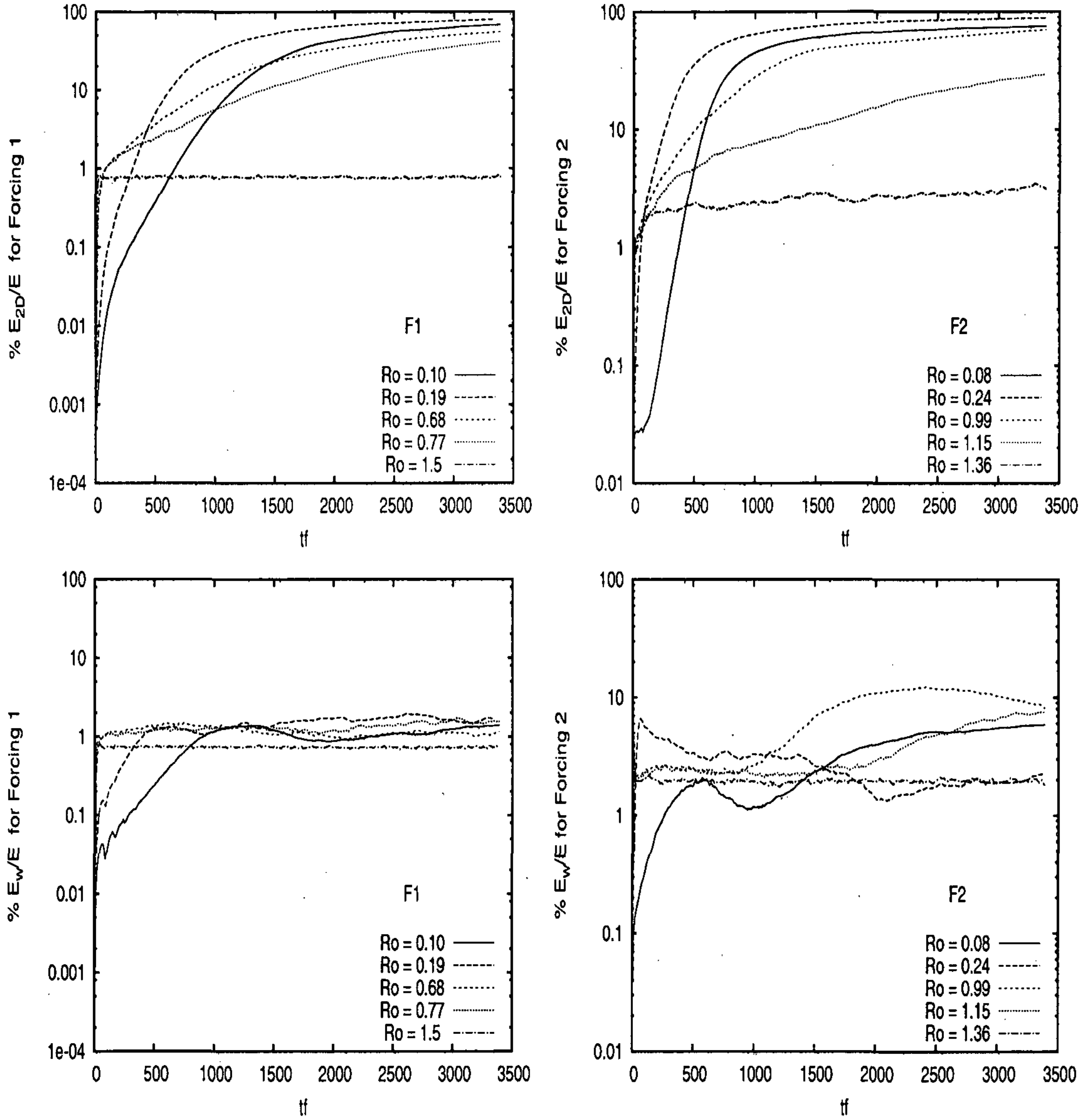

Figure 6.1: The timeseries of 2D and w energies normalized by the instantaneous value of total energy E are shown for different Ro. Timeseries of E_{2D}/E are shown in the top panels for simulations forced with F1 (left) and F2 (right). For both forcings, we observe that for larger Ro, the timeseries reach stationarity more quickly. The largest percentage of E_{2D} is reached for Ro $= 0.19$ for forcing F1 (top left), and for Ro $= 0.24$ for forcing F2 (top righ).

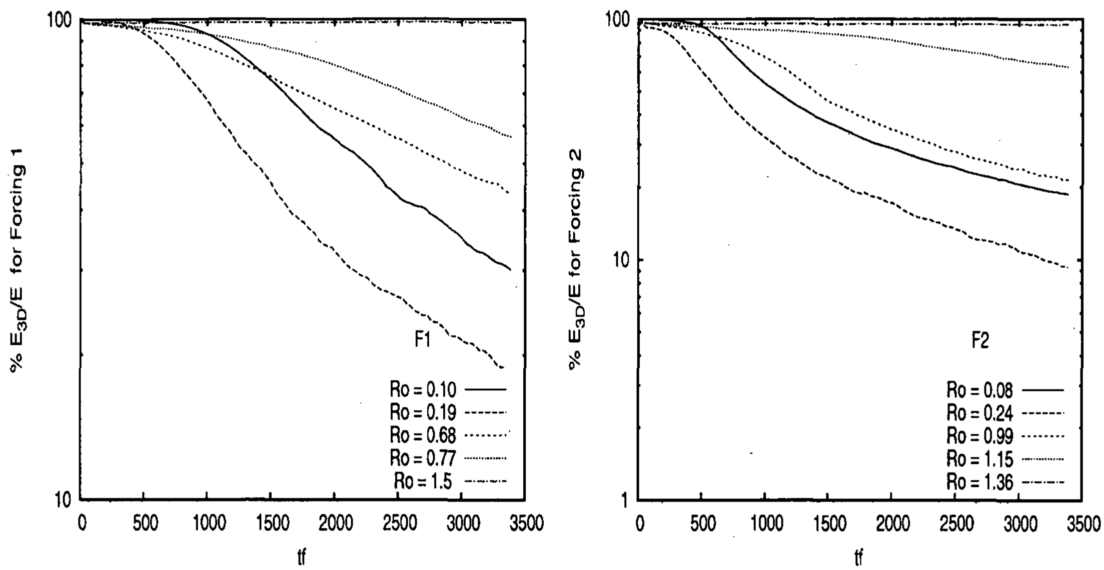

Figure 6.2: Timeseries of 3D energy normalized by the instantaneous total energy E are shown for different Ro and for simulations forced with F1 (left) and F2 (right).

(for both forcing types). For Rossby numbers lower than ≈ 0.2, the ratio of 2D to total energy remains large, but is smaller than the peak reached at Ro ≈ 0.2. This is observed for both forcing schemes. For all Ro, and both forcing types, E_w remains small. However, note that for some simulations using F2, E_w becomes approximately 10 % of the total energy.

Overall, these results show a change of behaviour consistent with the three regimes identified in decay simulations (Bourouiba and Bartello (2007)). In fact, we observe a weakly rotating regime similar to non-rotating turbulence, with a transition to an intermediate Ro regime characterized by a growth of E_{2D}/E, with a peak of the growth rate at Ro ≈ 0.2, and a third regime in which the growth rate of E_{2D} decreases as Ro $\rightarrow 0$. Figure 6.3 shows timeseries of E_{2D}, E_w and E_{3D} normalized by the total energy for a Ro in the weak rotation regime and another in the intermediate regime. It clearly illustrates the difference between weakly rotating and intermediate Ro regimes for both the F1 and F2 forcings.

For the simulations in the intermediate Ro regime, the 2D energy has not reached

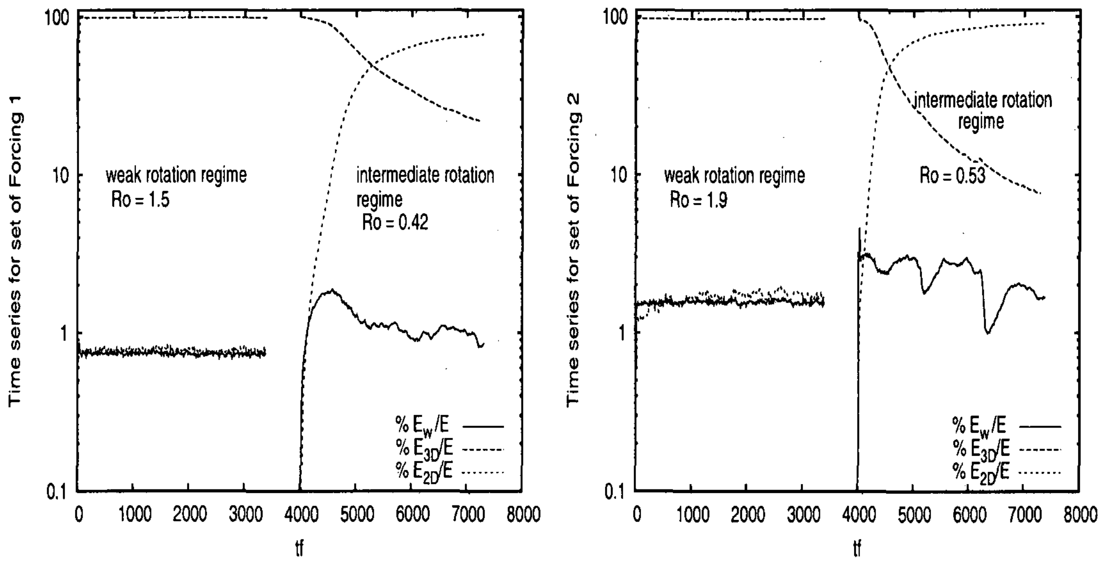

Figure 6.3: Time series of $E_{3D}/E, E_{2D}/E$, and E_w/E for simulations with (left) Ro = 1.5 and Ro = 0.42 for F1, and with (right) Ro = 1.9, and Ro = 0.53 for F2. The timeseries with the smaller Ro are offset for clarity.

stationarity by the end of the simulations (see figure 6.1 top left for example). This is also the case for Ro_{2D}. Nonetheless, some of the statistics of the flow reach quasi-stationarity. These include Ro and the rate of transfer between the 3D and the 2D modes (see figure 6.4 right for example). This quasi-stationarity is reached for times beyond an adjustment period which led us to choose the time window $t > 65$ for our averaging. In addition, for $t \geq 65$ all the simulations satisfy the condition of nondimensional time $\tilde{t} = ft \gg 1/\mathrm{Ro}^2$, for which the near-resonant interactions are active (Newell, 1969).

Using the decomposition introduced in §6.2 the spectral energy equations can be decomposed as (omitting dissipation)

$$\frac{\partial \mathrm{E}_{3\mathrm{D}}}{\partial t}(\boldsymbol{k} \in W_{\boldsymbol{k}}, t) = (F + T_{33\to 3} + T_{32\to 3} + T_{3w\to 3})(\boldsymbol{k} \in W_{\boldsymbol{k}}, t), \tag{6.7}$$

$$\frac{\partial \mathrm{E}_{2\mathrm{D}}}{\partial t}(\boldsymbol{k} \in V_{\boldsymbol{k}}, t) = (T_{22\to 2} + T_{33\to 2})(\boldsymbol{k} \in V_{\boldsymbol{k}}, t), \tag{6.8}$$

$$\frac{\partial \mathrm{E}_{\mathrm{w}}}{\partial t}(\boldsymbol{k} \in V_{\boldsymbol{k}}, t) = (T_{2w\to w} + T_{33\to w})(\boldsymbol{k} \in V_{\boldsymbol{k}}, t), \tag{6.9}$$

where the total spectral transfers are distinguished by the types of interactions they involve, eg. $33 \rightarrow 2$ stands for the interactions between two 3D wave modes that contribute to the 2D equation. Note that the $T_{jk \rightarrow i}$ terms are symmetric in j and k. The growth of energy in the 2D modes is a direct consequence of the transfer of the injected energy to the 2D modes via $T_{33 \rightarrow 2}(k_h, t)$.

In decaying turbulence, Bourouiba and Bartello (2007) used the integrated 2D-3D transfer term $T_{33 \rightarrow 2}$ in the spectral energy equations (6.7 - 6.9) in order to quantify the level of coupling between the 2D and the 3D modes. In the current study, we take into account the level of forcing in order to accurately compare the level of nonlinear coupling between 2D and 3D modes. As a result, in figure 6.4, we show the time-average of the ratio between the integrated 2D-3D transfer and the energy forcing input to the 3D modes defined as

$$\frac{\overline{T_{23}}}{F}(\mathrm{Ro}) = \frac{\overline{T_{23t}(t;\mathrm{Ro})}}{F} = \frac{\overline{\sum_{\boldsymbol{k} \in V_k} T_{33 \rightarrow 2}(\boldsymbol{k}, t; \mathrm{Ro})}}{F}, \tag{6.10}$$

with $\overline{()}$ representing the time-average.

For both types of forcing, the proportion of the injected energy that is transferred to the 2D modes has a maximum at Ro between 0.2 and 0.3—and decreases for both smaller and larger Ro. The intermediate Ro range identified in decay simulations showed the same nonmonotonic behaviour of the integrated 2D-3D transfer. Note that the overall shape of the curve is very similar from one forcing type to the other, but the amplitudes are different. The rate of injected energy transferred to the 2D modes for flows forced with F2 is higher than the rate of transfer when the flow is forced with F1. This indicates that a set of scales or modes are possibly more efficiently triggering the dominant 3D-to-2D transfers, and that these modes or scales contain more energy when using forcing F2 compared to F1. A more detailed examination of the scales involved in the 2D-3D transfers is needed to pursue this discussion. However, our first hint comes from asymptotic theories of rotating turbulence based on a timescale separation—as Ro $4\!\rightarrow 0$— between the slow (2D) modes and the wave (3D) modes.

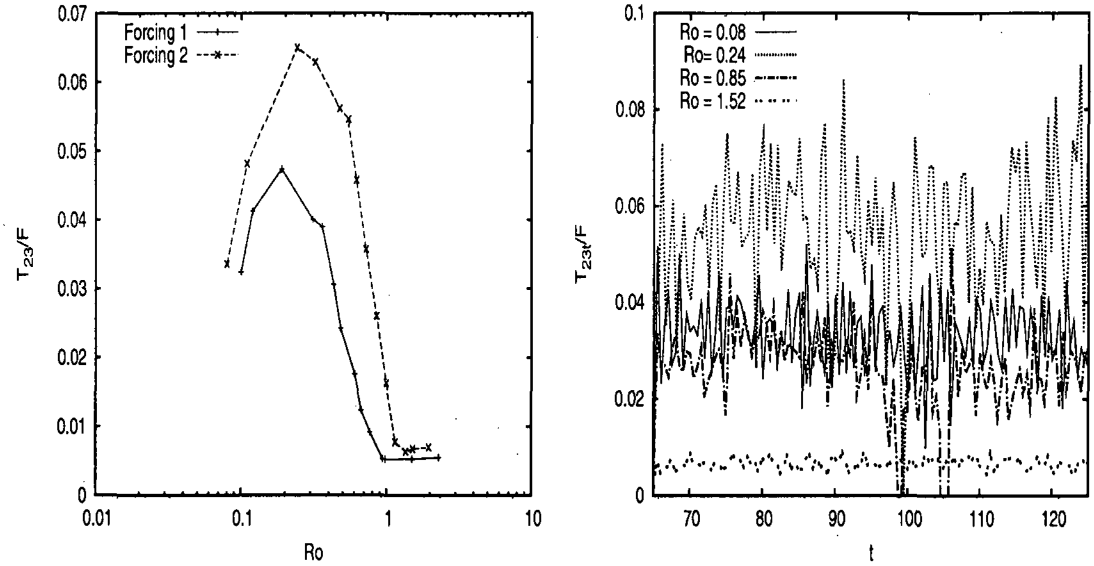

Figure 6.4: $\overline{T_{23}/F}(\mathrm{Ro})$ (6.10) as a function of the Rossby number for forcing F1 and F2 (left), and the time series of the transfer T_{23t}/F for F2 (right).

In this limit, Waleffe (1992) showed that triple-wave resonant interactions lead to most of the 3D energy being concentrated in large vertical scales.

In order to investigate the role of vertical scale in the 3D-to-2D transfer, we plot the integrated transfer to forcing ratio (6.10), but with a filtering based on the vertical scale of the 3D modes. The two 3D modes of the triad interaction $33 \to 2$ have opposite vertical wavenumbers in order to satisfy a triad with $\boldsymbol{k}+\boldsymbol{p}+\boldsymbol{q}=0$. We can thus compute (time dependence is omitted)

$$\begin{aligned} T_{23z}(\mathrm{Ro}) &= \sum_{\boldsymbol{k}\in V_k} T_{33\to 2}(\boldsymbol{k}|z;\mathrm{Ro}) \\ &= \sum_{\boldsymbol{k}\in V_k} \sum_{\{\boldsymbol{p}\in W_k \| p_z|=z\}} \sum_{\{\boldsymbol{q}\in W_k \| q_z|=z\}} T(\boldsymbol{k}|\boldsymbol{p},\boldsymbol{q};\mathrm{Ro}). \end{aligned} \tag{6.11}$$

Figure 6.5 shows the time averaged $T_{23z}(\mathrm{Ro})/F$ for various vertical scales, for both forcings F1 and F2. In the intermediate Ro range, we observe that for both F1 and F2, the overall injection of energy via $33 \to 2$ interactions comes predominantly from 3D modes with vertical wavenumbers $k_z \leq 12$. That is, the 3D-to-2D transfers mainly

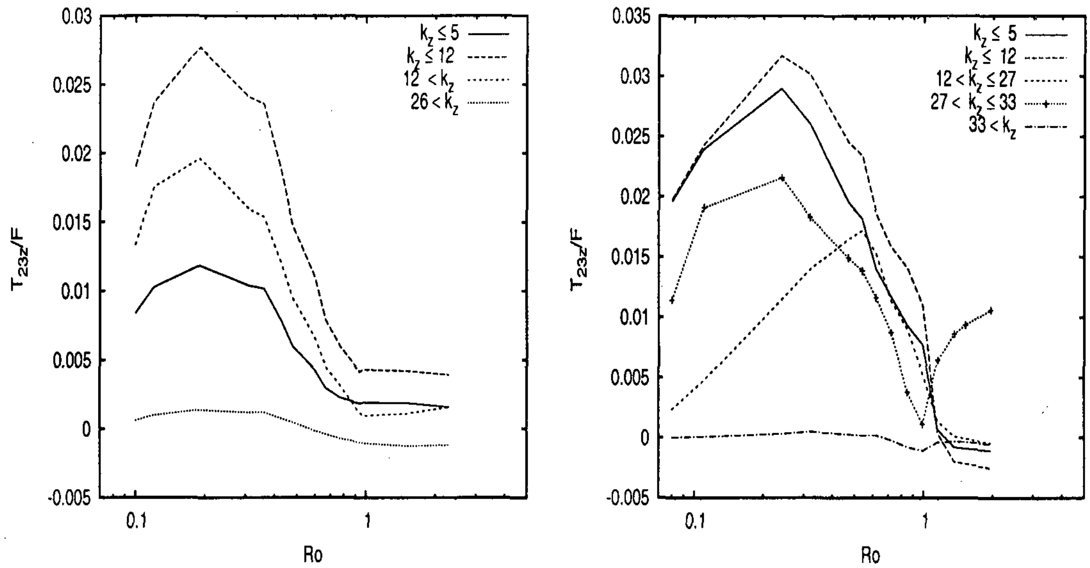

Figure 6.5: Time average $\overline{T_{23z}}/F(\mathrm{Ro})$ as a function of the Rossby number and filtered by the vertical scales of the 3D modes exchanging energy with the 2D mode. The set of simulations forced with forcing types (left) F1 and (right) F2 are displayed. The spectral vertical layer forced ($27 < k_z \leq 33$) by F2 is marked by stars.

involve wave modes with medium to large vertical scales. This is true even for F2, where the small vertical scales (with $27 < k_z \leq 33$) are being excited. This shows that the 3D energy is first transferred to the large vertical scales, which in turn interact with the 2D modes.

Figure 6.6 shows the $T_{23}(\mathrm{Ro})/F$ transfer filtered by the horizontal scale of the 2D modes. We find that the 3D-to-2D transfers involve 2D modes of large horizontal scales ($k_h < 13$). This is true even for F1, which forces small horizontal wavenumbers $28 \leq k_h \leq 33$. Assuming local interactions, one would then expect energy to be injected in 2D modes with k_h of the order of $26 - 28$. This is not the case.

We conclude that the dominant 3D-to-2D transfers are done by interactions between large vertical scale 3D modes and large horizontal 2D scales, regardless of the 3D forcing. This direct injection of energy into the large 2D scales urges us to have a closer look at the detailed spectral energy transfers and examine the horizontal scales of the 3D modes with $k_z \leq 12$ involved in the 3D-to-2D transfers. This is the subject of the next section.

6.5 Spectra, nonlinear transfers and dominant nonlocal interactions

From the previous section we found that the 2D scales receiving most of the 3D energy injection correspond to $k_h \leq 13$. In this section we discuss the energy spectra of the 3D, 2D, and w modes, and introduce detailed energy transfer spectra calculated in order to analyze the 3D scales of the dominant 3D-to-2D energy transfers. We mainly discuss the flows forced using F1 and F2. In addition a comparison using F3 is also presented.

Figure 6.7 shows the time-averaged spectra of the simulations with Ro in transition from the intermediate to the weak rotation range ($\mathrm{Ro} > 0.2$). In the weak rotation regime the energy spectra are not greatly affected by rotation. For both forcings the E_{2D} spectra are similar to E_{3D} spectra. For decreasing Ro, we see an

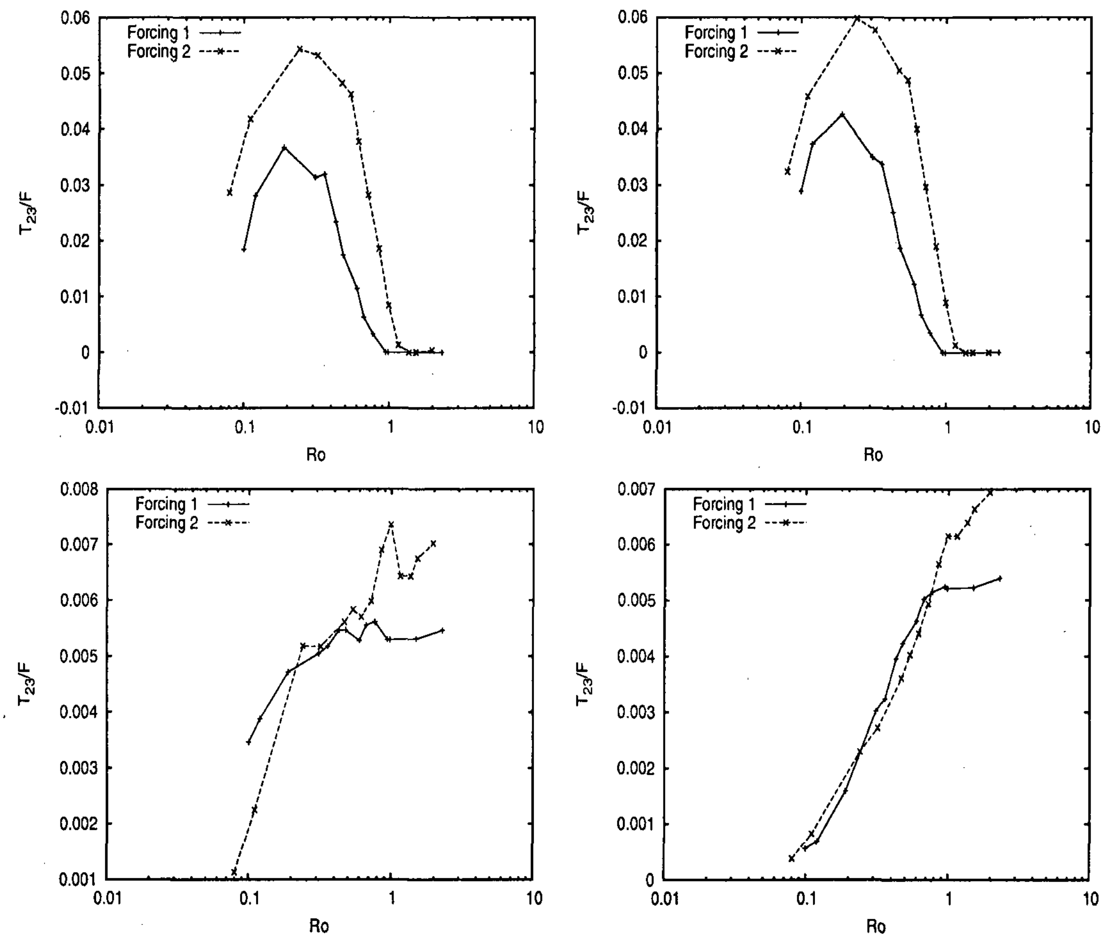

Figure 6.6: Time average $\overline{T_{23}/F}$ as a function of the Rossby number and filtered by the horizontal scale of the 2D mode. The results for both forcing F1 and F2 are displayed. The transfer to 2D modes with (top left) $k_h < 6.5$, (top right) $k_h < 13$, (bottom left) $k_h > 13$, and (bottom right) $k_h > 26$ are displayed.

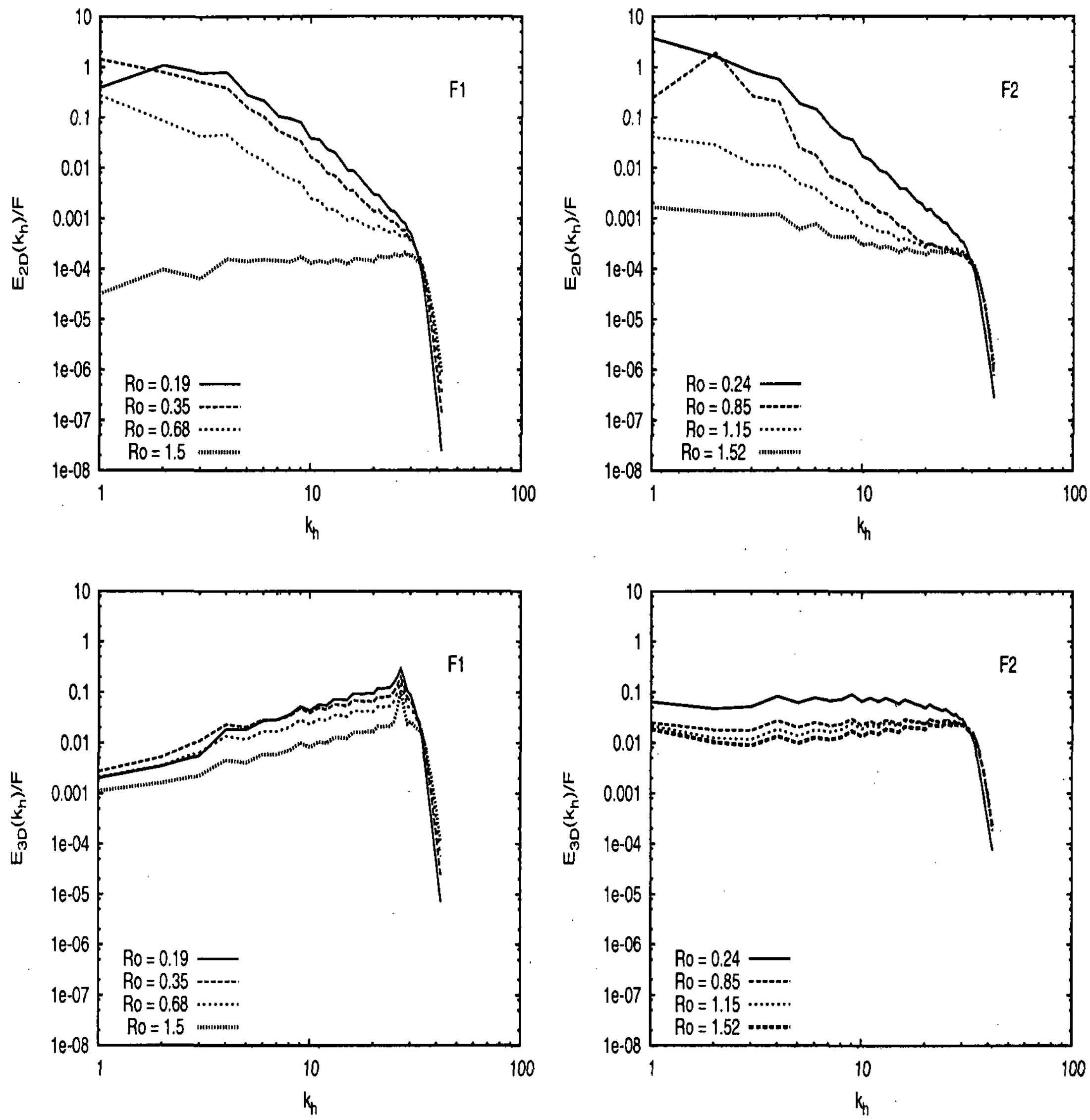

Figure 6.7: Time averaged horizontal energy spectra normalized by the input of energy F. E_{2D}/F and E_{3D}/F are shown in the top and bottom panels, respectively. The left panels show the results obtained using F1, and the right panels show those obtained using F2.

increase of 2D energy in large horizontal scales and a steepening of the E_{2D} slope. This is consistent with the energy transfers into low wavenumber 2D modes discussed in the previous section. When larger horizontal scales become the most energetic 2D scales, $E_{2D}(k_h)$ reaches a slope of $\sim k_h^{-p}$, with $p \geq 3$. The main difference between the Ro ranges is the steepening of the 2D energy spectrum. That is, for 0.2 $\leq$Ro $<$ 1 the accumulation of 2D energy in the large scales of the domain increases with decreasing Ro.

In order to identify the 3D horizontal scales responsible for most of the 3D-to-2D transfers and thus the steepening of $E_{2D}(k_h)$, we examine the spectral energy transfers, denoted $T_{33\to2}(\boldsymbol{k})$. They measure the energy exchange between a given 2D mode of wavevector $\boldsymbol{k} = (k_h, 0)$, and a pair of 3D modes, $(\boldsymbol{p}, \boldsymbol{q})$, such that $\boldsymbol{p}$ and $\boldsymbol{q}$ lie in particular prescribed spectral regions. We divide the spectral space into three disjoint regions $\mathcal{A}, \mathcal{B}$ and $\mathcal{C}$. We can thus define truncated velocity fields $\boldsymbol{u}^{\mathcal{A}}$, $\boldsymbol{u}^{\mathcal{B}}$, $\boldsymbol{u}^{\mathcal{C}}$, $\boldsymbol{u}^{\mathcal{AB}}$, $\boldsymbol{u}^{\mathcal{AC}}$, $\boldsymbol{u}^{\mathcal{BC}}$. For example

$$\boldsymbol{u}^{\mathcal{AB}}(\boldsymbol{k}) = \begin{cases} \boldsymbol{u}(\boldsymbol{k}), & \text{if } \boldsymbol{k} \in \mathcal{A} \text{ or } \boldsymbol{k} \in \mathcal{B}, \\ 0, & \text{if } \boldsymbol{k} \notin \mathcal{A} \text{ and } \boldsymbol{k} \notin \mathcal{B}, \end{cases}$$

or

$$\boldsymbol{u}^{\mathcal{A}}(\boldsymbol{k}) = \begin{cases} \boldsymbol{u}(\boldsymbol{k}), & \text{if } \boldsymbol{k} \in \mathcal{A}, \\ 0, & \text{if } \boldsymbol{k} \notin \mathcal{A}. \end{cases}$$

Using the truncated velocity fields we calculate detailed spectral transfers analogous to those calculated for isotropic turbulence in Domaradski (1988). A couple of filtering steps similar to those detailed in Domaradski and Rogallo (1990) allow us to obtain the energy transfers between the triads $\boldsymbol{k} + \boldsymbol{q} + \boldsymbol{p} = 0$ formed of one 2D mode of wavevector $\boldsymbol{k}$, and all the pairs of 3D modes satisfying various combinations of $\boldsymbol{p}$ and $\boldsymbol{q}$. For example $T^{\mathcal{AB}}$ has either $\boldsymbol{p}$ or $\boldsymbol{q}$ in $\mathcal{A}$ and the other in $\mathcal{B}$

$$T^{\mathcal{AB}}_{33\to2}(\boldsymbol{k} \in V_{\boldsymbol{k}}) = \sum_{\{\boldsymbol{q}\in W_{\boldsymbol{k}} \ \& \ \boldsymbol{q}\in\mathcal{A}\}} \ \sum_{\{\boldsymbol{p}\in W_{\boldsymbol{k}} \ \& \ \boldsymbol{p}\in\mathcal{B}\}} T(\boldsymbol{k}, \boldsymbol{p}, \boldsymbol{q}). \tag{6.12}$$

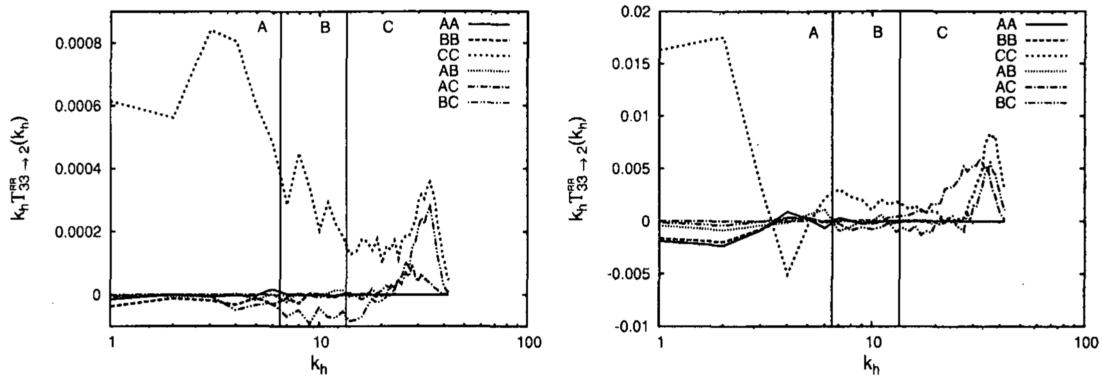

Figure 6.8: Time averaged horizontal transfer spectra $T^{RR}_{33\to2}(k_h)$ defined in (6.12), with R being either region A, B or C, and for the simulation forced with F1 (left), and another forced with F2 (right). $T^{\mathcal{AA}}_{33\to2}(k_h)$, $T^{\mathcal{BB}}_{33\to2}(k_h)$, $T^{\mathcal{CC}}_{33\to2}(k_h)$, $T^{\mathcal{AB}}_{33\to2}(k_h)$,$T^{\mathcal{AC}}_{33\to2}(k_h)$,$T^{\mathcal{BC}}_{33\to2}(k_h)$ are labelled AA, BB, CC, AB, AC, and BC, respectively. The lines of separation between the disjoint regions of the spectral domain $\mathcal{A}, \mathcal{B}$ and $\mathcal{C}$ are shown by the straight vertical lines.

Figure 6.8 compares the transfer spectra $T^{\mathcal{AA}}_{33\to2}(k_h)$, $T^{\mathcal{BB}}_{33\to2}(k_h)$, $T^{\mathcal{CC}}_{33\to2}(k_h)$, $T^{\mathcal{AB}}_{33\to2}(k_h)$, $T^{\mathcal{AC}}_{33\to2}(k_h)$,$T^{\mathcal{BC}}_{33\to2}(k_h)$ labelled AA, BB, CC, AB, AC, and BC, respectively. We display the transfers for the simulations forced with forcing F1 and F2 and averaged between time 100 and 125. The disjoint regions of the spectral space are such that region $\mathcal{A}$ contains the modes with $k_h < 6.5$, $\mathcal{B}$ contains the modes with $6.5 \leq k_h < 13$, and $\mathcal{C}$ contains the modes with $k_h \geq 13$. The delimitations between the three regions are specifically marked for the 2D modes in the figure. The choice of these delimitations between the regions was made in order to ensure that $k_{hmaxA}/k_{hminC} = 2$, with k_{hmaxA} the largest wavenumber in spectral region $\mathcal{A}$ and k_{hminC} the smallest wavenumber of region $\mathcal{C}$. When the transfers are positive, the 2D modes are receiving energy from the 3D modes, and the vice versa. When interpreting these transfers, note that they do not involve an exchange of energy between 2D modes, but only between the 2D and the two other 3D modes involved in the triad. For example, in region $\mathcal{A}$, the curve denoted AA corresponds to the transfers of type

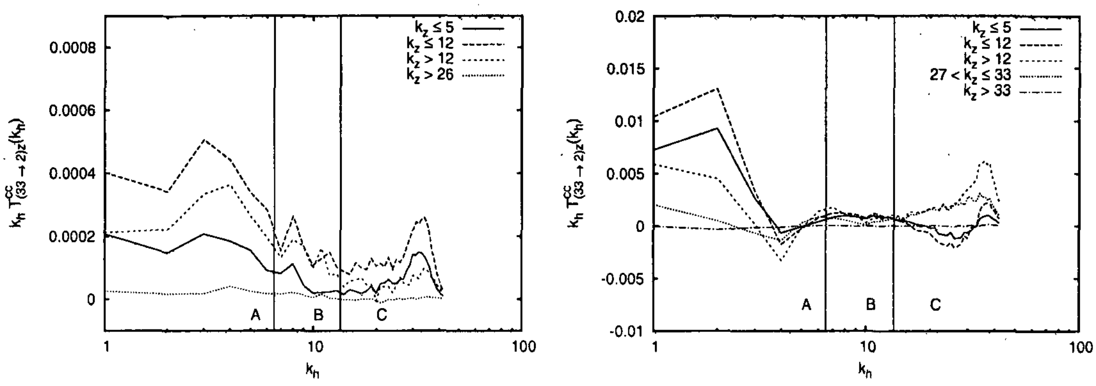

Figure 6.9: $T^{CC}_{33\to2}(k_h)$ averaged between $t = 100$ and $t = 125$ and filtered according to the vertical wavenumber k_z of the 3D modes. The simulation forced with F1 is on the left and F2 is on the right.

$AA \to A$ in which all three modes of the triad are in region $\mathcal{A}$. In region $\mathcal{B}$, the same curve denoted AA corresponds to transfers of type $AA \to B$, in which the two 3D modes are in region $\mathcal{A}$ and the 2D mode of the triad is in region $\mathcal{B}$. From figure 6.8 we conclude that $T_{33\to2}$ is dominated by transfers of 3D energy from region $\mathcal{C}$ into 2D modes in region $\mathcal{A}$. These transfers are denoted $CC \to A$. Note that this holds for both F1, which forces in region $\mathcal{C}$ and F2, which forces predominantly in region $\mathcal{A}$. In other words large scale 2D modes are excited by small horizontal scale 3D modes.

We now focus on the $CC \to A$ transfers. Figure 6.9 shows the dominant $T^{CC}_{33\to2}(k_h \in V_{\boldsymbol{k}})$ filtered by the vertical scale of the two 3D modes. Most of the energy transfer $CC \to A$ involves 3D wavemodes with vertical wavenumber smaller than $k_z \approx 12$. Even when using F2, which forces modes with specific vertical scales such that $27 < k_z \le 33$, the modes with k_z less than 12 remain the dominant source of energy for the 2D large scale modes of region $\mathcal{A}$.

To summarize, we found that, first, irrespective of the forcing scale, the 3D modes that are dominantly involved in the 3D-to-2D transfers are those of small frequencies. These are 3D modes with small horizontal wavenumber (region $\mathcal{C}$) and medium to

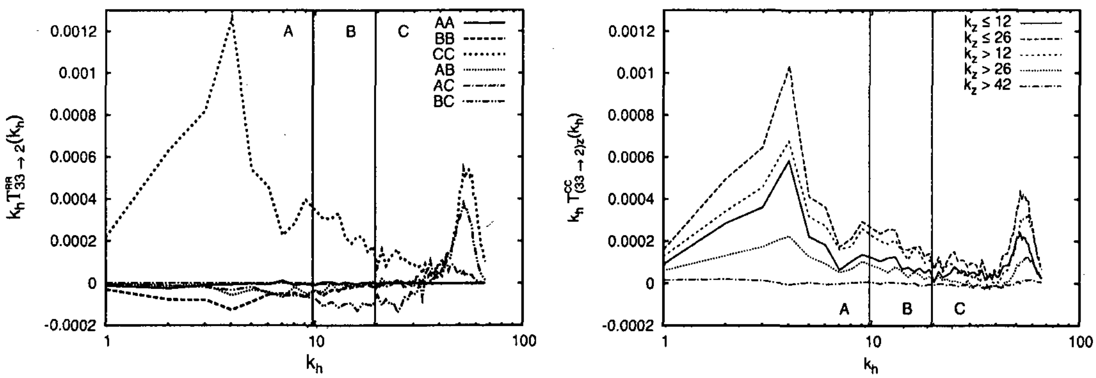

Figure 6.10: Time-averaged horizontal energy transfer spectra for the simulation forced with F4. On the left, we show $T^{RR}_{33\to 2}(k_h)$ defined in (6.12), with R being the region A, B or C. On the right we show $T^{\mathcal{CC}}_{33\to 2}(k_h)$ filtered by the vertical scale of the 3D modes. The line of separation between the disjoint regions of the spectral domains $A, \mathcal{B}$ and $\mathcal{C}$ are shown by the straight vertical lines.

small vertical wavenumbers ($k_z < 12$). The dominant role played by the 3D modes of small frequency in horizontal region $\mathcal{C}$ is consistent with the anisotropy generation in favour of small frequencies by the $33 \to 3$ resonant interactions (Waleffe, 1993). Note, however, that near-resonances may also play a role (Smith and Lee, 2005). A second result is that the dominant $33 \to 2$ interactions are nonlocal in scale, with $CC \to A$ interactions dominating.

In order to test the robustness of these results, we performed simulations with higher resolutions (200^3). This allows for a larger spectral separation between regions $\mathcal{A}$ and $\mathcal{C}$. We used the forcing F3 detailed in table 6.1. F3 forces wavnumbers with $39 \leq k_h \leq 42$. As before, we define disjoint regions $\mathcal{A}, \mathcal{B}$ and $\mathcal{C}$ such that the ratio between the largest forced mode in region $\mathcal{C}$ and the smallest horizontal scales of region $\mathcal{B}$ is 2. The larger wavenumber of region $\mathcal{B}$ is twice as large as the largest wavenumber in the spectral region $\mathcal{A}$. This gives that $\mathcal{A}$ corresponds to $k_h < 9.75$; $\mathcal{B}$ to $9.75 \leq k_h < 19.5$, and $\mathcal{C}$ to $k_h \geq 19.5$.

Figure 6.10 shows the detailed $T_{33\to 2}(k_h)$ (6.12) averaged over the time interval

[100, 125]. We find that, as before, the 3D-to-2D transfers are dominated by interactions $33 \rightarrow 2$ of the type $CC \rightarrow A$, with 3D modes of medium to large vertical scales and $k_z < 26$. The nonlocality of the dominant interactions leading to the increase of 2D energy is thus robust to the extension of the inertial range.

6.6 V_k modes dynamics

6.6.1 Downscale enstrophy transfer

Classical two-dimensional turbulence phenomenology predicts a direct enstrophy cascade spectral slope of -3 for scales smaller than the forcing scale and an inverse energy cascade spectral slope of $-5/3$ for scales larger than the forcing scale. Note, however, that steeper than -3 spectra are observed for the enstrophy cascade spectral range in simulations of classical two-dimensional turbulence (e.g. McWilliams, 1984).

For rotating turbulence, several scaling derivations have been attempted. However, for moderately small Ro simulations forced in medium scales, a steeper slope (near -3) was found for the range of scales larger than the forcing scales (e.g. Smith and Waleffe, 1999; Chen et al., 2005). This -3 scaling is distinct from that of classical two-dimensional turbulence (for which the -3 slope is valid for wavenumbers larger than the forcing wavenumber), suggesting that the 2D modes dynamics in rotating flows is distinct from that of classical two-dimensional turbulence. In this section we revisit this conclusion in light of the results of the previous section.

In the previous section we found that the 3D-to-2D interactions are nonlocal and inject the energy directly into the medium to large 2D scales. This finding could explain the steep scaling for the horizontal 2D spectrum observed in both the present simulations, and previous literature results on forced rotating flows.

In figures 6.11-6.12 we examine the energy spectra $E_{2D}(k_h)$, $E_w(k_h)$, $E_{3D}(k_h)$, and

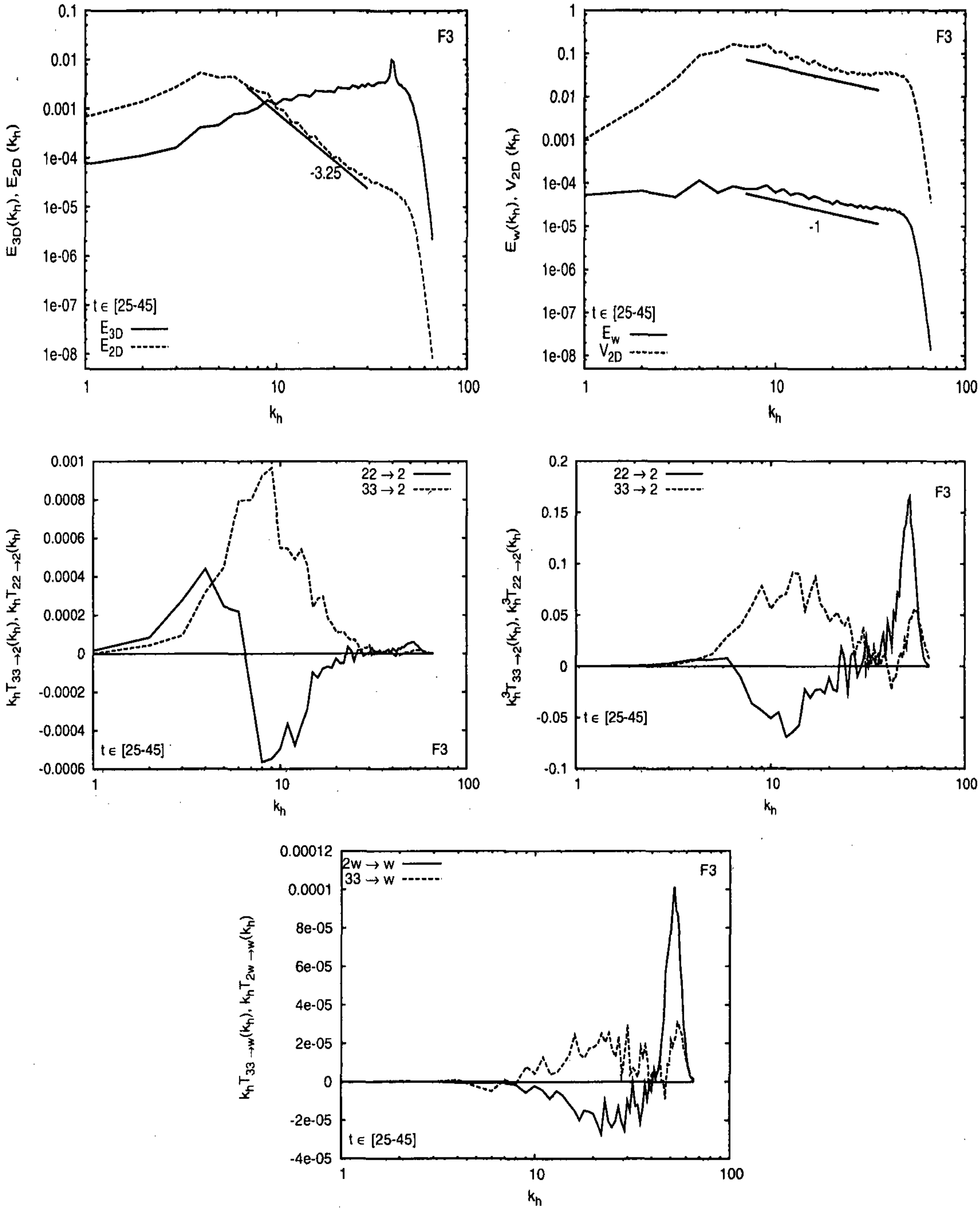

Figure 6.11: Time averaged spectra in $t \in [25,45]$. Top left: $E_{2D}(k_h)$ and $E_{3D}(k_h)$. Top right: $E_w(k_h)$ and $V_{2D}(k_h)$. Middle left: transfer spectra of 2D energy. Middle right: transfer spectra of 2D enstrophy V_{2D}. Bottom panel: Transfer spectra of E_w.

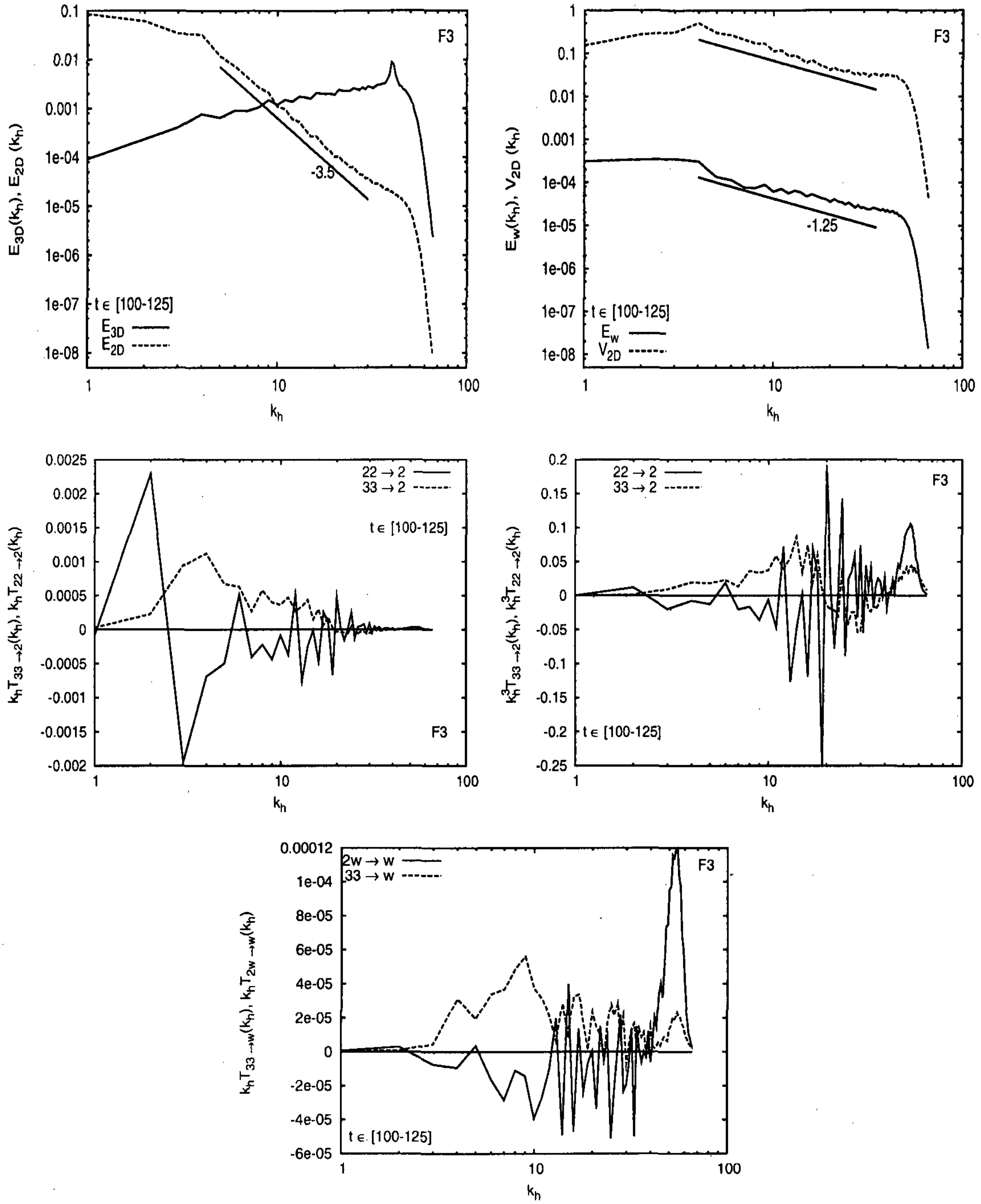

Figure 6.12: same as figure 6.11, but for time $t \in [100,125]$.

the 2D enstrophy spectrum $V_{2D}(k_h)$ defined as

$$V_{2D} = \frac{1}{2} \sum_{\boldsymbol{k} \in V_k} |\boldsymbol{\omega}_z(\boldsymbol{k})|^2, \tag{6.13}$$

where $\boldsymbol{\omega}_z$ is the vertical component of the vorticity field. We also show the transfers of energy via $22 \rightarrow 2$, $2w \rightarrow w$, $33 \rightarrow 2$, and $33 \rightarrow w$ interactions. In addition, we display the equivalent transfers of enstrophy V_{2D}. In figure 6.11 the transfers are averaged for times between 25 and 45, and in figure 6.12, they are averaged for early times between 100 and 125. The early time window corresponds to a regime for which $E_{2D} < E_{3D}$, while the later time window corresponds to a regime of build up of the 2D energy, where $E_{2D} > E_{3D}$. Forcing F3, like F1, excites the small 3D horizontal scales, with $k_h \in [39,\ 42]$.

The slope for the $E_{2D}(k_h)$ spectrum (top left corner) steepens with time (from -3.25 for $t \in [25, 45]$ to -3.5 for $t \in [100, 125]$) and corresponds to the spectral range of modes transferring 2D enstrophy to small 2D scales (see enstrophy transfer spectra in the middle right panels). Note that, the later time enstrophy transfer is noisier than that observed in the early time. An ensemble averaging of the simulations would reduce these fluctuations. We nevertheless see that the enstrophy injected is transferred from the injected modes to the small dissipation scales with k_h above 50 (figure 6.11-6.12). Although very limited, the $22 \rightarrow 2$ interactions (displayed in the middle left panels) do show the presence of a range of 2D inverse energy transfer from the scale at which the $CC \rightarrow A$ interactions inject E_{2D} to the largest horizontal scales. Thus, it appears that the 2D dynamics in the present forced rotating simulations are similar to that of a classical two-dimensional turbulence forced in medium-to-large horizontal scales.

We display the transfer terms for w in 6.11-6.12 bottom panels. Recall that the w mode equation (6.9) is similar to that of a passive scalar advected by 2D velocity field via the $T_{2w\rightarrow w}(\mathrm{k}_h)$ transfer term and with a source term $T_{33\rightarrow w}(k_h)$. In fact, from figure 6.11-6.12, we observe that the transfers $T_{2w\rightarrow w}(k_h)$ (bottom panels) are consistent with this. The $T_{33\rightarrow w}(k_h)$ term is injecting E_w into medium to large horizontal scales. The $T_{2w\rightarrow w}(k_h)$ advection term is then transferring the injected E_w to the dissipation scales, as expected for a passive scalar.

In addition, we find that the spectra of $V_{2D}(k_h)$ and $E_w(k_h)$ have similar slopes that are close to -1 , which is in agreement with the classical dynamics expected for a passive scalar advected in a two-dimensional turbulent flow (Lesieur, 1997). Indeed, in figures 6.12 and 6.11 we find that the ≈ -1 slopes found for both $V_{2D}(k_h)$ and $E_w(k_h)$ appears for the range of modes that corresponds to the downscale V_{2D} and E_w transfers. Similarly to the 2D energy spectrum, the 2D enstrophy and E_w spectra steepen with time when the 2D energy is concentrated in the smallest wavenumbers of the domain.

6.6.2 Long-time 2D dynamics in the large scales

So far, we observed that the 2D dynamics in the intermediate Ro range is quite similar to that of classical two-dimensional turbulence forced in large scales through the non-local $CC \rightarrow A$ interactions. It is associated with a small range of E_{2D} inverse transfer and an ≈ -3 energy spectral slope coinciding with the range of direct downscale V_{2D} transfer. In some respects, then, the 2D modes exhibit behaviour similar to that of classical two-dimensional turbulence forced at large scales. This comparison has limitations. In fact, classical two-dimensional turbulence does not show asymmetry between positive and negative vortices, denoted cyclones and anticyclones, respectively. The 2D projection of forced rotating turbulence in the intermediate Ro regime does show such an asymmetry (e.g. Bartello et al., 1994; Bourouiba and Bartello, 2007; Smith and Lee, 2005) and it is common in geophysical flows. In this section we consider the extent to which the 2D dynamics of the forced rotating flow is analogous to the classical two-dimensional turbulence in the long-time limit. Does the similarity between the two hold for the long-time dynamics as well?

On the one hand, one might expect the 2D energy to grow indefinitely, such as would occur in forced 2D turbulence without large scale dissipation. The growing 2D

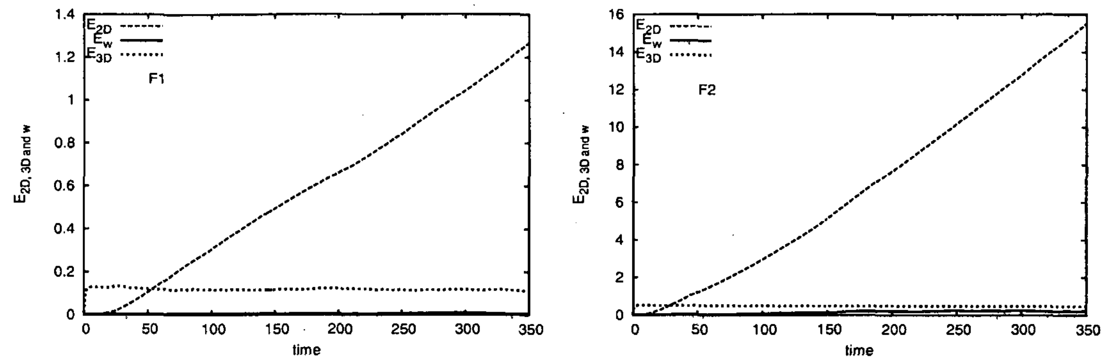

Figure 6.13: Time series of E_{2D}, E_{3D}, and E_w for the long simulations forced with a forcing of F1 and constant instantaneous input of $F = 5.8 \times 10^{-2}$ (left), and F2 with a constant instantaneous input of $F = 4.7 \times 10^{-1}$ (right).

energy would accumulate into the largest scales of the domain and would lead to what is refereed to as condensation, for which large-scale vortices intensify and generate very steep energy spectra (Smith and Yakhot, 1993; Borue, 1994; Chertkov et al., 2007). Recently, 2D energy condensation was observed to cause a slope transition in the 2D energy spectra from the predicted $-5/3$ to a much steeper -3 slope (Chertkov et al., 2007). When the condensate forms in classical two-dimensional turbulence, nonlocal interactions become important. Nazarenko and Laval (2000) showed that the slopes of the spectra inside the condensate vortex cores are ≈ -4, which is steeper than that of the background flow (≈ -3).

On the other hand, it may be that the 2D flow generated in rotating turbulence eventually becomes unstable, leading to 2D-to-3D energy transfers which become an opposing mechanism to the $CC \rightarrow A$ energy transfers identified previously. In fact, some studies have shown that two-dimensional vortices can be unstable to 3D perturbations, particularly at high Ro (Ngan et al., 2004, 2008).

We performed longer simulations of forced flows using F1 and F2. The parameters were chosen to obtain flows in the intermediate regime identified in §6.4. The flow forced with F1 had a constant forcing input of $F = 5.8 \times 10^{-2}$, an average Rossby number of 0.36 and was run up to $t = 650$. The flow forced with F2 had a constant forcing input of $F = 4.7 \times 10^{-1}$, an average Rossby number of $\text{Ro} = 0.62$ and was run up to $t = 350$.

Figure 6.13 shows the timeseries of E_{2D}, E_{3D} and E_w for $t \in [0, 350]$. For both F1 and F2, the 2D energy increases and does not suggest a tendency toward saturation. To the contrary, growth of E_{2D} is reminiscent of the 2D energy timeseries for forced two-dimensional flows with condensate formation displayed in Chertkov et al. (2007).

Figures 6.14-6.15 show snapshots of horizontal slices of the vertical component of the total vorticity and the 2D vorticity for the simulation forced by F1. We observe the generation of large scale structures that intensify with time, reflecting the dominance of 2D energy over 3D energy in the timeseries 6.13. Ultimately, we see the emergence of a couple of vortices, with a much more intense cyclonic than anticyclonic vortex.

Figure 6.16 shows the time evolution of the 2D energy spectrum for F1 (results were similar with F2). It shows the steepening of $E_{2D}(k_h)$ and the transition from a slope of about -3.25 to a steeper slope when the 2D energy starts accumulating in the smallest wavenumbers. The increase of 2D energy would imply an increase of the Rossby number so that the regime of the flow would eventually change. However, we do not observe such a change. In fact, timeseries of the total and 2D Rossby numbers show that the total Ro does not vary much over the simulation. While Ro_{2D} does increase with time, it remains smaller than Ro and below 0.15 even at long times 650. In fact, due to the steepening of $E_{2D}(k_h)$ the energy in the small 2D scales is negligible compared to the total energy contained in the medium to small 3D scales, and our Rossby numbers are based on vorticity field.

In addition, we compared the nonlinear timescales of 2D and 3D modes as a function of k_h. This is done using estimates of $\text{Ro}_{2D}(k_h) = k_h\sqrt{2k_h E_{2D}(k_h)}/f$ and $\text{Ro}_{3D}(k_h) = k_h\sqrt{2k_h E_{3D}(k_h)}/f$ (not shown). We found that the 2D nonlinear timescale is fastest in region $\mathcal{A}$, while the fastest nonlinear 3D modes are in region $\mathcal{C}$. That is, the $CC \to A$ interactions correspond to interactions between fastest nonlinear 3D and 2D modes.

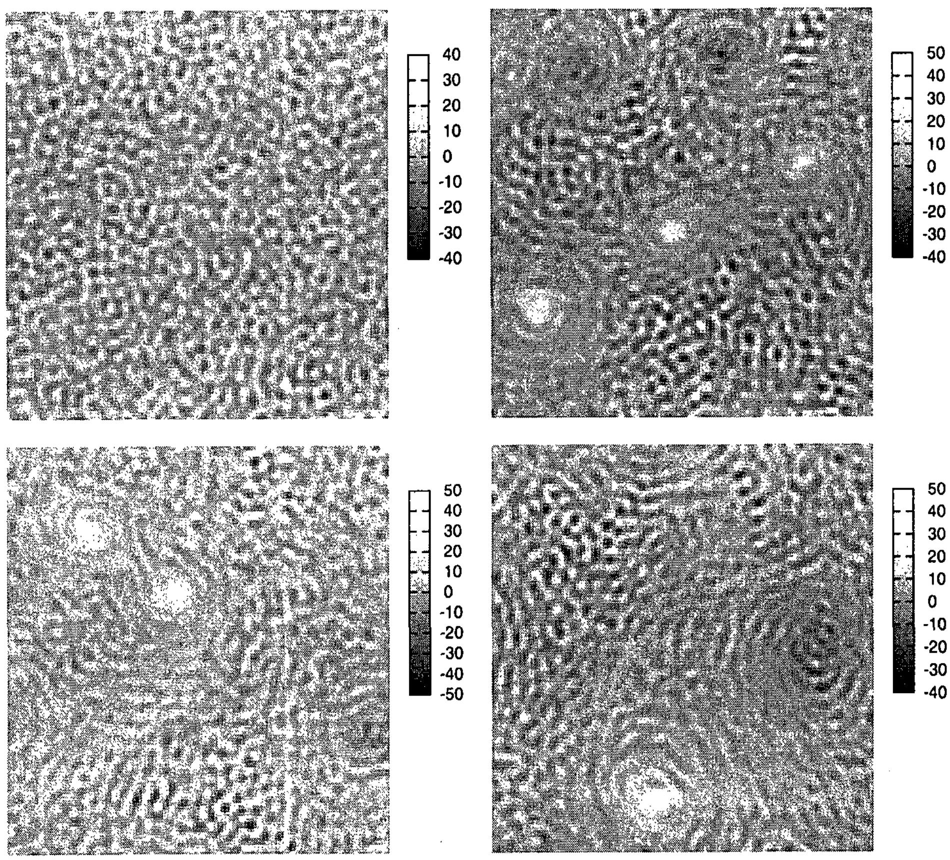

Figure 6.14: Snapshots of a horizontal slice of the total vertical vorticity forced with F1. Top left: $t_1 = 7.5$. Top right: $t_2 = 135$. Bottom left: $t_3 = 167.4$. Bottom left: $t_4 = 317.4$ The vortices intensify due to a merger process leading to the formation of dominant 2D large scale structures.

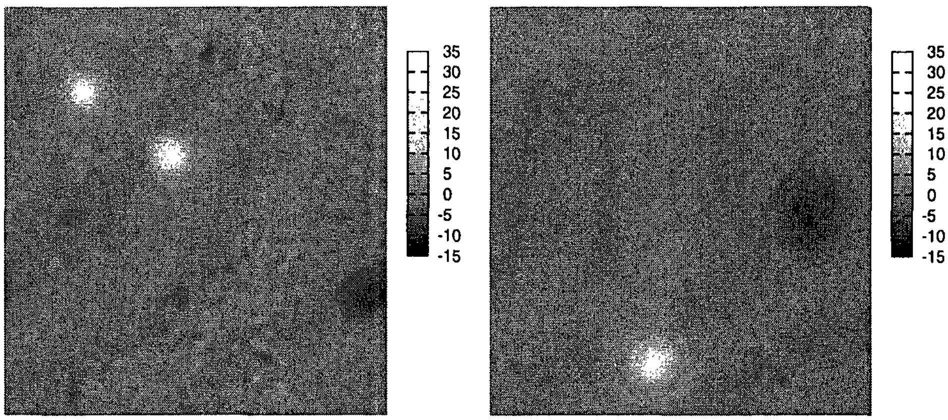

Figure 6.15: Snapshots of a horizontal slice of the 2D vorticity forced with F1. Right panel: $t_2 = 167.4$. Left panel: $t_4 = 317.4$. These 2D vorticity snapshots correspond to the lower two panels of figure 6.14. The 2D energy is increasing and leading to the formation of large scale intensifying vortices. The cyclones are more intense than the anticyclones (see legend for maxima vorticity values).

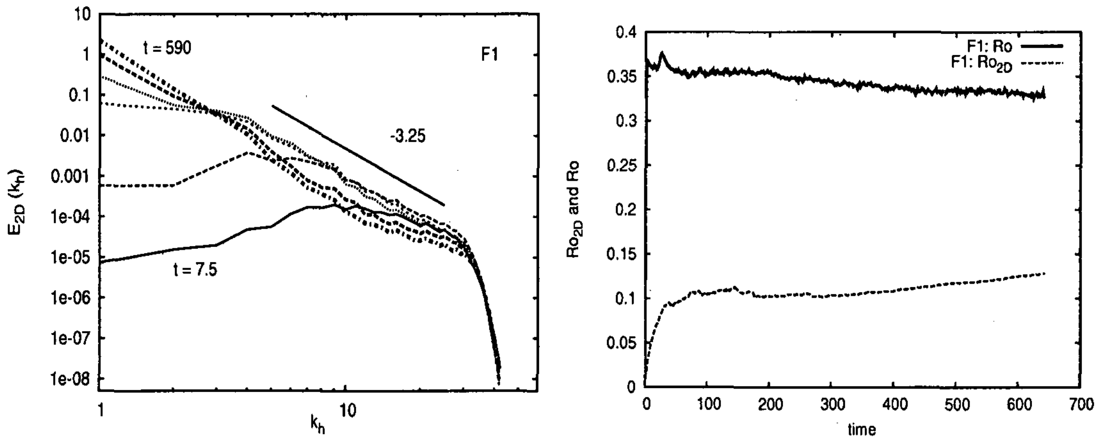

Figure 6.16: On the left: the time evolution of the 2D energy spectra for simulations forced with F1. The spectra have been averaged on short time intervals. On the right: the time series of the Ro_{2D} and Ro for the same simulation.

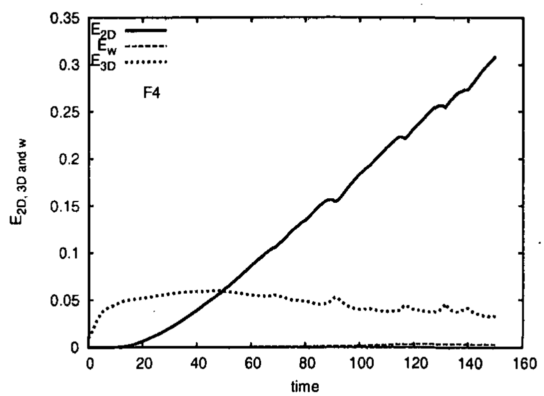

Figure 6.17: Timeseries of E_{2D}, E_{3D}, and E_w for the simulation forced with F4.

The long simulations show a tendency for E_{2D} to accumulate in the largest scales in a manner similar to that observed in two-dimensional turbulence. No destabilization of the large scale 2D flow appears to stall the growth of E_{2D}. As mentioned, such an instability has been seen in other studies, at least at large Ro. There, large scale 2D flow was unstable to large horizontal small vertical 3D structures. In other words, there was a 2D-to-3D energy transfer via interactions of type $AA \rightarrow A$. In this case, $T_{33\rightarrow 2}(k_h)$ transfer spectra of type $AA \rightarrow A$ would be negative and large in region $\mathcal{A}$. However, in the present simulations using F1, large horizontal 3D scales are not energetic, and with F2, only a small portion of the large horizontal 3D modes (i.e., with $27 < k_z \leq 33$) are. As a result, we implement a fourth forcing scheme, F4, which excites the largest horizontal 3D scales for all vertical scales (see table 6.1). With F4, we directly force the lower k_h 3D modes. This can allow for the $AA \rightarrow A$ interactions to play a more dominant role and, if negative, could lead to a saturation of E_{2D} in the long time limit.

We used a 200^3 resolution and integrated until $t = 150$ with an average Ro≈ 0.23 for $t > 80$. Figure 6.17 shows timeseries of 2D and 3D energies for this simulation. We observe a clear increase of E_{2D} with time, which does not seem to tend toward stationarity or saturation. However, there are short timed decreases in E_{2D} with a corresponding increase in E_{3D}. This could suggest a sudden destabilization processes

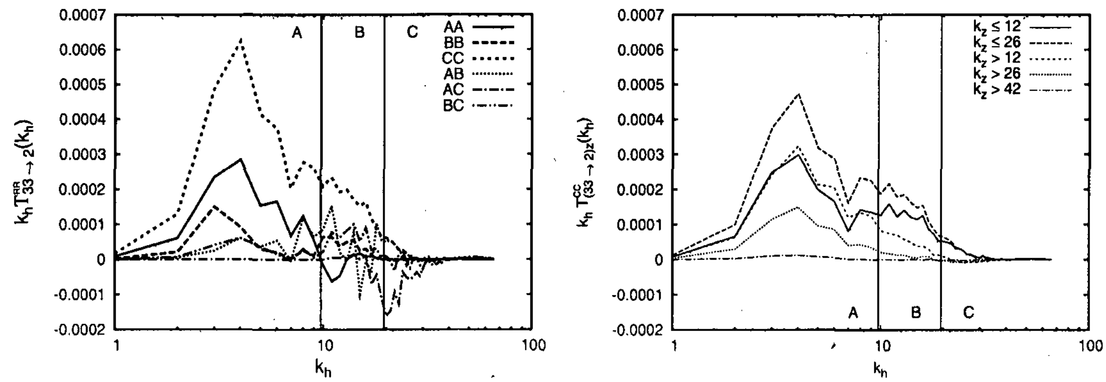

Figure 6.18: Same as 6.10, but for the simulations forced using F4, and for time $t \in [100,\ 125]$.

of the 2D flow. Nevertheless, we observe that overall, forcing the large 3D horizontal scales does not lead to a notable reduction of the increase in the 2D energy.

Figure 6.18 shows the energy $T_{33\to2}(k_h)$ transfers filtered like in (6.12). As before, the scales involved in the most dominant $33 \to 2$ interactions remain those of type $CC \to A$. In addition, we find that the $AA \to A$ interactions are positive: they transfer energy into the 2D field. It thus appears that the $CC \to A$ interactions are those that dominate the 3D-to-2D interactions irrespective of which 3D modes are forced. We also recover that the dominant 3D vertical scales transferring the energy to the large horizontal scale 2D modes are again those of medium to large vertical scales ($k_z \leq 26$).

Finally, figure 6.19 shows snapshots of horizontal slices of total and 2D vertical vorticity fields forced with F4 (at time 142.5). The merging of vortices led to fewer, but more intense coherent vortices. Note that we observe that anticyclones also merge with time, but do not have stable and intense cores as do their cyclonic counterparts. Finally, the same observations hold for the simulations forced using F1 and F2 (not shown). This asymmetry between the cyclones and the anticyclones is not new. It has already been observed in previous forced rotating (e.g. Smith and Waleffe, 1999; Chen et al., 2005) and decaying (e.g. Bourouiba and Bartello, 2007) turbulence

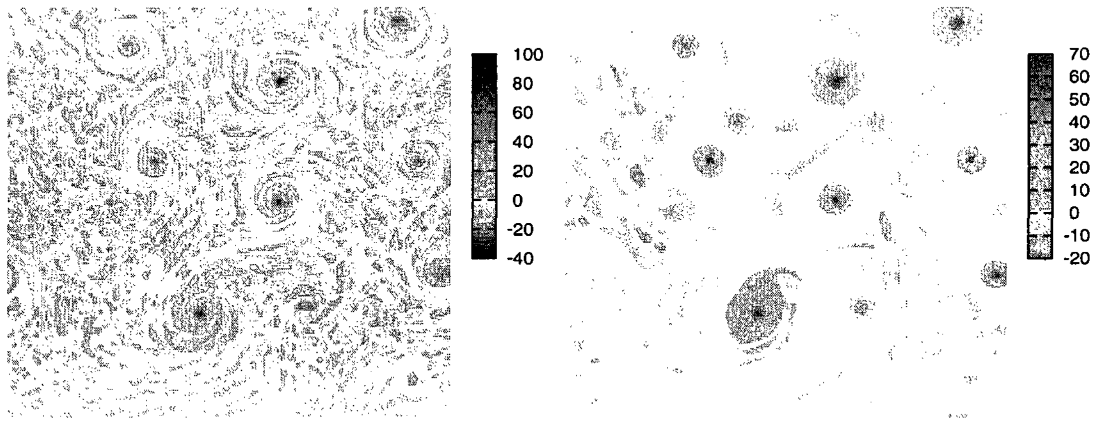

Figure 6.19: Snapshots of a horizontal slices of total (left)and 2D (right) vertical vorticity fields at time $t = 142.5$ forced with F4. Note that some of the cyclones are more than three times as intense as the anticyclones.

simulations. This late time asymmetry remains the fundamental distinction between classical two-dimensional turbulence and the 2D dynamics of the intermediate Ro regime in rotating turbulence.

6.7 Conclusion

We examined forced rotating turbulence over a range of Ro and with various forcing configurations. We first showed that an intermediate Ro range exists in forced turbulence, and that this is robust to various forcing schemes and resolutions. We found that the interactions responsible for the increase of 2D energy in the intermediate Ro range are nonlocal in wavenumber space. They involve a direct injection of energy from small frequency 3D modes directly into the medium to large horizontal 2D scales. This nonlocality of the interactions is robust to the change of forcing schemes and resolutions.

The nonlocal direct injection of energy into relatively large horizontal scale 2D modes showed that the steep ≈ -3 slope observed in the present and previous forced rotating turbulence flow simulations is not due to an inverse energy cascade range particular to rotating turbulence, but coincides with the spectral modes where the direct 2D enstrophy downscale transfers are taking place. In this respect, the 2D dynamics generated by rotating forced turbulent flows is similar to classical two-dimensional hydrodynamics, forced in the large scales.

We investigated whether the 2D flow dynamics would remain similar to forced classical two-dimensional turbulence for long time. Using long-time simulations and various forcings, we showed that the 2D long-time dynamics of the forced intermediate Ro range reach a state similar to the that observed in classical two-dimensional turbulence and in MHD simulations(e.g. Alexakis et al., 2006), in which energy accumulates in the largest scales of the domain.

Our findings suggest that in order to model the large scales in rotating flows in the intermediate Ro range one needs to assume nonlocality of the nonlinear interactions forcing the large horizontal scales. For example, such an approach was developed for classical two-dimensional turbulence (e.g. Nazarenko and Laval, 2000), who assumed nonlocality of interactions to derive a scaling different than that of the Kolmogorov -Kraichnan model based on local interactions. In the case of rotating flows, the nonlocality of the interactions would have to be assumed for the 3D-to-2D transfers.

Finally, note that the results of Smith and Lee (2005) showed that near-resonant interactions had a tendency to concentrate the energy into the small frequency 3D modes for moderately small Ro. Our results are consistent with this finding. In fact, our results combined with those of Smith and Lee (2005) suggest the following picture for the intermediate Ro range: near-resonant interactions concentrate 3D energy into the small frequency modes (region $\mathcal{C}$ with small k_z). These modes are characterized by small linear frequencies and relatively large nonlinear frequencies and they excite 2D modes of large horizontal scales (in region $\mathcal{A}$), with zero linear frequencies and fast nonlinear frequencies via the $33 \to 2$ ($CC \to A$) triad interactions. The 2D dynamics of rotating flows on its own can be modeled by classical two-dimensional turbulence, except for the asymmetry observed between intense cyclones and weaker anticyclones.

The mechanism generating this asymmetry remains to be clarified, but an instability of the anticyclonic vortices due to background rotation is strongly suspected to be at the root.

Chapter 7

Conclusions

The Coriolis force has a subtle, but significant impact on the dynamics of geophysical and astrophysical flows. When the rotation is strong, Ro goes to zero and three-dimensional flows are observed to two-dimensionalize. However, this nonlinear phenomenon was not well understood and literature results seemed contradictory. The overall aim of this work has been to clarify and study how the nonlinear dynamics in turbulent flows are modified by rotation for a range of Rossby numbers less than one. We isolated the nonlinear interactions, and studied how the rate of rotation affects their behaviour. Our approach was to solve the equations with direct numerical simulations complemented with theory. We also investigated numerical uncertainties related to this study. Our findings are listed below:

- **Identified three rotating ranges in decaying rotating turbulence (Chapter 3)**:
  - Using simulations of decaying turbulent flows subjected to 33 different rotating rates, we identified non-monotonic dynamics as $Ro \longrightarrow 0$, with three distinct rotating ranges. The *large* ($Ro > 1$), the *intermediate* ($0.03 < Ro < 1$) and the *small Ro* ($Ro < 0.03$) ranges.
  - We show that the *intermediate Ro* range is characterized by a maximum leakage of energy from 3D to 2D modes for $Ro \approx 0.2$. This transfer is associated with a maximum of vertical vorticity skewness, also reached at

$Ro \approx 0.2$. These findings are robust to the change of domain size.

- The *small Ro* range shows a reduced conversion of 3D-to-2D energy and a reduced asymmetry. This regime is consistent with the 2D dynamics being quasi-decoupled from the background wave turbulence, but a further computationally-demanding study was needed for the study of this last range.

- **Investigated discreteness effects with key resonant and near-resonant interactions (Chapter 4):**

  - In most numerical simulations of turbulence and experimental settings, the domains are periodic and bounded, respectively. In periodic or finite domains, the modes satisfying the resonance equations are integers. Studies of wave-turbulence problems other than rotating turbulence showed the existence of a discreteness effect. The effect can be considered as twofold. First, there is an effect intrinsic to the finite property of bounded domains, due to the existence of only integer-wavenumbers versus the real-wavenumbers. Second, there is an effect due to the truncation of the wavenumbers or resolutions used in a particular bounded domain considered.

  - In the small and intermediate regimes identified in Chapter 3, resonant and near-resonant interactions play an important role. We quantified finite-size effects on the number of exact and near-resonant interactions resolved by a given computational domain as a function of the truncation wavenumber and the Rossby number. We constructed a kinematic model of resonant and near-resonant interactions and investigated whether the production of an energy cascade via these key interactions is affected by the discreteness effect. We showed that the discreteness of wavenumbers in a periodic domain can lead to a freezing of the nonlinear transfers between modes dominated by resonant inertial wave interactions. This freezing occurs for nonlinear broadenings below a freezing threshold Ro_f, which we quantified for various resolutions and initial conditions. Given the relatively small value of Ro_f and its weak dependence on resolution, we submit that most numerical simulations on rotating turbulence carried out so far would have been free of discreteness effects.

- In finite domains, we also showed the existence of a minimum finite nonlinear broadening Ro_{min} under which 3D-2D interactions do not exchange energy. We quantified Ro_{min} for different resolutions. The values found are comfortably below the Ro used in most numerical simulations of rotating turbulence.

- We also identified another nonlinear broadening threshold, Ro_c. For $Ro < Ro_c$, the number of $32 \to 3$ interactions is larger than the triple wave interactions. In this regime, the freezing of the vertical energy transfers predicted by some theories is possible. Finally, for simulations with $Ro > Ro_f$ for which the number of interactions scale as in an infinite domain, if a decoupling or a reduced energy transfer is observed, it is an intrinsic dynamical property of the flow in the bounded domain considered.

- **Studied the small Ro regime by testing the predictions of asymptotic theories of decoupling (Chapter 5):**

  - We used equilibrium statistical mechanics complemented with numerical simulations of a rotating flow model in the limit of the Reynolds number $\to \infty$. We derived the equilibrium spectra to which the inviscid system is expected to relax during the 2D-3D decoupling phase.

  - Numerically, we foud a first decoupled phase for $t < t_\star$, and a coupled phase for $t > t_\star$, with $t_\star \approx 2/Ro^2$. Thus, the prediction of decoupling of the wave and zero-frequency modes in the asymptotic limit of $Ro \to 0$ is valid and observable.

  - We found that beyond $t_\star$, the set of invariants become slowly-varying, but continue to play a constraining role on the short-time dynamics of the rotating flow.

- For both coupled and decoupled time phases, we found a reduction of the vertical energy transfers to small vertical scales.
- Finally, the inviscid results confirm the existence of a mechanism causing the growth of E_{2D} and the intermediate Ro regime observed in decaying turbulence simulations. This mechanism vanishes with $Ro \to 0$, depends nonmonotonically on Ro and is inherent to the rotating flow dynamics.

• **Showed the existence of the intermediate *Ro* regime for forced turbulence and a predominance of nonlocal interactions (Chapter 6):**

- We showed that the three regime separation prevails in forced turbulence, and that this is true for various 3D forcing scales and configurations. The rate of energy transfer from the 3D to the 2D modes peaks around $Ro \approx 0.2$ whether the forcing is in the small or large horizontal length scales.
- We showed that the dominant transfers from the 3D to the 2D modes are nonlocal and that this is true for all forcing schemes used. This nonlocality is found to be robust and to inject energy from the small frequency 3D modes directly into the medium to large horizontal 2D scales.
- We showed that after the early-time dynamics, the steep ≈ -3 slope of the observed 2D energy spectrum corresponds to a direct downscale 2D enstrophy transfer. This suggests that the 2D dynamics emerging from rotating forced flow is similar to that of classical two-dimensional turbulence and that the former could possibly be modelled by the latter, except for the asymmetry observed between the intense cyclones and the weaker anticyclones. The asymmetry remains to be clarified, but an instability of the anticyclonic vortices due to the presence of rotation is suspected to be at the root of the problem.

– Using long-time simulations and various forcings, we showed that the 2D long-time dynamics of the forced intermediate Ro range reach a state similar to that observed in classical two-dimensional turbulence and in MHD flows, in which energy accumulates in the largest scales of the domain.

Our findings helped clarify the dynamics of small-to-intermediate Ro numbers relevant for parts of the atmosphere and ocean. In fact, identifying that turbulence can be seen as a source of energy for the generation of large atmospheric and oceanic structures instead of a dissipation term can have important consequences for atmospheric and oceanic models. The nonlocality of the interactions in scale also suggests a change in the parameterization of subgridscale processes (such as turbulence) used in such models. These modifications could greatly improve predictability.

A phenomenology assuming dominant nonlocal interactions needs to be developed for rotating turbulence. The classical Kolmogorov phenomenology assumes locality of interactions, as does proposed phenomenologies predicting, for example, a -2 spectrum for rotating turbulence (e.g. Zhou, 1995; Canuto and Dubovikov, 1997; Müller and Thiele, 2007). Furthermore, a full study is needed to identify the type of instability leading to the asymmetry of the vorticity fields in the intermediate Ro regime.

More generally, given the presence of finite domain effects, we must refine theories of wave-turbulence by specifically formulating theories that can be verified by numerical and lab experiments carried out in bounded domains. Nazarenko (2006) initiated these developments for example for water-waves. That approach must be extended to inertial waves.

Finally, inertial and Alfvén waves, despite major differences in their dispersion relations, share some common features. Alfvén wave turbulence shows a tendency toward two-dimensionalization of the magnetohydrodynamic flows studied. However, the properties of these wave-turbulence problems found in plasma are still not well understood. A cross pollination between the findings for inertial waves presented here and the research on Alfvén wave turbulence would be very beneficial for the development of new tools and theoretical frameworks facilitating the study of MHD turbulence. In particular, the existence and properties of the intermediate Ro regime with a strong two-dimensionalization of the flow and the small Ro regime which is analogous to the "slaved" regime in Alfvén waves (Nazarenko, 2007) are concepts with a great deal in common.

Appendix A

Inviscid analysis with helicity

Using the total energy (5.2.1), (5.6) can be re-written as

$$E = \langle \boldsymbol{u}\, \boldsymbol{u}^* \rangle = \langle e(\boldsymbol{k}) \rangle = \sum_{\boldsymbol{k}} |a_+(\boldsymbol{k})|^2 + |a_-(\boldsymbol{k})|^2, \tag{A.1}$$

where $\langle \cdot \rangle$ is the ensemble average. The total helicity can be written as

$$H = \langle \boldsymbol{u}\, \boldsymbol{\omega}^* \rangle = \sum_{\boldsymbol{k}} k(|a_+(\boldsymbol{k})|^2 - |a_-(\boldsymbol{k})|^2), \tag{A.2}$$

with $k = |\boldsymbol{k}| = \sqrt{k_h^2 + k_z^2}$. Consider the phase space of $4N$ elements $(\Re(a_+(k_1)),$ $\Im(a_+(k_1)), \Re(a_-(k_1)), \Im(a_-(k_1)),..., \Im(a_-(k_N)))$, with N the number of Fourier modes. The most probable probability density function in the phase space, or *Gibbs canonical distribution*, reads

$$P_{\alpha,\beta} = C\exp(-\alpha E - \beta H) = C\exp\sum_{\boldsymbol{k}} -\left((\alpha + k\beta)|a_+(\boldsymbol{k})|^2 + (\alpha - k\beta)|a_-(\boldsymbol{k})|^2\right), \tag{A.3}$$

where C is the normalization constant of $P_{\alpha,\beta}$ such that $\int_{4N} P_{\alpha,\beta} = 1$, giving

$$C^{-1} =$$

$$\int_{R^{4N}} \exp\left[-\sum_{\boldsymbol{k}}(\alpha+k\beta)|a_+(\boldsymbol{k})|^2+(\alpha-k\beta)|a_-(\boldsymbol{k})|^2\right] d^N\Re(a_+)d^N\Im(a_+)d^N\Re(a_-)d^N\Im(a_-)$$

$$= \left[\frac{1}{2}\sqrt{\frac{\pi}{\alpha + k\beta}}\right]^{2N}\left[\frac{1}{2}\sqrt{\frac{\pi}{\alpha - k\beta}}\right]^{2N}, \tag{A.4}$$

where (α,β) are the Lagrange multipliers determined by the average energy and helicity, respectively. The modal mean energy spectra can be derived using (A.1)

$$\langle e(\boldsymbol{k})\rangle = \langle |a_+(\boldsymbol{k})|^2 + |a_-(\boldsymbol{k})|^2\rangle = \frac{2\alpha}{\alpha^2 - k^2\beta^2}, \tag{A.5}$$

placing conditions on $(\alpha,\ \beta)$ such that $\beta \neq 0$, and for all k, $\frac{\alpha}{\beta} > k$. Equation (A.5) leads to a horizontal mean energy spectrum (in the cylindrical truncation)

$$\langle E(k_h)\rangle = \gamma 4\pi \frac{k_h}{\sqrt{\alpha^2 - k_h^2\beta^2}} \ln\left|\frac{k_T + \sqrt{\gamma^2 - k_h^2}}{k_T - \sqrt{\gamma^2 - k_T^2}}\right|, \tag{A.6}$$

with $\gamma = \frac{\alpha}{\beta}$ and for $\beta \neq 0$, $\gamma^2 > k_h^2$. Similarly the vertical mean energy spectra reads

$$\langle E(k_z)\rangle = (\frac{\alpha}{\beta^2})2\pi \ln\left|\frac{\alpha^2 - k_z^2}{(\alpha^2 - k_T^2\beta^2) - k_z^2}\right|, \tag{A.7}$$

with an additional condition $(\frac{\alpha}{\beta})^2 \neq k_z^2$. In the limit of large k_T, $E_0 = \langle E\rangle$ and $H_0 = \langle H\rangle$, where E_0, H_0 are the total initial energy and helicity (assumed to be conserved and known). Using the spectra obtained for both the energy and the helicity, approximate values for α and β can be obtained.

Bibliography

R. V. Abramov and A. J. Majda. Statistically relevant conserved quantities for truncated quasigeostrophic flow. *Proc. Natl. Acad. Sci*, 100:3841–3846, 2003.

A. Alexakis, P. D. Mininni, and A. Pouquet. On the inverse cascade of magnetic helicity. *Astrophys. J.*, 640:335–343, 2006.

J. D. Anderson. *A history of aerodynamics and its impact on flying machines.* Cambridge University Press, 1997.

R. Asselin. Frequency filter for time integrations. *Mon. Wea. Rev.*, 100:487–490, 1972.

A. Babin, A. Mahalov, and B. Nicolaenko. Global splitting, integrability and regularity of 3d euler and navier-stokes equations for uniformly rotating fluids. *Eur.J. Mech. B/Fluid*, 15:291–300, 1996.

A. Babin, A. Mahalov, and B. Nicolaenko. On nonlinear baroclinic waves and adjustment of pancake dynamics. *Theor. Comput. Fluid Dyn.*, 11:215–235, 1998.

J. Bardina, J. H. Ferziger, and R. S. Rogallo. Effect of rotation on isotropic turbulence: computation and modelling. *J. Fluid Mech.*, 154:321–336, 1985.

C. Baroud, B. Plapp, Z.-S. She, and H. Swinney. Anomalous self-similarity in a turbulent rapidly rotating fluid. *Phys. Rev. Lett.*, 88:114501–1–4, 2002.

P. Bartello. Geostrophic adjustment and inverse cascades in rotating stratified turbulence. *J. Atmos. Sci.*, 52:4410–4428, 1995.

P. Bartello and T. Warn. Self-similarity of decaying two-dimensional turbulence. *J. Fluid Mech.*, 326:357–372, 1996.

P. Bartello, O. Métais, and M. Lesieur. Coherent structures in rotating three-dimensional turbulence. *J. Fluid Mech.*, 273:1–29, 1994.

F. Bellet, F. Godeferd, J. Scott, and C. Cambon. Wave-turbulence in rapidly rotating flows. *J. Fluid Mech.*, 23:81–121, 2006.

D. J. Benney and P. G. Saffman. Nonlinear interactions of random waves in a dispersive medium. *Proc. R. Soc. London*, Ser. A, 289:301–320, 1966.

G. P. Bewley, D. P. Lathrop, L. R. M. Maas, and K. R. Screenivasan. Inertial waves in rotating grid turbulence. *Phys. Fluids*, 19:071701–1–4, 2007.

A. A. Bidokhti and D. J. Tritto. The structure of a turbulent free shear layer in a rotating fluid. *J. Fluid Mech.*, 241:469–502, 1992.

V. Borue. Spectral exponents of enstrophy cascade in stationary two-dimensional homogeneous turbulence. *Phys. Rev. Lett.*, 71:3967–3970, 1993.

V. Borue. Inverse energy cascade in stationary two-dimensional homogeneous turbulence. *Phys. Rev. Lett.*, 72:1475–1478, 1994.

W. J. Bos and J.-P. Bertoglio. Dynamics of spectrally truncated inviscid turbulence. *Phys. Fluids*, 18:071701–1–4, 2006.

L. Bourouiba. Model of truncated fast rotating flow at infinite Reynolds number. *Phys. Fluids*, 20:075112–1–14, 2008.

L. Bourouiba and P. Bartello. The intermediate Rossby number range and 2d-3d transfers in rotating decaying homogeneous turbulence. *J. Fluid Mech.*, 587:139–161, 2007.

J. P. Boyd. *Chebyshev & Fourier Spectral Methods*. Springer-Verlag, 1989.

C. Cambon and L. Jacquin. Spectral approach to non-isotropic turbulence subjected to rotation. *J. Fluid Mech.*, 202:295–317, 1989.

C. Cambon, N. N. Mansour, and F. S. Godeferd. Energy transfer in rotating turbulence. *J. Fluid Mech.*, 337:303–332, 1997.

C. Cambon, R. Rubinstein, and F. S. Godeferd. Advances in wave turbulence: Rapidly rotating flows. *New J. Phys.*, 6:73–102, 2004a.

C. Cambon, R. Rubinstein, and F. S. Godeferd. Advances in wave turbulence: Rapidly rotating flows. *New J. Phys.*, 6:73–102, 2004b.

V. M. Canuto and M. S. Dubovikov. Physical regimes and dimensional structure of rotating turbulence. *Phys. Rev. Lett.*, 78:666–669, 1997.

Q. Chen, S. Chen, G. L. Eyink, and D. D. Holm. Resonant interactions in rotating homogeneous three-dimensional turbulence. *J. Fluid Mech.*, 542:139–164, 2005.

M. Chertkov, C. Connaughton, I. Kolokolov, and V. Lebedev. Dynamics of energy condensation in two-dimensional turbulence. *Phys. Rev. Lett.*, 99:084501–1–4, 2007.

A. J. Chorin. *Applied Mathematical Sciences: Vorticity and turbulence.* Springer-Verlag, 1994.

C. Cichowlas, P. Bonaiti, F. Debbasch, and M. Brachet. Effective dissipation and turbulence in spectrally truncated euler flows. *Phys. Rev. Lett.*, 95:264502–1–4, 2005.

C. Connaughton, S. Nazarenko, and A. Pushkarev. Discreteness and quasiresonances in weak turbulence of capillary waves. *Phys. Rev. E*, 63:046306–1–4, 2001.

G. G. Coriolis. Mémoire sur les équations du mouvement relatif des systèmes de corps. *J. Ec. Polytech.*, 15:142–154, 1835.

A. Craya. *Contribution à l'analyse de la turbulence associée à des vitesses moyennes.* P.S.T.Ministère de l'Air 34, 1958.

P. A. Davidson. *Turbulence: an introduction for scientists and engineers.* Oxford University Press, 2004.

P. A. Davidson, P. J. Staplehurst, and S. B. Dalziel. On the evolution of eddies in a rapidly rotating system. *J. Fluid Mech.*, 557:135–144, 2006.

S. C. Dickinson and R. R. Long. Oscillating grid turbulence including effects of rotation. *J. Fluid Mech.*, 126:315–333, 1983.

J. A. Domaradski. Analysis of energy transfer in direct numerical simulations of isotropic turbulence. *Phys. Fluids*, 31:2747–2749, 1988.

J. A. Domaradski and R. S. Rogallo. Local energy transfer and nonlocal interactions in homogeneous, isotropic turbulence. *Phys. Fluids*, 2:413–426, 1990.

W. Dunham, editor. *The genius of Euler: Reflection on his life and work.* The Mathematical Association of America, 2007.

L. Euler. Découverte d'un nouveau principe de mécanique. *Mémoires de l'académie des sciences de Berlin*, 6:185–217, 1752.

R. Fjortoft. On the changes in the spectral distribution of kinetic energy for two-dimensional non-divergent flow. *Tellus*, 5:225–230, 1953.

D. G. Fox and S. A. Orszag. Inviscid dynamics of two-dimensional turbulence. *Phys. Fluids*, 16:169–171, 1972.

U. Frisch. *Turbulence.* Cambridge University Press, 1995.

S. Galtier. Weak inertial-wave turbulence theory. *Phys. Rev. E*, 68:015301(R)–1–4, 2003.

S. Galtier, S. Nazarenko, A. C. Newell, and A. Pouquet. A weak turbulence theory for incompressible MHD. *J. Plasma Phys.*, 63:447–488, 2000.

F. S. Godeferd and L. Lollini. Direct numerical simulations of turbulence with confinement and rotatoin. *J. Fluid Mech.*, 393:257–308, 1999.

H. Görtler. On forced oscillations in rotating fluids. In *5th Midwestern Conf. on Fluid Mech.*, pages 1–10, 1957.

H. P. Greenspan. *The Theory of Rotating Fluid.* Cambridge University Pres, 1968.

K. E. Heikes and T. Maxworthy. Observations of inertial waves in a homogeneous rotating fluid. *J. Fluid Mech.*, 125:319–345, 1982.

J. R. Herring. Approach of axisymmetric turbulence to isotropy. *Phys. Fluids*, 17: 859–872, 1974.

R. Hide. On the dynamics of rotating fluids and planetary atmospheres: a summary of some recent work. *Pure Appl. Geophys.*, 121:365–374, 1983.

R. Hide and A. Ibbertson. An experimental study of Taylor columns. *icarus*, 5: 279–290, 1966.

R. Hide and M. J. Lighthill. On slow transverse flow past obstacles in rapidly rotating fluid. *J. Fluid Mech.*, 32:251–272, 1968.

E. J. Hopfinger, K. F. Browand, and Y. Gagne. Turbulence and waves in a rotating tank. *J. Fluid Mech.*, 125:505–534, 1982.

M. Hossain. Reduction in the dimensionality of turbulence due to strong rotation. *Phys. Fluids*, 6:1077–1080, 1994.

A. Ibbetson and D. J. Tritton. Experiments on turbulence in a rotating fluid. *J. Fluid Mech.*, 68:639–672, 1975.

L. Jacquin, O. Leuchter, C.Cambon, and J. Mathieu. Homogeneous turbulence in the presence of rotation. *J. Fluid Mech.*, 220:1–52, 1990.

J. A. Johnson. The stability of shearing motion vertical in a rotating fluid. *J. Fluid Mech.*, 17:337–352, 1963.

Y. Kaneda, T. Gotoh, and N. Bekki. Dynamics of inviscid truncated model of two-dimensional turbulent shear flow. *pof*, 7:1225–1234, 1989.

E. Kartashova. Exact and quasiresonances in discrete water wave turbulence. *Phys. Rev. Lett.*, 98:214502–214502, 2007.

E. Kartashova. Wave resonances in systems with discrete spectra. In V. E. Zakharov, editor, *Nonlinear Waves and Weak Turbulence*, pages 95–129. American Mathematical Society, 1998.

E. Kartashova. Weakly nonlinear theory of finite-size effects in resonators. *Phys. Rev. Lett.*, 72:2013–2016, 1994.

A. N. Kolmogorov. The local structure of turbulence in incompressible viscous fluid for very large Reynolds number. *Dok. Akad. Nauk. SSSR*, 30:301–305, 1941.

R. H. Kraichnan. Inertial ranges in two-dimensional turbulence. *Phys. Fluids*, 10: 1417–1423, 1967.

R. H. Kraichnan. Helical turbulence and absolute equilibrium. *J. Fluid Mech.*, 59: 745–752, 1973.

R. H. Kraichnan. Statistical dynamics of two-dimensional flow. *J. Fluid Mech.*, 67: 155–175, 1975.

P. K. Kundu. *Fluid Mechanics.* Academic Press, 1990.

T. Lee. On some statistical properties of hydrodynamical and magneto-hydrodynamical fields. *Q. Appl. Math*, 10:69–78, 1952.

B. Legras, P. Santangelo, and R. Benzi. High-rsolution numerical experiments for forced two-dimensional turbulence. *Europhys. Lett.*, 5:37–42, 1988.

M. Lesieur. *Turbulence in Fluids.* Kluwer, third edition, 1997.

C. C. Lin. *Statistical theories of turbulence.* Princeton University Press, 1961.

Y. V. Lvov, S. Nazarenko, and B. Pokorni. Discreteness and its effects on water-wave turbulence. *Physica D*, 218:24–35, 2006.

A. J. Majda and X. Wang. *Nonlinear Dynamics and Statistical Theories for Basic Geophysical Flow.* Cambridge University Press, 2006.

P. S. Marcus and C. Lee. Jupiter's Great Red Spot and zonal winds as self-consistent, one-layer, quasigeoestrophic flow. *CHAOS*, 4:269–286, 1994.

A. D. McEwan. Inertial oscillations in a rotating fluid cylinder. *J. Fluid Mech.*, 40: 603–640, 1969.

A. D. McEwan. Laboratory demonstration of angular momentum mixing. *Geophys. Fluid Dyn.*, 5:283–311, 1973.

A. D. McEwan. Angular momentum diffusion and the initiation of cyclones. *Nature*, 260:126–128, 1976.

J. C. McWilliams. The emergence of isolated coherent vortices in turbulent flow. *J. Fluid Mech.*, 146:21–43, 1984.

G. K. Mikhailov and S. Y. Stepanov. Leonhard euler and his contribution to the development of mechanics. *J. App. Math. Mech.*, 71:157–167, 2007.

P. Moin and K. Mahesh. Direct numerical simulation: A tool in turbulence research. *Annu. Rev. Fluid Mech.*, 30:539–578, 1998.

Y. Morinishi, K. Nakabayashi, and S. Q. Ren. Dynamics of anisotropy on decaying homogeneous turbulence subjected to system rotation. *Phys. Fluids*, 13:2912–2922, 2001.

C. Morize and F. Moisy. Energy decay of rotating turbulence with confinement effects. *Phys. Fluids*, 18:065107–1–9, 2006.

C. Morize, F. Moisy, and M. Rabaud. Decaying grid-generated turbulence in rotating tank. *Phys. Fluids*, 17:095105–1–11, 2005.

W.-C. Müller and M. Thiele. Scaling and transfer in rotating turbulence. *Europhys. Lett.*, 77:34003–1–5, 2007.

A. H. Nayfeh. *Perturbation Methods.* Wiley, 1973.

S. Nazarenko. Sandpile behaviour in discrete water-wave turbulence. *J. Stat. Mech.*, L02002, 2006. URL `doi:10.1088/1742-5468/2006/02/L02002`.

S. Nazarenko. 2d enslaving for MHD turbulence. *New J. Phys.*, 9:307–1–14, 2007.

S. Nazarenko and J.-P. Laval. Non-local two-dimensional turbulence and batchelor's regime for passive scalars. *J. Fluid Mech.*, 403:301–321, 2000.

A. C. Newell. Rossby wave packet interactions. *J. Fluid Mech.*, 35:255–271, 1969.

K. Ngan, D. N. Straub, and P. Bartello. Three-dimensionalization of freely-decaying two-dimensional turbulence. *Phys. Fluids*, 16:2918–2932, 2004.

K. Ngan, D. N. Straub, and P. Bartello. Dissipation of synoptic-scale flow by small-scale turbulence. *J. Atmos. Sci.*, 65:766–791, 2008.

S. A. Orszag and G. S. Patterson. Numerical simulations of three-dimensional homogeneous isotropic turbulence. *Phys. Rev. Lett.*, 28:76–79, 1972.

A. Persson. How do we understand the Coriolis force? *Bull. Amer. Met. Soc.*, 79: 1373–1385, 1998.

O. M. Phillips. Energy transfer in rotating fluids by reflection of inertial waves. *Phys. Fluids*, 6:513–520, 1963.

H. Poincaré. *Sience et Méthode.* Flammarion, 1908.

J. Proudman. On the motion of solids in a liquid possessing vorticity. *Proc. Roy. Soc. (London)*, A92:408–424, 1916.

A. Pushkarev. On the komolgorov and frozen turbulence in numerical simulation of capilarity waves. *Eur. J. Mech. B/Fluids*, 18:345–351, 1999.

E. J. Reese and B. A. Smith. Evidence of vorticity in the Great Red Spot. *Icarus*, 9: 474–486, 1968.

L. F. Richardson. *Weather Prediction by Numerical Process.* Cambridge University Press, 1922.

P. H. Rothe and J. P. Johnsto. Free shear layer behaviour in rotating systems. *J.Fluids Eng.*, 101:117–120, 1979.

R. Salmon, G. Holloway, and M. C. Hendershott. The equilibrium statistical mechanics of simple quasi-geostrophic models. *J. Fluid Mech.*, 75:691–703, 1976.

L. M. Smith and Y. Lee. On near resonances and symmetry breaking in forced rotating flows at moderate rossby number. *J. Fluid Mech.*, 535:111–142, 2005.

L. M. Smith and F. Waleffe. Transfer of energy to two-dimensional large scales in forced, rotating three-dimensional turbulence. *Phys. Fluids*, 11:1608–1622, 1999.

L. M. Smith and V. Yakhot. Bose condensation and small-scale structure generation in random force driven 2d turbulence. *Phys. Rev. Lett.*, 71:352–355, 1993.

G. Sparrow. *The planets: A journey through the solar system.* Quercus, 2006.

M. Tanaka and N. Yokoyama. Effects of discretization of the spectrum in water-wave turbulence. *Fluid Dyn. Res.*, 34:199–216, 2004.

G. I. Taylor. Motion of solids in fluids when the flow is not irrotational. *Proc. Roy. Soc. (London)*, A93:99–113, 1917.

G. I. Taylor. Experiments on the motion of solid bodies in rotating fluids. *Proc. Roy. Soc. (London)*, A104:213–218, 1923.

S. C. Traugott. Influence of solid-body rotation on screen-produced turbulence. *Nat. Advis. Comm. Aero. Wash. Tech. Note*, page 4135, 1958.

D. J. Tritton. Stabilization and destabilization of turbulent shear flow in a rotating fluid. *J. Fluid Mech.*, 241:503–523, 1992.

D. J. Tritton. Turbulence in rotating fluids. In P. Roberts and A. M. Soward, editors, *Rotating fluids in geophysics*, pages 104–138. Academic Press Inc., 1978.

M. L. Waite and P. Bartello. Stratified turbulence dominated by vortical motion. *J. Fluid Mech.*, 517:281–308, 2004.

F. Waleffe. The nature of triad interactions in homogeneous turbulence. *Phys. Fluids*, 4:350–363, 1992.

F. Waleffe. Inertial transfers in the helical decomposition. *Phys. Fluids*, 5:677–685, 1993.

T. Warn. Statistical mechanical equilibria of the shallow water equations. *Tellus*, 38A:1–11, 1986.

H. T. Witt and P. N. Joubert. Effect of rotation on turbulent wake. In *Proc. 5th Symp. on Turbulent Shear Flow*, pages 21.25–21.30. Cornell, 1985.

Y. K. Y. Yamazaki and R. Rubeinstein. Dynamics of inviscid truncated model of rotating turbulence. *J. Phys. Soc. Jap*, 71:81–92, 2002.

P. K. Yeung and Y. Zhou. Numerical study of rotating turbulence with external forcing. *Phys. Fluids*, 10:2895–2909, 1998.

A. Youssef and P. S. Marcus. The dynamics of jovian white ovals from formation to merger. *Icarus*, 162:74–93, 2003.

V. E. Zakharov, A. O. Korotkevich, A. N. Pushkarev, and A. I. Dyachenko. Mesoscopic wave turbulence. *JETP Lett.*, 82:544–548, 2005.

Y. Zhou. A phenomenological treatment of rotating turbulence. *Phys. Fluids*, 7: 2092–2094, 1995.